

On the Stability of Supersonic Boundary Layers with Injection

Thesis by
Bryan E. Schmidt

In Partial Fulfillment of the Requirements for the
degree of
Doctor of Philosophy

The Caltech logo, consisting of the word "Caltech" in a bold, orange, sans-serif font.

CALIFORNIA INSTITUTE OF TECHNOLOGY
Pasadena, California

2016
Defended May 12, 2016

© 2016

Bryan E. Schmidt
ORCID: 0000-0001-9193-7760

All rights reserved

ACKNOWLEDGEMENTS

I would first like to thank Professor Joe Shepherd for the opportunity to work in his research group while at Caltech. He has made the past five years a great pleasure. I am immensely grateful for his mentorship, guidance, and encouragement. I value the friendship we have built working together. I also thank Professor Hans Hornung who has also been a very valuable mentor to me during my time as a Ph.D. student. I am honored to have worked with these two men and to be a part of each of their legacies. Bahram Valiferdowsi has been instrumental in keeping the machinery of the Ludwieg tube laboratory running smoothly, and he has been a pleasure to work with. I am grateful for the friendship we have formed.

I would like to thank Professors Tim Colonius and Joanna Austin for being a part of my thesis committee and for the time they have invested in reviewing my work. I am thankful for the time Professor Guillaume Blanquart has spent reviewing my work and providing helpful insights. Ravi Ravichandran has served as a mentor for me and has invested in my career. He has also inspired me with his efforts to promote STEM education, particularly the partnership between GALCIT and Base11 which I have had the privilege to have been a part of. Much of the financial support for my Ph.D. work has come from the Foster and Coco Stanback STEM Fellowship, which is a direct result of this partnership.

I consider myself fortunate to have shared a laboratory and worked with a number of excellent researchers and human beings during my time at Caltech. In particular I thank Professor Nick Parziale for mentoring me and helping me to develop as a researcher during the beginning of my graduate career. Dr. Joe Jewell was a pleasure to work with and contributed to my development as well. Andrew Knisely has been a good friend and collaborator, and I am thankful that Professor Austin brought him to the T5 laboratory in 2014.

I would like to thank the other past and present members of Professor Shepherd's research group. In particular, Dr. Josué Melguizo-Gavilanes has been very generous with his time and patient with me as he explained to me the subtleties of CFD and OpenFOAM specifically. Dr. Neal Bitter has been a good friend and colleague, and I enjoyed our time spent together working out puzzles in high speed fluid mechanics. His insights have been valuable to this work. I was fortunate to have mentored and worked with Nick Mejia during his time at Caltech in the summer of 2015. Rich

Kennedy and Jason Schlup had a very successful Ae104c project designing and building the pneumatic valve in the Ludwieg tube that enabled me be much more productive in the laboratory. Stephanie Coronel, Jean-Christophe Veilleux, and Drs. Rémy Mevel and Jason Damazo have been a pleasure to work with.

I also formed significant friendships with Professor Daniel Araya and Dr. Brock Bobbitt. I enjoyed spending time with them and discussing both our respective research projects and life in general. Both of them contributed many helpful pieces of advice and comments on my work. I am also thankful for their excellent examples of fatherhood and am grateful that I had them to learn from and didn't have to go first. I value the time our families were able to share with each other.

During my time at Caltech I am proud to have been a part of the GALCIT softball team and prouder of the fact that we have won four championships together. Playing softball with Nick Parziale, Joe Jewell, Jason Rabinovitch, Jason Schlup, Reeve Dunne, Dustin Summy, Andrew Knisely, and others has been one of my favorite parts of life outside the laboratory in graduate school.

I am grateful for the many caring teachers and mentors who have helped me succeed academically and pushed me to be better throughout my education. Professor Dennis Kochman at Caltech and Professors James T'ien, Joe Prahl, and Paul Barnhart at Case Western Reserve University have had a particularly significant impact.

I would like to thank my church family at Lake Avenue Church in Pasadena for being a loving and supporting network of friends for my family and I during my time at Caltech. I am particularly thankful for the friendship and mentorship of Pastor Jeff Liou who has contributed greatly to my personal growth. I am also especially grateful for the friendship of the members of my small group: Brock and Lindsay Bobbitt, Aaron and Daisy Rosales, Josh and Jacqueline Olson, Bassem and Amber Wahbi, Ben and Julie Immink, Anton and Nataliya Dubrovskiy, Hyun-Sik and Ok-Young Kim, Jon and Jeni Yackley, and Ryan and Eva Black.

I am very thankful for the loving support of my parents Jayne and Eric Schmidt and my siblings Cory and Karyn Schmidt, without whom I would not have achieved the level of success that I have. I am also grateful to the many members of my extended family who have supported me throughout my academic career including my time at Caltech. This thesis is partially dedicated to them.

I am most indebted to my family: Karina, Lukas, and Ottery. Their unconditional love has made my graduate work enjoyable. I am particularly thankful for my wife Karina, who has been exceedingly patient, kind, and supportive throughout my Ph.D. I could not ask for a better partner, teammate, and friend. This thesis is also dedicated to them.

Finally, I thank God for His overly abundant grace. To paraphrase Eric Liddell: God made me love science, and when I work I feel His pleasure. *Soli Deo gloria.*

*It is the glory of God to conceal a matter
But the glory of kings is to search out a matter
Proverbs 25:2*

ABSTRACT

The problem of supersonic flow over a 5 degree half-angle cone with injection of gas through a porous section on the body into the boundary layer is studied experimentally. Three injected gases are used: helium, nitrogen, and RC318 (octafluorocyclobutane). Experiments are performed in a Mach 4 Ludwieg tube with nitrogen as the free stream gas. Shaping of the injector section relative to the rest of the body is found to admit a "tuned" injection rate which minimizes the strength of shock waves formed by injection. A high-speed schlieren imaging system with a framing rate of 290 kHz is used to study the instability in the region of flow downstream of injection, referred to as the injection layer. This work provides the first experimental data on the wavelength, convective speed, and frequency of the instability in such a flow. The stability characteristics of the injection layer are found to be very similar to those of a free shear layer. The findings of this work present a new paradigm for future stability analyses of supersonic flow with injection.

PUBLISHED CONTENT AND CONTRIBUTIONS

- Parziale, N. J., J. S. Damazo, B. E. Schmidt, P. S. Wang, H. G. Hornung, and J. E. Shepherd (2015). “Pulsed Laser Diode for use as a Light Source for Short-Exposure, High-Frame-Rate Flow Visualization”. In: *AIAA SciTech 2015*. AIAA-2015-0530. AIAA.
- Schmidt, B. E. (2014). *Compressible Flow Through Porous Media with Application to Injection*. Internal Report FM 2014.001. California Institute of Technology.
- Schmidt, B. E., N. P. Bitter, H. G. Hornung, and J. E. Shepherd (2014). “Experimental Investigation of Gas Injection into the Boundary Layer on a Slender Body in Supersonic Flow”. In: *Aviation 2014: Stability and Transition*. AIAA-2014-2496. AIAA.
- (2015). “Injection into Supersonic Boundary Layers”. In: *AIAA Journal*. doi: 10.2514/1.J054123.
 - Schmidt, B. E. and J. E. Shepherd (2015a). “Analysis of Focused Laser Differential Interferometry”. In: *Aviation 2015: Ground Testing*.
 - (2015b). “Analysis of focused laser differential interferometry”. In: *Applied Optics* 54.28, pp. 8459–8472.
 - (2015c). “Oscillations in cylinder wakes at Mach 4”. In: *Journal of Fluid Mechanics* 785.
 - (2016). “Measurements of instability in supersonic flow with injection by time-resolved flow visualization”. In: *AIAA SciTech 2016*. AIAA-2016-0599. AIAA.

TABLE OF CONTENTS

Acknowledgements	iii
Abstract	vii
Published Content and Contributions	viii
Table of Contents	ix
List of Illustrations	xi
List of Tables	xxi
Chapter I: Introduction	1
1.1 Applications of Injection	1
1.2 Remaining Issues	5
1.3 Project Scope and Outline	6
Chapter II: Facility & Test Procedure	8
2.1 Ludwig Tube	8
2.2 Pneumatic Valve	9
2.3 Test Articles	13
2.4 Injected Gases	19
2.5 OpenFOAM Computations	22
Chapter III: Diagnostics	27
3.1 Measurement Technique Review	27
3.2 Surface Measurements	28
3.3 FLDI Analysis	28
3.4 High-speed Schlieren Technique	29
Chapter IV: Results	35
4.1 Full-field Imaging	35
4.2 High-speed Imaging	43
4.3 OpenFOAM Computations	57
Chapter V: Analysis	78
5.1 Full Field Data	78
5.2 Instability Wave Analysis	82
Chapter VI: Summary and Conclusions	100
6.1 Introduction	100
6.2 Facility & Test Procedure	101
6.3 Diagnostics	102
6.4 Results	102
6.5 Analysis	104
6.6 Conclusions	107
6.7 Recommendations for Future Work	107
Bibliography	110
Appendix A: Mass Diffusion in OpenFOAM	116
Appendix B: Machine Drawings	122

Appendix C: Analysis of Focused Laser Differential Interferometry	143
C.1 Introduction	143
C.2 FLDI Theory	144
C.3 Computational Method	148
C.4 Software Verification	152
C.5 Simulated Measurements	164
C.6 Conclusions	175
Appendix D: Experimental Conditions	177

LIST OF ILLUSTRATIONS

<i>Number</i>	<i>Page</i>
1.1 Sketch of the flow field associated with injection into a supersonic flow. Velocity profiles are shown in blue before and after injection.	1
2.1 Solid model of the Caltech Ludwieg tube shown with the Mach 4 nozzle. The overall length of the facility is 23.5 m. Republished with permission of AIAA. From Schmidt et al. (2015); permission conveyed through Copyright Clearance Center, Inc.	8
2.2 Section view of the Ludwieg tube nozzle with the upstream diaphragm station labeled. Flow is from left to right.	9
2.3 Section view of the Ludwieg tube with the valve installed. The valve is shown in both the closed (a) and open (b) positions. The sections of the cylinder are labeled upstream and downstream corresponding to the direction of flow in the Ludwieg tube.	11
2.4 Comparison of the bench test data with the numerical ODE model described in this section.	12
2.5 A photograph of the installed valve in a partially-opened position.	12
2.6 <i>Left:</i> Pitot pressure traces from a run with a diaphragm and a run with the valve. The effective opening time of the valve is about 40 ms and the resulting run time is approximately 60 ms. <i>Right:</i> Power spectra of pitot pressure during the steady run time for a shot with a diaphragm and a shot with the valve. The valve reduces the noise level in the tunnel by a factor of about 2-3 across all frequencies. High-frequency spikes in both spectra are due to electrical noise.	13
2.7 Both models used in this work. One has a cylindrical injector section (top) and the other has a conical section (bottom). The ruler scale is in inches. Republished with permission of AIAA. From Schmidt et al. (2015); permission conveyed through Copyright Clearance Center, Inc.	14
2.8 5x-magnified images of the surface of injectors. The red line in the lower right corner of each image is 100 μm . Republished with permission of AIAA. From Schmidt et al. (2015); permission conveyed through Copyright Clearance Center, Inc.	14

2.9	Exploded view and assembly of solid model of the test article with the cylindrical injector. Threaded segments of the aluminum tube are colored yellow. Holes for the PCB pressure transducers are visible on the frustum section.	16
2.10	Sketch illustrating 1-D porous flow. The porous media has thickness h and cross-sectional area A . If the flow is incompressible, the flow rate is related to the pressure drop by Equation 2.1.	17
2.11	Sketch of porous flow through an axisymmetric geometry such as the cylindrical injector used in this work. The injector has inner radius r_i and outer radius r_o	17
2.12	Pressure vs. mass flow rate data for air for both injectors fit with Equation 2.13 to determine permeabilities. Republished with permission of AIAA. From Schmidt et al. (2015); permission conveyed through Copyright Clearance Center, Inc.	20
2.13	3-D model of an RC318 molecule. The black spheres represent carbon atoms and the green spheres are fluorine atoms. Image by Fvasconcellos - Own work, Public Domain.	21
2.14	Refined computational grid for the OpenFOAM simulations.	26
3.1	Schematic and wiring diagram for a schlieren imaging setup with a pulsed laser diode light source. Light paths are shown as dashed lines, electrical connections are solid arrows. A: turning mirror, B: concave mirror ($f = 150$ cm), C: diverging lens, D: focusing lens, K: schlieren cutoff, P: phase object.	31
3.2	Example timing diagram for the camera and light source. The timing of this diagram is not specific to any particular experimental case but is simply to show the desired scheme. Republished with permission of AIAA. From Parziale, Damazo, et al. (2015); permission conveyed through Copyright Clearance Center, Inc.	32
3.3	Spectral response chart for the Phantom v710 camera. The black curve is the total response. The orange arrow marks 905 nm, the wavelength of the laser light source. Chart ©Vision Research, Inc. .	33
3.4	Output of the laser diode measured with a photodetector. The full width at half maximum is shown in red, and is 30 ns for a nominal 25 ns pulse.	34

4.1	Sketch of Fedorov's hypothesis of a negatively-sloped injector compensating for the additional displacement thickness created by injection. The graphic on the right shows the desired idealized shock pattern on a cone model: only the shock at the tip of the cone is present. Republished with permission of AIAA. From Schmidt et al. (2015); permission conveyed through Copyright Clearance Center, Inc.	36
4.2	Example schlieren images with the conical injector. The free stream gas and injected gas for these cases is air.	37
4.3	Example schlieren images with the cylindrical injector.	38
4.4	Full-field images with a 40 ns-pulse width from three cases with nitrogen injection at different injection rates. The injector is marked by red lines and the PCB locations are shown with blue lines.	41
4.5	Full-field images with a 40 ns-pulse width from three cases with different injected gases but the same value of δ . The injector is marked by red lines and the PCB locations are shown with blue lines.	41
4.6	Injection layer thickness measured at the rear of the injector section, normalized by the injection length, plotted versus the non-dimensional mass flux F . High Reynolds number cases have a nominal unit Reynolds number of 18×10^6 per meter.	43
4.7	Transition location measured from the front of the injector section plotted against the non-dimensional mass flux F .	43
4.8	Images from a sample case to illustrate the image processing routine. Images (a) through (e) represent stages in the routine with (a) being the raw image and (e) being the final, processed image.	44
4.9	Processed image showing instability waves to be analyzed by autocorrelation. The yellow dashed lines show the region used for autocorrelation.	47
4.10	Autocorrelation curve for the image shown in Figure 4.9. The peak at non-zero lag corresponds to a wavelength of 9 mm.	47
4.11	Histogram of measured wavelengths for an example case. The red line shows a fitted log-normal distribution.	48
4.12	Wavelength normalized by the injector length plotted against the non-dimensional injection rate F for all cases analyzed. The wavelength is measured directly for helium and nitrogen injection and calculated assuming Taylor's hypothesis for RC318 injection.	49

4.13	Series of images of a case with nitrogen injection showing the propagation of waves. Their velocity is determined by cross correlating the region in the images where the waves are present.	50
4.14	Correlation curve for the example case shown in Figure 4.13. The lag, indicated by the red arrows, is converted to a velocity by multiplying by the framing rate.	50
4.15	Distribution of measured velocities for the example case.	51
4.16	Convective velocity normalized by the free stream velocity plotted versus the non-dimensional mass flux F for all cases studied.	51
4.17	Example image from a case with RC318 injection. The colored dots on the left side of the image represent the location of the injection layer edge determined by the Canny, log, Roberts, zero-cross, Prewitt, and Sobel edge-detection methods.	52
4.18	Power spectral density plots from the Prewitt and Sobel methods for the example RC318 injection case. Peaks are observed at 24.5 kHz for both methods.	53
4.19	Response of the PCB pressure transducers in the cone frustum to mechanical vibration. They are labeled in the figure legend according to their distance from the cone tip, measured along the surface of the model.	54
4.20	Spectra from the PCB pressure transducers for four example experiments with injection.	55
4.21	Spectra from transducer 1 for the three injection cases shown in Figure 4.20 compared to the turbulent baseline shown in Figure 4.20a.	56
4.22	Frequency from image analysis and pressure transducers. The frequency from image analysis for the helium and nitrogen injection cases is computed using Taylor's hypothesis while the frequency in the RC318 cases is computed directly from the image processing routine.	57
4.23	Profiles taken at the rear of the injector section for the various grid resolutions tested.	59
4.24	Relative difference in the flow variables plotted as a function of y for the grid with a resolution of $69 \mu\text{m}/\text{cell}$ compared to the most refined grid ($38 \mu\text{m}/\text{cell}$).	59
4.25	Total relative difference (see Equation 4.5) in flow variables as a function of grid resolution.	60

4.26	Results from the three computations with nitrogen injection. Coloring corresponds to density, with the color scale normalized to each case. The value for the non-dimensional mass flux F is given in the upper-left for each case.	61
4.27	Location of wall-normal profiles for all OpenFOAM cases. They are located 120 mm, 132.5 mm, 152 mm, 172 mm, 180.6 mm, 189.2 mm, 197.8 mm, and 206.4 mm from the cone tip, measured along the surface of the model. The case with nitrogen injection with $u_{\text{inj}} = 16 \text{ m/s}$ is shown as an example.	61
4.28	Evolution of flow variables for cases with nitrogen injection. Profiles are taken at the locations indicated in Figure 4.27. Black, blue, and red curves correspond to cases with low, medium, and high rates of injection listed in Table 4.1, respectively.	63
4.29	Mass fraction of injected nitrogen at the wall as a function of s , the variable measured along the cone surface. Here, $s = 0$ corresponds to the end of the injector section. Black, blue, and red curves correspond to increasing injection rate with injection velocities listed in the legend.	64
4.30	Results from the three computations with helium injection. Coloring corresponds to density, with the color scale normalized to each case. The value for the non-dimensional mass flux F is given in the upper-left for each case.	65
4.31	Evolution of flow variables for cases with helium injection. Profiles are taken at the locations indicated in Figure 4.27. Black, blue, and red curves correspond to cases with low, medium, and high rates of injection listed in Table 4.1, respectively.	67
4.32	Mass fraction of helium at the wall as a function of s , the variable measured along the cone surface. Here, $s = 0$ corresponds to the end of the injector section. Black, blue, and red curves correspond to increasing injection rate with injection velocities listed in the legend.	68
4.33	Results from the three computations with RC318 injection. Coloring corresponds to density, with the color scale normalized to each case. The value for the non-dimensional mass flux F is given in the upper-left for each case.	69

4.34 Evolution of flow variables for cases with RC318 injection. Profiles are taken at the locations indicated in Figure 4.27. Black, blue, and red curves correspond to cases with low, medium, and high rates of injection listed in Table 4.1, respectively.	71
4.35 Mass fraction of RC318 at the wall as a function of s , the variable measured along the cone surface. Here, $s = 0$ corresponds to the end of the injector section. Black, blue, and red curves correspond to increasing injection rate with injection velocities listed in the legend.	72
4.36 Experimental measurements of the injection layer thickness measured at the rear of the injector section compared with the displacement thickness at the same location from the OpenFOAM computations (indicated with "OF" in the legend).	73
4.37 Profiles taken at the rear of the injector section for cases with all three injected gases. Cases are selected such that the value of δ^* is similar for all three.	76
4.38 Profiles taken 206.4 mm from the cone tip for cases with all three injected gases. Cases are selected such that the value of δ^* is similar for all three.	77
5.1 δ , measured at the rear of the injector section, normalized by the length of the injector L_{inj} plotted against the dimensionless momentum flux ratio J for all experimental and computational data. The black line is a fitted power law curve considering only data from nitrogen and helium injection cases. The expression for the curve is given in Equation 5.3. The \oplus symbol indicates the tuned condition.	79
5.2 Transition location x_{tr} , measured from the front of the injector section, normalized by the injection layer thickness δ measured at the rear of the injector plotted against the velocity ratio of the injected gas to the free stream gas.	81
5.3 Wavelength normalized by the injector length plotted against the non-dimensional injection momentum flux J for all cases analyzed. The wavelength is measured directly for helium and nitrogen injection and calculated assuming Taylor's hypothesis for RC318 injection. Vertical error bars reflect only uncertainty due to measurement error.	82

5.4 Convective velocity normalized by the free stream velocity plotted versus the non-dimensional momentum flux J for all cases studied. Vertical error bars represent uncertainty due to measurement error, including pixel-locking.	83
5.5 Frequency from image analysis and pressure transducers. The frequency from image analysis for the helium and nitrogen injection cases is computed using Taylor's hypothesis while the frequency in the RC318 cases is computed directly from the image processing routine.	83
5.6 Sample image of instability waves in a cone boundary layer at a unit Reynolds number of 9×10^6 per meter. Yellow arrows indicate the crests of three consecutive waves, and blue vertical lines indicate the locations of the first four pressure transducers. The fifth transducer is outside the viewing window of the camera to the right of the image in the figure.	85
5.7 Spectra from the pressure transducers on a straight cone under the same conditions as the visualization in Figure 5.6. The spectra show growth of an instability around 46 kHz that breaks down to a turbulence at or before the location of the final transducer. The insert shows the spectrum of the first transducer so that the peak at 45.9 kHz can be clearly perceived.	86
5.8 Sketch of a two-dimensional free shear layer flow. Two streams with different velocities and potentially different densities and specific heats are initially separated by a splitter plate and allowed to mix downstream of the plate. A mean velocity profile is sketched in the mixing region. Stream 1 is the high-speed stream and stream 2 is the low-speed stream by definition.	88
5.9 Streamlines in a frame convecting with structures in a shear layer. There are stagnation points for each stream between the structures.	91
5.10 Example momentum profile for a case with nitrogen injection. The curvature thickness δ_c is indicated with black dashed lines.	92
5.11 Wavelength normalized by δ_c using the values in Table 5.1 for the experiments performed with the lower unit Reynolds number condition (9×10^6 per meter nominally).	93

5.12	Ratio of the measured experimental value of wave convective speed to that predicted using Equation 5.14 (tabulated in Table 5.2) plotted against J for cases with a nominal unit Reynolds number of 9×10^6 per meter.	95
5.13	Convective Mach number M_c plotted as a function of the wall-normal coordinate y for three example cases. Profiles are taken at the rear of the injector section.	97
A.1	Schmidt number as a function of temperature for each injected gas diffusing into nitrogen.	118
A.2	Comparison of results of the diffusion box test case for nitrogen.	119
A.3	Comparison of results of the diffusion box test case for nitrogen assuming $Sc = 1$ in Equation A.8.	120
A.4	Comparison of results of the diffusion box test case for helium.	120
A.5	Comparison of results of the diffusion box test case for RC318.	121
C.1	Schematic of an FLDI setup. The two beams are shown as blue and green. Regions where the beams overlap are shown as striped. The coordinate system shown will be the one used throughout this paper.	145
C.2	Illustration of a prism (here, a Wollaston prism). The incident beam of arbitrary polarization is split into two beams by an angle σ , and the two beams at the exit have mutually orthogonal polarization. The ordinary ray is linearly polarized in the direction of beam separation and the extraordinary ray is polarized 90 degrees from the direction of separation.	145
C.3	Computed beam widths (out to $1/e^2$) within 30 mm of the best focus. One beam is outlined in red and the other in blue. The width of the beams at the waist is too small to see on this scale.	150
C.4	Polar grid cross-section non-dimensionalized by the local beam waist size	151
C.5	Transfer function $H_w(k)$ for a single beam for 1-D sinusoidal disturbances in x in an infinitesimally-thin plane at $z = 0$	154
C.6	Transfer function of Equation C.16 plotted for various values of L . As L increases, or, as more signal away from best focus is considered, the error function in Equation C.16 contributes a k^{-1} rolloff beginning at lower values of k . This leads to attenuation of high-wavenumber disturbances away from best focus.	155

C.7	Transfer function $H_w(k)$ for a single beam for uniform 2-D sinusoidal disturbances in x between $z = \pm 10$ mm centered at $z = 0$	155
C.8	Transfer function $H_w(k)$ for a single beam for uniform 2-D sinusoidal disturbances in x between $z = \pm 30$ mm centered at $z = 0$	156
C.9	Transfer function $H(k)$ for the two-beam FLDI for 1-D sinusoidal disturbances in x in an infinitesimally-thin plane at $z = 0$	157
C.10	Transfer function $H(k)$ for the two-beam FLDI for uniform 2-D sinusoidal disturbances in x between $z = \pm 10$ mm centered at $z = 0$	158
C.11	Transfer function $H(k)$ for the two-beam FLDI for uniform 2-D sinusoidal disturbances in x between $z = \pm 30$ mm centered at $z = 0$	158
C.12	Convergence study for the transfer function shown in Figure C.11. The red square indicates the chosen resolution.	159
C.13	Normalized FLDI output signal for sinusoidal disturbances within ± 10 mm of the focus in z , corresponding to the transfer function plotted in Figure C.10.	160
C.14	A solid model of the chamber for the argon jet with dimensions given in mm. The coordinate system shown corresponds to the orientation of the coordinate system of the FLDI beams.	161
C.15	161
C.16	Steady-state result of OpenFOAM computation of the flow out of the argon jet. Velocity vectors are shown on the left and streamlines on the right. Both are superimposed on a contour plot of argon mass fraction. L_{jet} is the length out of the page (in z) that the cross-section shown here extends.	162
C.17	Index of refraction field from the OpenFOAM computation with spline interpolation.	163
C.18	Experimental vs. numerical data for the argon jet experiments detailed in Table C.2. The letters marking each data point correspond to the configurations in Table C.2. The line is the ideal line $y = x$	164
C.19	Cone model used in T5 studies	167
C.20	168
C.21	Output of the FLDI simulation compared to the input boundary layer wave packet density disturbance. The y -axis on the left corresponds to the FLDI output and the y -axis on the right corresponds to the input density at the location of the beams at $z = 0$	170

C.22	Output of the FLDI simulation, scaled with Equation C.27, compared to the input boundary layer wave packet for the optimum value of $Z = 12.6$ mm.	171
C.23	PSD of the FLDI simulation, scaled with Equation C.27 and optimum Z value, compared to the PSD of the input boundary layer wave packet.	171
C.24	173

LIST OF TABLES

<i>Number</i>	<i>Page</i>
2.1 Properties of injected gases at 295 K.	21
2.2 Sutherland coefficients for the three injected gases to be used in calculating viscosity in Equation 2.18.	23
4.1 Flow conditions for the OpenFOAM computations.	58
4.2 Estimated Gladstone-Dale constants for the three gases at a wavelength of approximately 600 nm and room temperature with the computed displacement thicknesses and thicknesses based on index of refraction calculated at the rear of the injector section for cases with $u_{\text{inj}} = 16, 40,$ and 3 m/s for nitrogen, helium, and RC318 injection, respectively.	75
5.1 Values of δ_c for momentum profiles at the beginning of the injector section for the OpenFOAM computations.	93
5.2 Values of $\frac{U_c}{U_\infty}$ computed with Equation 5.14 and the data from the OpenFOAM computations using the lower point of curvature in the momentum profile to determine the conditions in stream 2. Profiles are taken at the rear of the injector section.	95
A.1 Parameters from the Lennard-Jones potential model for the three gases for computing diffusion coefficients.	117
C.1 Optical parameters for simulated FLDI.	148
C.2 Argon jet configurations tested (dimensions in mm).	163
C.3 Boundary layer edge conditions for T5 shot 2789.	166
C.4 Boundary layer wave packet parameters.	169
C.5 Wave packet properties tested with fixed value of Z.	172

Chapter 1

INTRODUCTION

Injection of gas into boundary layers in hypersonic flight has the potential to enable the next generation of high speed vehicles. Flight at hypersonic Mach numbers presents a unique set of challenges, among which are high heating loads that create a need for thermal protection systems and challenges related to supersonic combustion ramjet (scramjet) propulsion. Figure 1.1 shows a sketch of a typical injection system and flow field. In this example, gas is injected orthogonally to the mean flow direction through a porous section in the wall. Injection modifies the velocity profile in the boundary layer as shown in the figure, and also changes the temperature, density, and sound speed profiles. Injection also creates a sudden increase in the displacement thickness of the boundary layer which causes a shock to form in the supersonic free stream. In this work the boundary layer downstream of injection is referred to as the *injection layer* to avoid confusion with conventional boundary layers.

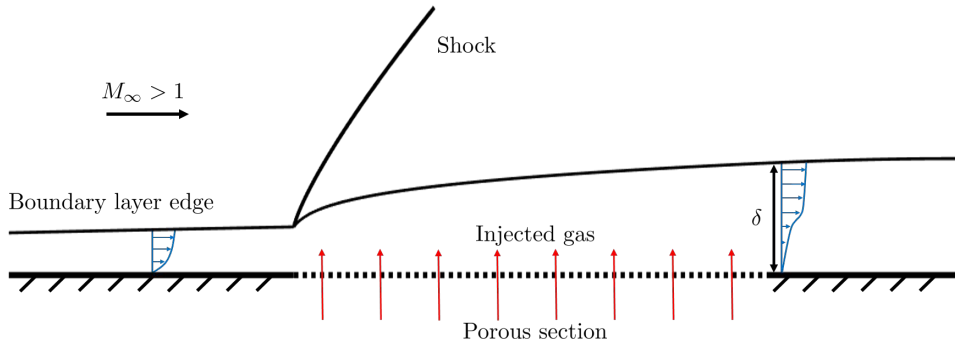


Figure 1.1: Sketch of the flow field associated with injection into a supersonic flow. Velocity profiles are shown in blue before and after injection.

The problem of injection into high speed boundary layers has been studied intermittently over the last half-century for a variety of reasons. The following section reviews some of this research. The work presented here addresses some of the remaining challenges associated with transition to turbulence in these flows.

1.1 Applications of Injection

This section outlines four of the applications for injection into high-speed boundary layers that have motivated studies in the past. These are film and transpiration

cooling, a surrogate for studying ablation, transition delay in hypervelocity boundary layers, and enhancement of scramjet performance. For a more complete discussion of the past work on this topic related to the first two applications, see Schneider (2010).

Film and transpiration cooling

Heating in high speed boundary layers is a significant issue that creates a need for substantial thermal protection systems on hypersonic vehicles. Traditionally these systems are passive, such as the ceramic tiles on the Space Shuttle. The primary drawback of such a system is additional vehicle weight, although lack of reusability due to ablation of the protective material is also a concern. Gas injection has been considered as an active thermal protection system because the layer of cold gas next to the vehicle surface behind the injector has a cooling effect (Aupoix et al., 1998; Cary and Hefner, 1971; Sahoo et al., 2005). The cold injected gas displaces the hot boundary layer fluid away from the vehicle surface, leading to a reduction in heat transfer. See e.g. Figure 7 of Marvin and Akin (1970). When the injected gas is blown tangentially to the surface of the vehicle it is referred to as film cooling, and orthogonally injected gas through a porous surface is called transpiration. Both of these have been studied in the literature.

Transpiration and film cooling are more effective in high speed flows than low speed flows, but covering the entirety or even the majority of a vehicle with such a thermal protection system is likely impractical and the weight savings compared to traditional passive systems may not be significant. Localized cooling, however, remains promising. Local cooling would allow placement of a window or instrument on the surface of a vehicle, which would not be possible if a passive system were used. An injector placed directly upstream of the instrument could cool that area actively while the rest of the vehicle is covered by a traditional passive system.

Egorov et al. (2015) performed a numerical study on a blunt geometry and showed that such a scheme could be effective. Cooling in this type of an arrangement is most effective while the interface between the injected gas and the free stream fluid remains laminar. Turbulence enhances mixing of the streams and therefore decreases cooling. This can be observed in Figure 7 of Marvin and Akin (1970) where the heating rate returns to its value prior to gas injection after transition to turbulence in the injection layer.

Ablation surrogate

Ablation is an extremely complex phenomenon as it involves the coupling of a host of effects including non-equilibrium gas dynamics, chemical reactions, outgassing, boundary layer stability, turbulence, and heat transfer. Understandably, then, researchers have sought to isolate some of the effects and study each in turn. Gas injection has been studied for this reason to decouple the outgassing of pyrolysis products from the other features of flow with ablation.

Some studies have concentrated on blunt geometries such as reentry capsules (Li et al., 2013), while others have instead focused on slender bodies (Marvin and Akin, 1970; Pappas and Okuno, 1960, 1964). The works cited here represent investigations where the stability and transition of the flow were considered. Pappas and Okuno (1960) observed that transition occurs earlier on a porous cone when higher blowing rates are employed and when the molecular weight of the injected gas is lower. This trend is corroborated in many other studies as well (Schneider, 2010), but Li et al. (2013) curiously found computationally that transpiration stabilized the second-mode instability on a flat plate and cone. The results of the current study could be extended to ablation like the investigations cited in this section, but this is not pursued here.

Transition delay

Boundary layer transition in hypersonic flows is dominated by the *second* or Mack mode, particularly when the wall is cold compared to the adiabatic wall temperature as is the case in hypersonic free flight (Mack, 1984). Current understanding of the Mack mode is summarized by Fedorov (2011) and Fedorov and Tumin (2011) and the interested reader is referred to these for further information. Fujii and Hornung (2001) and Wagnild et al. (2009) have shown that the strength of the Mack mode instability can be reduced via acoustic absorption by non-equilibrium effects in the boundary layer gas. This occurs if the time scale of translational/rotational and vibrational energy exchange in the gas molecules is on the same order as the acoustic waves responsible for destabilizing the boundary layer (typically about 1 MHz) and if the vibrational energy states in the gas are sufficiently populated. Both of these conditions are met for carbon dioxide in hypersonic flows.

Leyva et al. (2009) and Jewell et al. (2012) performed experiments in the T5 hypervelocity shock tunnel at Caltech to determine if transpiration of carbon dioxide into an air boundary layer through a porous injector on a sharp cone could delay

transition. The injector in these studies was approximately 40 mm long and began 135 mm from the cone tip.

The data from these studies suggest a delay in transition for carbon dioxide injection compared to argon injection, which would not have the non-equilibrium effects required for acoustic absorption. They are inconclusive, however, regarding the overall efficacy of carbon dioxide injection versus no injection. The results are further complicated by the fact that Fedorov, Malmuth, et al. (2001) showed that a porous surface such as the one on the injector section absorbs acoustic energy and therefore contributes to stabilization of the Mack mode. Furthermore, Fedorov, Soudakov, et al. (2014) found that injection in such a configuration has a destabilizing effect when non-equilibrium effects are not considered. More work is warranted on this subject, but the current study focuses on low-enthalpy flow where non-equilibrium effects are not important and therefore the potential application of transition delay in hypersonic boundary layers is not kept in mind.

Scramjet performance

Scramjet engines are considered by many to be the best method for propulsion at very high Mach numbers in the atmosphere, and improving scramjet performance is an active research topic. Gas injection in scramjet inlets in particular has a number of promising benefits. In this application a small fraction of the vehicle's fuel is injected in the inlet prior to the gas reaching the combustor, where the remainder of the fuel is injected.

Barth, Wheatley, et al. (2013) demonstrated that injection in scramjet inlets not only produces the cooling effect described earlier in this section, but also significantly reduces skin friction drag. This is important because skin friction drag in the inlet forms a substantial fraction of the total scramjet drag, as much as 25%. The effect is enhanced if combustion occurs. The mechanism seems to be twofold. First, the modification of the velocity profile reduces the slope of the velocity curve at the wall, thereby reducing skin friction. Secondly, combustion causes dilatation that further favorably modifies the velocity profile and the temperature rise associated with combustion reduces the magnitude of turbulent velocity fluctuations, which in turn reduces the Reynolds shear stress.

Second, flow separation due to compression in scramjet inlets is a potential issue that can degrade performance. Laminar boundary layers are more prone to separation than turbulent boundary layers (Ogorodnikov et al., 1972), so trips are often

employed to encourage transition to turbulence (Berry et al., 2001). Injection destabilizes the boundary layer, so injection in the engine inlet could eliminate the need for physical trips.

Finally, Gehre et al. (2015) and Barth, Wise, et al. (2015) show that if the injected fuel in the inlet mixes sufficiently with the air in the free stream and is combusted, significant gains are made in overall engine efficiency. These gains are primarily due to the production of radical species and heating in the inlet region that promote combustion in the combustor. All of these effects are much stronger if the interface between the injected gas and the free stream is turbulent.

1.2 Remaining Issues

The current study is focused on addressing issues related to the implementation of injection for localized transpiration cooling and fuel injection in scramjet inlets. Attention is given to the mechanics of the flow field and although the results of this work have design implications, the design of an injection system is not considered directly. Effects are subdivided into inviscid and viscous categories.

Formation of waves

Transpiration causes an abrupt increase in the displacement thickness of the boundary layer, which the free stream perceives the same as a change in the geometry of the body. The supersonic flow is turned in response to these changes by oblique shock waves and expansion waves. The strength of the shock waves is dependent on the injection rate and body geometry, but they can be strong enough to be detrimental to performance, particularly in internal flows.

For instance Ogawa et al. (2015) found that the shock wave formed at the beginning of the injector in a scramjet inlet was reflected several times in the narrow channel and caused substantial pressure losses depending on the injection rate. They found that for their geometry the benefits of injection were counteracted by the total pressure loss. The amount of fuel that could be injected while maintaining a net benefit was also limited to avoid larger pressure losses.

Wave formation is more important in internal flows than external flows, but Schmidt et al. (2015) demonstrate that the shock wave at the beginning of the injector in an external flow can be strong enough to create an adverse pressure jump capable of causing the incoming boundary layer to transition to turbulence. Effective cooling is dependent on a laminar flow downstream of injection, so immediate transition

to turbulence would substantially limit the usefulness of transpiration for cooling. The mitigation of waves is therefore important for the implementation of injection systems for both applications considered.

Flow stability

Clearly in both applications the state of the boundary layer downstream of injection, whether laminar or turbulent, is of importance. A laminar injection layer is crucial for effective cooling because of reduced transport of heat compared to a turbulent layer. In scramjet inlets, turbulence decreases the efficacy of cooling at the wall, but it also substantially promotes mixing which is necessary for efficient combustion. Combustion must occur in the inlet in order for the benefits of injection to be fully realized.

Even so, the stability of this flow has not been studied in great detail. The vast majority of experimental data pertaining to stability are transition locations, and though these are useful, they contribute little to the understanding of the underlying physics of the transition process. A handful of numerical studies have been performed to analyze stability characteristics of supersonic flows with injection, e.g. Li et al. (2013), but experimental measurements are scarce (Schneider, 2010). Flow stability with injection of a foreign gas, i.e. one that is different from the free stream gas, is more difficult to analyze computationally because fluid properties are dependent on the local composition, which means that the transport equations are coupled to the Navier-Stokes equations. Stability studies of this kind are even more rare, but in most practical applications of injection the injected gas would differ from the free stream gas. These factors motivate an experimental investigation of the stability properties of supersonic flow with injection, including injection of foreign gas species.

1.3 Project Scope and Outline

The instability in supersonic flow with injection is analyzed in this work. A method for diminishing the strength of waves formed by injection by modifying the body geometry is also presented. Experiments are performed in the Caltech Mach 4 Ludwieg tube with a 5-degree half-angle cone as the base model because of its canonical shape. Injection is achieved by transpiration through a porous injector section on the model, and three gases with different molecular weights are injected. The primary aim of the study is to characterize the disturbances that lead to transition in this flow.

The Ludwieg tube facility and the test article are described in Chapter 2 along with computations of the base flow. The choice of injected gases is also explained. In Chapter 3 the high-speed schlieren technique used to measure instability waves in the flow is described and is accompanied by a review of potential measurement techniques that were also considered. Results of the experiments are given in Chapter 4. Data processing routines are also presented in this chapter. The results are analyzed in Chapter 5, and the work is summarized and concluded in Chapter 6.

Chapter 2

FACILITY & TEST PROCEDURE

The test facility and experimental apparatus are presented in this chapter. The Ludwieg tube is described with special attention given to modifications made to the facility for the current work. The test article is then described and the flow through the porous injector section is analyzed. The choice of injected gases is explained and the properties of the gases are given. The flow meter and calibration technique are also described. Finally, the setup for numerical simulations of the experiments in OpenFOAM is presented.

2.1 Ludwieg Tube

Experiments for this work were performed in the Caltech Ludwieg Tube. The facility is described in detail by Mouton (2007) and summarized here. It consists of a 17 m-long, 300 mm-diameter tube, a nozzle, test section, and dump tank. Experiments in this work exclusively use the axisymmetric Mach 4 nozzle described in Section 6.2 of Mouton (2007). The nozzle has an exit diameter of 315 mm. A perspective view of the Ludwieg tube is shown in Figure 2.1.

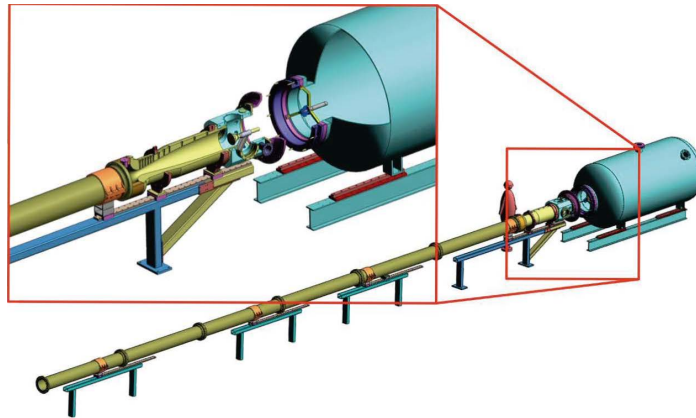


Figure 2.1: Solid model of the Caltech Ludwieg tube shown with the Mach 4 nozzle. The overall length of the facility is 23.5 m. Republished with permission of AIAA. From Schmidt et al. (2015); permission conveyed through Copyright Clearance Center, Inc.

Most Ludwieg tubes use diaphragms to separate the high- and low-pressure sections. A diaphragm is either inserted between the test section and dump tank, referred

to here as a downstream diaphragm configuration, or just ahead of the nozzle contraction, called an upstream diaphragm configuration. When it is operated with a diaphragm, the Caltech Ludwieg Tube uses an upstream diaphragm configuration as shown in Figure 2.2 because the facility has issues with starting when a downstream diaphragm is used. This is described in Section 6.3 of Mouton (2007). When operated with a diaphragm, the nozzle, test section, and dump tank are evacuated and the driver tube is pressurized until the diaphragm ruptures. When the diaphragm breaks, a weak shock wave propagates through the nozzle and test section and a non-steady expansion wave propagates away from the nozzle in the driver tube and reflects from the tube end wall. These processes establish steady supersonic flow in the test section, and the reservoir conditions upstream of the nozzle contraction remain constant until the reflected expansion wave returns to the nozzle-driver tube junction.

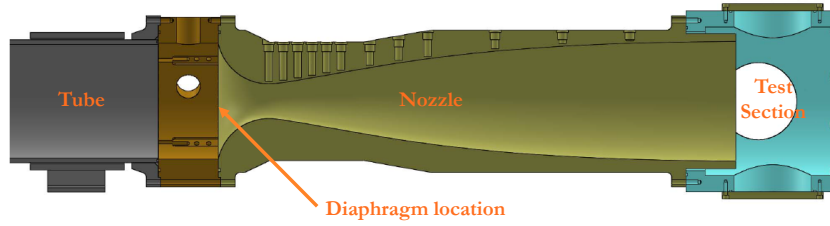


Figure 2.2: Section view of the Ludwieg tube nozzle with the upstream diaphragm station labeled. Flow is from left to right.

Nitrogen is used as the test gas in this work, and the reservoir temperature in the driver tube is nominally 297 K. The driver pressure can be varied between 100 and 600 kPa, but is determined by the strength of the diaphragm used when the facility is operated with a diaphragm. Assuming quasi-1D, isentropic flow of a perfect gas with a free stream Mach number of 4.0, the free stream temperature is 68 K, the velocity is 672 m/s, and the unit Reynolds number is between $5 - 25 \times 10^6$ per meter depending on the reservoir pressure. The maximum test time is fixed by the length of the driver tube and is approximately 100 ms.

2.2 Pneumatic Valve

Operating the facility with a diaphragm has several drawbacks. First, the stagnation pressures that can be accessed are limited by commercially available diaphragms. Polycarbonate film diaphragms are used, and can only be bought in thicknesses of 25 μm , 127 μm , and 254 μm , meaning that only three nominal conditions can be

used. The strength of a diaphragm with a given thickness varies, however, making it difficult to repeat test conditions precisely. Second, the broken diaphragm creates disturbances that propagate into the test section, adding to the free stream noise level of the facility. Finally, the diaphragm needs to be changed after each run, placing a lower limit on the turnaround time of about 30 minutes.

To address these issues, a fast-acting valve based loosely on the one used in the Hypersonic Ludwieg tube Braunschweig (HLB) (Estorf et al., 2003) was designed and installed in the Caltech Ludwieg Tube to replace the diaphragm. A solid model of the installed valve is shown in Figure 2.3. The primary component of the valve is a pneumatic cylinder that is suspended in the center of the Ludwieg tube driver. A plug is attached to the shaft of the cylinder, which creates a seal in the nozzle throat, separating the high pressure driver from the low-pressure test section until the run begins, just as a diaphragm would. Operation is as follows. The upstream side of the cylinder is pressurized with the downstream side open to the ambient air in the laboratory, moving the plug into the throat of the nozzle (top of Figure 2.3). With the plug in place, the nozzle, test section, and dump tank are evacuated while the driver tube is pressurized with the test gas. When the desired stagnation pressure is reached in the driver section, the upstream side of the cylinder is opened to the laboratory air and the downstream side is pressurized. When the force on the piston inside the cylinder becomes sufficiently high to overcome the force due to the pressure difference across the plug, the plug quickly moves out of the nozzle throat and joins with the cylinder housing, forming a smooth center body (bottom of Figure 2.3). Steady flow in the test section is achieved once the plug is secure against the housing.

Besides the requirement that the valve fit inside a 16.2 cm-diameter shroud, the primary requirement for the valve is that the plug must move far enough to fully retract from the converging part of the nozzle while leaving sufficient time for steady test flow once the valve is open, and it must not recoil upon reaching the open position. The design point is 15 cm in 20 ms for a 500 kPa stagnation pressure condition. Opening time is expected to be longer than this for lower-pressure conditions, but as long as the opening time is sufficiently less than 100 ms the tunnel will still have a satisfactory steady run time. Operation of the pneumatic cylinder is modeled assuming isentropic expansion and compression inside the cylinder and quasi-steady Fanno flow through the exhaust line which is open to the atmosphere from the upstream section of the cylinder. The fill line is assumed to be closed

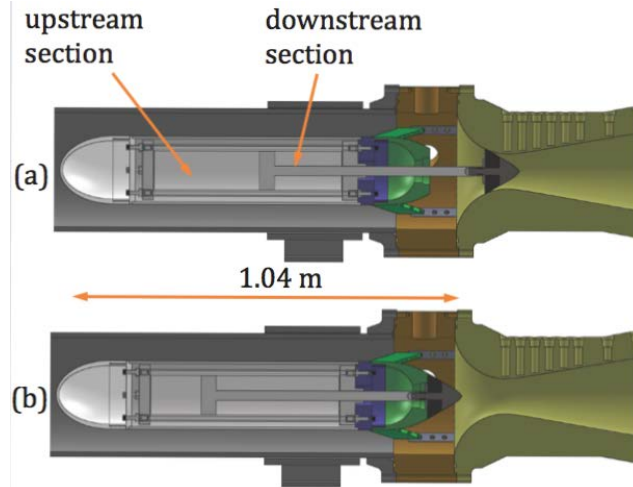


Figure 2.3: Section view of the Ludwieg tube with the valve installed. The valve is shown in both the closed (a) and open (b) positions. The sections of the cylinder are labeled upstream and downstream corresponding to the direction of flow in the Ludwieg tube.

once the piston begins to move. These assumptions lead to a system of three ODEs describing a nonlinear spring-mass-damper system and can be integrated numerically using standard Runge-Kutta methods.

The valve was bench tested to validate the numerical model using string to hold the plug in place to simulate the pressure difference during a run. The string was cut to simulate the start of a run after pressurizing the cylinder. The position of the plug was measured with a Keyence LK-G407 laser range finder. Figure 2.4 shows a comparison between the numerical ODE model and the performance of the valve, indicating the utility of the model for design purposes.

The valve was designed iteratively with the numerical solution to the model until a suitable design was obtained. To minimize cost, the cylinder chosen is an off-the-shelf Parker pneumatic cylinder. The piston is enclosed in a streamlined cylindrical shroud to minimize perturbation to the flow. The sealing face of the plug, shown in black in Figure 2.3, is made from polyurethane and is designed to match the slope of the nozzle contour when the piston is in the closed position. The end of the plug is made from aluminum and is a streamlined shape. The cylindrical shroud is made from PMMA and the upstream end of the shroud is rapid-prototyped nylon to reduce the weight of the structure. Its shape is an ellipsoid and the surface is roughened to encourage boundary layer transition and therefore minimize flow separation at the trailing end of the plug. Pressurized gas to operate the valve is supplied from the

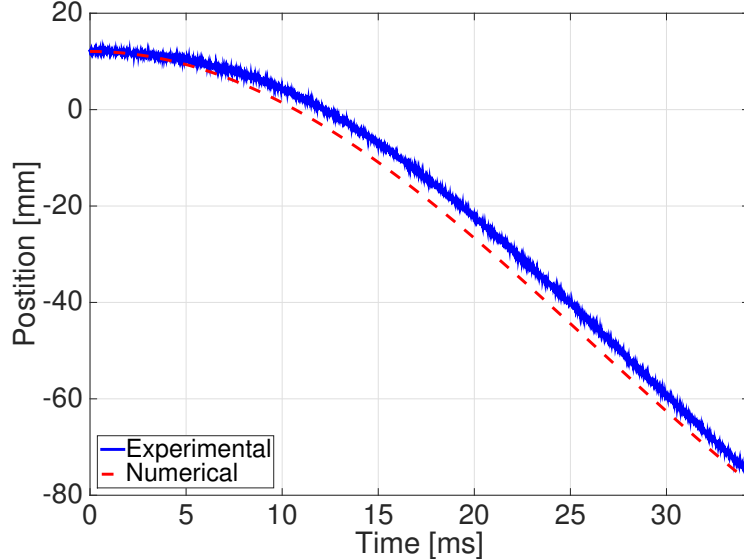


Figure 2.4: Comparison of the bench test data with the numerical ODE model described in this section.

compressed gas cylinders used to fill the driver tube. A photograph of the installed valve is shown in Figure 2.5.

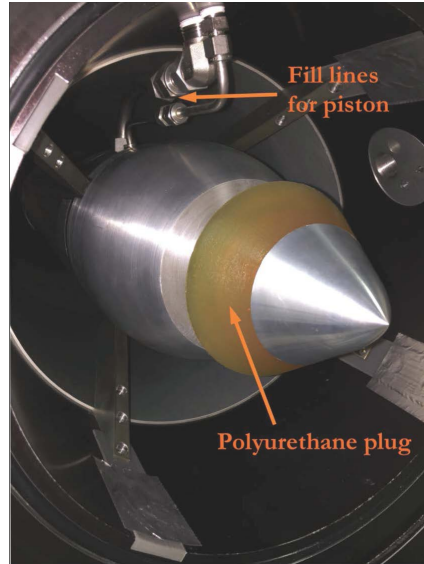


Figure 2.5: A photograph of the installed valve in a partially-opened position.

Figure 2.6 shows the free stream pitot pressure traces and spectra for nominal 300 kPa-reservoir pressure runs with a diaphragm and the valve. The left-hand plot shows that the opening process of the valve reduces the total test time from 100 ms to about 60 ms. This is not detrimental, however, as 60 ms still provides for over 100 flow times for a 30 cm-long test article. The right-hand plot reveals that the

valve reduces the noise in the stagnation pressure across all frequencies by a factor of 2-3. The RMS noise level in stagnation pressure is reduced from 1-2% to 0.7%.

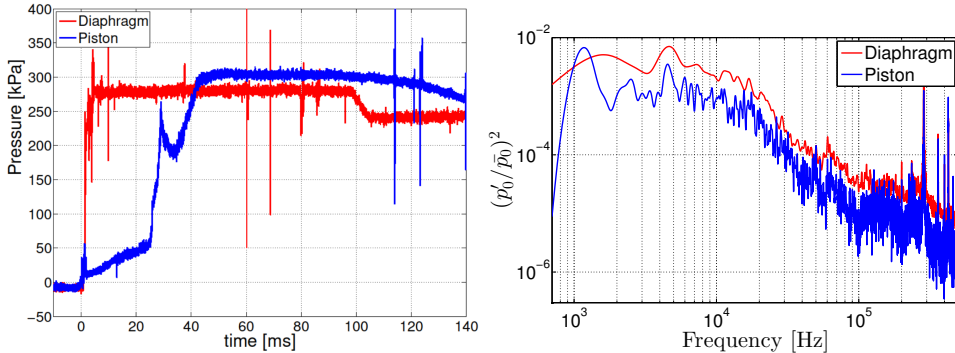


Figure 2.6: *Left:* Pitot pressure traces from a run with a diaphragm and a run with the valve. The effective opening time of the valve is about 40 ms and the resulting run time is approximately 60 ms. *Right:* Power spectra of pitot pressure during the steady run time for a shot with a diaphragm and a shot with the valve. The valve reduces the noise level in the tunnel by a factor of about 2-3 across all frequencies. High-frequency spikes in both spectra are due to electrical noise.

The other advantages of the valve over operation with the diaphragm are that the tunnel can be operated at any pressure between the limits of 100 kPa and 600 kPa instead of only those determined by available diaphragms. Test conditions are also now repeatable to within a few percent (see e.g. Appendix D). Additionally, the Ludwieg tube does not need to be opened after each run to replace a diaphragm, so the turnaround time is reduced from 30 minutes to about 12 minutes. The remaining gas in the driver tube after a run does not need to be evacuated after each experiment as it does when using a diaphragm, so there is also a cost savings associated with using less gas in the driver per shot along with the cost savings of no longer needing to purchase diaphragms to operate the tunnel.

2.3 Test Articles

Two test articles are used in this work, both based on a sharp-tipped 5 degree half-angle cone. The tip radius is measured to be 300 μm . This radius is sufficiently small that the entropy layer is swallowed before the injector section is reached and therefore the cone tip can be treated as sharp (Stetson, 1987). The models are shown in Figure 2.7. Both have an aluminum tip section that is 131 mm long measured along the surface of the cone, followed by a 40 mm long injector section, followed by a frustum. The frustum is made from Delrin, a machinable plastic. One model has a conical injector and is only used to examine the effects of shaping the injector. The

other has a cylindrical injector, and this article is used to analyze the instability in the flow. The frustum section of this model is instrumented with five PCB 132A31 piezoelectric pressure transducers along its length.

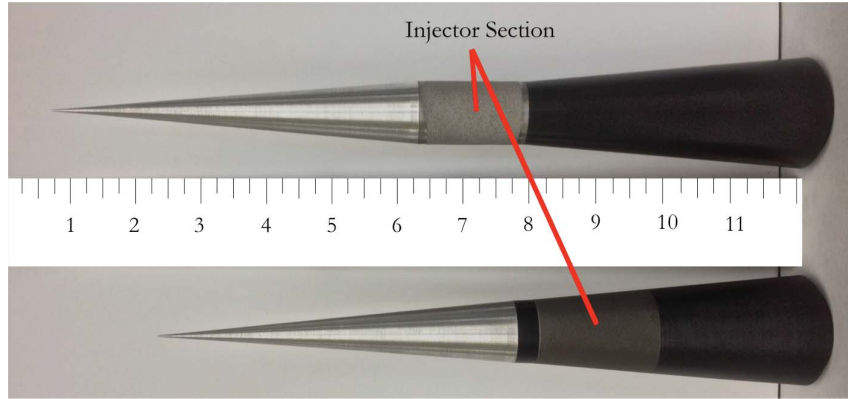
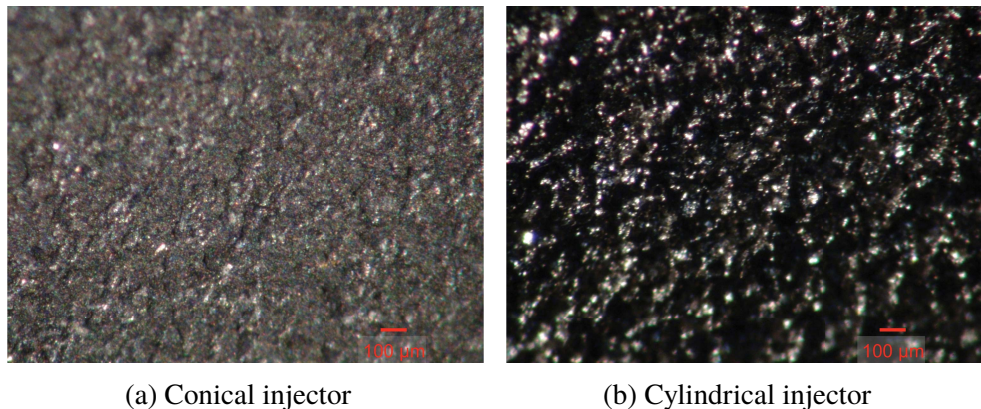


Figure 2.7: Both models used in this work. One has a cylindrical injector section (top) and the other has a conical section (bottom). The ruler scale is in inches. Republished with permission of AIAA. From Schmidt et al. (2015); permission conveyed through Copyright Clearance Center, Inc.

The injectors are manufactured by Mott Corporation and are made of sintered stainless steel. The surface area of the injectors is $2.66 \times 10^{-3} \text{ m}^2$. Magnified images of the injectors are shown in Figure 2.8.



(a) Conical injector

(b) Cylindrical injector

Figure 2.8: 5x-magnified images of the surface of injectors. The red line in the lower right corner of each image is $100 \mu\text{m}$. Republished with permission of AIAA. From Schmidt et al. (2015); permission conveyed through Copyright Clearance Center, Inc.

The models are assembled on a 1/2-inch diameter aluminum tube. The cone tip, injector, and rear frustum interlock. The cone tip has 1/2"-13 internal threads to match the threading on the end of the tube. The tube has slots that line up with the

injector to facilitate the flow of gas from the tube to the injector. An O-ring at the rear of the frustum section ensures that gas does not escape through the rear of the model. Sections of the tube are threaded and twist-on 1/2"-13 nuts are used on these sections. One nut tightens the frustum, injector, and cone tip together. The other tightens against the sting sleeve, which interlocks with the back of the frustum. The sting sleeve fits in the sting in the Ludwieg tube test section. A plastic end cap is used between the back of the sting sleeve and the corresponding twist-on nut, and a slot is cut in the end cap to allow wires from the PCB sensors to pass through. A 1/2-inch Swagelok fitting is fixed to the rear end of the aluminum tube which mates with the injected gas plumbing line. A solid model of the assembly and an exploded view are shown in Figure 2.9. Machine drawings for the parts, including the pneumatic valve components, are included in Appendix B.

Porous Flow Analysis

The flow through the porous material of the injectors is modeled using the compressible version of Darcy's Law. Darcy's Law is a well-known relation between the flow rate and pressure difference for low Reynolds number flows through porous media (Dullien, 1979). The derivation is straightforward from conservation of momentum. The 1-D, steady, incompressible equation is

$$Q = \frac{\kappa A}{\mu} \frac{p_1 - p_2}{h} , \quad (2.1)$$

where Q is the volumetric flow rate, p_1 and p_2 are the pressures at the beginning and end of the porous media section, respectively, h is the thickness of the media, A is the cross-sectional area, μ is the viscosity of the fluid, and κ is the permeability of the media (see Figure 2.10). Permeability is the key parameter that relates the pressure drop to the flow rate and has units of area. It must be determined experimentally.

A compressible version of Equation 2.1 can be derived from the continuity and momentum equations. The analysis here follows closely that of Shepherd and Begeal (1988). The injectors in this work are axisymmetric, so the continuity equation is

$$\frac{d}{dr} (\rho u) + \frac{\rho u}{r} = 0 , \quad (2.2)$$

which reduces to

$$\rho u r = \frac{\dot{m}}{2\pi L} = \text{constant} \quad (2.3)$$

for a cylinder of length L , where \dot{m} is the mass flow rate. The geometry is shown in Figure 2.11 and is slightly different from that shown in Figure 2.10.

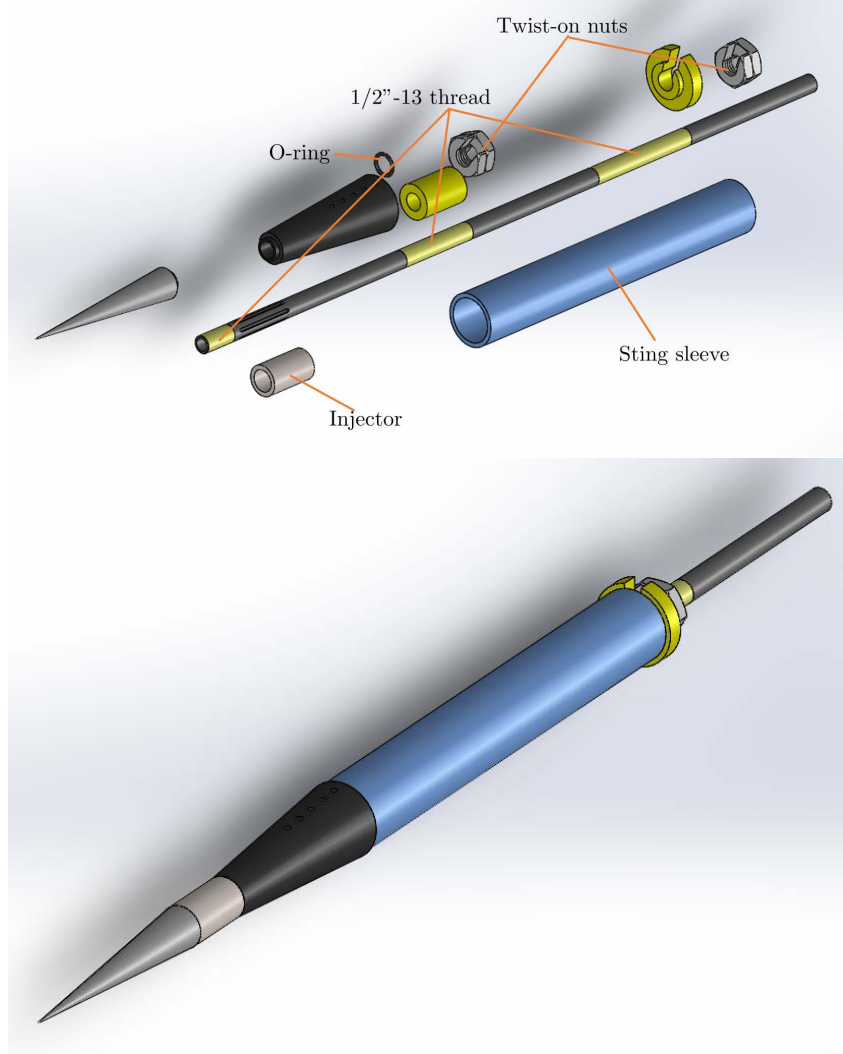


Figure 2.9: Exploded view and assembly of solid model of the test article with the cylindrical injector. Threaded segments of the aluminum tube are colored yellow. Holes for the PCB pressure transducers are visible on the frustum section.

The momentum equation is a balance between viscous forces and the pressure drop across the porous material:

$$-\frac{dp}{dr} = \frac{\rho u^2 C_D}{\bar{d}} . \quad (2.4)$$

In this expression \bar{d} is a characteristic length of the porous material. A common assumption is that the media can be approximated as a bed of closely-packed spheres. In this case \bar{d} is the mean sphere diameter.

C_D is a drag coefficient for the media. If the Reynolds number based on \bar{d} ($Re_{\bar{d}}$) is small, then the Forchheimer equation (Forchheimer, 1901) can be used to calculate

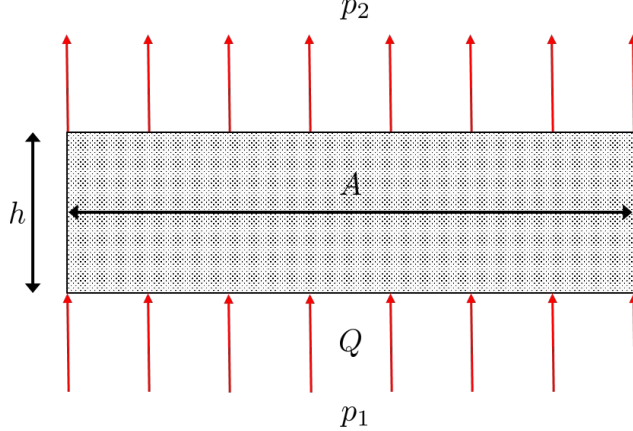


Figure 2.10: Sketch illustrating 1-D porous flow. The porous media has thickness h and cross-sectional area A . If the flow is incompressible, the flow rate is related to the pressure drop by Equation 2.1.

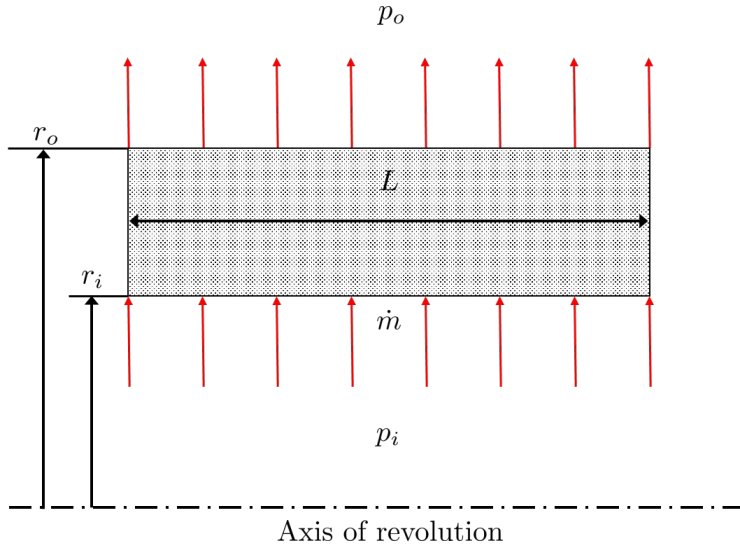


Figure 2.11: Sketch of porous flow through an axisymmetric geometry such as the cylindrical injector used in this work. The injector has inner radius r_i and outer radius r_o .

the drag coefficient:

$$C_D = \frac{\bar{d}^2}{\kappa} \left(\frac{1}{Re_{\bar{d}}} + \frac{\lambda}{\bar{d}} \right) . \quad (2.5)$$

κ is again the permeability of the media, and λ is the Forchheimer constant, which is a property of the media that must also be determined experimentally. The Forchheimer constant can be related to the permeability by the Carman-Kozeny expression for the permeability of a bed of packed spheres:

$$\kappa = \frac{\bar{d}^2 \epsilon^3}{180(1 - \epsilon)^2} , \quad (2.6)$$

and the Ergun relation for the Forchheimer constant:

$$\frac{\kappa}{\lambda} = \frac{\bar{d}\epsilon^3}{1.8(1-\epsilon)} . \quad (2.7)$$

ϵ in these equations is the porosity, or volume fraction of empty space, of the porous material (Macdonald et al., 1979). According to the manufacturer of the injectors this is equal to 0.4. Equations 2.5, 2.6, and 2.7 can be combined to give

$$C_D = \frac{\bar{d}}{\kappa} \left(\frac{\mu}{\rho u} + \frac{\bar{d}}{100(1-\epsilon)} \right) . \quad (2.8)$$

A set of experiments was performed to simultaneously measure the pressure inside the injectors and the gas mass flow rate using a Kulite XT-190 piezoresistive pressure transducer and a Sensirion EM1 flow meter, respectively, to determine the properties of the porous media. The two terms in Equation 2.8 can first be compared to determine if both are necessary to model the flow through the injectors. According to the manufacturer, the mean pore size is on the order of $10 \mu\text{m}$, so this can be used as an estimate for \bar{d} that is assumed to be accurate within an order of magnitude. The viscosity of air at room temperature is $1.9 \times 10^{-5} \text{ kg/m s}$, and the largest mass flow rate in this set of calibration experiments is 4.5 g/s . Using these values, the second term in Equation 2.8 is at most 5% of the first term and can be neglected. This simplifies the expression for the drag coefficient to

$$C_D = \frac{\bar{d}\mu}{\kappa\rho u} . \quad (2.9)$$

Equation 2.9 can be substituted into Equation 2.4 to give

$$-\frac{dp}{dr} = \frac{u\mu}{\kappa} . \quad (2.10)$$

The velocity u can be expressed in terms of the mass flow rate by using Equation 2.3:

$$-\rho \frac{dp}{dr} = \frac{\dot{m}\mu}{2\pi L\kappa} . \quad (2.11)$$

Equation 2.11 is integrated from p_i to p_o in p and from R_i to R_o in r by expressing the density as a function of pressure using the ideal gas law and assuming isothermal flow through the porous media. The resulting expression is

$$p_i^2 - p_o^2 = \frac{\dot{m}\mu RT}{\pi L\kappa} \ln \left(\frac{r_o}{r_i} \right) . \quad (2.12)$$

In the experiments performed in this work the pressure outside the injector is of the order 1 kPa while the pressure required to drive flow through the injector is of the order 100 kPa, so $p_o^2 \ll p_i^2$ and p_o^2 can be neglected in Equation 2.12. The final relation between pressure and mass flow rate is

$$p_i^2 = \frac{\dot{m}\mu RT}{\pi L\kappa} \ln \left(\frac{r_o}{r_i} \right) . \quad (2.13)$$

From Equation 2.13, it is clear that if pressure and mass flow rate are measured simultaneously then the permeability κ is the only unknown parameter and can be determined by linear least squares. Figure 2.12 shows the data from the calibration experiments with a fit of Equation 2.13 to determine the permeability. κ is equal to $3.5 \pm .003 \times 10^{-12} \text{ m}^2$ for the cylindrical injector and $1.1 \pm .0006 \times 10^{-14} \text{ m}^2$ for the conical injector. Uncertainties are determined by the 95% confidence interval of the least-squares fit and the measurement uncertainties in pressure and mass flow rate. These values are typical of those reported for sintered stainless steel (Frederking et al., 1986).

2.4 Injected Gases

Pappas and Okuno (1960) observed that the molecular weight of the injected gas affects the transition location on a porous cone in Mach 4.8 flow. The choice of injected gas is therefore considered to be an important parameter in the investigation of the instability that leads to transition in this work. Nitrogen was chosen as one injected gas because it is simpler to model since the free stream gas is also nitrogen and diffusion of species need not be considered. Helium was selected as a second injected gas because it is the lightest gas available (that does not require additional safety measures to use) and therefore produces the largest deviations in behavior. The properties of helium are similar to those of hydrogen which is a candidate scramjet fuel, making it particularly relevant to the application of injection in scramjet inlets.

Helium is approximately seven times lighter than nitrogen, so a gas that is seven times heavier than nitrogen (a molecular weight of 196 g/mol) was sought as the final injected gas. Most substances with molecules of that size are not gases at room temperatures, and many that are gases are highly toxic, corrosive, combustible, and/or prohibitively expensive. Refrigerants were seen as a category of fluids that may fit the criteria of being a gas at room temperature, non-toxic, compatible with most materials, non-reactive, and reasonably priced. One refrigerant, RC318, fits these criteria and has a molecular weight of 200 g/mol. Figure 2.13 shows a 3-D

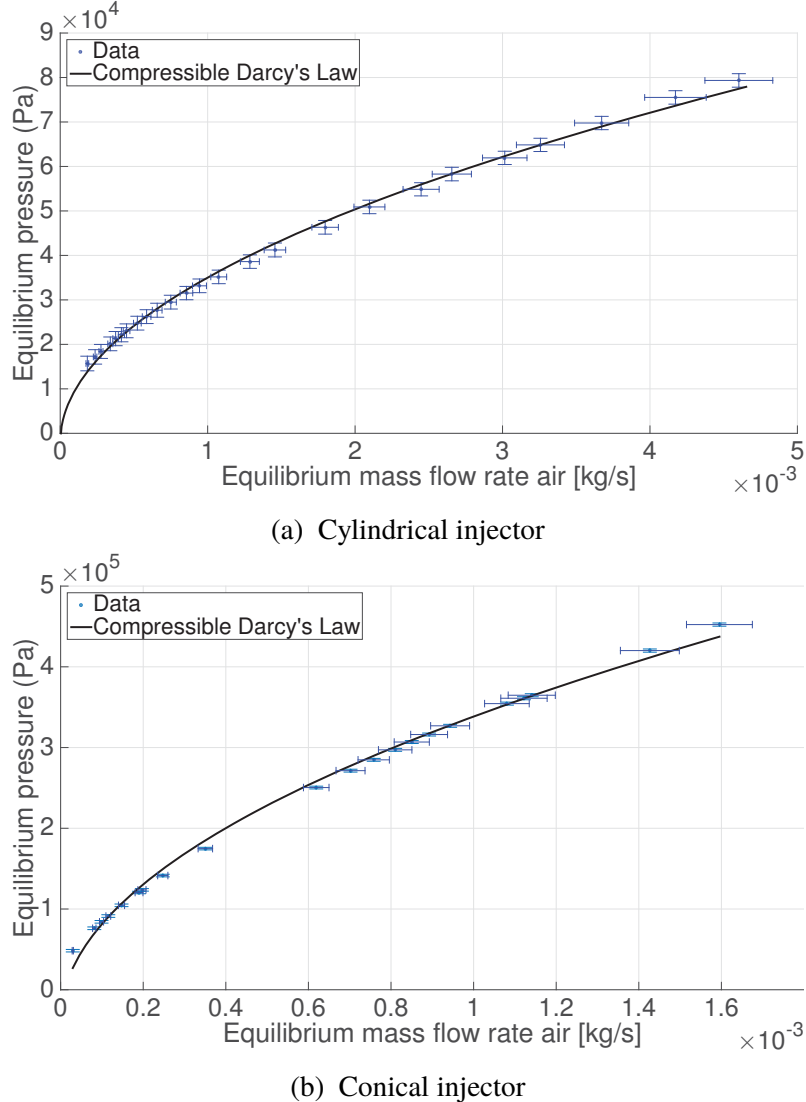


Figure 2.12: Pressure vs. mass flow rate data for air for both injectors fit with Equation 2.13 to determine permeabilities. Republished with permission of AIAA. From Schmidt et al. (2015); permission conveyed through Copyright Clearance Center, Inc.

ball-and-stick model of an RC318 molecule. The black spheres represent carbon atoms and the green spheres are fluorine atoms.

RC318 is a fluorocarbon, its IUPAC name is octofluorocyclobutane. It is effectively a cyclobutane molecule where all the hydrogen atoms have been replaced with fluorine atoms. It has few documented applications, but is used in the production of semiconductor materials and is therefore readily available. It is chemically inert under most conditions, as the carbon-fluorine bond is extremely strong, often listed as the strongest in organic chemistry (O'Hagan, 2008). Properties and safety hazards

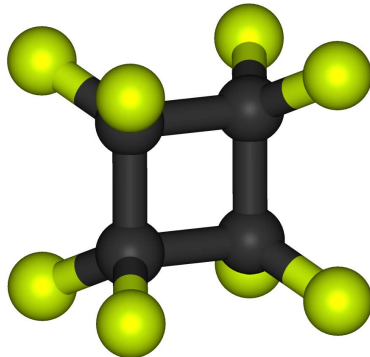


Figure 2.13: 3-D model of an RC318 molecule. The black spheres represent carbon atoms and the green spheres are fluorine atoms. Image by Fvasconcellos - Own work, Public Domain.

are detailed in the safety data sheet provided by Praxair (Praxair Inc., 2015). Some properties of the three selected injected gases for this work at 295 K are summarized in Table 2.1.

Gas	Formula	Molecular weight (W) [g/mol]	Specific heat ratio (γ)	Sound speed [m/s]
Helium	He	4.00	1.67	1011
Nitrogen	N ₂	28.02	1.4	350
RC318	C ₄ F ₈	200.04	1.054	114

Table 2.1: Properties of injected gases at 295 K.

Flow Rate Measurement

The mass flow rate of the injected gas is measured directly by an Omega FMA1742A thermal flow meter. The meter outputs a voltage that is linearly proportional to the mass flow rate, but the constant of proportionality depends on the properties of the gas. The meter was calibrated for each gas using a King Instruments rotameter in series with the thermal meter. During experiments, the thermal meter is in series with the injector and is approximately 3 m upstream of the test section. Flow through the injector is started several seconds before the wind tunnel is started to ensure that steady flow has been established and the flow meter gives an accurate reading. The meter has a rated accuracy of 1.5% of the full scale reading. The uncertainty used for error propagation is twice this value to conservatively account for potential errors incurred by the calibration process.

2.5 OpenFOAM Computations

The experiments performed in this work were complemented by simulations using the open-source finite-volume CFD package OpenFOAM (Weller et al., 1998) to lend additional insight into the flow physics. The solver used is a hybrid scheme based on the PISO algorithm and the Kurganov-Tadmor scheme developed by Kräpelin et al. (2015). The resulting hybrid method is accurate across a wide range of Mach numbers, from 0.01 to 3 or higher.

The simulations are performed as laminar computations of the compressible unsteady Navier-Stokes Equations including species transport. The mass and momentum conservation equations take their usual form, neglecting body forces:

$$\frac{\partial \rho}{\partial t} + \underline{\nabla} \cdot (\rho \underline{u}) = 0 \quad , \quad (2.14)$$

$$\frac{\partial \rho \underline{u}}{\partial t} + \underline{\nabla} \cdot (\rho \underline{u} \otimes \underline{u}) = -\underline{\nabla} p + \underline{\nabla} \cdot \underline{\tau} \quad . \quad (2.15)$$

The fluid is assumed to be Newtonian and Stokes' hypothesis is used to ensure zero bulk viscosity (F. M. White, 1991):

$$\lambda = -\frac{2}{3}\mu \quad . \quad (2.16)$$

The stress tensor τ is then

$$\underline{\tau} = -\frac{2}{3}\mu (\underline{\nabla} \cdot \underline{u}) \underline{I} + \mu (\underline{\nabla} \underline{u} + (\underline{\nabla} \underline{u})^T) \quad , \quad (2.17)$$

where \underline{I} is the identity tensor and superscript T indicates a transpose operation.

The gases are treated as perfect gases that obey the Sutherland formula for the temperature-dependence of viscosity:

$$\mu = A_s \frac{T^{\frac{3}{2}}}{T + T_s} \quad , \quad (2.18)$$

where A_s and T_s are coefficients for a given gas and are tabulated for common gases. Sutherland coefficients for RC318 were fitted using data from NIST. Coefficients for all three gases are given in Table 2.2. Transport and thermodynamic properties are calculated with a mass-weighted average where multiple species are present, which is an approximation that can incur some errors.

Species are conserved according to the species transport equation:

$$\frac{\partial \rho Y_i}{\partial t} + \underline{\nabla} \cdot (\rho \underline{u} Y_i) = -\underline{\nabla} \cdot \underline{j}_i \quad . \quad (2.19)$$

Gas	As [$\mu\text{Pa}\cdot\text{s}$]	Ts [K]
Helium	1.484	79.4
Nitrogen	1.407	111
RC318	1.34	299.7

Table 2.2: Sutherland coefficients for the three injected gases to be used in calculating viscosity in Equation 2.18.

Y_i is the mass fraction of species i and \underline{j}_i is the flux of species i due to diffusion. The species production term is omitted here because the flow studied is non-reactive. Diffusion is assumed to occur according to Fick's Law, neglecting mass diffusion due to temperature and pressure gradients (Kee et al., 2003). The diffusive flux \underline{j}_i is given by

$$\underline{j}_i = -\rho D_{i,m} \nabla Y_i . \quad (2.20)$$

$D_{i,m}$ is the mass diffusivity for species i into the mixture m . When \underline{j}_i is written in terms of mass fractions instead of mole fractions, conservation of species is not guaranteed. The constraint

$$\Sigma Y_i = 1 \quad (2.21)$$

is strictly enforced to ensure continuity instead of computing a correction velocity in the expression for \underline{j}_i as is done in many reacting flow solvers (Kee et al., 2003). This introduces some error in cases where the molecular weights of the species are significantly different. In mixtures with only two components, such as the ones in the flow studied here, Equation 2.21 is satisfied by solving Equation 2.19 only for one species, for instance the free stream gas, and then determining the mass fraction of the other species, the injected gas in this example, by solving Equation 2.21, i.e.

$$\frac{\partial \rho Y_1}{\partial t} + \nabla \cdot (\rho \underline{u} Y_1) = \nabla \cdot (\rho D_{1,m} \nabla Y_1) \quad (2.22)$$

and

$$Y_2 = 1 - Y_1 \quad (2.23)$$

are solved sequentially.

Mass diffusivity is calculated by assuming a Schmidt number of unity:

$$Sc_{i,m} = \frac{\mu_m}{(\rho D)_{i,m}} = 1 . \quad (2.24)$$

This is accomplished by setting ρD equal to μ_m for a given species since the diffusivity never appears by itself but is always multiplied by the density. μ_m is

the mixture viscosity, so this assumption means that the mass diffusivity is the same for both species in the binary mixture, but changes as a function of both temperature and composition. The true diffusion coefficient for a binary mixture is insensitive to composition but is a function of temperature. The assumptions made concerning mass diffusion are examined in more detail in Appendix A. The analysis there concludes that the handling of diffusion by OpenFOAM introduces errors in cases with helium-nitrogen and RC318-nitrogen diffusion, so some degree of discrepancy between the computational and experimental results is expected for helium and RC318 injection cases. Even in these cases, errors in the OpenFOAM computations in the handling of diffusion of species and mixture-averaged properties such as viscosity are confined to the thin layer where both gases exist in appreciable amounts and therefore are not likely to significantly impact the overall solutions.

The energy equation is formulated in terms of the mass-specific enthalpy h :

$$\frac{\partial}{\partial t} \left[\rho \left(h + \frac{\underline{u} \cdot \underline{u}}{2} \right) \right] + \nabla \cdot \left[\rho \underline{u} \left(h + \frac{\underline{u} \cdot \underline{u}}{2} \right) \right] = \frac{\partial p}{\partial t} + \nabla \cdot (\tau \cdot \underline{u}) - \nabla \cdot \underline{q} . \quad (2.25)$$

\underline{q} is the heat flux vector, and energy production by chemical reaction has again been neglected. The heat flux is assumed to obey Fourier's law and includes transport of enthalpy by diffusion,

$$\underline{q} = -\kappa \nabla T + \sum j_i h_i . \quad (2.26)$$

κ is the thermal conductivity, h_i is the enthalpy carried by species i , and j_i is again the diffusive flux of species i , calculated with Equation 2.20. There is no correction in the energy equation to ensure conservation of species as there is in the transport equation (Equation 2.23), so this term is susceptible to errors associated with writing Fick's Law in terms of the mass fractions without implementing a correction velocity to ensure species conservation.

The thermal conductivity is approximated by a modified Eucken model,

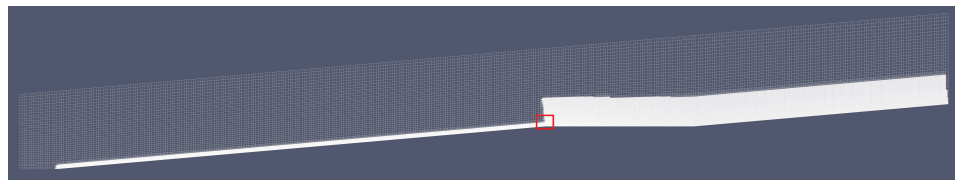
$$\kappa = \mu (1.32c_v + 1.77R) . \quad (2.27)$$

Here R is the specific gas constant and c_v is the specific heat at constant volume. This model gives constant Prandtl numbers of 0.69, 0.67, and 0.74 for nitrogen, helium, and RC318 respectively.

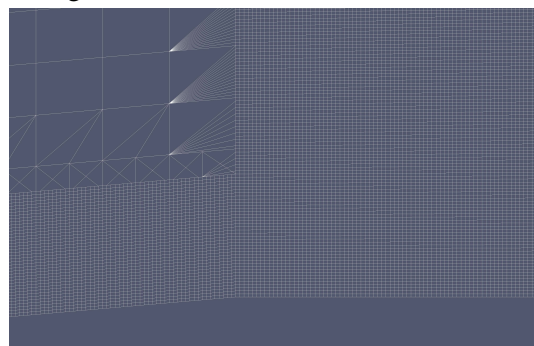
The flow is solved on a 2-D axisymmetric grid which extends from 10 mm ahead of the cone tip to 70 mm downstream of the end of the injector section. A quasi-steady state is first reached on a coarse grid, then the result is mapped to the refined grid

shown in Figure 2.14 and the solution is again marched forward in time until a new quasi-steady state is reached. Waves appear in the injection layer downstream of the injector so the flow is never truly steady for the entire field but the flow ahead of the injector does become steady after a sufficient number of time steps (see Section 4.3). Cells are clustered near the wall (see Figure 2.14b), extending just beyond the interface of the injected gas and the free stream gas. A study was performed to ensure sufficient spatial resolution for grid independence; the final refined grid has a total of 755857 points with a resolution of $45 \mu\text{m}$ per cell in the refined region, which gives a Reynolds number based on cell size of 405. For comparison, gradients in the injection layer occur over a region of approximately 3-10 mm depending on the case.

Boundary conditions are chosen to match the conditions in the Ludwieg tube test section with a free stream pressure of 1.32 kPa: the free stream gas is nitrogen, the temperature is 68 K and the velocity is 672 m/s. Outflow boundary conditions are zero-gradient for all variables, both at the downstream end of the domain and at the top boundary above the model. The velocity of the injected gas is prescribed as uniform across the injector surface and the pressure is allowed to match the pressure in the flow above the injector. The temperature of the injected gas is fixed at 295 K. Solid walls are treated as adiabatic and a no-slip condition is applied to the velocity. The test time in the Ludwieg tube is too short for the adiabatic condition to be reached in experiments, but the adiabatic wall temperature differs from room temperature by only 15% in these experiments so the adiabatic condition is used in the simulations for simplicity without a significant loss in accuracy.



(a) Computational grid for OpenFOAM simulations. The red box shows the location of the zoomed image in 2.14b.



(b) Zoomed image of the grid showing the refined portion near the wall.

Figure 2.14: Refined computational grid for the OpenFOAM simulations.

Chapter 3

DIAGNOSTICS

The diagnostics used in the experiments in this work are described in this chapter. A brief review of relevant experimental techniques is conducted. The selected surface measurement scheme is then described. A thorough analysis of the focused laser differential interferometry (FLDI) technique is performed, and the justification for using other techniques is given. The high-speed schlieren imaging method used in this work is then described.

3.1 Measurement Technique Review

Based on preliminary linear stability analysis performed by Schmidt et al. (2015), the characteristic frequency of the instability waves in the injection layer is expected to be on the order of 50-100 kHz. Several measurement techniques have been used to detect flow phenomena in this frequency range in supersonic flows. A brief summary of some of these techniques is presented here.

Hot-wire anemometry is a common method for detecting velocity fluctuations in subsonic flows, and it has been used in some high-speed facilities as well. Kovansz-nay (1950) highlights some of the challenges of using this technique in supersonic flows. In order to attain the frequency response required in this regime, the wire must be very thin, which makes it prone to breakage, particularly during establishment of steady flow. Furthermore, the response of the probe is sensitive not only to velocity fluctuations, but also to fluctuations in density and temperature. Nonetheless, many researchers have successfully used hot-wire probes to measure instability waves in supersonic and hypersonic boundary layers.

PCB piezoelectric pressure transducers have also been used successfully to measure wall pressure fluctuations in supersonic boundary layers (see e.g. Laurence, Wagner, Hanneman, et al. (2012) and Ward et al. (2013)). Typically the transducers are flush-mounted to the model surface. These transducers have a resonant frequency in excess of 1 MHz. The transducers are sensitive to vibration of the model, so care must be taken to distinguish the pressure fluctuations in the flow from model vibration when analyzing the output from the transducers.

Parziale et al. (2015) report detection of Mack-mode waves in a hypervelocity

boundary layer with frequencies in excess of 1 MHz using focused laser differential interferometry (FLDI). This technique uses a two-beam focused interferometer to detect density fluctuations along the line of sight of the instrument, and is explained in further detail in Section 3.3.

Schlieren and shadowgraph techniques have been used by researchers to study phenomena in compressible flows for well over a century. Laurence, Wagner, Hanneman, et al. (2012) report using high-speed imaging at several hundred kHz to make time-resolved measurements of instability waves in a hypersonic cone boundary layer. They used a pulsed, incoherent laser light source to limit the effective exposure time of a high-speed camera to visualize the waves. Images were cross-correlated to detect the phase speed and a spatial Fourier analysis was performed to measure their wavelength. The results agree well with simultaneous surface measurements made with piezoelectric pressure transducers. Laurence, Wagner, and Hanneman (2014) present additional techniques for measuring density fluctuations in high speed flows based on the schlieren visualization method.

3.2 Surface Measurements

Schlieren visualization in preliminary experiments show that the instability waves appear at the interface between the injected gas and the free stream gas, which is several millimeters away from the surface of the cone model. This may limit the usefulness of surface measurements in this work, however the signature of the waves is still expected to propagate to the wall. PCB piezoelectric pressure transducers were chosen because of their commercial availability, small size, high frequency response, and successful use by other researchers. The frustum section of the cone model is instrumented with five PCB 132A31 transducers along its length (see the machine drawing in Appendix B), and they are sampled at 2 MHz with a PCI-6133 data acquisition card.

3.3 FLDI Analysis

A thorough analysis of FLDI was conducted as part of this work and was published as Schmidt and Shepherd (2015a). That article is reproduced in Appendix C as its conclusions are relevant to the final choice of optical diagnostics for this research. A focused laser differential interferometer is a line-of-sight point-wise optical measurement technique that is sensitive to refractive index changes in the flow. A key advantage of FLDI is its increased sensitivity at its best focus, which allows it to filter out disturbances at the edges of the flow in a wind tunnel test section where

turbulent shear layers corrupt many other optical techniques. The output of an FLDI is measured with a photodetector, which means that it is both potentially quantitative regarding the magnitude of the refractive index change in the test field and has a very high frequency response, on the order of 10 MHz. One of the main findings of Schmidt and Shepherd (2015a), however, is that in order for the density change measured by the FLDI to be quantified, some knowledge regarding the geometry of the flow field and the density field itself must be known *a priori*.

3.4 High-speed Schlieren Technique

FLDI was carefully weighed against high speed schlieren imaging like that performed by Laurence, Wagner, and Hanneman (2014). FLDI has an order of magnitude higher frequency response, is more sensitive, and is potentially quantitative in terms of the density change measured, which would make measurements of amplification rate possible. The schlieren technique, however, is a line-of-sight field measurement as opposed to a line-of-sight point measurement and could therefore yield more information about the instability waves than a point measurement method like FLDI. Furthermore, the schlieren technique is easier to implement, particularly if multiple FLDI measurement locations are required.

Ultimately the schlieren technique was selected because it was determined to be better suited to study the instability in flow with injection. Because the instability has not been studied previously in the experimental configuration used in this work, it is unknown *a priori* where the instability waves will form for a given injected gas and flow rate. This makes accurate placement of the FLDI beams impossible without a field measurement beforehand. Additionally, the advantages of FLDI over schlieren for this problem are not significant. The frequency of the instability waves is predicted to be on the order of 50-100 kHz, which is accessible by many commercial high-speed cameras. Shadowgraph images taken by Pappas and Okuno (1964) clearly show the development of instability waves, so the additional sensitivity of the FLDI compared to schlieren visualization is not necessary in this case. Finally, because the character of the instability waves is unknown, in contrast to the Mack-mode waves in a hypersonic boundary layer studied in the example in Section C.5, it would not be possible to make quantitative measurements of the density fluctuations or growth rate with FLDI according to the conclusions of Schmidt and Shepherd (2015a). Finally, both Laurence, Wagner, and Hanneman (2014) and Schmidt and Shepherd (2015b) were able to make time-resolved measurements of fluctuations in supersonic flows with schlieren imaging, which suggests strongly that a similar

method could successfully be applied to the flow in this work.

A description of a high-speed imaging system nearly identical to the one used in this work is given by Parziale, Damazo, et al. (2015). Images are acquired with a Phantom v710 high speed CMOS camera. It is capable of a frame rate of 7530 fps at its maximum resolution of 1280 x 800 pixels but can achieve frame rates up to 1.4 million fps with reduced resolution. Pixels are 20 μm square and have 12-bit depth. The most significant limitation of the camera for this application is the minimum exposure time. If a continuous light source such as an LED is used, the practical minimum exposure time to illuminate an image is approximately 1 μs . Assuming the instability waves propagate at a velocity close to that of the free stream, an exposure time of 1 μs means that the waves will propagate more than 0.5 mm in a single exposure, causing appreciable motion blur.

The solution is to use a pulsed light source to limit the effective exposure time of the system. Haley and Smy (1988) performed pioneering work using a pulsed laser diode for schlieren visualization, although at that time laser diodes were quite expensive and not as practical as light sources as they are today, and high-speed cameras did not nearly have the capabilities of modern CMOS cameras. Modern commercially available laser diodes are capable of providing pulses with widths between 20-100 ns that are sufficiently strong to illuminate schlieren images. The diode is powered by a current controller. In this work the controller is a PicoLAS LDP-V 03-100 UF3 laser diode driver. It can supply pulses of up to 3.5 A at a repetition rate of up to 2 MHz at a duty cycle of 2% at 3 A. The light from the diode is expanded and then propagated through a typical Z-type schlieren setup. A schematic of the setup is shown in Figure 3.1.

The timing of the system is as follows. The camera sends a pulse when the shutter opens, which is sent to a Berkeley Nucleonics Model 555 pulse delay generator. The delay generator then sends a pulse of the desired light pulse width to the current controller, which sends an amplified current pulse to the laser diode. The current controller is supplied by a steady 15 V DC power supply. The outputs from the camera, pulse delay generator, and current controller are monitored with an oscilloscope. Figure 3.2 shows a qualitative timing diagram for the camera and light source. The delay is determined experimentally by changing the delay time until the light pulse is synchronized with the camera. The light source used in this work is capable of producing a continuous pulse train which allows the optics to be aligned and the pulse delay to be determined in real time.

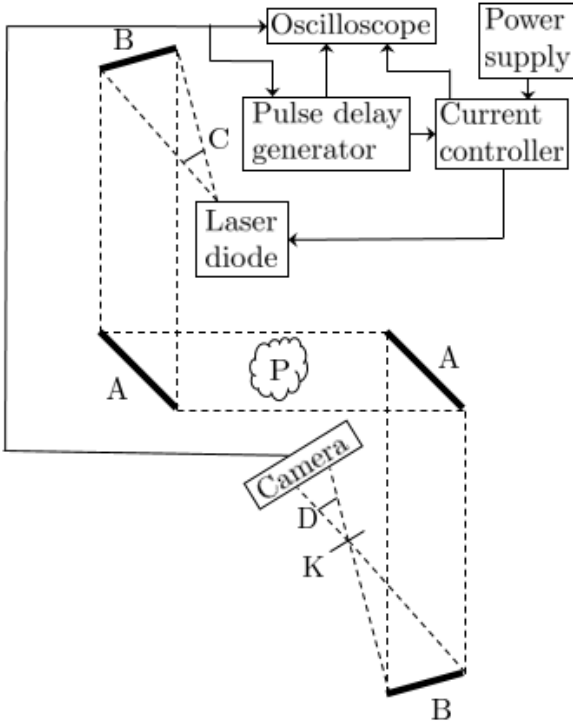


Figure 3.1: Schematic and wiring diagram for a schlieren imaging setup with a pulsed laser diode light source. Light paths are shown as dashed lines, electrical connections are solid arrows. A: turning mirror, B: concave mirror ($f = 150$ cm), C: diverging lens, D: focusing lens, K: schlieren cutoff, P: phase object.

Using a laser as a light source for schlieren imaging has several well-known issues which are outlined in detail in Section 7.1 of Settles (2001). First, temporally coherent light is generally not good for imaging because it creates artifacts like speckle and fringes that corrupt the image. Second, diffraction tends to occur around sharp edges in the image plane. Finally, laser light is also spatially coherent and can be focused to a very small point. This creates difficulties at the schlieren cutoff and generally produces a binary cutoff effect instead of a proper schlieren image.

A laser light source does have some advantages over a white-light source, however. First, the narrow-band emission alleviates chromatic aberrations. Narrow-band emission also allows researchers to use a narrow-band filter in front of the camera to filter out any luminescence in the flow that would otherwise corrupt a schlieren image. This is not a concern in the present work as the flow is nonreactive. An infrared diode in particular has an additional advantage. The sensitivity of a schlieren system to a phase object is proportional to the change in index of refraction, which

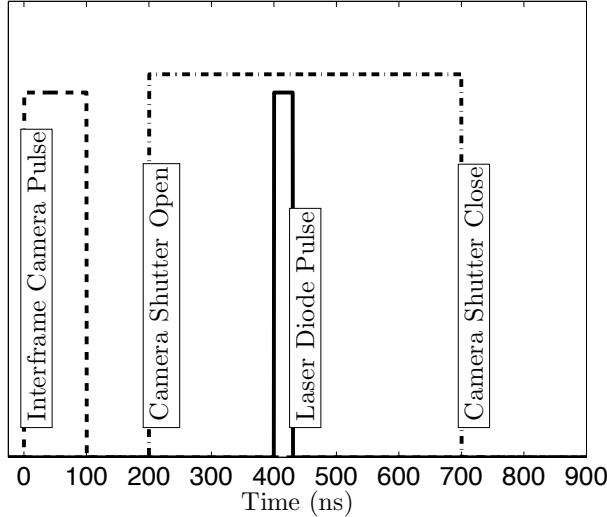


Figure 3.2: Example timing diagram for the camera and light source. The timing of this diagram is not specific to any particular experimental case but is simply to show the desired scheme. Republished with permission of AIAA. From Parziale, Damazo, et al. (2015); permission conveyed through Copyright Clearance Center, Inc.

is given by the Gladstone-Dale relation in a gas,

$$n = K\rho + 1 \quad . \quad (3.1)$$

The Gladstone-Dale constant K increases for increasing illumination wavelength, meaning that a schlieren system with an infrared light source will be more sensitive than one with a visible light source, all other parameters held equal.

The laser diode used in this work is a Laser Components 905D3S3J08, and its properties address many of the disadvantages listed above, making it ideal for imaging in the present application. It has a maximum forward current of 40 A with a duty factor of 0.1%. Light from the diode has a wavelength of 905 nm, which is in the near-infrared range, and has a spectral bandwidth of 7 nm. This relatively broad bandwidth for a laser dramatically reduces the coherence length of the light and eliminates the majority of the speckle and fringes that would appear

with a more monochromatic source. Furthermore, the diode is composed of a 3 x 3 stacked emitter array instead of a single emitter, which helps to reduce both spatial and temporal coherence. The emitter size is $200 \times 250 \mu\text{m}$, also fairly large for a laser aperture. The reduced spatial coherence and large aperture eliminates the difficulties with using a traditional knife-edge schlieren cutoff that are typically encountered with laser light sources. These properties coincidentally make this diode very inexpensive, on the order of \$100 per diode, especially compared to the cost of highly coherent lasers with much better beam quality. Finally, since the light is in the near-infrared band, the schlieren system is inherently more sensitive than a system using visible light for the reasons explained above. The Phantom v710 camera is reasonably sensitive at this wavelength, as shown in Figure 3.3, and is about as sensitive at 905 nm as it is to blue light in the visible spectrum.

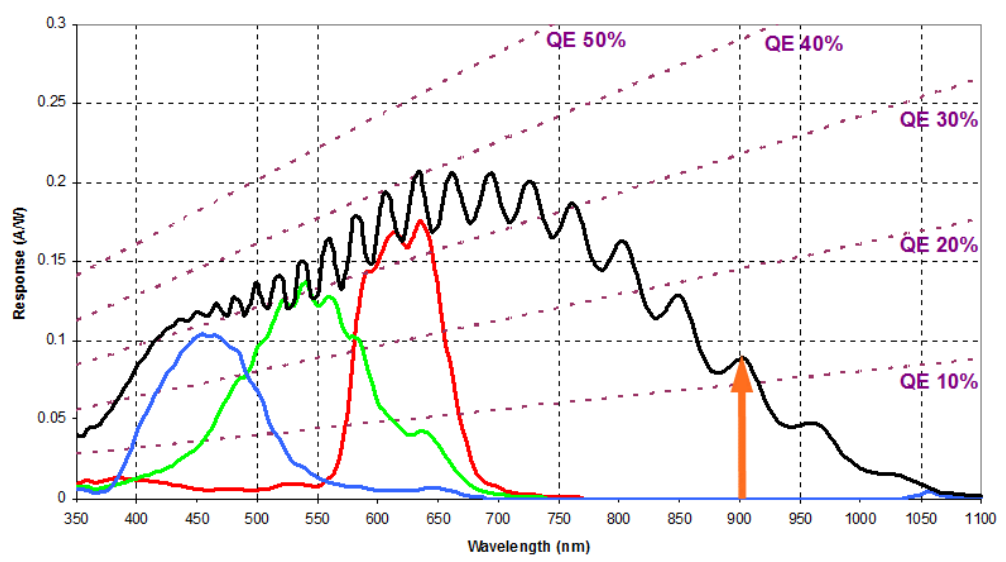


Figure 3.3: Spectral response chart for the Phantom v710 camera. The black curve is the total response. The orange arrow marks 905 nm, the wavelength of the laser light source. Chart ©Vision Research, Inc.

The primary disadvantages of this light source are first that the infrared emission makes alignment of the system difficult. Once the system is aligned, however, no further difficulties resulting from the wavelength of the light are encountered. Second and more importantly, the small size of the diode emitter makes the depth of field of the imaging system quite large, on the order of 1-2 meters. The width of the region in focus is larger than the width of the test section of the Ludwieg tube, which means the system is sensitive to the turbulent shear layers on the edges of the core flow in the wind tunnel described in Section 3.3. Disturbances from these

shear layers appear in the images and must be accounted for when the images are processed and analyzed. This is discussed in Section 4.2.

The output of the diode for a nominal 25 ns pulse is plotted in Figure 3.4. The output is measured with a Thorlabs APD110A avalanche photodetector, which has a rise time of < 1 ns. The full width at half maximum of the output is 30 ns, and the shape of the pulse is reasonably square. Data from the photodetector was recorded with a Tektronix DPO2024 digital oscilloscope.

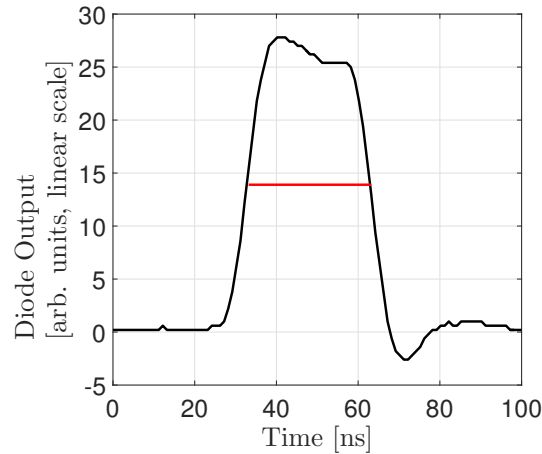


Figure 3.4: Output of the laser diode measured with a photodetector. The full width at half maximum is shown in red, and is 30 ns for a nominal 25 ns pulse.

C h a p t e r ~ 4

RESULTS

Experimental results are given in this chapter. Data from experiments with low-speed images of the full flow field are presented first. This includes a set of experiments that demonstrate the mitigation of waves formed by injection by shaping of the test article, and a set of experiments that focus on properties of the injection layer and transition location. Next, results from high-speed imaging cases are presented. Image processing routines are discussed, as are algorithms for extracting properties of the instability waves from the images. Finally, results from the OpenFOAM simulations are presented. All experimental run conditions can be found in Appendix D.

4.1 Full-field Imaging

Minimization of waves

A set of experiments was performed to investigate the effect of shaping the injector section of the model on the waves formed by injection. This initial work was inspired by a hypothesis of Fedorov, who suggested that an injector section with a negative slope could compensate for the increased displacement effect of injection and minimize the strength of waves for a "tuned" injection flow rate. The concept was validated numerically by Fedorov, Soudakov, et al. (2014). Figure 4.1 shows a sketch of the idea. The added displacement creates an effective surface, which matches the slope of the model ahead of the injector for the tuned flow rate, and therefore no waves propagate into the inviscid region of the flow. The two injectors described in Section 2.3 are used to test the hypothesis experimentally.

The experiments performed for this subsection differ slightly from the other experiments in this work. They were performed before the Ludwieg tube was configured to operate with nitrogen as the free stream gas, so the free stream gas in these experiments is air. The injected gas is likewise air. They were also performed before the installation of the pneumatic valve described in Section 2.2, so diaphragms were used to operate the Ludwieg tube in these runs. Since only the mean flow field is being observed in this study and not the properties of the instability, a continuous white light LED (Cree X-Lamp MC-E Cool White) was used as a light source instead of the pulsed laser diode for improved image quality. Images were acquired

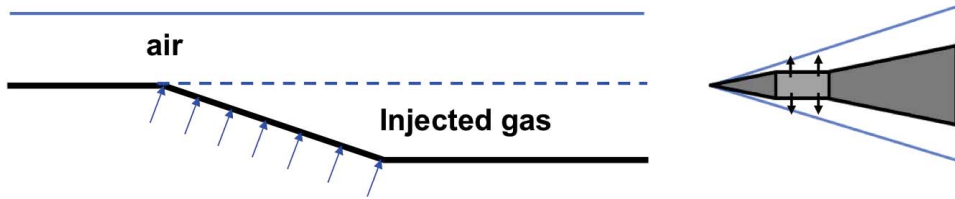


Figure 4.1: Sketch of Fedorov’s hypothesis of a negatively-sloped injector compensating for the additional displacement thickness created by injection. The graphic on the right shows the desired idealized shock pattern on a cone model: only the shock at the tip of the cone is present. Republished with permission of AIAA. From Schmidt et al. (2015); permission conveyed through Copyright Clearance Center, Inc.

at 3000 fps with an exposure time of $30 \mu\text{s}$. The data from these experiments is reported in Schmidt et al. (2015).

In this chapter, a parameter F is used to report the mass flow rate of the injected gas.

It is defined as

$$F = \frac{(\rho u)_{\text{inj}}}{(\rho u)_{\infty}} . \quad (4.1)$$

It is the mass flux of the injected gas divided by the mass flux of the free stream. $(\rho u)_{\text{inj}}$ is calculated by dividing the mass flow rate measured by the flow meter by the surface area of the injector. This parameter is used because it is common in the literature, e.g. Pappas and Okuno (1960). In Chapter 5 it will be noted that F is not appropriate for scaling many of the quantities measured in the experiments and its use will be discontinued, but its use is retained here for the sake of continuity with past studies and because no rigorous analysis of the results is presented in this section.

Four example schlieren images from experiments with the conical injector are shown in Figure 4.2. Red vertical lines on the cone model are drawn to show the location of the porous section. The value of F for each case is shown in yellow on the appropriate image.

The image in the upper left with $F = 0$ has no injection and is the baseline case for these experiments. A characteristic propagates from the joint of the cone tip section and the front of the injector due to the very small disruption to the solid surface. The oblique shock wave from the cone tip is visible in the region above the cone. The shock angle is measured from the images to be $15 \pm 0.1^\circ$. This angle matches the shock angle calculated from the Taylor-Maccoll solution (Taylor and Maccoll, 1933) for Mach 4 flow over a 5° half-angle cone. The non-dimensional

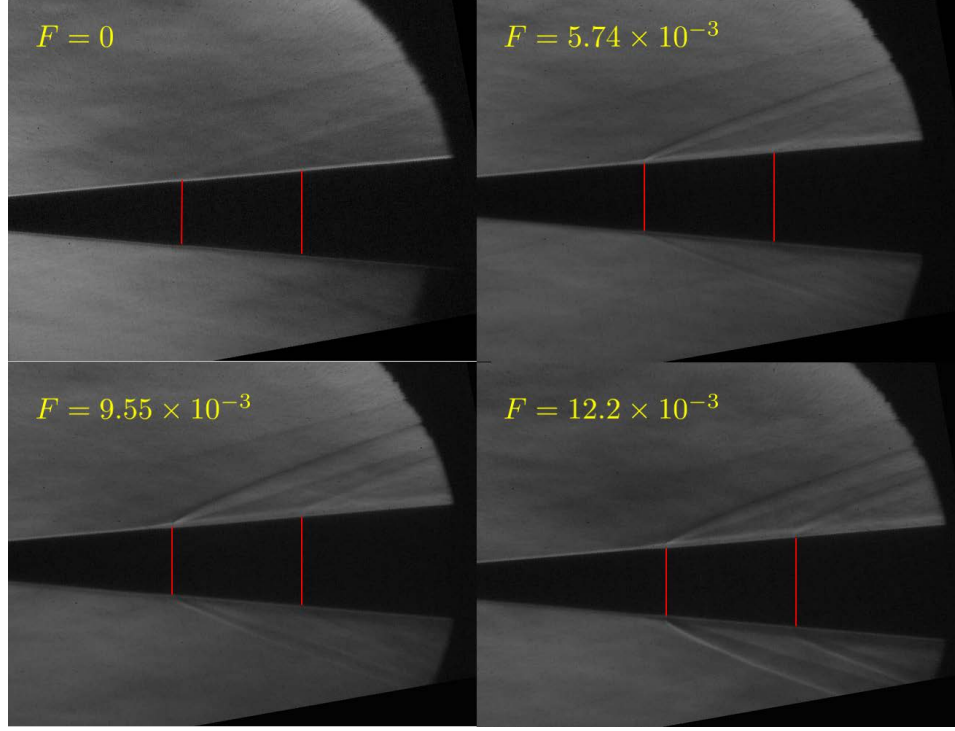


Figure 4.2: Example schlieren images with the conical injector. The free stream gas and injected gas for these cases is air.

pressure jump $\Delta p/p_1$ for this shock is 0.084 ± 0.016 calculated from perfect gas shock relations.

A shock stronger than the one generated at the cone tip is visible at the beginning of the injector section in all three cases with non-zero injection rate, as predicted in Section 1.2. The angle of this shock is $21 \pm 0.1^\circ$ in all cases studied. The shock is curved, so making a precise measurement of the shock angle at the cone surface is difficult. A shock angle of 21° gives a non-dimensional pressure jump of 1.00 ± 0.02 for the incoming flow that has already been processed by the shock from the cone tip. This shock is therefore about 13 times stronger than the shock at the tip of the cone and significantly impacts the state of the injection layer downstream. Closer examination of the data from these experiments reveals that the shock created by injection causes bypass transition of the injection layer immediately downstream of the start of the injector section, likely due to separation of the incoming boundary layer. It is for this reason that the experiments studying the instability in the layer do not use the model configuration with the conical injector.

For cases with higher injection flow rates, a second shock forms at the rear of the injector. This shock serves to redirect the inviscid region of the flow as the injection

layer adjusts to match the angle of the cone frustum downstream of the injector. The flow pattern is the one that would be predicted if the additional displacement resulting from injection were replaced by a convex bump on the surface of the cone.

Experiments with the cylindrical injector were conducted to examine the effect of shaping the injector. Figure 4.3 shows four example images from these experiments. The injector is again marked with red vertical lines and F is shown for each case in yellow.

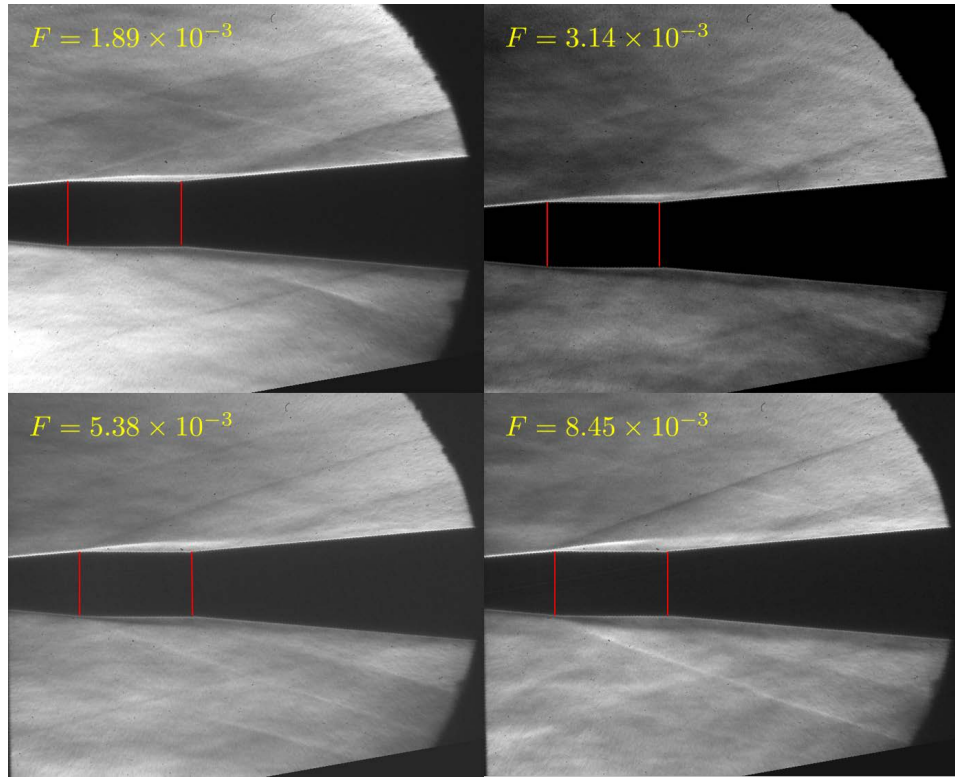


Figure 4.3: Example schlieren images with the cylindrical injector.

Three flow regimes are possible for this configuration. If the injection flow rate is high enough, the additional displacement caused by injection overcomes the effect of the negative slope of the injector and a shock will still be produced at the beginning of the injector section as in the cases with the conical injector in Figure 4.2. This is demonstrated by the bottom two images in Figure 4.3. Even so, at the highest mass flow rate tested in this set of experiments the shock angle is $18 \pm 0.1^\circ$ relative to the slope of the cone tip ahead of the injector, which corresponds to a non-dimensional pressure jump of 0.442 ± 0.017 , about half of that caused by the shock formed by injection with the conical injector. Shaping of the injector is therefore beneficial compared to an injector that matches the slope of the surface of the model for

reducing the strength of waves formed by injection even if the tuned flow rate is exceeded.

The second regime is illustrated by the picture in the upper-left of Figure 4.3. If the injection flow rate is low enough (or zero), the displacement of the injected gas is not enough to compensate for the negative slope of the injector and a Prandtl-Meyer expansion forms at the beginning of the injector section. This forms a favorable pressure gradient for the boundary layer, so no destabilization occurs.

The third regime is the tuned condition described above. This is shown in the upper-right picture in Figure 4.3. The injection flow rate is such that the slope of the interface between the injected gas and the free stream gas matches the slope of the cone tip ahead of the injector section and no perceivable waves are generated. Some compression waves are observed where the injection layer edge meets the edge of the frustum section. These form because a cylindrical injector is evidently not the proper shape to entirely compensate for injection on a cone model; some curvature is likely needed to minimize all waves. Finding the correct injector shape for a given geometry is beyond the scope of the current work, but it could be done computationally using an Euler flow solver and an optimization algorithm. The experiments presented here validate Fedorov's hypothesis and demonstrate that waves generated by injection can be mitigated by shaping the injector.

Injection layer properties

The remaining experiments to be described in this chapter are performed with the model with the cylindrical injector section and the diagnostics described in Sections 3.2 and 3.4. Before the instability waves were measured in detail, a set of experiments were performed where the full flow field was imaged with the pulsed laser light source. These experiments allow trends in injection layer thickness and mean transition location with respect to injection rate to be examined. The determination of where the instability waves begin to appear for a given condition is also very important because it aids in determining where best to place the camera's field of view when the waves are analyzed at a high frame rate.

The images in these experiments have a resolution of 912 x 240 pixels with a scale of 0.18 pixels per millimeter. The pulse width is set to 40 ns to provide good illumination while still freezing the motion of structures in the injection layer so that the transition location can be determined. Images are recorded at 30,262 frames per second. This is not nearly fast enough for image pairs to be correlated in time, but

it allows a large quantity of images to be recorded for averaging purposes.

Runs were performed at nominal unit Reynolds numbers of 9×10^6 per meter and 18×10^6 per meter for each injection rate. It should be noted that because the free stream temperature is effectively the same for every run, the Reynolds number in the test section of the Ludwieg tube depends only on the density in the free stream, which in turn only depends upon the free stream pressure. Therefore effects of Reynolds number, pressure, and free stream density cannot be decoupled from one another.

Figure 4.4 shows images from three cases with different injection rates with nitrogen injection. The injector is again marked by red lines in the images and the locations of the PCB pressure transducers are marked by blue lines on the cone frustum. The injection rates are reported as F on each image in the figure. The unit Reynolds number for all three of these cases is nominally 9×10^6 per meter. The injection layer thickness δ is measured at the rear of the injector section for consistency. This choice is arbitrary because the injection layer thickness is observed to scale similarly with injection rate at a fixed location along the model. The trends observed in Figure 4.4 are that δ increases and the transition location moves forward with increasing injection rate.

Figure 4.5 shows a similar set of images but for cases with different injected gases. The nominal unit Reynolds number is again 9×10^6 per meter. The injection rates were chosen such that δ is approximately the same for all three cases, and each one is a tuned case. It is observed that a lighter injected gas causes the transition location to move forward. Both of the observed trends for transition location agree qualitatively with the findings of Pappas and Okuno (1960). The instability waves in the three cases also appear to have different character depending on the injected gas. In helium, the waves appear as large-amplitude "rolling" structures reminiscent of those observed in free shear layers, e.g. by Brown and Roshko (1974). The waves in the nitrogen injection cases are lower-amplitude and more sharply inclined. Waves in RC318 injection cases are difficult to visualize in single images because they have a very long wavelength, but slow oscillations in the interface are visible if a sequence of images is viewed as a movie. Transition in RC318 cases appears to be influenced by the compression waves generated where the interface of the two gases meets the wall on the frustum rather than purely being due to the instability of the injection layer. The waves are analyzed quantitatively and in more detail in Sections 4.2 and 5.2.

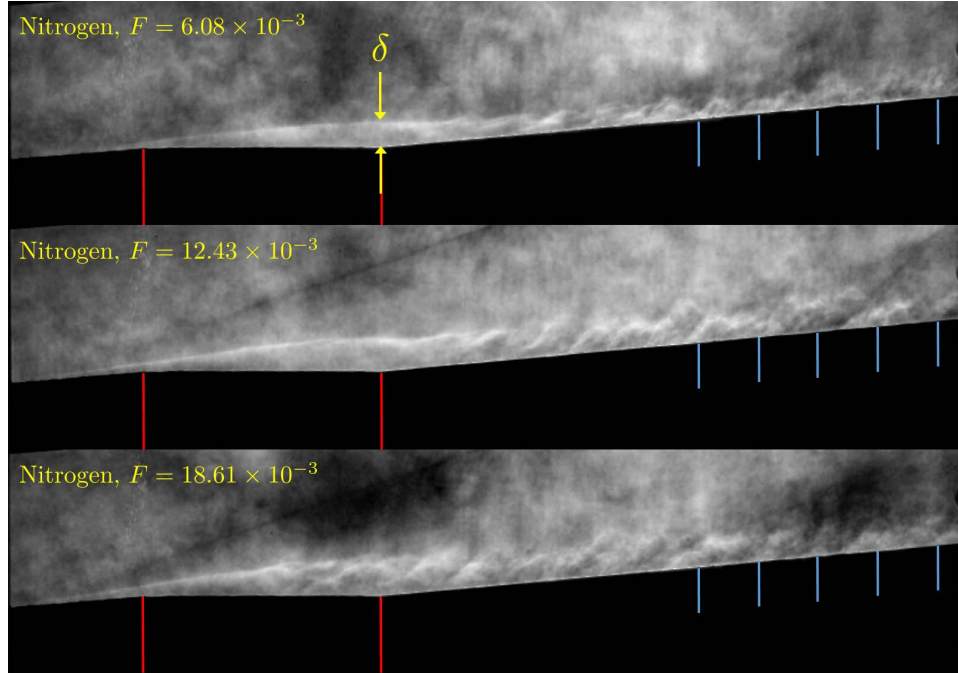


Figure 4.4: Full-field images with a 40 ns-pulse width from three cases with nitrogen injection at different injection rates. The injector is marked by red lines and the PCB locations are shown with blue lines.

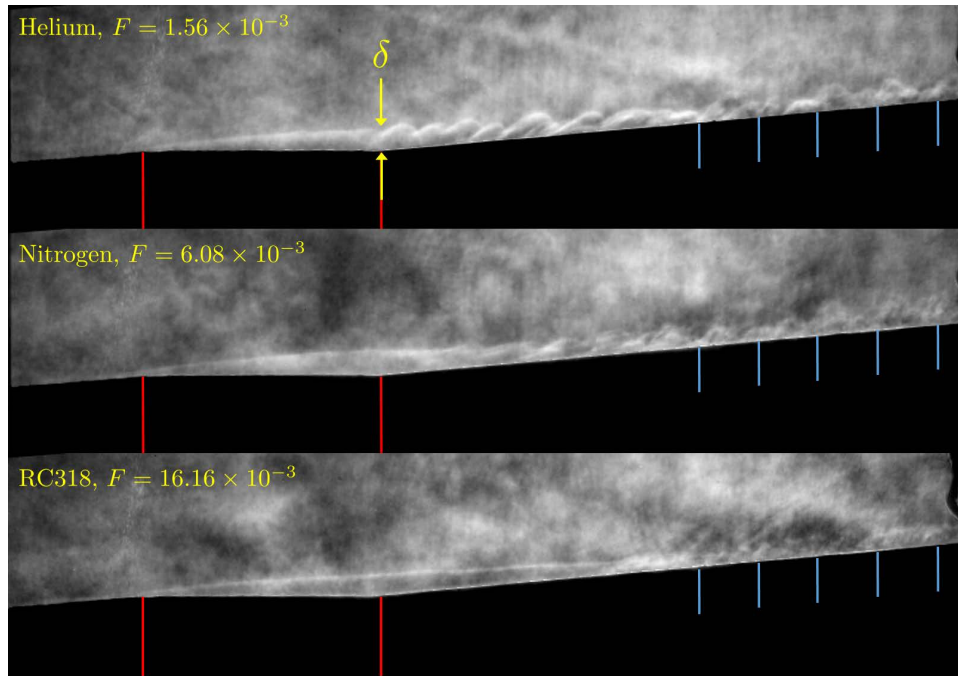


Figure 4.5: Full-field images with a 40 ns-pulse width from three cases with different injected gases but the same value of δ . The injector is marked by red lines and the PCB locations are shown with blue lines.

Comparing Figures 4.3, 4.4, and 4.5 reveals that the conditions that result in a tuned case do not depend directly on F , but rather on the displacement thickness δ . This supports the idea that F is not the appropriate parameter for systematically reporting results as alluded to earlier in this section.

Figures 4.4 and 4.5 also demonstrate the quality of the images acquired with the pulsed laser diode light source. The images in Figures 4.4 and 4.5 have been minimally post-processed, with only some contrast enhancement and partial background subtraction. The effective incoherence of the light source gives nearly speckle-free images, although there is some non-uniformity in the illumination across the image and between multiple images from the same experiment.

The visual injection layer thickness δ is plotted versus F in Figure 4.6. δ is non-dimensionalized by the length of the injector L_{inj} , but this choice is arbitrary. Solid symbols have a nominal unit Reynolds number of 9×10^6 per meter while hollow symbols have a nominal unit Reynolds number of 18×10^6 per meter. This labeling scheme is used throughout the remainder of this chapter and in Chapter 5. The vertical error bars represent the uncertainty in δ due to the finite resolution of the images. Horizontal error bars are calculated from both the uncertainty in measured injection mass flow rate and the uncertainty in free stream conditions (assumed to be $\pm 5\%$ for all variables) using standard error propagation. Note that δ varies by about a factor of three for the injection rates studied.

The distance from the front of the injector to the mean transition location is plotted versus F in Figure 4.7. The transition distance is measured along the surface of the model, and is determined by observing where the interface between the injected gas and free stream gas ceases to be smooth and laminar. Making this determination with an optical method is admittedly less precise than with a surface measurement like thermocouples or pressure transducers as is commonly done for boundary layers, but it is sufficient to determine trends in the data. It is reported in dimensional units here so that the location of the transition front can be more readily compared with the geometry of the model. The vertical error bars represent the uncertainty in transition location due to unsteadiness in its position, as this is much larger than the width of a pixel. Figure 4.7 shows the same trends that are suggested by Figures 4.4 and 4.5 and observed by Pappas and Okuno (1960), namely that the transition location moves forward with increasing injection rate, increasing unit Reynolds number, and for lighter injected gases.

The data shown in Figures 4.6 and 4.7 are analyzed more closely in Section 5.1.

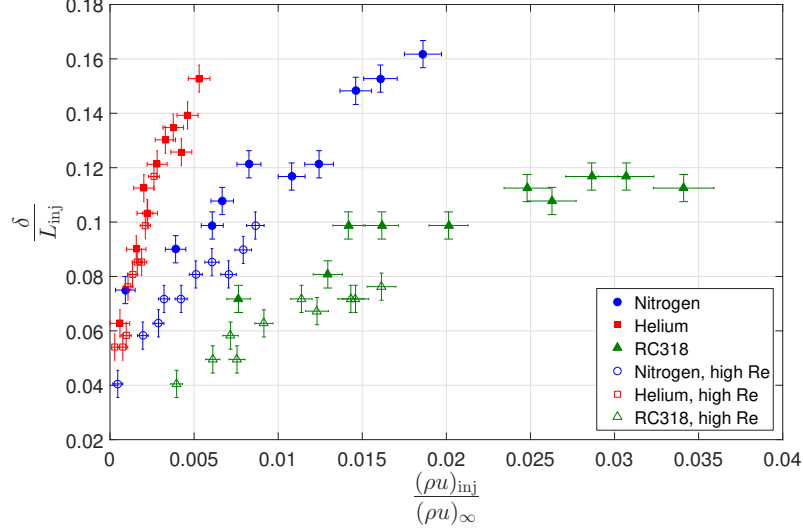


Figure 4.6: Injection layer thickness measured at the rear of the injector section, normalized by the injection length, plotted versus the non-dimensional mass flux F . High Reynolds number cases have a nominal unit Reynolds number of 18×10^6 per meter.

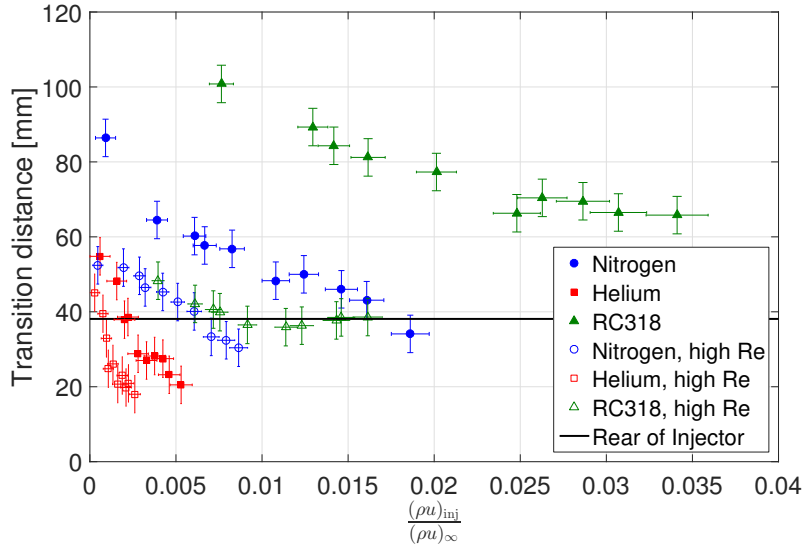


Figure 4.7: Transition location measured from the front of the injector section plotted against the non-dimensional mass flux F .

4.2 High-speed Imaging

Experiments at the same nominal conditions as those in Section 4.1 were performed at a reduced resolution but much higher frame rate to analyze the instability waves in the injection layer. The resolution used is 224 x 64 pixels at the same scale of 0.18 pixels per millimeter. The reduction in resolution allows images to be recorded at a frame rate of 289,361 frames per second. The pulse width of the laser diode is

reduced to 25 ns to decrease motion blur and the duty factor. At these conditions the duty factor is 0.72%, much higher than the rated maximum of 0.1% for the diode, but reducing the forward current to 3 A from the rated value of 40 A prevents it from being damaged. A set of 10,000 images is acquired for each case, so statistics can be generated at each condition from a single tunnel run.

Image processing routine

An extensive image processing routine is employed to treat the raw images before wave properties are extracted. Figure 4.8 illustrates the routine, beginning with a raw image and ending with the final image that is to be analyzed. The image comes from a case with nitrogen injection at the low unit Reynolds number free stream conditions (9×10^6 per meter).

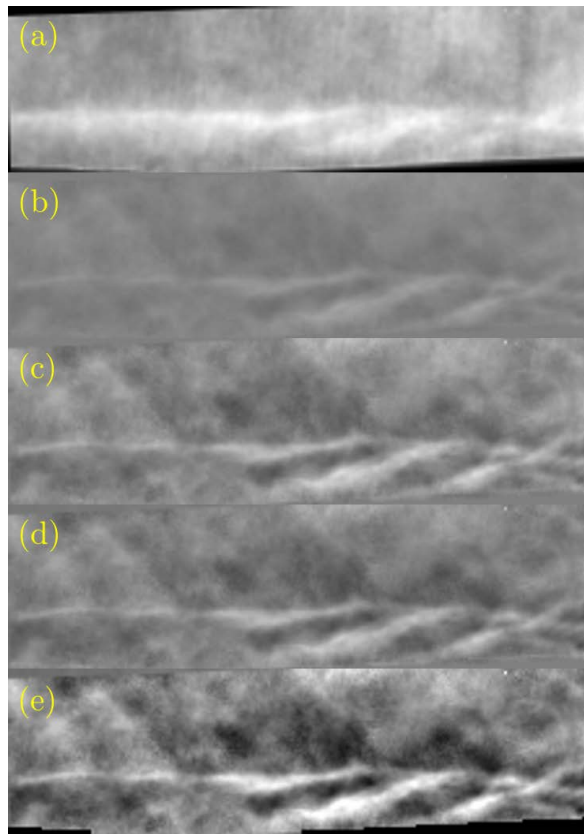


Figure 4.8: Images from a sample case to illustrate the image processing routine. Images (a) through (e) represent stages in the routine with (a) being the raw image and (e) being the final, processed image.

Image (a) shows a raw image recorded by the camera. The image is rotated so that the interface between the injected gas and free stream gas is horizontal. This simplifies the automated analysis routine described later in this section. Next, a

mean image is constructed by averaging 200 images before and after the image being processed. This is done for each image in the sequence of 10,000 for a given case. The mean image is used to create a correction image that, when subtracted from the mean image, forms an image that is uniformly gray with pixel intensities of 0.5 for each pixel. That correction image is subtracted from the image being processed. This subtraction eliminates speckle and other artifacts from the imaging system and accentuates flow features that are changing in time from image to image, such as the instability waves in the injection layer. The resulting image in the example in Figure 4.8 is image (b).

MATLAB's `imadjust` function is then used to enhance the contrast in the image. The function linearly maps pixels from the current intensity map to a new one by specifying high and low cutoffs for the input image and the output image. Any pixel with a value above the high input cutoff or below the low input cutoff is mapped to the high or low output cutoff, respectively. Pixels with values between the cutoffs in the input image are mapped linearly to the new image. This is image (c) in Figure 4.8. This step would be sufficient for a single image with appropriate cutoffs, but non-uniformities in the light output from the diode for different pulses are amplified by the previous step in the routine, so images in a sequence can have very different mean brightness. This makes cross-correlation between images difficult, and must be corrected.

Illumination is made uniform by shifting the mean of each column of pixels in the image to 0.5. This is done by simply subtracting a fixed value μ from each pixel in the column that is the difference between the current mean intensity of the column and the desired value of 0.5. For a vector of length N with elements x_i and mean value \bar{x} , μ is given by

$$\mu = \bar{x} - 0.5 \quad . \quad (4.2)$$

It is clear that μ can be subtracted from each x_i to give a mean of 0.5 by employing the definition of the mean,

$$0.5 = \bar{x} - \mu = \frac{\sum x_i}{N} - \mu = \frac{\sum (x_i - \mu)}{N} = \bar{x}' \quad . \quad (4.3)$$

Here x' is the shifted version of x with a new mean. The resulting image is image (d) in Figure 4.8.

The final step in the routine is to enhance the contrast of the processed image, but this cannot be done by again employing MATLAB's `imadjust` function because the mean intensity of each image must be maintained for the reason explained above.

The intensity map of the image is stretched such that either the darkest pixel in the image has a value of 0 or the brightest pixel has a value of 1, whichever is closer to the current map, and the other pixels are mapped linearly such that the mean intensity of the image is maintained. Finally, the edge of the model is found using a Canny filter on the mean image formed in the first step of the routine, and the model is superimposed on the final image in black. The resulting processed image is labeled (e) in Figure 4.8. This routine also amplifies the noise from the shear layers at the edges of the test section described in Section 3.4. The image analysis routines presented in this section rely primarily on auto- and cross-correlation of the images, but the noise from the turbulent shear layers is largely uncorrelated. This allows instability waves to be studied in spite of noise created by the large depth of field of the imaging system.

Image analysis: Wavelength

The wavelength of the instability waves in cases with nitrogen and helium injection can be determined directly from the images. The wavelengths in cases with RC318 injection are too long to be determined accurately with the field of view of the imaging system, so wavelength in these cases is calculated by measuring convective speed U_c and frequency and invoking Taylor's hypothesis:

$$U_c = \lambda f \quad . \quad (4.4)$$

Wavelengths are determined using autocorrelation. The accuracy of autocorrelation is limited only by the digitization of the image. The uncertainty is therefore approximately 200 μm . Figure 4.9 shows a sample image relative to a full-field image like that in Figure 4.4. The dashed yellow lines show the region of the image that is used for autocorrelation; it is centered on the interface between gases. The correlated region is translated horizontally to produce the autocorrelation curve.

The autocorrelation curve is shown in Figure 4.10. The curve displays a peak value of 1 at a lag of zero as do all autocorrelation curves, but also shows a peak with non-zero lag. This peak corresponds to the wavelength of the waves observed in the image, about 9 mm for this image.

Many images for a given case do not show instability waves. Transition is an unsteady process, so waves occasionally appear before or after the field of view of the imaging system and are not measured. Large disturbances are also occasionally produced in the free stream which create turbulent bursts in the injection layer.

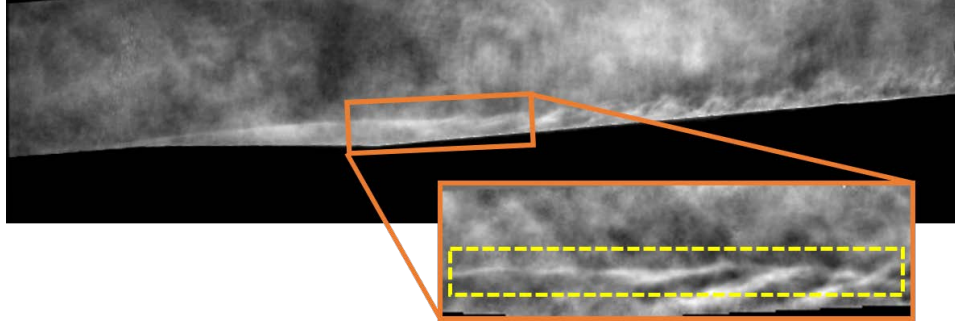


Figure 4.9: Processed image showing instability waves to be analyzed by autocorrelation. The yellow dashed lines show the region used for autocorrelation.

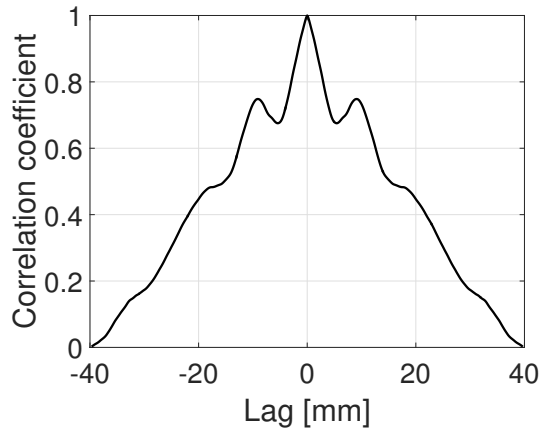


Figure 4.10: Autocorrelation curve for the image shown in Figure 4.9. The peak at non-zero lag corresponds to a wavelength of 9 mm.

Several logic steps are employed by the analysis algorithm to ensure that only the instability waves are analyzed by the routine.

Criteria are placed on the absolute value of the peak at non-zero lag, its relative magnitude relative to the magnitude of the curve at the local minimum between the peak at non-zero lag and the maximum at zero lag, and the slope of the curve between the local minimum and the peak at non-zero lag. The cutoff values for these criteria are somewhat arbitrary and were determined by examining individual images where a wavelength was apparent and those where no wavelength appeared and adjusting the values until the correct result was obtained. Changing the cutoff values by small amounts does not change the result of the algorithm significantly. For a given case with 10,000 images, 2000-4000 images will typically contain a wavelength that meets the criteria.

The measured wavelengths can be plotted in a histogram, like the one in Figure 4.11. Determination of a single wavelength that is representative of the case is made by

fitting a probability distribution to the population. An appropriate distribution is the log-normal distribution, which assumes that the logarithm of the data follows a normal distribution. This solves the difficulty of using a normal distribution, which can have zero or negative values, which is obviously non-physical for wavelengths. The maximum of the fitted distribution is taken to be the wavelength for the condition being studied, with the standard deviation representing the uncertainty.

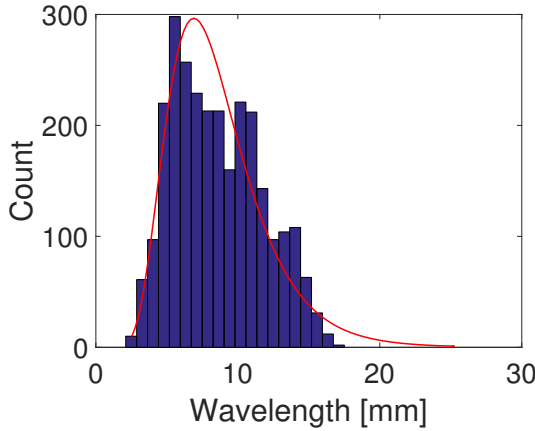


Figure 4.11: Histogram of measured wavelengths for an example case. The red line shows a fitted log-normal distribution.

Wavelength normalized by the injector length is plotted versus F in Figure 4.12 for all cases. Recall that the wavelength for RC318 is not measured directly, but computed with Taylor's hypothesis. The injection layer is too thin for the wavelength to be measured in cases with the high nominal unit Reynolds number and nitrogen injection, so it is only reported for cases with helium injection. Vertical error bars represent the standard deviation of the underlying distribution for each case.

The wavelength appears to be relatively constant for each injected gas. Recall that the displacement thickness of the injection layer δ varies by a factor of three with increasing F for each injected gas. This means that the wavelength of the instability waves does not scale with the displacement thickness of the injection layer, a trait not shared by waves in boundary layers.

Image analysis: Convective speed

The convective speed of the instability waves can be determined relatively easily by image cross-correlation. The high, constant framing rate allows each image to be correlated with several images before or after itself. The same region used to detect the wavelength is used for cross-correlation. In nitrogen and helium injection cases, only images with waves present are correlated with their neighbors to avoid

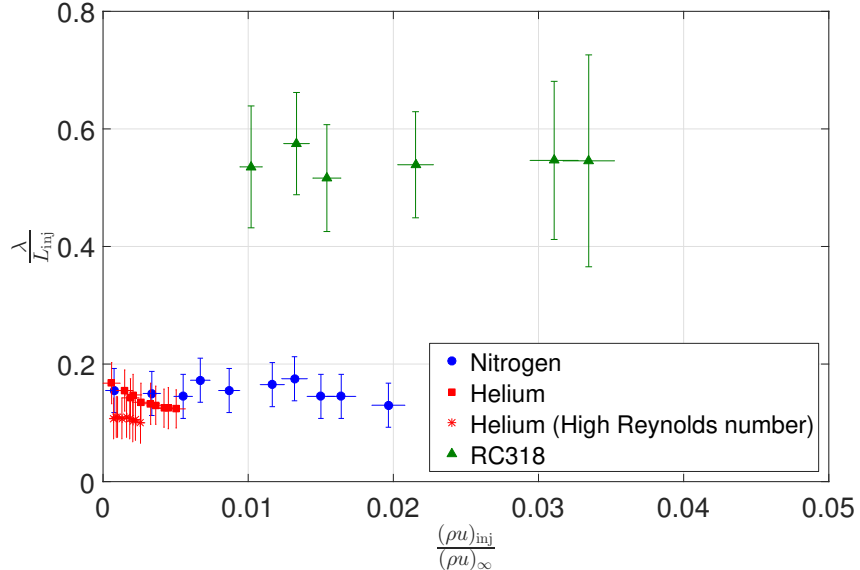


Figure 4.12: Wavelength normalized by the injector length plotted against the non-dimensional injection rate F for all cases analyzed. The wavelength is measured directly for helium and nitrogen injection and calculated assuming Taylor's hypothesis for RC318 injection.

incorrectly tracking other phenomena, such as turbulent bursts. In cases with RC318 injection cross-correlation is attempted near the interface of the gases for all images, so the results in those cases are less accurate than those for nitrogen and helium injection.

Images are correlated with each of the four previous images in an attempt to mitigate pixel locking. Figure 4.13 shows a sequence of images from a case with nitrogen injection. The frame rate is sufficiently high that the waves move a very short distance, only a few millimeters, between images. Motion of the waves is indicated by the arrow in the figure.

As with wavelength detection, a criteria is applied to a correlation curve to determine if a velocity can be reliably measured. An example correlation curve is shown in Figure 4.14. In order to be accepted for velocity measurement, the peak of the curve must occur at a non-zero lag and must have an absolute value greater than a specified cutoff. The value for the cutoff is again somewhat arbitrary, but one is chosen that gives 1000-2000 velocity measurements for most cases. The lag is converted to a velocity by multiplying by the framing rate, assuming a constant velocity between frames.

The histogram in Figure 4.15 shows the distribution of measured velocities for the

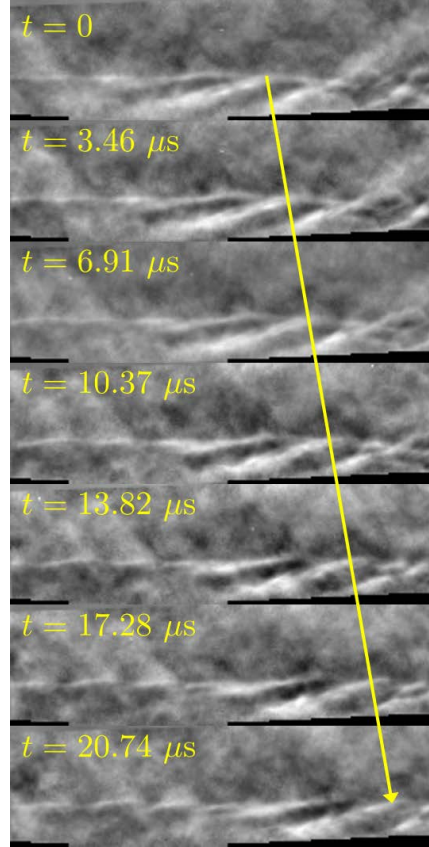


Figure 4.13: Series of images of a case with nitrogen injection showing the propagation of waves. Their velocity is determined by cross correlating the region in the images where the waves are present.

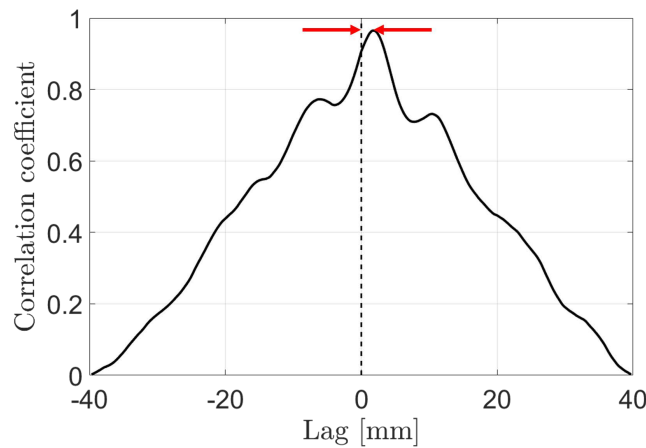


Figure 4.14: Correlation curve for the example case shown in Figure 4.13. The lag, indicated by the red arrows, is converted to a velocity by multiplying by the framing rate.

sample case presented in this section. Significant pixel locking is present, evidenced

by the gaps between bins in the histogram. This is to be expected given the short distance traversed by the waves between images.

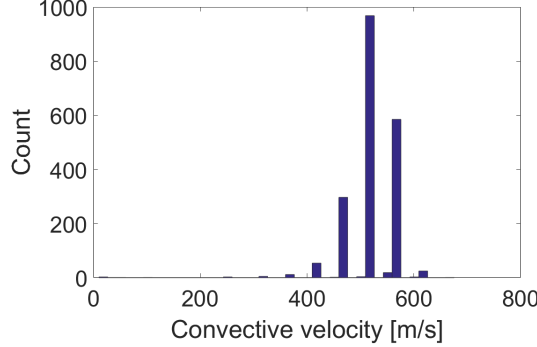


Figure 4.15: Distribution of measured velocities for the example case.

The mean and standard deviation of the population are used to calculate a single value and uncertainty for a given case. Figure 4.16 shows measured convective velocities for all cases. Error bars for the RC318 cases are quite large, reflecting the reduced accuracy in those measurements because images with waves could not be reliably identified. The data shows no discernible trend for nitrogen injection with increasing injection mass flow rate, while for helium injection an increase in convective velocity is observed and for RC318 injection it appears that the velocity may be decreasing. This data is more closely analyzed in Section 5.2.

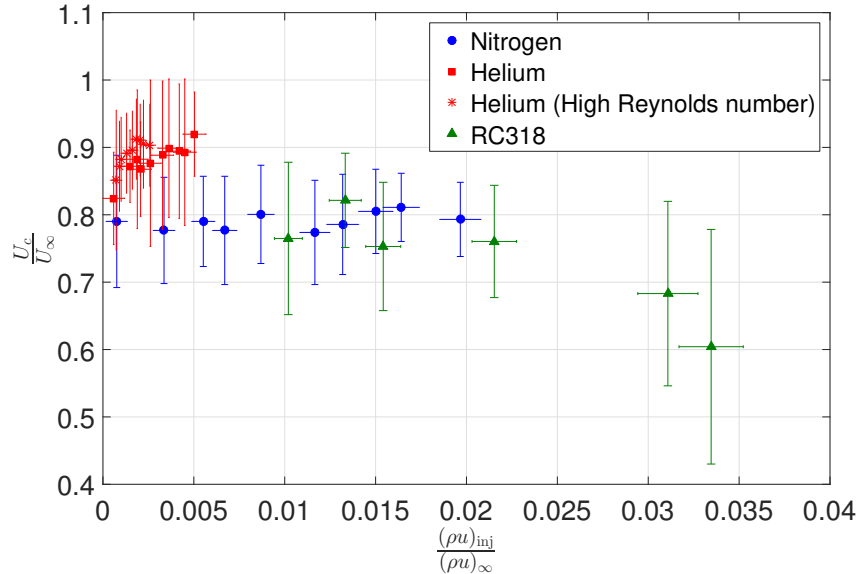


Figure 4.16: Convective velocity normalized by the free stream velocity plotted versus the non-dimensional mass flux F for all cases studied.

Image Analysis: Frequency

The frequency of the waves is determined from imaging by invoking Taylor's hypothesis for nitrogen and helium injection cases. With RC318 injection, however, it can be measured directly in most cases. The edge of the injection layer in these cases is reasonably stable in time and easy to see with the naked eye, so edge-detection routines are used to find a point along the edge and track it from image to image. Its position moves up and down as waves pass, and the frequency can be extracted by temporal Fourier analysis.

It is not expected that the edge will be able to be located in each individual image, particularly if a burst of turbulence is passing. All six edge-finding methods available in MATLAB are therefore used to increase the chance that at least one method will consistently detect the edge and extract a frequency. The Canny, log, Roberts, and zero-cross methods are omni-directional while the Prewitt and Sobel methods search for either horizontal or vertical edges. The edge of the injection layer is horizontal in the images, so the Prewitt and Sobel methods are instructed to search for a horizontal edge. Thresholds for the methods are determined by trial and error.

Figure 4.17 shows an example image to illustrate the success of the edge-detection routines. The concentric colored dots represent where each of the six methods indicates the edge of the injection layer is. Each method successfully locates the desired edge in this image.

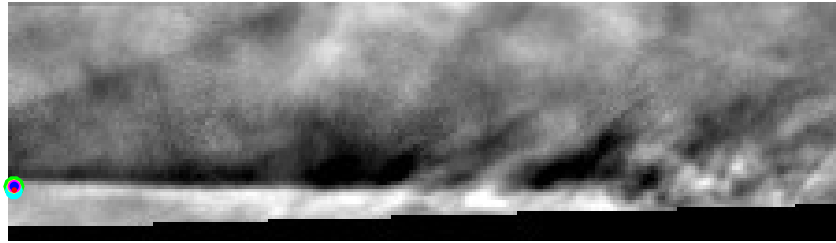


Figure 4.17: Example image from a case with RC318 injection. The colored dots on the left side of the image represent the location of the injection layer edge determined by the Canny, log, Roberts, zero-cross, Prewitt, and Sobel edge-detection methods.

The position of the edge is recorded in time for each edge-detection method and a temporal Fourier analysis is performed for each. In some cases none of the methods show a significant peak in the spectrum, but most cases exhibit a peak for at least one method. The Prewitt and Sobel methods are successful most often, likely because they can be instructed to search for only horizontal edges which prevents them from being fooled by noise in the images. Figure 4.18 shows power spectral density

spectra for the Prewitt and Sobel methods for the example case; both exhibit a peak at 24.5 kHz.

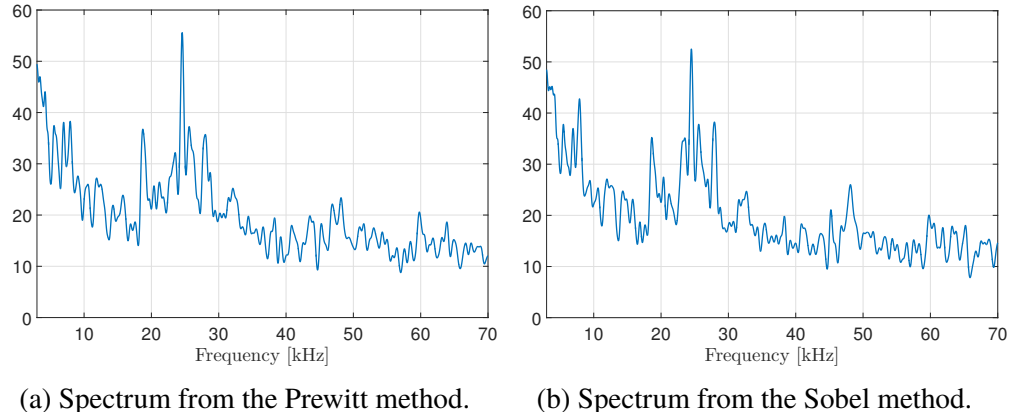


Figure 4.18: Power spectral density plots from the Prewitt and Sobel methods for the example RC318 injection case. Peaks are observed at 24.5 kHz for both methods.

PCB frequency results

Data from the PCB pressure transducers were also analyzed for each case. Temporal Fourier analysis was applied to detect frequencies. Many cases, particularly for nitrogen injection, do not show a significant peak in the spectra for any of the transducers. This could have several causes. First, the instability waves are not consistently present in the flow field, and in order to be detected by the pressure transducers they need to not only be present but also occur very near to the transducers which are quite small (diameter 3.2 mm). This could prevent the transducers from detecting a single frequency. Second, the pressure fluctuations from the instability waves may be somewhat localized to the interface between the injected gas and free stream gas and do not propagate to the wall of the model consistently. Finally, the transducers may be located too far behind the onset of transition to measure the frequency of the waves before they break down to turbulence. The location of the transducers relative to the transition location can be seen for a few cases in Figures 4.4 and 4.5.

In some cases, however, a discernible peak is seen in the PCB spectra. Piezoelectric pressure transducers are sensitive to mechanical vibration, and since the model has a high stiffness and low mass the characteristic frequency of the model's vibration is expected to be in the range of 10-100 kHz, similar to the frequency of the instability waves. The response of the five PCB transducers in the model to vibration was tested by striking the sting in the Ludwieg tube test section with a rubber mallet.

The resulting spectra are shown in Figure 4.19. The transducers show strong mechanical vibrations around 20 kHz, but the signal is fairly broad band and the energy is concentrated below 50 kHz. Transducer 4 at 211 mm from the cone tip shows particular sensitivity to vibration.

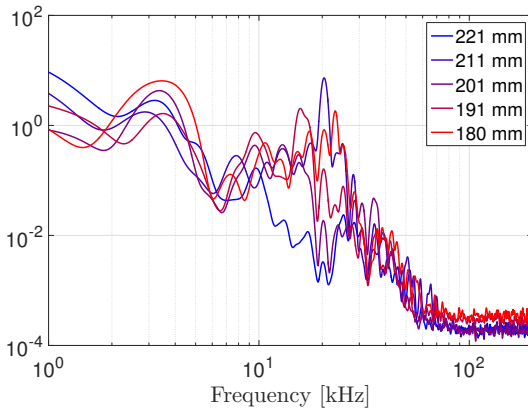


Figure 4.19: Response of the PCB pressure transducers in the cone frustum to mechanical vibration. They are labeled in the figure legend according to their distance from the cone tip, measured along the surface of the model.

Four example spectra from experiments are shown in Figure 4.20. The plot in the upper-left (4.20a) is for a case where the boundary layer is tripped using a trip wire upstream of the injector and the injection layer is fully turbulent by the time it reaches the first transducer. This serves as a baseline case where no peaks are visible in any of the spectra. Note that transducer 4 shows a strong peak at around 20 kHz in all four cases shown, but recall that this is due to mechanical vibration and not pressure disturbances in the flow.

The remaining plots show spectra from cases with injection of the three different gases. The peak with nitrogen injection (plot 4.20b) is quite weak and only visible in the spectrum of transducer 1, but it is discernible when compared to the fully turbulent case and the spectra for the other gases. The spectra for helium injection (plot 4.20c) show a much stronger peak compared to the peak in the spectra for nitrogen injection. This is likely due in part to the much higher sound speed in helium, as pressure fluctuations due to acoustic waves are related to density fluctuations by $\Delta p = a^2 \Delta \rho$. Assuming the density fluctuations are of the same order in each case, the pressure fluctuations detected by the pressure transducers will be stronger if the injected gas has a higher sound speed, such as helium compared to nitrogen. The peak in the spectra for RC318 injection (4.20d) occurs in the same

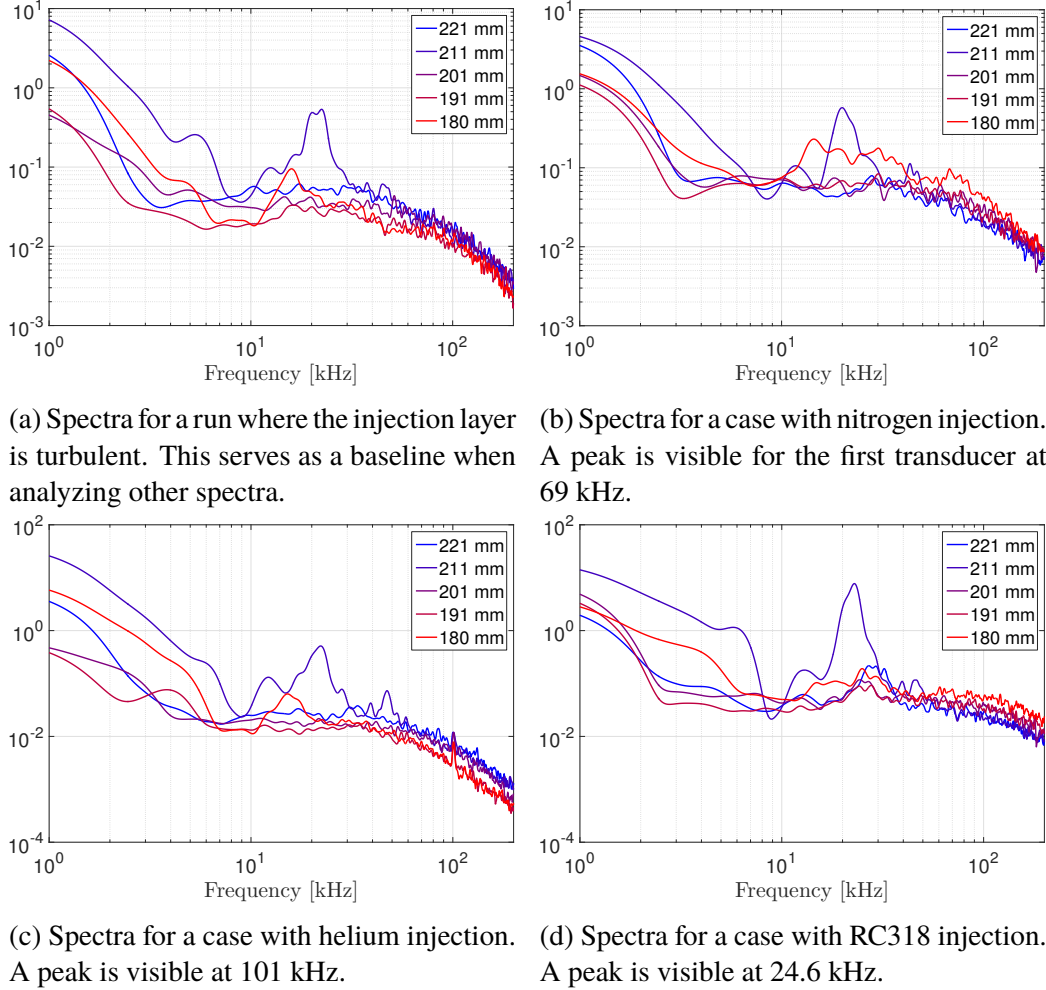
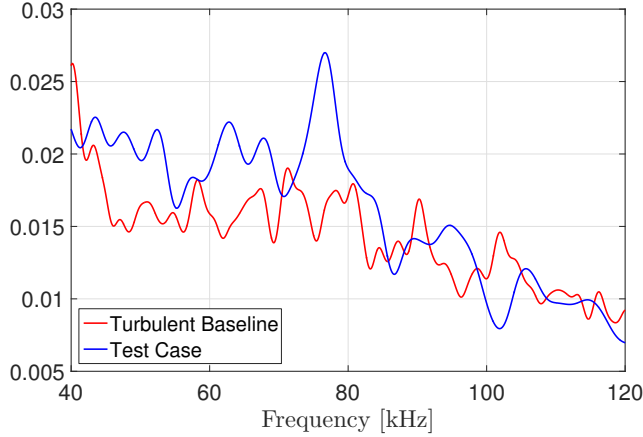


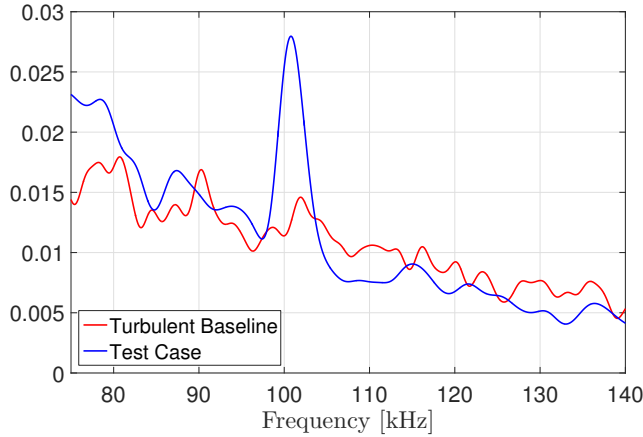
Figure 4.20: Spectra from the PCB pressure transducers for four example experiments with injection.

frequency band as mechanical vibrations, but the peak is distinguishable in several of the PCB spectra when they are compared to spectra from the other cases.

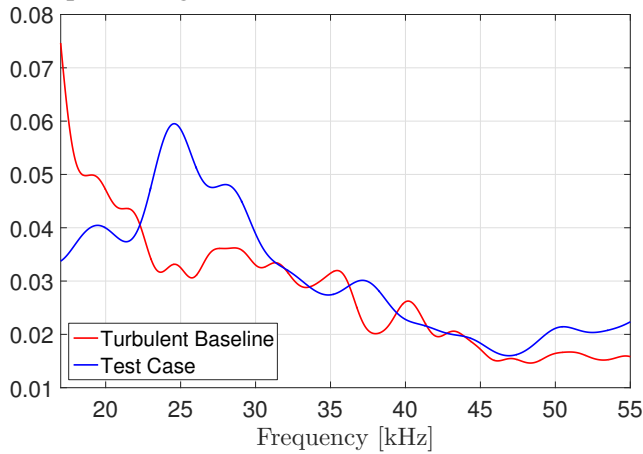
Figure 4.21 shows the spectra from transducer 1 for each injection case shown in Figure 4.20 compared to the spectrum from the turbulent baseline case. The axes have been adjusted to make the peaks easier to discern. The scales have also been adjusted such that the baseline noise levels are similar for the two cases being compared.



(a) Comparison of transducer 1 spectra for a case with nitrogen injection versus the turbulent baseline case. Compare to Figure 4.20b.



(b) Comparison of transducer 1 spectra for a case with helium injection versus the turbulent baseline case. Compare to Figure 4.20c.



(c) Comparison of transducer 1 spectra for a case with nitrogen injection versus the turbulent baseline case. Compare to Figure 4.20d.

Figure 4.21: Spectra from transducer 1 for the three injection cases shown in Figure 4.20 compared to the turbulent baseline shown in Figure 4.20a.

Frequency Results

Frequency data from image analysis and the pressure transducers are plotted together in Figure 4.22. The uncertainties in the nitrogen and helium visualization data are propagated from the wavelength and velocity data. Uncertainty in frequency for the RC318 visualization data and all pressure transducer data is calculated from the full width at half maximum of the peak in the spectra. The frequency is relatively constant for nitrogen injection cases, increases with increasing injection mass flow rate for helium injection cases, and decreases slightly with increasing injection mass flow rate for RC318 injection cases. The data are analyzed in more detail in Section 5.2.

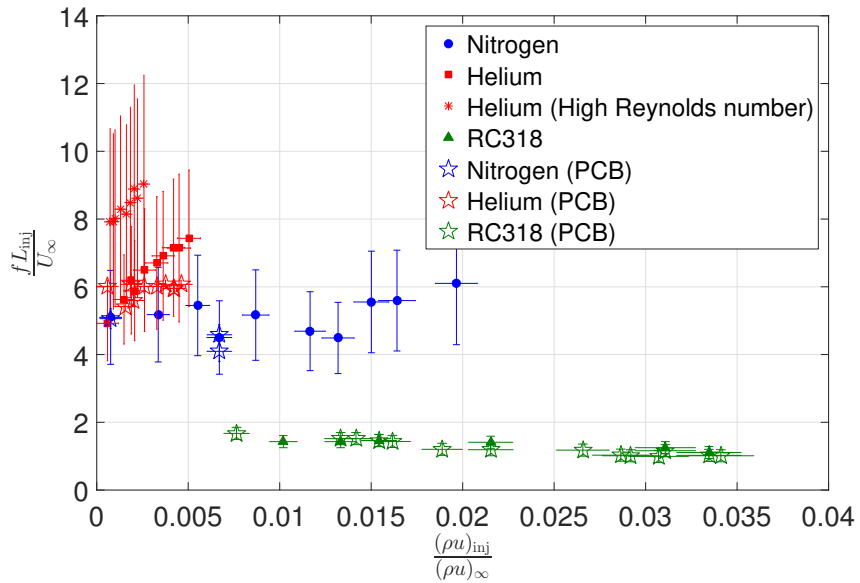


Figure 4.22: Frequency from image analysis and pressure transducers. The frequency from image analysis for the helium and nitrogen injection cases is computed using Taylor's hypothesis while the frequency in the RC318 cases is computed directly from the image processing routine.

4.3 OpenFOAM Computations

Nine cases were computed in OpenFOAM (see Section 2.5), three injection rates for each of the three injected gases. The injection rate is varied by specifying the velocity of the injected gas as it exits the injector. Flow conditions are listed in Table 4.1. The non-dimensional mass flux F is averaged across the surface of the injector since the density is not uniform due to the zero-gradient boundary condition on the pressure. The non-dimensional momentum flux J is also listed in Table 4.1 for reference.

Injected gas	u_{inj} [m/s]	$F = \frac{(\rho u)_{\text{inj}}}{(\rho u)_{\infty}}$	$J = \frac{(\rho u^2)_{\text{inj}}}{(\rho u^2)_{\infty}}$
Nitrogen	6	2.75×10^{-3}	0.28×10^{-4}
Nitrogen	16	7.56×10^{-3}	1.80×10^{-4}
Nitrogen	35	19.67×10^{-3}	10.25×10^{-4}
Helium	20	1.20×10^{-3}	0.38×10^{-4}
Helium	40	2.65×10^{-3}	1.59×10^{-4}
Helium	70	5.21×10^{-3}	5.42×10^{-4}
RC318	3	10.35×10^{-3}	0.51×10^{-4}
RC318	7	26.06×10^{-3}	2.78×10^{-4}
RC318	12	50.60×10^{-3}	9.14×10^{-4}

Table 4.1: Flow conditions for the OpenFOAM computations.

Grid independence

The case with nitrogen injection at $u_{\text{inj}} = 16$ m/s was computed on eight grids with different levels of refinement to assess the independence of the solution to the grid resolution. Resolutions in the refined region near the wall are 191, 145, 113, 85, 69, 57, 45, and 38 $\mu\text{m}/\text{cell}$, corresponding to Reynolds numbers based on cell size of 1719, 1305, 1017, 765, 621, 513, 405, and 342, respectively. The grid used for the computations in this work has a resolution of 45 $\mu\text{m}/\text{cell}$. Convergence criteria such as the value of y^+ at the wall, commonly used for boundary layers, are not well-suited to this flow because the steepest gradients of the flow variables occur near the interface of the gases and not at the wall like they do for boundary layers. Images of the full flow field show very little qualitative difference for all grid resolutions. Profiles of flow variables are taken vertically from the rear of the injector section for a quantitative comparison and plotted against y , the coordinate normal to the wall.

A second check can be performed on these profiles by examining the relative difference, $(x_{\text{coarse}} - x_{\text{fine}}) / x_{\text{fine}}$, for each flow variable x as a function of y for grids of different resolutions. This is shown in Figure 4.24 for grids with resolutions of 38 $\mu\text{m}/\text{cell}$ (the most refined grid) and 69 $\mu\text{m}/\text{cell}$. The maximum error occurs where the gradient is steepest, but it does not exceed about 10% through the majority of the domain, which is likely on the order of the errors incurred due to approximations regarding diffusion. This agreement provides further support for adequate convergence of the test grid.

Finally, the sum of the relative differences squared between each grid σ (Equation 4.5 for flow variable x and resolution i) and the most highly-resolved grid are plotted in

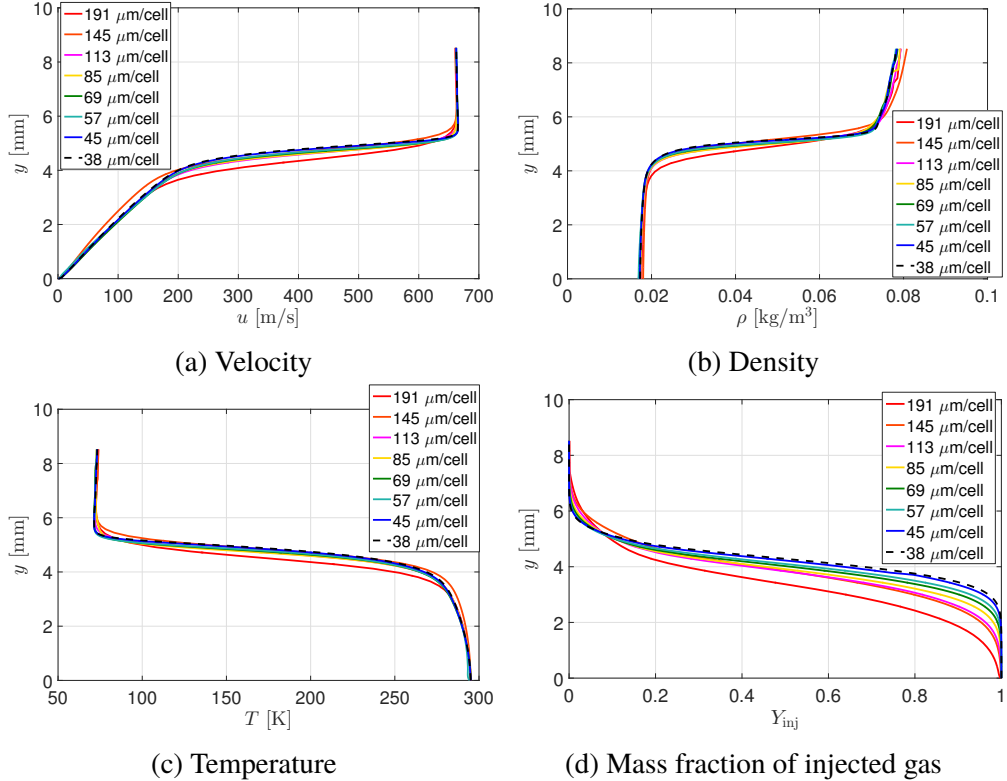


Figure 4.23: Profiles taken at the rear of the injector section for the various grid resolutions tested.

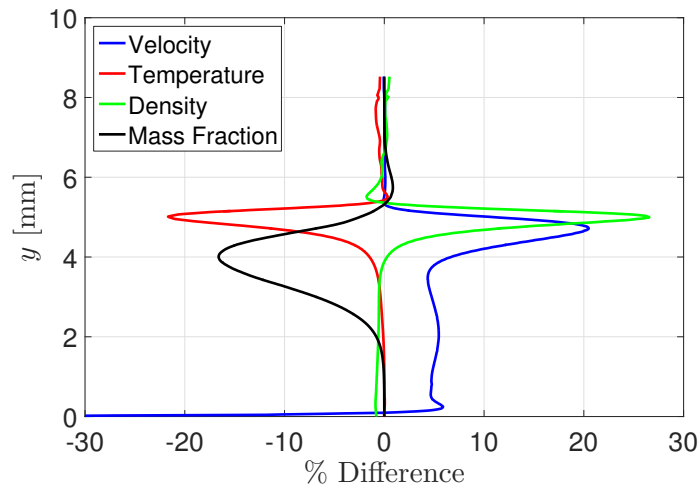


Figure 4.24: Relative difference in the flow variables plotted as a function of y for the grid with a resolution of $69 \mu\text{m}/\text{cell}$ compared to the most refined grid ($38 \mu\text{m}/\text{cell}$).

Figure 4.25,

$$\sigma_{x,i} = \sum \left(\frac{x_{\text{coarse},i} - x_{\text{fine}}}{x_{\text{fine}}} \right)^2 . \quad (4.5)$$

The absolute values of σ_x mean little, but measuring convergence this way allows the accuracy of each grid resolution to be assessed for all flow variables simultaneously. The value of σ is similar for the three finer resolutions, indicating adequate convergence at 45 $\mu\text{m}/\text{cell}$.

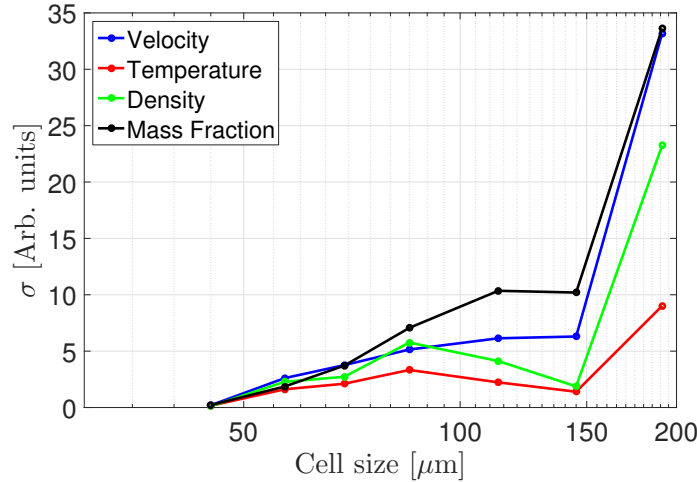


Figure 4.25: Total relative difference (see Equation 4.5) in flow variables as a function of grid resolution.

Nitrogen results

Figure 4.26 shows the flow field for the three cases with nitrogen injection. The coloring represents the density, with blue to red corresponding to low to high density. The color scale is normalized for each individual case so that flow features can be more easily identified.

The flow field looks qualitatively similar to the schlieren images in Figure 4.4. The thickness of the injection layer increases with increasing injection rate and a shock is produced at the start of the injector section for sufficiently high injection rate. Some waviness is present in the interface region for the two lower injection rates, but the properties of these waves are not expected to be similar to the ones in the experiment, as they may be influenced by the grid.

Eight wall-normal profiles are taken for each case to analyze flow variables. Locations are marked by orange arrows in Figure 4.27. One profile is taken of the incoming boundary layer near the end of the cone tip section, three profiles are taken over the injector, and four are taken on the frustum section downstream of the injector section. The distances measured along the cone surface from the tip of the cone for each profile are 120 mm, 132.5 mm, 152 mm, 172 mm, 180.6 mm,

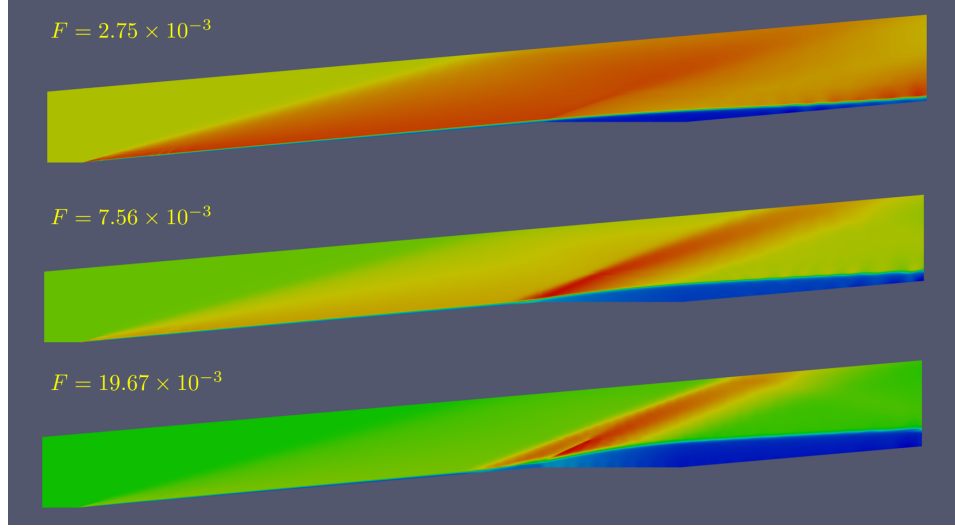


Figure 4.26: Results from the three computations with nitrogen injection. Coloring corresponds to density, with the color scale normalized to each case. The value for the non-dimensional mass flux F is given in the upper-left for each case.

189.2 mm, 197.8 mm, and 206.4 mm, respectively. The data is interpolated to 1000 equally-spaced points on each profile.

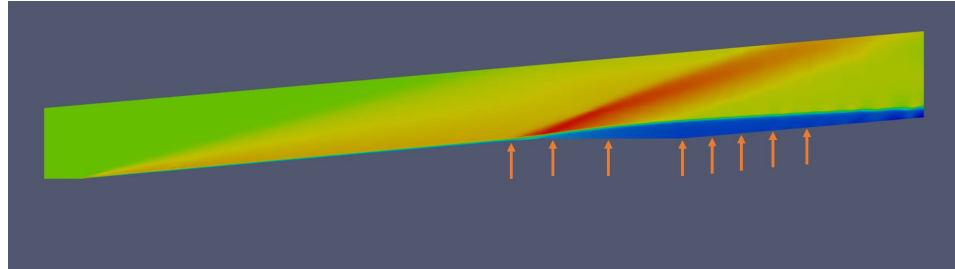


Figure 4.27: Location of wall-normal profiles for all OpenFOAM cases. They are located 120 mm, 132.5 mm, 152 mm, 172 mm, 180.6 mm, 189.2 mm, 197.8 mm, and 206.4 mm from the cone tip, measured along the surface of the model. The case with nitrogen injection with $u_{\text{inj}} = 16$ m/s is shown as an example.

Profiles of tangential velocity, density, temperature, and mass fraction of the injected nitrogen are shown in Figure 4.28. Black, blue, and red curves represent the three injection rates studied from lowest to highest, respectively, listed in Table 4.1. The case with the highest injection rate produces a strong shock wave at the beginning of the injector, which is evident in the second profile, taken just past the beginning of the injector section. The effect of nitrogen injection is to displace the velocity, density, and temperature profiles in y over the injector, and they return to profiles typical of a boundary layer over the frustum as the streamwise momentum and

temperature diffuse through the injection layer. The distance that the profiles are displaced depends on the injection rate, but the injection rate apparently has little effect on the profile shapes otherwise.

The injected nitrogen diffuses into the free stream gas fairly quickly in the case with lowest injection rate, but the mass fraction at the wall remains nearly unity for the other cases and the injected nitrogen diffuses notably more slowly. The mass fraction of injected nitrogen at the wall is plotted as a function of distance from the end of the injector along the surface of the frustum section in Figure 4.29. The color scheme is the same as the one used in Figure 4.28. The concentration at the wall is higher for cases with higher injection rates, and hardly deviates from unity in the case with highest injection rate over the entire frustum. The mass fraction in the case with lowest injection rate appears that it may asymptote to a non-zero value, but this cannot be determined with certainty from these results.

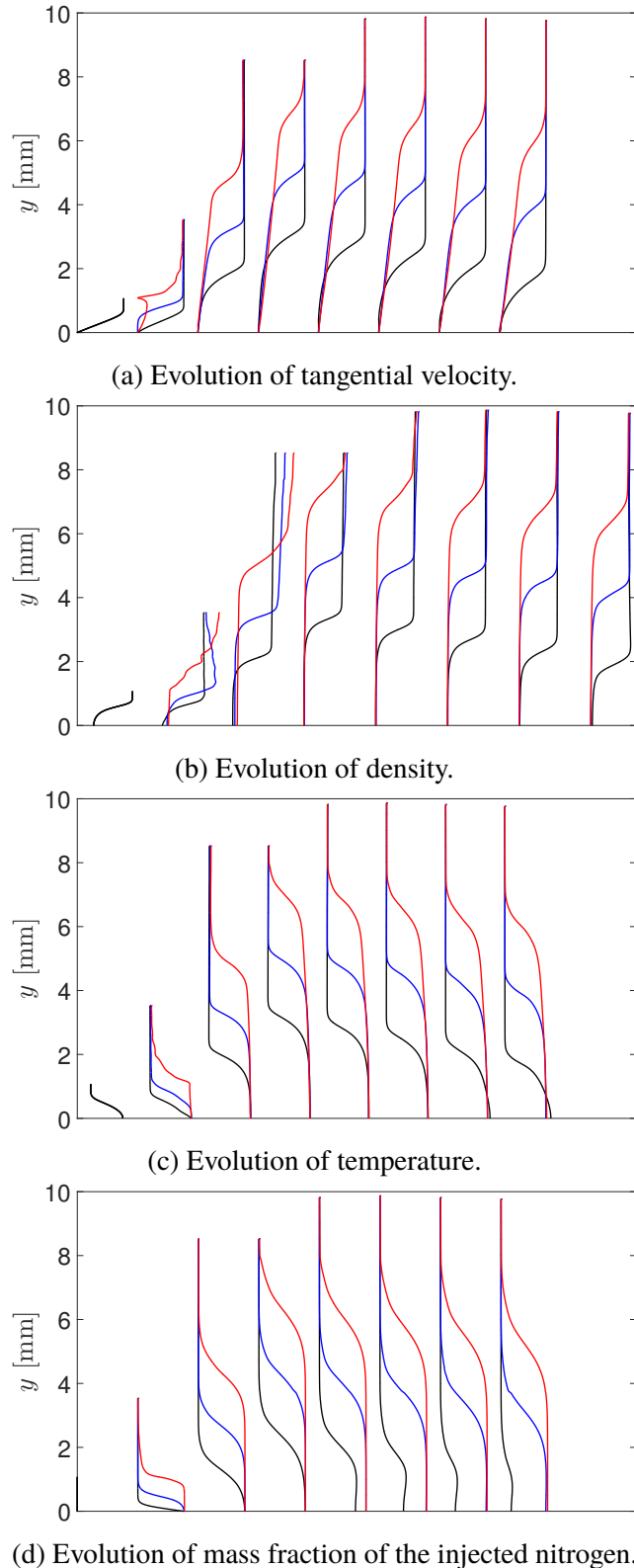


Figure 4.28: Evolution of flow variables for cases with nitrogen injection. Profiles are taken at the locations indicated in Figure 4.27. Black, blue, and red curves correspond to cases with low, medium, and high rates of injection listed in Table 4.1, respectively.

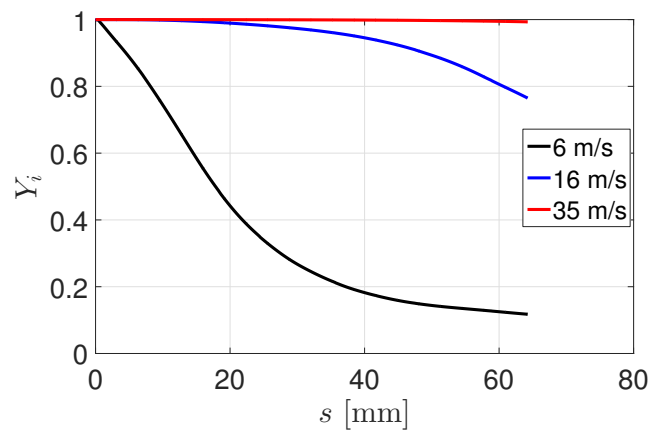


Figure 4.29: Mass fraction of injected nitrogen at the wall as a function of s , the variable measured along the cone surface. Here, $s = 0$ corresponds to the end of the injector section. Black, blue, and red curves correspond to increasing injection rate with injection velocities listed in the legend.

Helium results

Figure 4.30 shows the density field for the three cases with helium injection. Coloring is again normalized to each individual case. The results are qualitatively similar to the schlieren images from the experiments. For the time step shown in the figure, the case with $u_{\text{inj}} = 40 \text{ m/s}$ shows "rolling" structures seen in the schlieren image with helium injection in Figure 4.5 (top image). The waves in the OpenFOAM simulations will not be analyzed in detail but it is interesting that the computations exhibit qualitatively similar waves as those observed in the experiments.

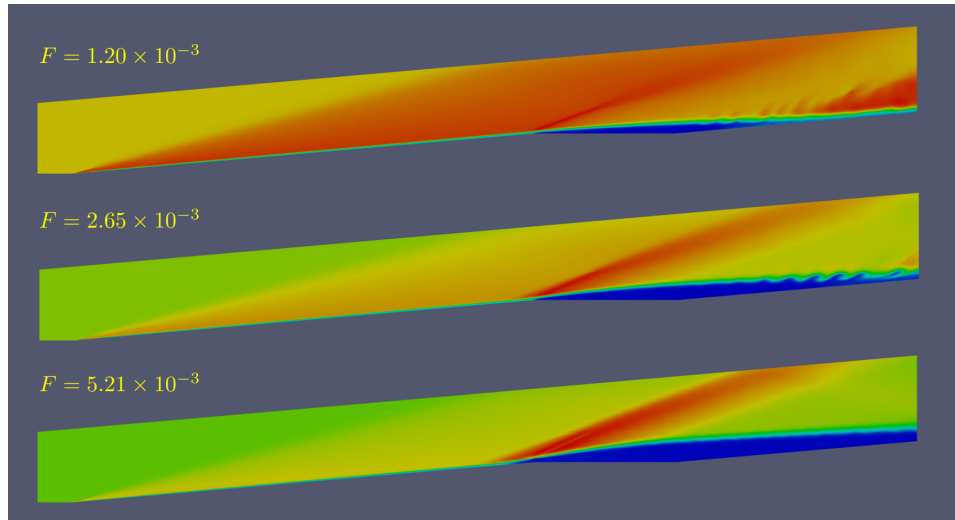


Figure 4.30: Results from the three computations with helium injection. Coloring corresponds to density, with the color scale normalized to each case. The value for the non-dimensional mass flux F is given in the upper-left for each case.

Profiles of tangential velocity, density, temperature, and mass fraction of helium are taken at the same locations shown in Figure 4.27. The profiles are shown in Figure 4.31. A strong shock is again formed at the beginning of the injector section for the cases with high injection rates. Some qualitative differences in the profiles between helium injection and nitrogen injection are apparent. Streamwise momentum diffuses much faster into the slow-moving helium than it does into nitrogen, due to helium's much lower inertia. The velocity profiles rapidly return to boundary layer-like profiles, and begin to do so even over the injector (profiles 3 and 4 in Figure 4.31a). The lower heat capacity of helium compared to nitrogen causes viscous heating to have a more pronounced effect where helium is present, and the temperature profiles develop local maxima. The temperature at the wall on the frustum also becomes dependent on the injection rate, because it depends strongly on the mass fraction of helium. The density profiles depend both on the temperature

and mass fraction of helium, and the net result is that the density profiles for helium injection look qualitatively similar to those for nitrogen injection.

The concentration of helium at the wall is plotted versus distance along the frustum section in Figure 4.32. The two cases with lower injection rates provide further evidence that the mass fraction of the injected gas at the wall may asymptote to a non-zero value, and the cases with helium injection reach a relatively constant value in a shorter distance than nitrogen injection cases for similar mass flow rates. Inspecting Figures 4.29 and 4.32 and Table 4.1 reveals that the helium concentration is higher at the wall than injected nitrogen for the same injection mass flow rate at a given s -location. This is likely a consequence of the free stream being displaced by a larger distance for injection of a lighter gas for a given injection rate. It should be kept in mind that the simulation is over-predicting the effect of diffusion for helium due to the unity Schmidt number assumption (see Appendix A), so these results should be tempered by a degree of skepticism.

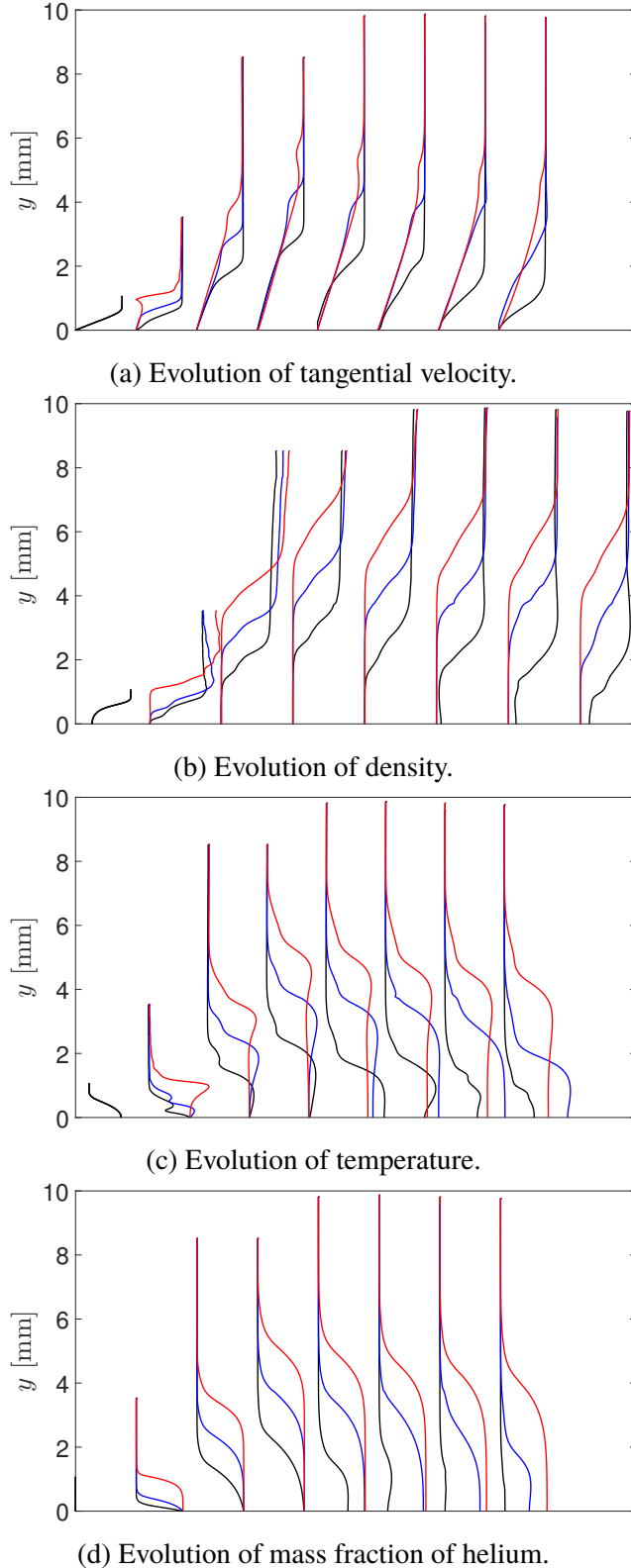


Figure 4.31: Evolution of flow variables for cases with helium injection. Profiles are taken at the locations indicated in Figure 4.27. Black, blue, and red curves correspond to cases with low, medium, and high rates of injection listed in Table 4.1, respectively.

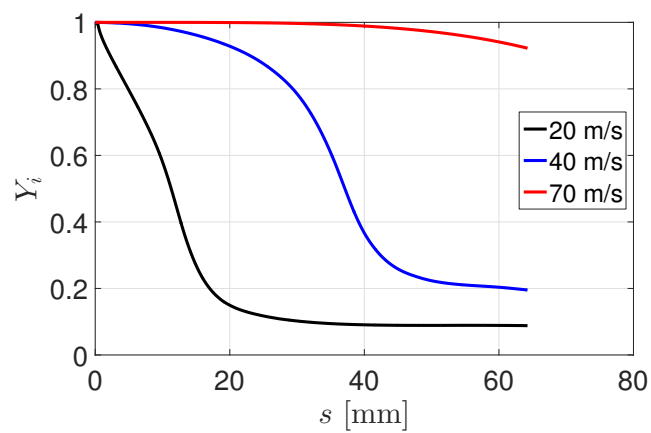


Figure 4.32: Mass fraction of helium at the wall as a function of s , the variable measured along the cone surface. Here, $s = 0$ corresponds to the end of the injector section. Black, blue, and red curves correspond to increasing injection rate with injection velocities listed in the legend.

RC318 results

Figure 4.33 shows the density field for the three cases with RC318 injection. Coloring is again normalized to each individual case, which makes the results look somewhat different from those presented in Figures 4.26 and 4.30. The injected RC318 has a very high density due to its high molecular weight, resulting in qualitatively different density fields compared to cases with nitrogen and helium injection, where the density of the injected gas is substantially lower than the free stream gas due to the higher temperature of the injected gas and lower molecular weight in the case of helium injection.

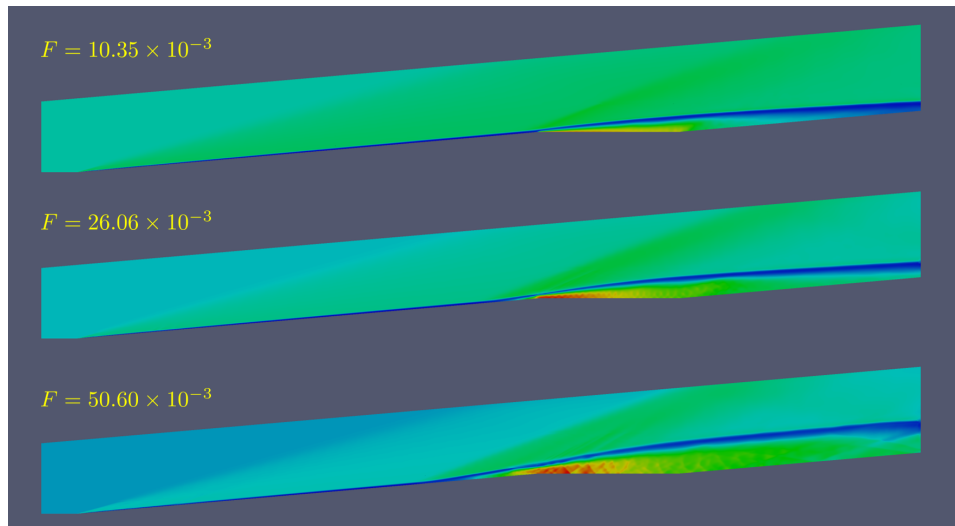


Figure 4.33: Results from the three computations with RC318 injection. Coloring corresponds to density, with the color scale normalized to each case. The value for the non-dimensional mass flux F is given in the upper-left for each case.

Profiles of flow variables are again taken at the same locations given in Figure 4.27 and are plotted in Figure 4.34. The velocity and temperature profiles are qualitatively similar to those for nitrogen injection, except that the streamwise momentum diffuses more slowly due to the higher inertia of the RC318. The velocity and temperature profiles are effectively displaced versions of the ones in the incoming boundary layer. The mass fraction profiles are also qualitatively similar to those for nitrogen injection.

The density profiles are quite different, however. The density is a function of both the local temperature and average molecular weight, so it depends on both the temperature and mass fraction distributions. Unlike in cases with nitrogen and helium injection where the density profile is monotonic because the low molecular weight of the injected gas and higher temperature both contribute to a lower density

near the wall, RC318's high molecular weight tends to increase the density which competes with the effect of temperature. The density profiles can then develop local maxima and minima between the wall and the free stream. This may have implications for the properties of the instability waves that form in the injection layer.

The mass fraction of RC318 at the wall is plotted in Figure 4.35. The concentration does not reach an approximately constant value by the end of the frustum in any of the cases with RC318 injection, which agrees with the trend observed by comparing Figures 4.29 and 4.32. The mass fraction of injected gas is again observed to decrease more rapidly for a heavier injected gas for similar injection mass flow rate by comparing Figures 4.29, 4.32, and 4.35 and Table 4.1. Recall again that the OpenFOAM solution is under-predicting the effect of diffusion for RC318 based on the findings presented in Appendix A.

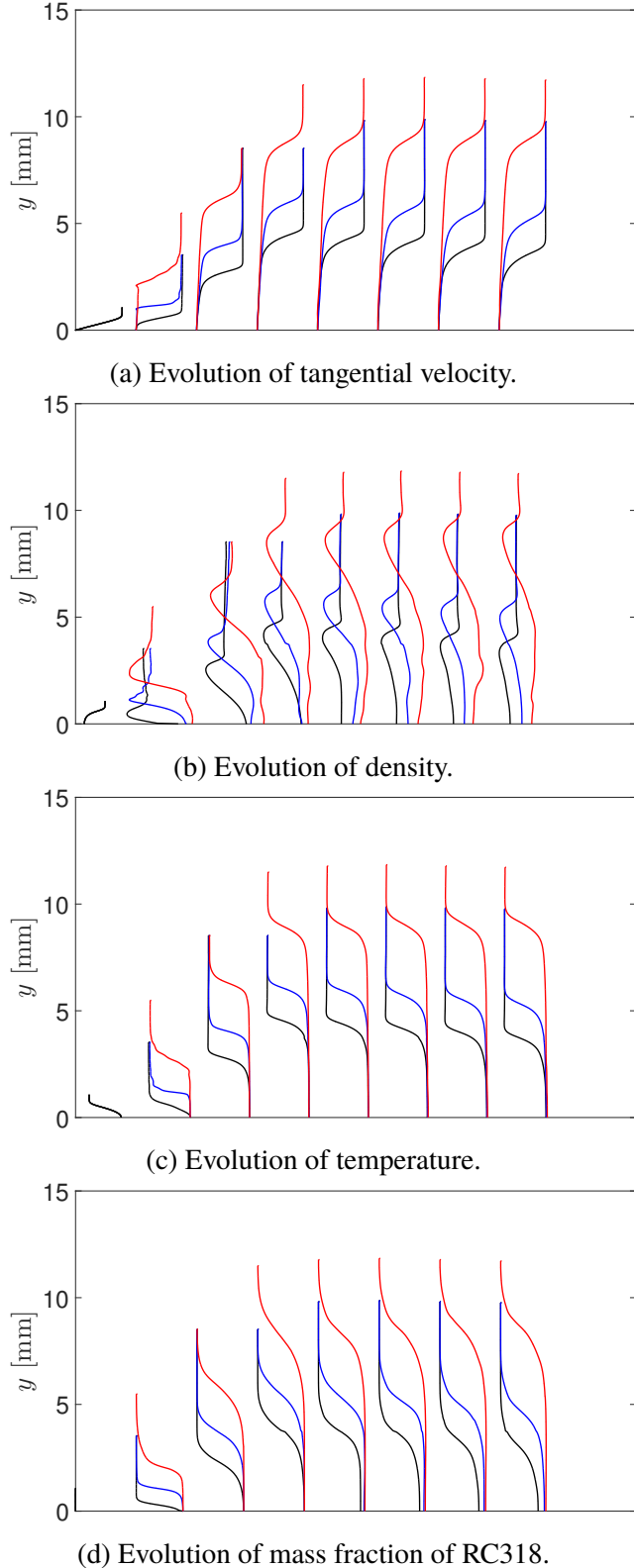


Figure 4.34: Evolution of flow variables for cases with RC318 injection. Profiles are taken at the locations indicated in Figure 4.27. Black, blue, and red curves correspond to cases with low, medium, and high rates of injection listed in Table 4.1, respectively.

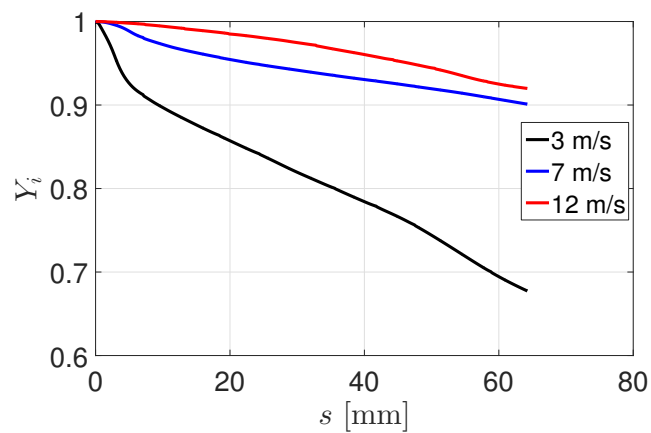


Figure 4.35: Mass fraction of RC318 at the wall as a function of s , the variable measured along the cone surface. Here, $s = 0$ corresponds to the end of the injector section. Black, blue, and red curves correspond to increasing injection rate with injection velocities listed in the legend.

Composite results

The computational results can be compared directly to experiments by measuring the displacement thickness of the injection layer in the computations at the rear of the injector. Displacement thickness in a compressible flow is defined as

$$\delta^* = \int_0^\infty \left(1 - \frac{\rho u}{\rho_\infty u_\infty}\right) dy . \quad (4.6)$$

This integral is computed numerically using trapezoidal integration for the profile taken at the rear of the injector section for each case and the result is plotted in Figure 4.36 along with the experimental measurements of δ presented in Figure 4.6.

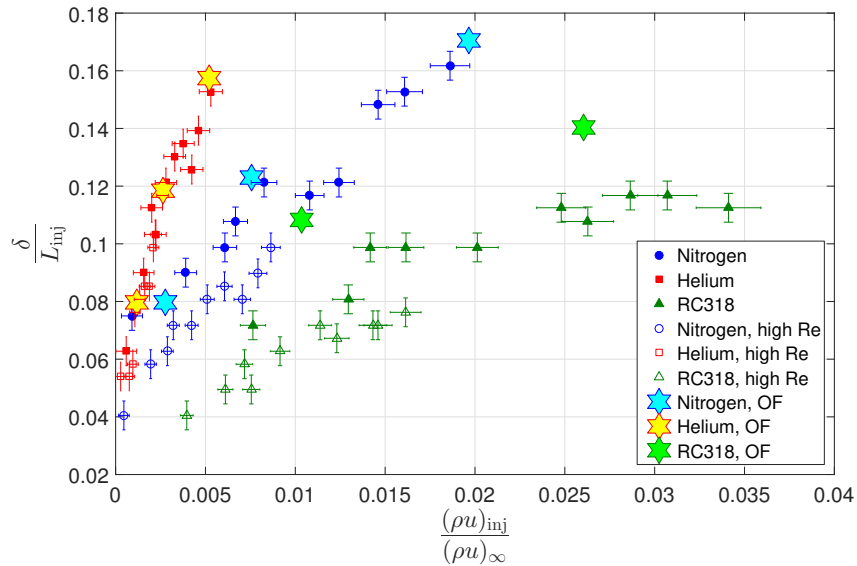


Figure 4.36: Experimental measurements of the injection layer thickness measured at the rear of the injector section compared with the displacement thickness at the same location from the OpenFOAM computations (indicated with "OF" in the legend).

Results from the nitrogen and helium injection cases agree remarkably well with the experimental results, but the displacement thickness in the RC318 cases is consistently higher than the measured value in the experiments. This disagreement is likely a result of the assumptions made by the solver in handling diffusion, which were identified as a possible issue for cases with RC318 injection in Section 2.5. OpenFOAM under-predicts diffusion of RC318, which would act to increase the displacement of the interface between gases from the wall in the computations. It is interesting that cases with helium injection do not also show significant disagreement between experiments and computations, this is likely just a fortunate coincidence for the specific flow studied. In all cases the disagreement is not too large, which

is a consequence of the errors being confined to the thin mixing region as stated in Section 2.5.

Another potential source of disagreement is that schlieren imaging is sensitive to gradients in the index of refraction of a gas, not the density. The two are related by the Gladstone-Dale relation (Equation 3.1):

$$n = K\rho + 1 \quad .$$

The Gladstone-Dale constant K is dependent on the wavelength of the light traversing the gas and also weakly dependent on temperature for a given gas, but can be quite different for different gases (Merzkirch, 1987). The Gladstone-Dale constant for a mixture of gases is dependent on the local composition,

$$K_{\text{mix}} = \sum K_i Y_i \quad . \quad (4.7)$$

Hence the index of refraction of a gas is sensitive not only to the local density but also to the local composition through K .

The index of refraction can be estimated along the profile at the rear of the injector from the OpenFOAM computations for each case to investigate whether there is an appreciable difference between the density and index of refraction profiles. A displacement thickness (Equation 4.6) can be calculated using $n - 1$ instead of the density to estimate the magnitude of the effect. Values for the Gladstone-Dale constant for several common gases are tabulated in Merzkirch (1987) at wavelengths of 589 and 633 nm and temperatures of 273 and 295 K. These values are used to estimate the Gladstone-Dale constants for nitrogen and helium assuming a similar relationship to wavelength and temperature for both gases. The Gladstone-Dale constant is not tabulated for RC318, but it can be estimated roughly from the Gladstone-Dale constant for other species with similar characteristics, such as carbon tetrafluoride, sulfur hexafluoride, and Xenon. Gladstone-Dale constants, the displacement thickness, and the thickness computed using the index of refraction (δ_{n-1}) are given in Table 4.2. Profiles are taken at the rear of the injector for cases with $u_{\text{inj}} = 16, 40$, and 3 m/s for nitrogen, helium, and RC318 injection, respectively.

The effect of varying Gladstone-Dale constant throughout the profile has little effect in cases with helium injection because the Gladstone-Dale constants for helium and nitrogen are similar. There is a small but appreciable effect with RC318 injection, but it acts to make the displacement thickness larger in visualization experiments,

Injected Gas	$K \times 10^3$ [m ³ /kg]	δ^* [mm]	δ_{n-1} [mm]
Nitrogen	0.238	4.92	4.92
Helium	0.196	4.73	4.75
RC318	0.11	4.34	4.49

Table 4.2: Estimated Gladstone-Dale constants for the three gases at a wavelength of approximately 600 nm and room temperature with the computed displacement thicknesses and thicknesses based on index of refraction calculated at the rear of the injector section for cases with $u_{\text{inj}} = 16, 40, and 3 m/s for nitrogen, helium, and RC318 injection, respectively.$

not smaller. Therefore the effect of composition on the Gladstone-Dale constant can be ruled out as a source of disagreement between the experiments and computations.

Three cases with different injected gases have similar values of δ^* , which allows profiles for these cases to be compared directly. Figure 4.37 shows profiles of the flow variables taken at the rear of the injector section for the three gases where $u_{\text{inj}} = 16, 40, and 3 m/s for nitrogen, helium and RC318 injection, respectively. The differences observed by comparing Figures 4.28, 4.31, and 4.34 are made much more apparent. Streamwise momentum diffuses downward much more rapidly in gases with lower density, where the kinematic viscosity $\nu = \frac{\mu}{\rho}$ is higher. Figure 4.37b clearly illustrates the drastic difference in the density profile of cases with RC318 injection compared to the lighter gases. The region where the density gradient is positive is approximately of the same length, but the density increases to a high value at the wall in the case of RC318 injection due to the increasing mass fraction of injected gas. Figure 4.37c shows the local maximum in the temperature profile in the case with helium injection, which is produced by the competition between heat capacity and mass fraction of injected gas, which does not occur in cases with nitrogen or RC318.$

It is also worth while to consider profiles taken some distance downstream from the injector for the three cases presented in Figure 4.37 so that the evolution of the profiles can be compared directly. Profiles taken at the furthest sampling location 206.4 mm from the cone tip are presented in Figure 4.38. The velocity profile at this location for the case with RC318 injection appears qualitatively similar to the one at the rear of the injector, and there remains an appreciably thick region of slow-moving fluid in the near-wall region. Streamwise momentum has diffused rapidly into the gas near the wall in the case with helium injection and the profile is significantly different from the other two. The density profile in the case with RC318 injection

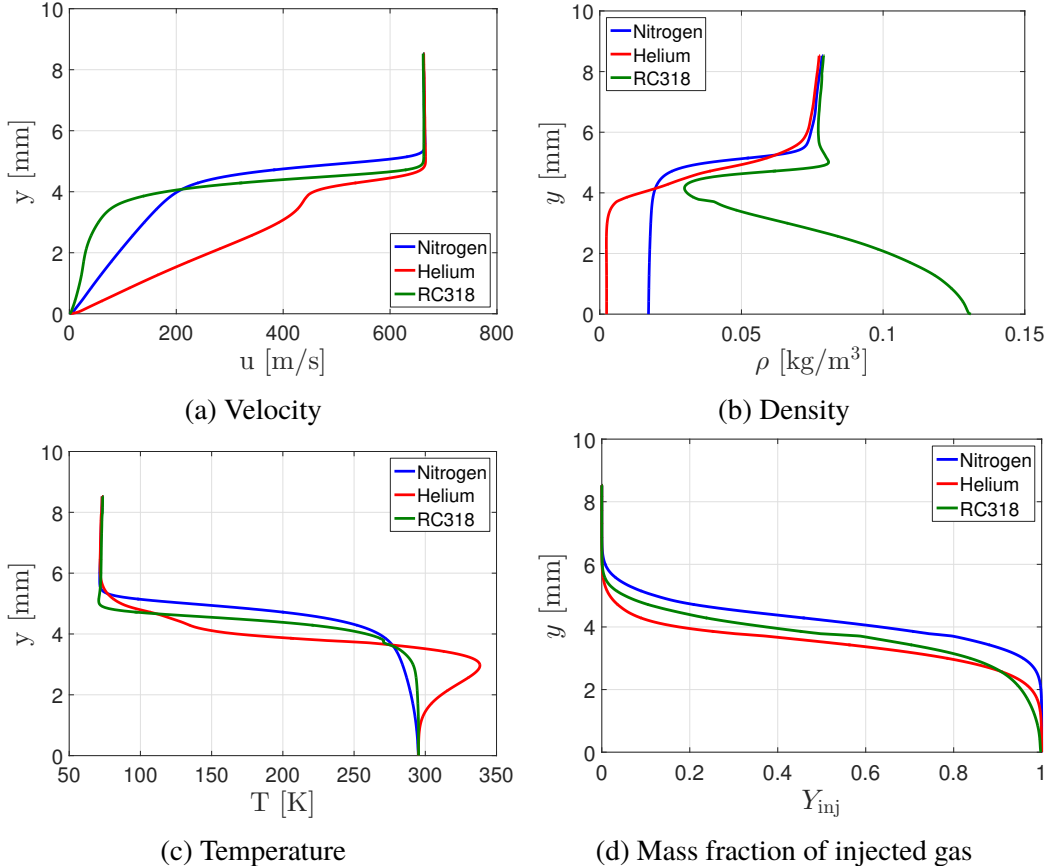


Figure 4.37: Profiles taken at the rear of the injector section for cases with all three injected gases. Cases are selected such that the value of δ^* is similar for all three.

still has a local minimum away from the wall, but the value of density at the wall has decreased below the free stream value due to diffusion of nitrogen to the wall. Figure 4.38c illustrates the higher wall temperature of helium due to its lower heat capacity.

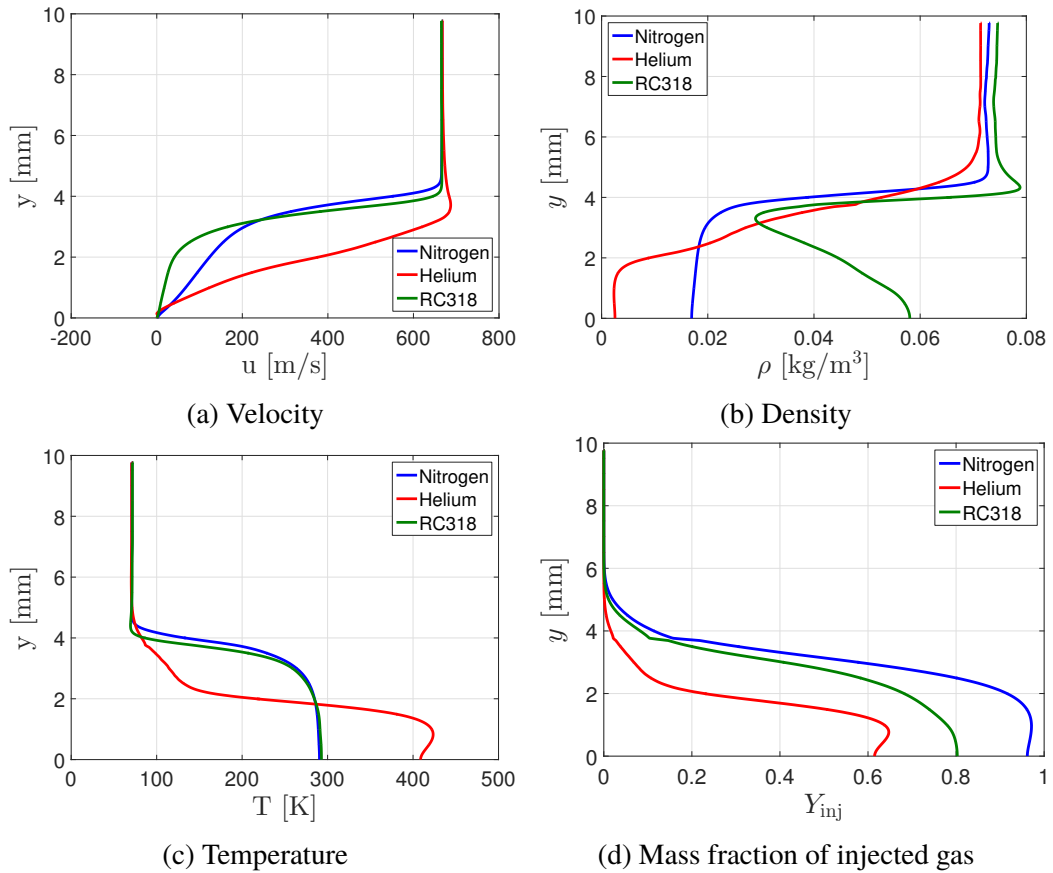


Figure 4.38: Profiles taken 206.4 mm from the cone tip for cases with all three injected gases. Cases are selected such that the value of δ^* is similar for all three.

Chapter 5

ANALYSIS

The results presented in Chapter 4 are analyzed in this chapter. The data from the full-field images in Section 4.1 are collapsed and the non-dimensional momentum flux J is shown to be a more appropriate parameter than the non-dimensional mass flux F for presenting and analyzing the data. Data from the high-speed imaging processing described in Section 4.2 is analyzed in conjunction with the results from the OpenFOAM computations to draw conclusions about the nature of the dominant instability in the flow. The properties of the instability are compared with those for the boundary layer on a cone without injection in the Caltech Ludwieg Tube measured using the same technique and with results for compressible mixing layers.

5.1 Full Field Data

It was found in Section 4.1 that the "tuned" condition does not depend on the injection mass flux F but rather on the injection layer thickness δ . Figures 4.6 and 4.36 show that δ does not only depend on F when different injected gases are considered. A new parameter to describe the injection rate that will collapse the data for δ is therefore desired.

One approach is to consider the injection process as a low-momentum jet in a supersonic crossflow. The trajectory of such a jet, which is related to the penetration height, is most strongly a function of the momentum flux ratio J :

$$J = \frac{\rho_j u_j^2}{\rho_\infty u_\infty^2} . \quad (5.1)$$

It can also depend upon the pressure, density, and temperature ratios of the jet to the free stream as well as the molecular weights and Mach numbers of the jet and free stream (Mahesh, 2013). Most empirical correlations take the form

$$\frac{y}{d} = \text{fn}\left(J, \frac{x}{d}\right) . \quad (5.2)$$

y is the height of the jet above the orifice, x is the coordinate along the direction of the free stream velocity, and d is a characteristic size of the jet, typically the jet diameter in the case of a circular orifice. The functional dependence on J and x/d is often cast as a power law, with different exponents on J and x/d .

At a fixed location x , then, the penetration height y can be considered to be a function of J only with a power law dependence. In the present work, y/d at the rear of the injector is equivalent to δ/L_{inj} where L_{inj} is the length of the injector section. The momentum flux of the injected gas is computed by assuming that the average pressure over the injector is the same for all experiments, which allows the density to be extracted from the measured mass flux. The pressure is determined by averaging the pressure at the injector exit in the OpenFOAM computations. This introduces additional uncertainty in J that is not present in F , which is accounted for in the error bars on subsequent plots.

Figure 5.1 shows both experimental and computational measurements of δ normalized by L_{inj} plotted against J . The black line represents a power law fit, where only the nitrogen and helium injection data have been included in the fit because of the discrepancy between experimental and computational measurements of δ for the RC318 data found in Section 4.3. The calculated fit is

$$\frac{\delta}{L_{\text{inj}}} = 1.256J^{0.333} + 0.0358 \quad . \quad (5.3)$$

Mahesh (2013) reports values between 0.276 and 0.5 for the exponent on J in his review article.

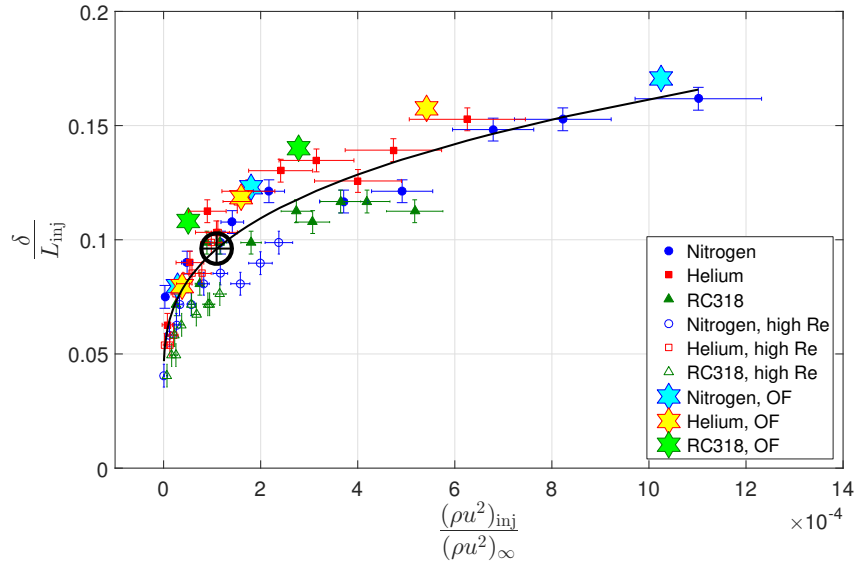


Figure 5.1: δ , measured at the rear of the injector section, normalized by the length of the injector L_{inj} plotted against the dimensionless momentum flux ratio J for all experimental and computational data. The black line is a fitted power law curve considering only data from nitrogen and helium injection cases. The expression for the curve is given in Equation 5.3. The \oplus symbol indicates the tuned condition.

The data is collapsed reasonably well by considering a dependence on J , and it approximately follows a power law. Computational data for RC318 injection cases are outliers, which may indicate that the disagreement between measurements of δ in experiments and computations is due at least in part to the invalidity of some assumptions made by the solver instead of exclusively because of the sensitivity of schlieren visualization to gradients in refractive index and not density alone, as explored in Section 4.3. In addition to collapsing the data for δ , using J as an abscissa produces more similar ranges for injection rate across the different injected gases and allows for more convenient comparison of results. For this reason wave properties will be plotted against J instead of F in Section 5.2. It should also be noted that because "tuning" of the injection rate to minimize shock formation appears to depend on δ , J also predicts tuning for a given injection geometry.

Collapsing the data for transition location by plotting against a single variable is far more difficult, as even boundary layer transition without injection depends on a wide range of parameters. For supersonic flow over a cone for instance, Stetson (1987) identifies Mach number, nosetip bluntness, angle of attack, unit Reynolds number, environmental effects such as wind tunnel noise, wall temperature, surface roughness, pressure gradient, mass transfer, real gas and non-equilibrium effects, body curvature, and vibration as major factors that influence the transition Reynolds number, and even this list is not exhaustive for all situations. In the present work, many of these variables are identical for all cases studied. A proposed functional form for the transition location x_{tr} presented in Figure 4.7 normalized by the injection layer thickness δ is

$$\frac{x_{\text{tr}}}{\delta} = \text{fn} \left(Re_L, \frac{u_{\text{inj}}}{u_{\infty}}, \frac{\rho_{\text{inj}}}{\rho_{\infty}}, \frac{T_{\text{inj}}}{T_{\infty}}, \frac{W_{\text{inj}}}{W_{\infty}}, \frac{\gamma_{\text{inj}}}{\gamma_{\infty}} \right) \quad (5.4)$$

and may include other variables as well.

A trial-and-error procedure reveals that for the experiments conducted for this work the transition location normalized by δ is primarily dependent on the ratio of the velocity of the injected gas to the free stream velocity. Figure 5.2 shows the collapse of the transition data when plotted in this manner. It is not known why this parameter achieves a suitable collapse of the data, and it may not apply to transition data for other studies with injection. Clearly more work is required in other facilities and with other model geometries to make a more definitive determination.

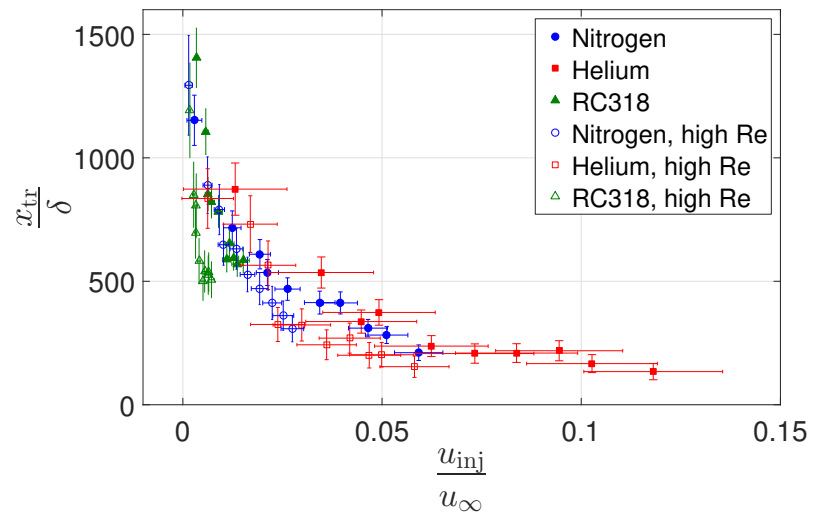


Figure 5.2: Transition location x_{tr} , measured from the front of the injector section, normalized by the injection layer thickness δ measured at the rear of the injector plotted against the velocity ratio of the injected gas to the free stream gas.

5.2 Instability Wave Analysis

Analysis of the data presented in Section 4.2 is begun by re-plotting the results using J as the abscissa instead of F . Figures 5.3, 5.4, and 5.5 show the dimensionless wavelength, convective velocity, and frequency, respectively, of the instability waves plotted against J . Recall from Section 4.2 that wavelength and convective velocity data in these plots represent populations. Vertical error bars for these points are the standard deviation of the population for each data point. An alternative measure of the uncertainty for each data point is the standard deviation of the mean, defined for large data sets as $\frac{\sigma}{\sqrt{N}}$ where σ is the standard deviation of the population and N is the number of samples. The standard deviation of the mean can also be estimated using a bootstrap method (W. Menke and J. Menke, 2012). The standard deviation of the mean is found to be one percent or less of the value of the mean, so the size of the error bars in the figures over-represents the actual uncertainty in the measurements.

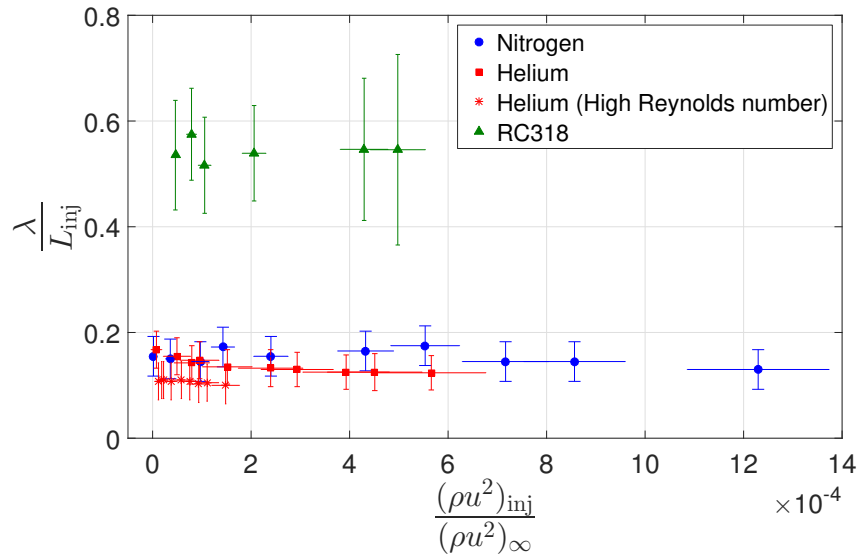


Figure 5.3: Wavelength normalized by the injector length plotted against the non-dimensional injection momentum flux J for all cases analyzed. The wavelength is measured directly for helium and nitrogen injection and calculated assuming Taylor's hypothesis for RC318 injection. Vertical error bars reflect only uncertainty due to measurement error.

Trends in the data can now be much more clearly discerned than in Section 4.2. Wavelength remains essentially constant across all injection rates studied for a given injected gas. Convective velocity increases for increasing injection rate with helium injection, increases more slowly with increasing injection rate with nitrogen injection, and decreases with increasing injection rate for RC318 injection. Trends

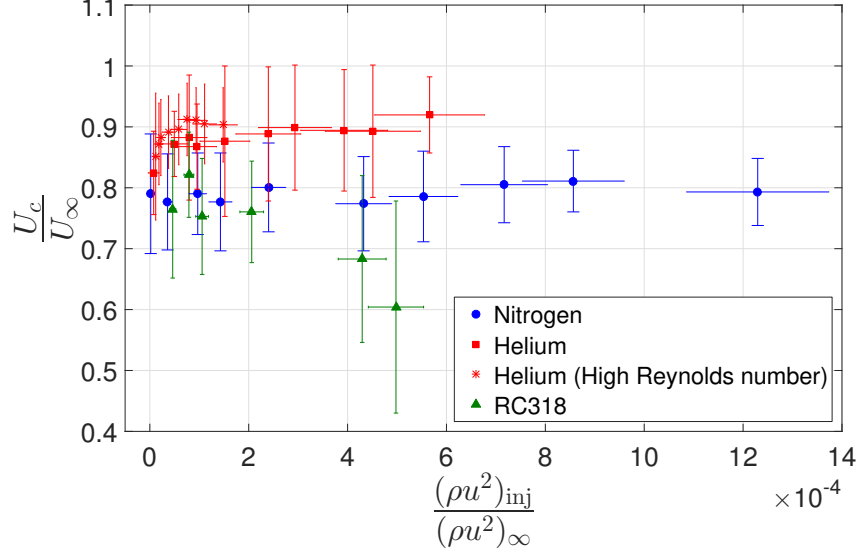


Figure 5.4: Convective velocity normalized by the free stream velocity plotted versus the non-dimensional momentum flux J for all cases studied. Vertical error bars represent uncertainty due to measurement error, including pixel-locking.

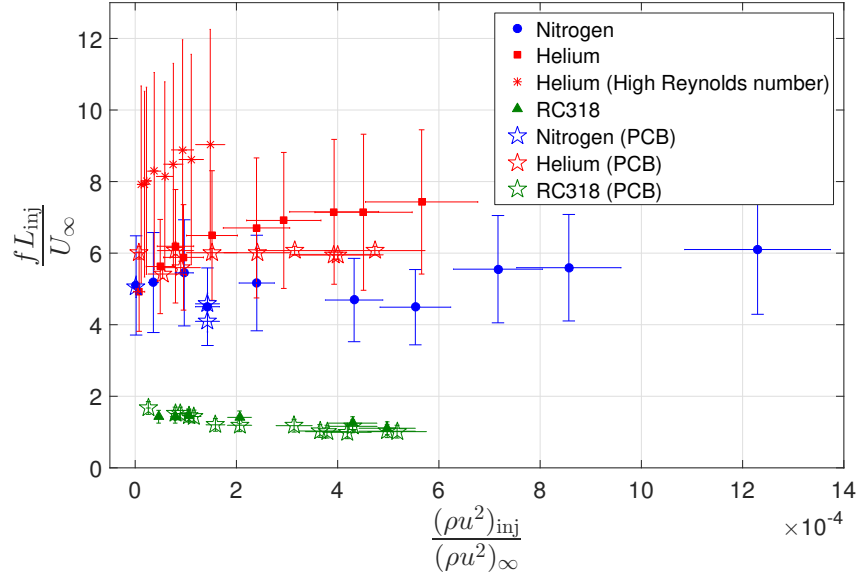


Figure 5.5: Frequency from image analysis and pressure transducers. The frequency from image analysis for the helium and nitrogen injection cases is computed using Taylor's hypothesis while the frequency in the RC318 cases is computed directly from the image processing routine.

in frequency are similar to those for convective velocity as a consequence of Taylor's hypothesis (Equation 4.4).

Fedorov, Soudakov, et al. (2014) and Schmidt et al. (2015) performed theoretical studies on the stability of flow with injection on the geometry used in the current

work using linear stability analysis. Both studies were performed with air injection into an air free stream, and so do not include effects of varying the injected gas. Both studies found that injection destabilizes several acoustic modes, but the mode with the highest growth rate is two-dimensional. The most amplified frequency, non-dimensionalized using the length of the injector and free stream velocity as in Figure 5.5, is found by Schmidt et al. (2015) to be approximately 5.2, which agrees with the frequency found for nitrogen injection in this work. Neither of these theoretical studies investigate the waves in the nonlinear regime, but the waves observed in this work by schlieren visualization are likely nonlinear.

The remainder of this chapter is devoted to characterizing the dominant instability in the test flow so that a framework can be developed for future studies. Supersonic flow with injection appears qualitatively similar to supersonic boundary layer flow and also compressible free shear layers, both of which have instabilities that have been extensively researched. The behavior of flow with injection is compared to each of these flows to determine which properties, if any, are shared.

High-speed boundary layers

As mentioned in Section 1.1, current understanding of the stability of high speed boundary layers is summarized by Fedorov (2011) and Fedorov and Tumin (2011). When the free stream Mach number is sufficiently high, transition is dominated by the two-dimensional Mack mode ("second mode") caused by trapped acoustic waves inside the boundary layer for sharp cone geometries. Otherwise transition is due to the growth of oblique Tollmien-Schlichting waves, often referred to as the "first mode" in the literature. Figure 10.10 of Mack (1984) shows the relative strengths of the first and second modes as a function of Mach number for a flat plate. This chart predicts that both modes may be active in the flow in the Caltech Ludwig Tube where $M_\infty = 4$. Linear stability calculations performed by Schmidt et al. (2015) confirm that both modes are unstable but that the first mode is dominant. Questions remain whether highly oblique waves can exist on a cone where the spanwise wavenumber is small compared to the local cone radius, but Tollmien-Schlichting waves do not necessarily have a small spanwise wavenumber and can be nearly two-dimensional.

Several experiments were performed in the Ludwig tube to analyze the dominant instability mode in the boundary layer on a straight cone with no injection. The model is the same as the one described in Section 2.3 but with no injector section. The cone tip is mated directly to a frustum section that has a female connection at

its front instead of a male connection like the one shown in Figure 2.9. The female frustum section is instrumented with five PCB pressure transducers, identical to the male frustum.

The same measurement and processing techniques were applied to these experiments as those described in Sections 3.4 and 4.2. The only difference is that the camera resolution is changed from 224 by 64 pixels to 384 by 40 pixels since the thickness of the boundary layer is much less than that of flow with injection. The change in resolution allows the framing rate to be increased from 289,361 frames per second to 345,177 frames per second.

Figure 5.6 shows a sample image from an experiment with a free stream unit Reynolds number of 9×10^6 per meter. Crests of consecutive waves are indicated in the figure. The local visual boundary layer thickness is determined from the images to be 0.9 mm. The wavelength of the instability waves is determined to be 11.7 ± 3 mm or $13\delta_{vis}$ and their convective speed is 557 ± 60 m/s or $0.83u_\infty$. Using Taylor's hypothesis, the frequency is 46.4 kHz. These values are typical of first-mode waves, as second-mode waves have a much shorter wavelength and higher frequency. The waves are potentially weakly oblique, evidenced by the fact that they are seldom observed in long trains of more than three or four consecutive waves. Second-mode waves have been visualized in trains of ten or more waves because of their two dimensional nature (Laurence, Wagner, Hanneman, et al., 2012).

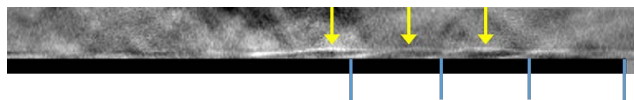


Figure 5.6: Sample image of instability waves in a cone boundary layer at a unit Reynolds number of 9×10^6 per meter. Yellow arrows indicate the crests of three consecutive waves, and blue vertical lines indicate the locations of the first four pressure transducers. The fifth transducer is outside the viewing window of the camera to the right of the image in the figure.

The pressure transducers on the cone frustum produce a strong signal at the frequency of the waves. The spectral density of the output of the five transducers is shown in Figure 5.7. The spectra are typical of an instability that grows as it progresses downstream before breaking down to turbulence. The insert in the figure shows the spectrum from the first transducer which exhibits a strong peak at 45.9 kHz, indicating excellent agreement between the optical measurement technique and surface measurements.

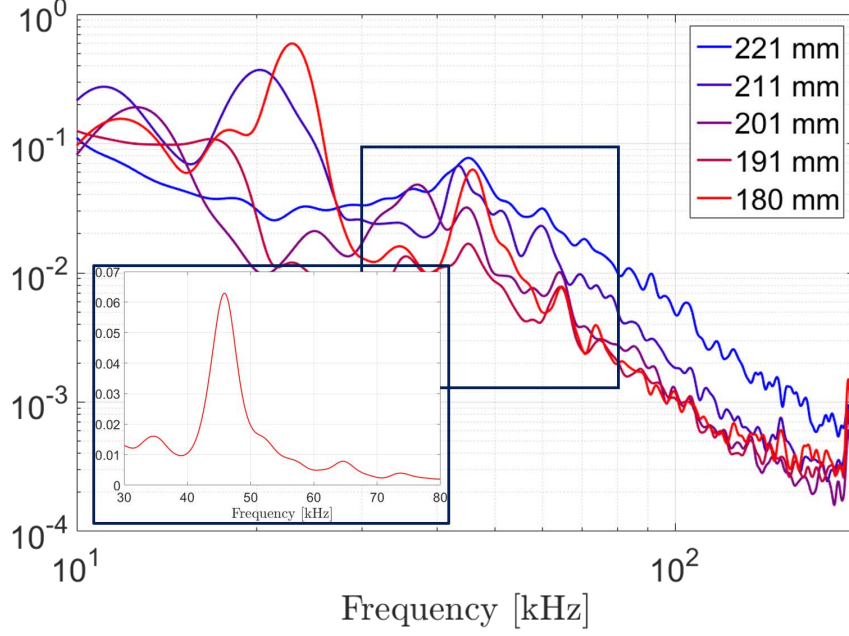


Figure 5.7: Spectra from the pressure transducers on a straight cone under the same conditions as the visualization in Figure 5.6. The spectra show growth of an instability around 46 kHz that breaks down to a turbulence at or before the location of the final transducer. The insert shows the spectrum of the first transducer so that the peak at 45.9 kHz can be clearly perceived.

The dominant instability in flow with injection is apparently different than the one present in the boundary layer on a straight cone with no injection. Characteristics of the instability waves in flow with injection depend on the injected gas, but comparing cases with nitrogen injection to the analysis of waves in the boundary layer eliminates this issue. The frequency of the waves in flow with nitrogen injection is substantially higher than the frequency observed in waves in the boundary layer, even though the injection layer is several times thicker than the boundary layer. This is the opposite behavior from what is observed in boundary layers, where the frequency scales inversely with boundary layer thickness (Mack, 1984). For second-mode waves,

$$f = A \frac{U_E}{2\delta} . \quad (5.5)$$

Here A is a constant of proportionality and the subscript E indicates boundary layer edge conditions. The frequency of first-mode waves also scales with $\frac{U_E}{\delta}$ although the constant of proportionality is quite different than the one in Equation 5.5. The wavelength of the first-mode waves in the boundary layer is also much longer, both in dimensional terms and in terms of the local layer thickness, than waves observed in flow with injection. Longer trains of waves are observed in flow with nitrogen

and helium injection, indicating that the disturbance is potentially two-dimensional. It can therefore be concluded that the instability in the injection layer is not the same as the first-mode instability present in the cone boundary layer with no injection.

It can also be concluded that injection does not activate a second-mode instability, or at least that the instability does not behave like the second mode for boundary layers. It can be observed from Figure 5.1 that the injection layer thickness varies by a factor of more than two in the experiments performed, yet Figure 5.3 indicates only a very weak dependence of wavelength on injection layer thickness, if there is any dependence at all. This is not at all like the behavior of the second mode in boundary layers given in Equation 5.5. Furthermore, Fedorov (2011) explains that second-mode disturbances grow because of acoustic waves trapped inside the boundary layer which turn around at the so-called sonic line where the phase speed of the waves is equal to the sum of the local velocity and sound speed,

$$U_c = u(y) + a(y) \quad . \quad (5.6)$$

It can be shown using the experimentally determined convective speed of the waves and the velocity and sound speed profiles from the OpenFOAM computations that there is no location where Equation 5.6 is satisfied for cases with helium injection, so this cannot be the mechanism for the instability in general.

Shear layers

Two-dimensional free shear layers are a canonical flow in fluid mechanics. Figure 5.8 illustrates the situation. Conditions as $y \rightarrow \pm\infty$ are well-defined as the conditions of streams 1 and 2, respectively. This flow is unstable due to the well-known Kelvin-Helmholtz instability of the interface between parallel streams at different velocities. In the remainder of this work stream 1 will be defined to be the high-speed stream.

A great deal of theoretical, computational, and experimental work has been devoted to the study of the instability in free shear layers, particularly when the flow can be approximated as incompressible as in liquid flows. Other approximations, such as assuming that $\rho_1 = \rho_2$ and/or $\gamma_1 = \gamma_2$ for shear layers in gases are also often employed. Studies where all three quantities, velocity, density, and the ratio of specific heats are allowed to be different for the two streams are less common. Papamoschou (1987) performed an extensive study of high-speed, variable density, heterogeneous ($\gamma_1 \neq \gamma_2$) shear layers for his Ph.D. thesis, and some of the results are also reported in peer-reviewed articles. The description that follows of the properties of the instability waves in these shear layers is reported mainly from his work.

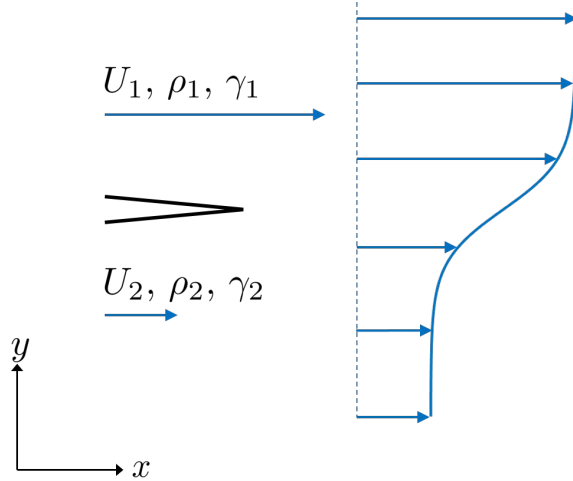


Figure 5.8: Sketch of a two-dimensional free shear layer flow. Two streams with different velocities and potentially different densities and specific heats are initially separated by a splitter plate and allowed to mix downstream of the plate. A mean velocity profile is sketched in the mixing region. Stream 1 is the high-speed stream and stream 2 is the low-speed stream by definition.

First, it should be noted that the instability of developing shear layers and the structures in turbulent shear layers are distinct from one another. However researchers have noted that the persistent large-scale structures in turbulent shear layers share many properties with the initial instability waves (Papamoschou and Roshko, 1988b). Therefore for characteristics such as wavelength and convective speed that are of interest in the current work, it is not unreasonable to compare with both the developing instability waves in laminar shear layers and the larger structures in developed shear layers.

The most common length scale used to non-dimensionalize features in both compressible and incompressible shear layers is the vorticity thickness δ_ω :

$$\delta_\omega = \frac{\Delta U}{\left(\frac{du}{dy}\right)_{\max}} . \quad (5.7)$$

ΔU is the velocity difference between streams 1 and 2, so the vorticity thickness is equivalently the maximum-slope thickness of the mean velocity profile. Dimotakis and Brown (1976) report values for the wavelength normalized by the vorticity thickness of $3.1 < \frac{\lambda}{\delta_\omega} < 5.0$ for incompressible shear layers in water. Brown and Roshko (1974) performed experiments on shear layers with both subsonic and supersonic streams with $\rho_1 \neq \rho_2$ and found that $\frac{\lambda}{\delta_\omega} = 2.9$. Papamoschou (1987) found that $\frac{\lambda}{\delta_\omega} = 3.2$ for similar experiments where the convective Mach number of the high-speed stream M_{c1} is less than unity. The concept of a convective Mach

number is discussed later in this section. It is noteworthy that the wavelength observed in free shear layers is approximately three vorticity thicknesses across a very wide range of conditions.

There is not a simple expression for the phase speed of unstable waves in a developing shear layer. Papamoschou (1987) performs a temporal linear stability analysis on small-amplitude disturbances of a compressible heterogeneous infinitesimal vortex sheet in Section 4.1 of that work. The disturbance to the velocity potential in stream j , ϕ_j , is assumed to take the form

$$\phi_j = \psi_j(y)e^{i\alpha(x-ct)} , \quad (5.8)$$

where ψ is the disturbance amplitude, α is the wavenumber (assumed to be real), and $c = c_r + i c_i$ is the complex phase speed of the disturbance. The governing equation from small-perturbation theory is

$$\frac{1}{a_j^2} \frac{D^2 \phi_j}{Dt^2} = \nabla^2 \phi_j . \quad (5.9)$$

Here a_j is the sound speed in stream j . The form of the general solution to this equation suggests the introduction of a convective Mach number M_{c_j} for each stream. The convective Mach number is the Mach number of each stream in the frame of reference moving with the disturbance:

$$M_{c_j} = \frac{U_j - c_r}{a_j} . \quad (5.10)$$

Implementing the boundary conditions that the disturbances must be finite at infinity, the velocities on either side of the vortex sheet must be equal to the motion of the sheet, and that the pressure is matched on either side of the sheet results in an eigenvalue problem for the phase speed c , with the solution being

$$\mu_1^4 (1 - \mu_2^2) = \left(\frac{\gamma_2}{\gamma_1} \right)^2 \mu_2^4 (1 - \mu_1^2) . \quad (5.11)$$

Here μ_j is the complex convective Mach number in stream j :

$$\mu_j = \frac{U_j - c_r}{a_j} - i \frac{c_i}{a_j} . \quad (5.12)$$

Equation 5.11 can be solved numerically for c given the conditions in the two streams. The stability of the vortex sheet can be determined by the sign of c_i , which

can be expressed as a function of M_{c_1} for a given ratio of sound speed (or density) and ratios of specific heats. Papamoschou and Roshko (1988a) found that the vortex sheet becomes stable for sufficiently high M_{c_1} , but the limiting value depends upon the other parameters. The limiting value is always found to be greater than unity.

A vortex sheet is obviously a simplification of a finite-thickness shear layer. As pointed out by Papamoschou (1987), in a shear layer there is no clear interface between the two streams, and all variables become a function of y , including the convective Mach number,

$$M_c(y) = \frac{u(y) - U_c}{a(y)} . \quad (5.13)$$

This means that there is always a subsonic sublayer where $M_c < 1$, so shear layers are always unstable even though compressibility does have a stabilizing effect (Papamoschou and Roshko, 1988b). As previously mentioned, there is not a simple method for finding the phase speed of disturbances in a compressible, heterogeneous shear layer of finite thickness. There is, however, a method to find the convective velocity of structures in a developed shear layer. This velocity is not expected to be substantially different from the phase speed of instability waves both because of the fact that structures in a developed shear layer inherit their properties from the initial instability (Papamoschou, 1987) and also because of the argument used to develop the expression for the structures' convective velocity.

The equation for convective velocity of large structures is commonly used in the literature. The essence of its derivation is given in Section 6 of Papamoschou and Roshko (1988b). The structures are observed in a reference frame convecting at U_c , the convective velocity of the structures. The formulation of a convective Mach number is the same in this case as in Equation 5.10 except U_c is substituted for c_r . Sketches of the streamlines in the convective frame are shown in Figure 5.9. There are stagnation points between the structures in this frame, which indicates that the total pressures of the streams must match. The nature and shape of the structures is not important to the argument, so long as structures exist between low- and high-speed streams. Assuming isentropic compression, the resulting relation is

$$\left(1 + \frac{\gamma_1 - 1}{2} M_{c_1}^2\right)^{\frac{\gamma_1}{\gamma_1 - 1}} = \left(1 + \frac{\gamma_2 - 1}{2} M_{c_2}^2\right)^{\frac{\gamma_2}{\gamma_2 - 1}} . \quad (5.14)$$

Given the conditions in the two streams, one can solve for U_c by finding the root of Equation 5.14 numerically. Papamoschou (1989) shows that although the two convective Mach numbers for the two streams may not be equal if $\gamma_1 \neq \gamma_2$ or

if a convective Mach number is sufficiently high to produce a shock wave along the stagnation line of one or both streams, the higher of the two convective Mach numbers is the important one in determining the effect of compressibility on the shear layer. This point will be discussed further later on in this section. It can be shown that Equations 5.11 and 5.14 give approximately the same result within a few percent for the velocity of the waves given the same free stream properties, so Equation 5.14 will be used to evaluate convective velocity going forward for simplicity.

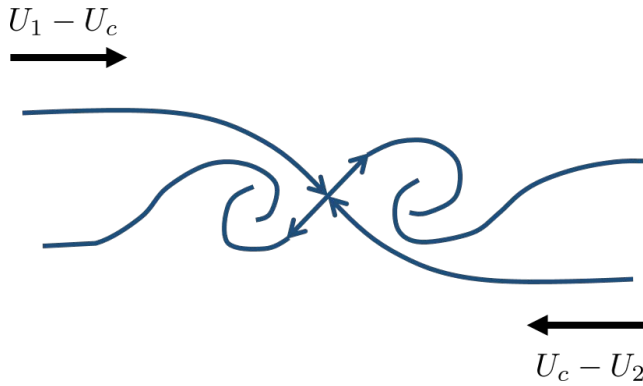


Figure 5.9: Streamlines in a frame convectiong with structures in a shear layer. There are stagnation points for each stream between the structures.

The comparison of the structures observed in flow with injection to structures in shear layers can begin with a comparison of wavelengths. As noted above, the wavelength of structures in shear layers scales with the vorticity thickness δ_ω , defined in Equation 5.7. The computed profiles reported in Section 4.3 can be used to calculate an equivalent length scale to non-dimensionalize the wavelengths observed in experiments.

Equation 5.7 cannot be applied directly to the velocity profiles because although there is a clear choice for the parameters for stream 1 (the free stream values over the cone), there is not a clear choice for stream 2 conditions because of the influence of the wall. This can be resolved by defining a new thickness δ_c , which is the vertical distance between the points of maximum curvature of the momentum profile. δ_c will be referred to in this work as the curvature thickness of the profile. It is roughly equivalent to δ_ω except that it allows for either or both of conditions 1 and 2 to be not well-defined. It is only required that there is an inflection region in the profile. The momentum profile is chosen instead of the velocity profile, motivated by the fact that many features in jets, wakes, and shear layers depend on the initial momentum thickness (Michalke, 1965). The velocity and momentum profiles yield very similar

results in most cases, with slight differences due to the fact that the density and velocity profiles evolve differently due to the presence of the wall and convection of the injected gas in the direction normal to the mean flow from the injector. This is not a concern in free shear layers where the velocity and density profiles behave similarly to one another. An example momentum profile for a case with nitrogen injection is shown in Figure 5.10 with the curvature thickness indicated.

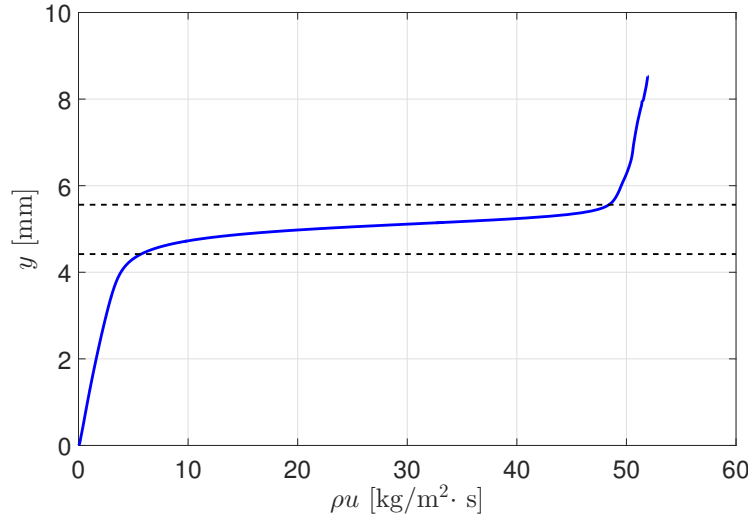


Figure 5.10: Example momentum profile for a case with nitrogen injection. The curvature thickness δ_c is indicated with black dashed lines.

δ_c increases with downstream distance as streamwise momentum diffuses downward from the free stream towards the wall, so the choice of streamwise location at which δ_c is evaluated is not arbitrary. It is assumed that the instability begins to develop nearly instantaneously as soon as the profiles are modified with injection and that the wavelength scales with the initial injection layer profiles at the beginning of the injector. Hence the profiles at the beginning of the injector are used to evaluate δ_c for each case. There is some difficulty in locating the furthest point of curvature from the wall in cases where a strong shock is present at the beginning of the injector section, so the uncertainty in δ_c is higher in these cases. Values for δ_c for each case are given in Table 5.1.

The value of δ_c is effectively constant for each injected gas within the degree of uncertainty in determining the points of maximum curvature. Figure 5.11 shows the experimental values for wavelength normalized by corresponding values for δ_c from Table 5.1. The values of δ_c are averaged over the injection rates so that there is a single value for each injected gas since the values of δ_c for a given gas are so similar. Data from the cases with helium injection performed at a higher unit Reynolds

Injected gas	$J = \frac{(\rho u^2)_{\text{inj}}}{(\rho u^2)_{\infty}}$	δ_c [mm]
Nitrogen	0.28×10^{-4}	0.71
Nitrogen	1.80×10^{-4}	0.70
Nitrogen	10.25×10^{-4}	0.70
Helium	0.38×10^{-4}	0.64
Helium	1.59×10^{-4}	0.65
Helium	5.42×10^{-4}	0.64
RC318	0.51×10^{-4}	0.72
RC318	2.78×10^{-4}	0.75
RC318	9.14×10^{-4}	0.76

Table 5.1: Values of δ_c for momentum profiles at the beginning of the injector section for the OpenFOAM computations.

number are not included because δ_c is a function of the free stream conditions in the wind tunnel and the computations all have a unit Reynolds number of 9×10^6 per meter.

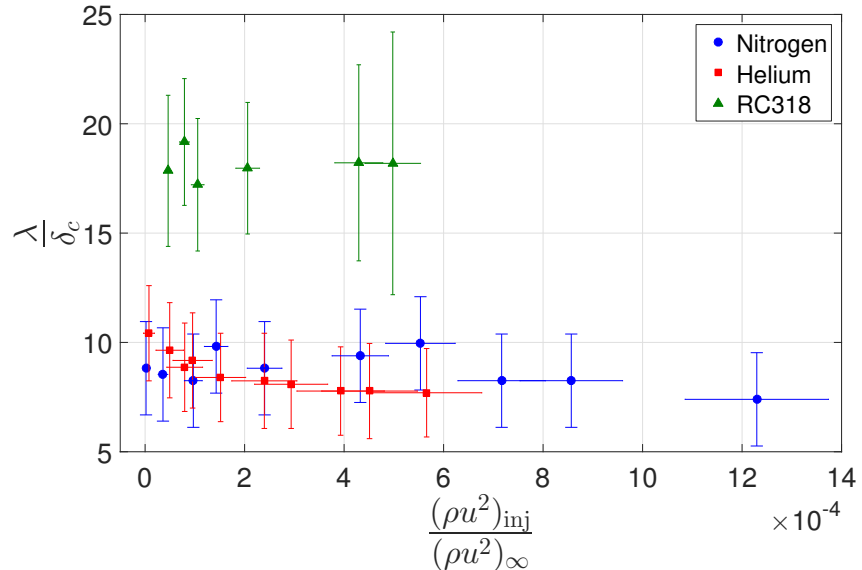


Figure 5.11: Wavelength normalized by δ_c using the values in Table 5.1 for the experiments performed with the lower unit Reynolds number condition (9×10^6 per meter nominally).

The results for nitrogen and helium injection collapse remarkably well to a value of $\frac{\lambda}{\delta_c} = 8.5$, and the results for RC318 injection are self-consistent in the sense that the measured wavelength and calculated δ_c are both approximately constant across all injection rates tested. The value of 8.5 is higher than the values reported

in the literature for $\frac{\lambda}{\delta_\omega}$ of between 3 and 5 for free shear layers, but there is a difference between the definitions δ_c and δ_ω used to normalize the wavelength so some discrepancy is expected. The values of $\frac{\lambda}{\delta_c}$ for RC318 injection cases are much higher than those for helium and nitrogen injection, however. This may be due to the fact that the momentum profile for RC318 injection has an additional inflection region close to the wall where the density reaches a local maximum which is not present in the velocity profile. This could change the scaling of the wavelength relative to the other cases where the momentum profile is monotonic. The fact that the curvature thickness collapses the wavelengths in each data set in this study much in the same way that the vorticity thickness collapses the wavelength data in free shear layers is evidence that the instability present in supersonic flow with injection may be of the same type as that active in supersonic shear layers.

Predicting a convective velocity for waves in the injection layer is not straightforward using Equation 5.14 and the data from the OpenFOAM computations. Condition 1 is obviously the free stream over the cone, but the choice of condition 2 is not clear because of the presence of the wall. Based on a similar argument to the one used to define δ_c , namely that the properties of the layer are governed by the inflection region in the momentum profile as long as the inflection point is sufficiently far from the wall, condition 2 can be specified at the lower point of curvature in the momentum profile which is indicated by the lower dashed line in Figure 5.10. Using this definition for condition 2, the value of U_c calculated from Equation 5.14 varies only slightly in the streamwise direction, so the choice of streamwise location for evaluating U_c is somewhat arbitrary. The profile used to compute U_c is the one at the rear of the injector, which is close to where the convective speed is measured in the experiments. The inflection point in the momentum profile is several δ_c s from the wall at this location. Table 5.2 lists the values for $\frac{U_c}{U_\infty}$ computed from Equation 5.14.

The values in Table 5.2 show the same qualitative trends for a given injected gas as those observed in Figure 5.4, namely that U_c increases with increasing injection rate for cases with nitrogen and helium injection and decreases slightly with increasing injection rate for cases with RC318 injection. Figure 5.12 shows the measured convective velocity for each experiment normalized by a corresponding predicted convective velocity from Table 5.2. Linear interpolation and extrapolation of the data in Table 5.2 is used to estimate the predicted convective velocity.

Using the lower point of curvature in the momentum profile to calculate the conditions in stream 2 for Equation 5.14 predicts the measured convective velocity almost

Injected gas	$J = \frac{(\rho u^2)_{\text{inj}}}{(\rho u^2)_{\infty}}$	$\frac{U_c}{U_{\infty}}$
Nitrogen	0.28×10^{-4}	0.75
Nitrogen	1.80×10^{-4}	0.79
Nitrogen	10.25×10^{-4}	0.81
Helium	0.38×10^{-4}	0.86
Helium	1.59×10^{-4}	0.91
Helium	5.42×10^{-4}	0.96
RC318	0.51×10^{-4}	0.70
RC318	2.78×10^{-4}	0.69
RC318	9.14×10^{-4}	0.67

Table 5.2: Values of $\frac{U_c}{U_{\infty}}$ computed with Equation 5.14 and the data from the OpenFOAM computations using the lower point of curvature in the momentum profile to determine the conditions in stream 2. Profiles are taken at the rear of the injector section.

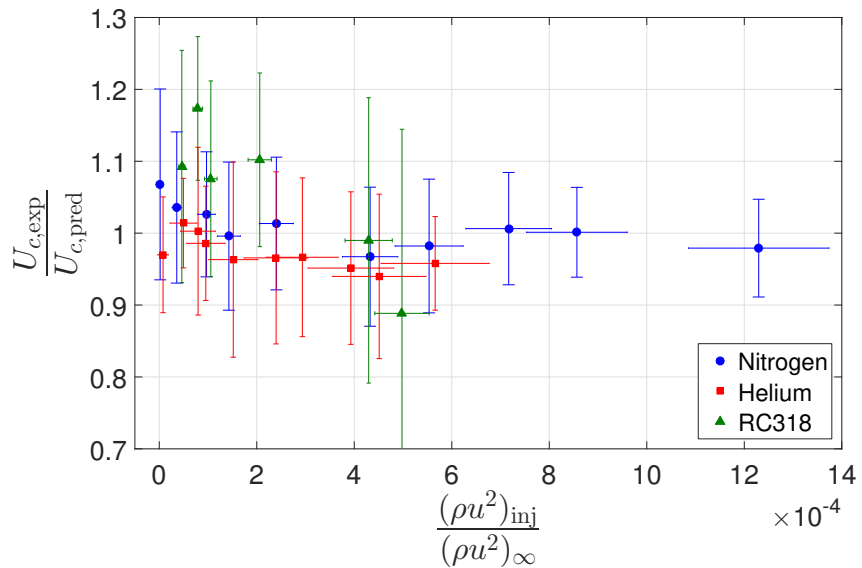


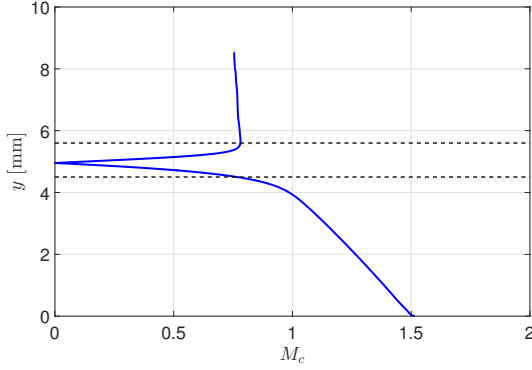
Figure 5.12: Ratio of the measured experimental value of wave convective speed to that predicted using Equation 5.14 (tabulated in Table 5.2) plotted against J for cases with a nominal unit Reynolds number of 9×10^6 per meter.

exactly for all cases. Recall from Section 4.2 that there is some additional uncertainty in computing the convective velocity in cases with RC318 injection because the long-wavelength structures are difficult to track with the limited camera resolution available. The fact that the convective velocity of structures in the injection layer can be so accurately predicted using a relation for free shear layers, along with the evidence provided by the scaling of the wavelengths, provides a strong case that

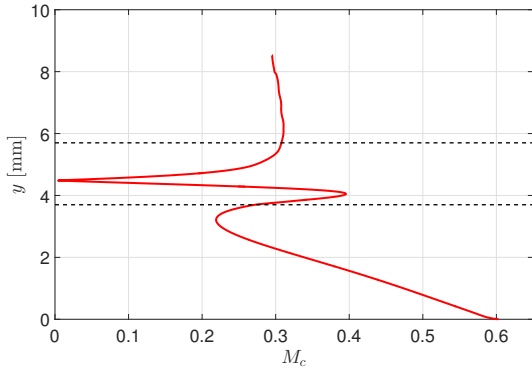
the instability present in the injection layer is of the Kelvin-Helmholtz type resulting from the inflection in the velocity profile.

If transition in flow with injection is due to shear layer instabilities, then the findings of past research efforts on shear layers can be brought to bear on understanding and predicting the behavior of flow with injection under different conditions, beyond just predicting the wavelength, velocity, and frequency of the waves. First, Brown and Roshko (1974) report that the vorticity thickness is lower for shear layers with a heavier gas in the high-speed stream, or, equivalently, for a lighter gas in the low-speed stream. The same qualitative trend is observed in the current work. Inspection of Table 5.1 shows that δ_c for the injection layer is indeed thinner for lighter injected gases which constitute the majority of the low-speed stream.

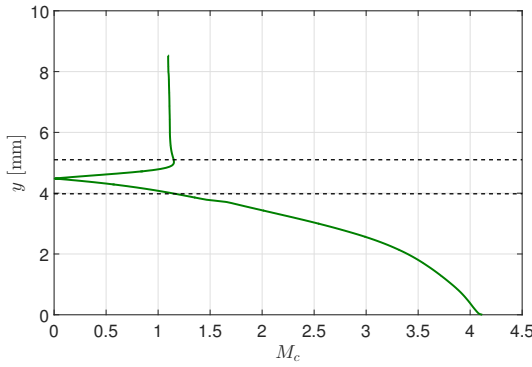
Since its introduction many researchers e.g. Papamoschou and Roshko (1988b) have noted the importance of the convective Mach number in representing the effect of compressibility on a shear layer. M_c is particularly important in predicting the amplification rate of disturbances in a compressible shear layer and therefore its stability. As noted by Papamoschou (1987), M_c is a function of y , the coordinate normal to the mean flow direction, in shear layers with finite thickness. This definition of M_c is given in Equation 5.13. M_c is plotted as a function of y at the rear of the injector section for three example cases, one for each injected gas, in Figure 5.13. The profiles of $M_c(y)$ are very similar for cases at injection rates other than the ones shown in the figure. Black dashed lines mark the location of the points of maximum curvature in each case's momentum profile which are used to specify the conditions of streams 1 and 2.



(a) $M_c(y)$ for an example case with nitrogen injection. The black dashed lines mark the location of the curvature points in the corresponding momentum profile.



(b) $M_c(y)$ for an example case with helium injection. The black dashed lines mark the location of the curvature points in the corresponding momentum profile.



(c) $M_c(y)$ for an example case with RC318 injection. The black dashed lines mark the location of the curvature points in the corresponding momentum profile.

Figure 5.13: Convective Mach number M_c plotted as a function of the wall-normal coordinate y for three example cases. Profiles are taken at the rear of the injector section.

It can first be noted that, defining stream 2 in this way, the convective Mach number for each stream is approximately equal, so there are no "asymmetric" cases as described by Papamoschou (1989) where the convective Mach number is supersonic in one stream and subsonic in the other. This avoids complications in choosing a convective Mach number to characterize the stability of the flow. The convective Mach number increases close to the wall and becomes supersonic in cases with nitrogen and RC318 injection. This is a feature that is not observed in free shear layers so it is unknown how this affects the transition process. It should also be noted that a subsonic sublayer exists in the center of the inflection region of the momentum profile where the convective Mach number is small in all cases, a feature also observed by Papamoschou and Roshko (1988b) for free shear layers.

It has been well-documented that the amplification of disturbances in a shear layer decreases with increasing M_c and therefore shear layers with higher convective Mach numbers are more stable. This explains the trend in transition location observed in the experiments performed in this study and also past studies that have observed the same trend. Recall from Figure 4.7 in Section 4.1 that the transition location moves downstream as the molecular weight of the injected gas decreases. Figure 5.13 shows that the convective Mach number increases with the molecular weight of the injected gas, enhancing the stability of the resulting injection layer.

M_{c1} and M_{c2} are subsonic in cases with nitrogen and helium injection and weakly supersonic in cases with RC318 injection. This difference may contribute to the different values observed in $\frac{\lambda}{\delta_c}$ (see Figure 5.11) along with the qualitative difference in density profile shape mentioned previously. Papamoschou (1987) observes a difference in $\frac{\lambda}{\delta_\omega}$ in free shear layers when the convective Mach number changes from subsonic to supersonic, although in his work the wavelength becomes shorter as the convective Mach number becomes supersonic, which is the opposite of what is observed here. Sandham and Reynolds (1991), Clemens and Mungal (1992), and others have also documented that oblique modes can become active in compressible shear layers when the convective Mach number is sufficiently high, which could also help explain why the waves have different characteristics in cases with RC318 injection.

The effect of the cone wall can be inferred qualitatively from the linear stability analysis of Zhuang et al. (1990). They consider a two-dimensional, constant density, homogeneous shear layer propagating in a confined two-dimensional channel with frictionless walls on both sides of the shear layer. The analysis cannot predict the

influence the profile shapes (density, temperature, etc.) of the injection layer have on the instability, but it does give some insight into how the walls interact with the shear layer. They find that for subsonic convective Mach numbers the walls have no discernible effect, but that the walls weakly destabilize the instability in cases with supersonic convective Mach number. Interestingly, they find that multiple instability modes are active in cases with supersonic convective Mach number and that the Kelvin-Helmholtz mode is not the most unstable mode. Disturbances are amplified by the reflection of acoustic waves generated in the shear layer from the walls. Both of these findings, that there are multiple unstable modes when the convective Mach number is supersonic and the modes are amplified by acoustic wave reflection, are similar to the findings of Mack (1984) for high-speed boundary layers. It may be that the cone wall has a similar influence on the injection layer in the current study.

The difference in behavior when the convective Mach number is supersonic in the presence of a wall or walls perhaps better explains the significant qualitative difference observed in the injection layer with RC318 as the injected gas compared to cases with the other two gases. If the most unstable mode is not of the Kelvin-Helmholtz type then it may very well exhibit a different scaling for its wavelength from the other cases which are Kelvin-Helmholtz unstable. The most unstable mode in cases with RC318 injection may also be oblique. The mode of the instability would not affect the predicted convective velocity, as the formulation of Equation 5.14 for predicting the convective velocity does not require that the waves be of any particular type, so long as they exist between two streams with different speeds.

Chapter 6

SUMMARY AND CONCLUSIONS

This work has provided primarily experimental evidence to support the hypothesis that the dominant instability in flow with injection is a shear layer instability and that the flow can be treated as a shear layer to predict its behavior, as long as care is taken to select the wall-normal location where the properties for the low-speed stream are computed. Data detailing the wavelength, convective speed, frequency, injection layer thickness, and transition location have been presented for a range of injection rates for three injected gases which have significantly different molecular weights. This chapter summarizes the thesis chapter by chapter, presents a set of conclusions, and then provides recommendations for future research.

6.1 Introduction

The problem of supersonic flow with mass injection through a porous wall is introduced and described. The motivations for previous studies of this flow are listed and some example studies are cited. The two applications considered to be most promising are localized transpiration cooling and the enhancement of scramjet performance by fuel injection in the engine inlet.

Injection of a cold gas has long been noted as a potential solution for handling the significant heating loads encountered in high-speed flight. An active cooling system of this type on a vehicular scale is considered to be impractical and would likely have little, if any, net benefit. Passive cooling systems e.g. ceramic tiles and other heat-resistant materials are ubiquitous on high-speed vehicles, but such systems do not allow for the inclusion of windows or sensing equipment on the surface of the vehicle. Localized transpiration of a cooling gas could enable this technology.

Several recent computational studies have identified the benefits of injecting a small amount of fuel through the walls of a scramjet inlet in enhancing overall engine performance. Fuel injection provides some cooling effect and also reduces skin friction drag, as well as producing radicals as the fuel reacts with the air entering the inlet. These radicals help to enhance the combustion efficiency when the air reaches the combustor and is reacted with the remaining majority of the fuel.

Two main issues are identified and addressed in this work. First is the formation of

waves by injection, particularly a strong oblique shock that forms at the beginning of the injector. The wave is strong enough in some cases to cause the layer of injected gas to transition to turbulence, dramatically reducing the efficacy of cooling. It also creates total pressure losses that can become significant in internal flows, such as scramjet inlets.

The second issue is that of the stability of the injection layer downstream of injection. Understanding the instabilities active in the flow that lead to transition to turbulence is of great importance for both applications. Turbulent flow has enhanced transport of temperature, meaning that the cooling effect of transpiration is significantly reduced after the layer has transitioned from laminar to turbulent. Turbulent mixing is crucial for combustion in scramjet inlets, so transition is highly desired in that application.

The current work seeks to address both of these issues by studying injection on a sharp 5-degree half-angle cone in the Mach 4 Ludwieg tube at Caltech.

6.2 Facility & Test Procedure

The Ludwieg tube facility is presented and described. A pneumatic fast-acting valve was designed, constructed, and implemented to replace the primary upstream diaphragm for operating the wind tunnel. Details of the design process as well as the many advantages of the valve over traditional diaphragm operation are reported. The run procedure of the Ludwieg tube both with diaphragms and the valve is described.

A description of the test article is given. The primary article is a 5-degree half-angle cone with a cylindrical porous injector section. The injected gas is supplied by a pipe that enters through the rear of the cone. Flow through the porous material is modeled using a compressible version of Darcy's Law to determine the permeability of the material.

The properties of the injected gas compared to those of the free stream gas has been observed to affect the transition location in similar previous studies, so three injected gases are used in this study: nitrogen, helium, and RC318 (octafluorocyclobutane). The free stream gas is nitrogen for the primary experiments. There is approximately a factor of 7 difference in the molecular weight of helium to nitrogen and nitrogen to RC318. Other properties of the three gases are given. A description of the measurement of the flow rate of the injected gas is given.

Computations performed using the reactingCentralFoam solver in OpenFOAM, an open source finite volume computational fluid dynamics package, are described.

The conditions for the computations are specified to match experimental conditions as closely as possible. The equations solved by the code are given and assumptions made by the solver are identified. Chief among these is the assumption of a unity Schmidt number for computing mass diffusivities based on the mixture viscosity and density. The assumption is examined in detail in Appendix A and implications for the results of the computations are given. The computational grid and boundary conditions are also described.

6.3 Diagnostics

Common diagnostic techniques for measuring instabilities in high-speed flows are identified. Hot-wire anemometry, piezoelectric and piezoresistive pressure transducers, laser interferometry, and high-speed photography are identified as potentially suitable techniques for the current work. PCB piezoelectric pressure transducers are selected as a surface measurement technique due to their commercial availability, small size, and high frequency response. The model is instrumented with five PCB 132A31 transducers along the frustum downstream of the injector section.

Laser interferometry, specifically focused laser differential interferometry (FLDI) is analyzed in detail in Appendix C. FLDI has a very high signal-to-noise ratio and frequency response, but it is effectively a point measurement and can only measure frequency quantitatively without *a priori* knowledge of the density field. Therefore FLDI was ruled out after consideration.

A high-speed schlieren visualization technique is selected as the primary diagnostic. The system uses a pulsed laser diode light source which limits the effective exposure time of the images to tens of nanoseconds. This freezes the motion of instability waves in the injection layer flow, allowing them to be analyzed. Images are acquired at several hundred kHz with a Phantom v710 high speed camera. The timing scheme for the camera and light source is described. The advantages and disadvantages of the selected laser light source compared to a traditional white light source are listed. Light from the laser diode is narrow-band but effectively incoherent, mitigating many of the issues typically associated with using a laser light source for visualization.

6.4 Results

Results of experiments with the cylindrical injector are compared to those performed with a frustum-shaped injector that matches the slope of the cone surface. The cylindrical injector is found to minimize the strength of the shock wave formed at the beginning of the injector. The negative slope of the injector compared to the

cone surface compensates for the increase in flow displacement due to injection. A "tuned" situation exists where the injection flow rate is such that the slope of the flow displacement matches that of the cone ahead of the injector and therefore no shock wave is produced.

Full-field images are presented of the test flow with injection of the three gases. The images are analyzed to measure the injection layer thickness δ at the rear of the injector section and the mean transition location of the injection layer. δ is found to increase with increasing injection mass flow rate and is higher for a given mass flow rate for lighter injected gases. Transition distance decreases with increasing injection rate, decreasing molecular weight of the injected gas, and increasing free stream unit Reynolds number. These findings agree with the results of other studies.

Results from experiments using a high frame rate of approximately 290 kHz are presented. 10,000 images are recorded from each case. The algorithm for processing the images is described. Analysis routines for measuring the wavelength, convective speed, and frequency of the instability waves from the images are reported.

In cases with helium and nitrogen injection several wavelengths are observed in each image. Wavelength is determined using an autocorrelation method, which is described in detail. Each test run produces a population of several thousand wavelengths, which are condensed to a mean value and standard deviation by fitting the population with a log-normal distribution. Wavelength cannot be measured directly for cases with RC318 injection in this study due to limitations of the optical system, so it is calculated using Taylor's hypothesis because the convective speed and frequency are known.

Convective velocity is measured in all cases by cross-correlation of image pairs where a wavelength is measured in one of the images. The high, constant framing rate used in these experiments makes cross-correlation simple and accurate. Waves move only a small fraction of their wavelength from frame to frame. Pixel-locking does occur, but the size of the population as well as cross-correlation of non-consecutive images help to mitigate this issue. The convective speed can be determined more reliably in cases with helium and nitrogen injection because small features can be readily identified. This is more difficult in cases with RC318 injection where the characteristic size of structures in the injection layer is significantly larger.

Frequency is difficult to measure directly in cases with helium and nitrogen injection and so is determined using Taylor's hypothesis. Frequency is measured in RC318

injection cases by using an edge-finding method to detect the edge of the injection layer in each image and tracking its motion in time. Prewitt and Sobel methods are found to work best for this as they search for edges with a specified orientation and are not fooled by edges created by noise at other orientations. A peak frequency is detected in the spectra of the PCB pressure transducers for some cases, and the frequencies measured by pressure transducers agree well with the frequencies determined by the optical method.

Results from the OpenFOAM computations are presented. A check for convergence of the grid is performed by evaluating one example case on grids with varying levels of refinement. The grid is determined to be sufficiently resolved with an acceptable processing time for a spatial resolution of $45 \mu\text{m}/\text{cell}$ in the most-refined region where the injection layer is present. Wall-normal profiles of velocity, density, temperature, and injected gas mass fraction are taken at several locations in the domain. Streamwise momentum is found to diffuse fastest for lighter injected gases. Lighter injected gases also feature a higher adiabatic wall temperature downstream of injection. The density profile with RC318 injection develops a local minimum away from the wall, which is a consequence of the competing effects of temperature and composition. Measurements of the displacement thickness in the computations compare favorably to the visual thickness measured in the experiments for cases with helium and nitrogen injection but not for RC318 injection. This is believed to be due most likely to the inaccuracy of the unity Schmidt number assumption for RC318-nitrogen diffusion.

6.5 Analysis

The momentum flux ratio J is presented as a more appropriate parameter for presenting results for this type of experiment than the mass flux ratio F which is used in the literature. J is shown to collapse the data for δ for different injected gases and unit Reynolds numbers and δ follows a power law dependence on J . This is the same scaling and dependence used for the penetration height of jets in supersonic crossflows.

The transition location normalized by δ is shown to collapse reasonably well when plotted against the velocity ratio of the injected gas to the free stream gas. It is unknown why this parameter successfully collapses the data, and it may be specific to the geometry of the model, the test facility, or both. More work is recommended to determine how universal this finding is.

The measured wavelength, convective velocity, and frequency of the waves are plotted against J and the uncertainties in each of these measurements are split into the uncertainty due to the experimental technique, governed mainly by the resolution of the camera, and natural variability in the flow. The wavelength for a given injected gas does not show a discernible trend with injection rate. The convective speed increases very slightly for nitrogen injection, increases for helium injection, and decreases slightly with RC318 injection with increasing injection rate. Frequency follows approximately the trends in convective velocity as a consequence of Taylor's hypothesis.

Properties of the instability waves in the injection layers are then compared to those of two well-characterized flows: high speed boundary layers and free shear layers. If instabilities in the injection layer can be determined to behave like those in a flow that has been extensively researched, then great strides can be made in understanding their physics with little additional effort. Trends, scaling, and the values of important non-dimensional properties are used to make the comparisons.

Transition in high-speed boundary layers is summarized. The dominant mode is dependent on the Mach number of the flow, but is either oblique Tollmien-Schlichting waves (the first mode) or two-dimensional waves due to the trapping of acoustic energy (the second mode). The frequency and wavelength of waves caused by both of these modes scale with the local boundary layer thickness. Experiments were performed to analyze the instability in the boundary layer on a straight cone with no injection in the Ludwieg tube. The results reveal long-wavelength waves with a frequency of 45 kHz that are thought to be due to the first mode. The frequency is identical for both the optical method and pressure transducers. This frequency agrees well with the predicted most-amplified frequency of both first- and second-mode waves from a linear stability analysis. The fact that neither the frequency nor the wavelength of waves in the injection layers vary significantly with δ indicates that their stability characteristics are not like those of boundary layers. Furthermore, the second mode instability requires a "sonic line" in the boundary layer profile where the disturbance phase velocity is equal to the sum of the local velocity and sound speed. Such a condition does not exist for cases with helium injection.

The findings of several studies of compressible, heterogeneous free shear layers are reported. The spacing between structures scales reasonably well with the local vorticity thickness for shear layers with widely varying properties. The convective

velocity can be computed knowing the velocities, sound speeds, and ratios of specific heats of the two streams of a shear layer using a relatively simple argument based on the idea that the two streams must have a common stagnation point in between structures in a shear layer in the frame of reference convecting with the structures.

Defining the high-speed stream for modeling the injection layer as a shear layer to be the free stream above the cone surface is an obvious choice. It is more difficult to define the conditions for the low-speed stream due to the presence of the wall. A thickness analogous to the vorticity thickness for shear layers, called the curvature thickness, is defined for injection layers. The wavelength of the waves in cases with helium and nitrogen injection is found to scale identically with the curvature thickness. The ratio of wavelength to curvature thickness is constant for cases with RC318 injection but the value of the ratio is different than the value for the other two cases.

The choice for defining the conditions for the low speed stream is the wall-normal location where the momentum profile has its lower point of high curvature (see Figure 5.10). This is roughly equivalent to the location of stream 2 in free shear layers, except that the density, temperature, and velocity are not constant between this wall-normal location and the wall in the case of the injection layer. Using this location to compute the convective speed for a free shear layer, the computed convective speed matches the experimental values within experimental uncertainty for all cases.

The characteristics of the wavelength and convective speed of the waves observed in flow with injection indicate that the instability can be treated and analyzed as a shear layer instability. Considering the injection layers as shear layers correctly predicts that the curvature thickness is lower for lighter injected gases. The convective Mach number for the injection layers is found to increase with increasing molecular weight of the injected gas and is subsonic for helium and nitrogen injection cases and slightly supersonic for cases with RC318 injection. Shear layers are known to be more stable as the convective Mach number increases. This explains the trend observed in the transition data, namely that transition distance decreases with lighter injected gases. The fact that the convective Mach number is supersonic for RC318 injection means that the presence of the wall likely creates multiple unstable modes for these cases, the most unstable of which is not the Kelvin-Helmholtz mode. This may explain why the wavelength is much longer in terms of curvature thicknesses for RC318 injection than it is for nitrogen and helium injection, where the Kelvin-Helmholtz

mode is likely the transition mechanism.

6.6 Conclusions

The primary findings of this work are as follows. First, shaping the injector section to compensate for the increased displacement effect of injection is effective in mitigating waves produced in the free stream flow. The parameter that determines proper minimization of the strength of the waves for a given injector geometry is the momentum flux of the injected gas normalized by the momentum flux of the free stream. The thickness of the injection layer is found to be a function of the dimensionless momentum flux and follows the same scaling as jets in supersonic crossflow. The characteristics of the instability waves in the injection layer are determined to be similar to those in a shear layer. Their wavelength scales with the so-called curvature thickness of the momentum profile, which is analogous to the scaling of waves in a shear layer with the vorticity thickness. The convective speed of waves in the injection layer can be accurately predicted using the well-known relation for the speed of waves in a free shear layer but the conditions for the low-speed stream must be taken at the lower curvature point in the momentum profile of the injection layer. Other properties of the injection layer regarding stability can be predicted from the convective Mach number of the waves using theory from shear layers.

6.7 Recommendations for Future Work

There is a large parameter space associated with the problem of supersonic flow with injection, and this work was only able to probe a small fraction of that space. For future studies in the Caltech Ludwieg Tube it would be interesting to experiment with model and injector geometries different from the ones used in this campaign to examine the effect of geometry on the injection layer properties, particularly the tuning effect and mean transition location. Accurate computational fluid dynamics simulations could assist with this process, particularly in attempting to find an injector and model shape combination than can minimize the formation of all waves, not only the strong oblique shock at the beginning of the injector. Injection parallel to the free stream was considered by Schmidt et al. (2014) as a method to stabilize the injection layer, but accelerating the injected gas to a speed comparable to that of the free stream would be very difficult, and the resulting flow would still be subject to wake instabilities, so it is unlikely that such a configuration would be successful.

Using other injected gases could also prove fruitful. In the current work, the

effects of molecular weight and ratio of specific heats of the injected gas are not separated from one another, but it may be worth while to attempt to vary these properties independently to the furthest extent possible and analyze their effects on the instability. Computations would also be beneficial for this type of study.

Other experimental techniques would complement the results of this study. Velocimetry, performed either with hot-wire anemometry or with optical techniques, would be very useful to verify the velocity profile in the injection layer computed from OpenFOAM. Hot-wire anemometry has the additional benefit of potentially being able to further corroborate measurements of frequency of the instability waves. Seeding the injected gas with particles for optical velocimetry may be difficult because of the small pore size of the injector, which is designed to filter particles larger than about $10 \mu\text{m}$. Experiments using techniques such as Rayleigh scattering or planar laser induced fluorescence (PLIF) to determine the species concentration and/or temperature in the injection layer would also be immensely helpful in understanding the diffusion processes. Inclusion of trace species such as acetone in the injected gas stream would be quite easy with the current setup.

It would also be interesting to perform similar analyses to the current study in other test facilities with different free stream Mach numbers, unit Reynolds numbers, noise characteristics, etc. Testing in a high-enthalpy environment such as in a shock tunnel would be more difficult than in traditional wind tunnels, but it is crucial to understand the effects of having conditions more similar to free flight than the cold flow of a Ludwieg tube. For instance, the temperature distribution is effectively reversed: the free stream gas is hot and the injected gas is cold in flow in a high-enthalpy facility and in flight, and it would be interesting to learn what effect this has on parameters like the convective Mach number.

Clearly computational studies with a CFD solver designed to more accurately solve binary diffusion of species in a high-speed, compressible flow with a wide range of Mach numbers than the one used in this work would be very beneficial. The solver used in this work is reasonably effective, but the unity Schmidt number assumption limits its accuracy in flows where diffusion is important such as this one. It may not be prohibitively difficult to simply modify the reactingCentralFoam solver to accept diffusion coefficients for each species which would be a significant improvement, but more sophisticated computational efforts would obviously be more effective. An in-depth computational or theoretical study of the stability properties of the flow that can account for different gases, is valid in the nonlinear regime, and does not rely

on a locally-parallel flow assumption, which is dubious near the injector, would also be extremely helpful in sorting out the underlying physics of the active instability or instabilities.

BIBLIOGRAPHY

- Aupoix, B., A. Mignosi, S. Viala, F. Bouvier, and R. Gaillard (1998). “Experimental and Numerical Study of Supersonic Film Cooling”. In: *AIAA Journal* 36.6.
- Azzazy, M., D. Modarress, and T. Hoeft (1987). “High sensitivity density fluctuation detector”. In: *Journal of Physics E: Scientific Instruments* 20.4, p. 428.
- Barth, J. E., V. Wheatley, and M. K. Smart (2013). “Hypersonic Turbulent Boundary-Layer Fuel Injection and Combustion: Skin-Friction Reduction Mechanisms”. In: *AIAA Journal* 51.9, pp. 2147–2157. doi: 10.2514/1.J052041.
- Barth, J. E., D. J. Wise, V. Wheatley, and M. K. Smart (2015). “Tailored fuel injection for performance enhancement in a Mach 12 scramjet engine”. In: *20th AIAA International Space Planes and Hypersonic Systems and Technologies Conference*. AIAA 2015-3614. AIAA.
- Berry, S. A., A. H. Auslender, A. D. Dilley, and J. F. Calleja (2001). “Hypersonic Boundary-Layer Trip Development for Hyper-X”. In: *Journal of Spacecraft and Rockets* 38.6, pp. 853–864.
- Biss, M. M., G. S. Settles, and S. R. Sanderson (2008). “Differential schlieren-interferometry with a simple adjustable Wollaston-like prism”. In: *Applied Optics* 47.3, pp. 328–335.
- Bitter, N. P. and J. E. Shepherd (2015). “Stability of highly cooled hypervelocity boundary layers”. In: *Journal of Fluid Mechanics* 778, pp. 586–620.
- Born, M. and E. Wolf (1999). *Principles of Optics*. 7th ed. Cambridge University Press.
- Brown, G. L. and A. Roshko (1974). “On density effects and large structure in turbulent mixing layers”. In: *Journal of Fluid Mechanics* 64, pp. 775–816.
- Cary, A. M. and J. N. Hefner (1971). “An Investigation of film-cooling effectiveness and skin friction in hypersonic turbulent flow”. In: *AIAA 4th Fluid and Plasma Dynamics Conference*. AIAA.
- Clemens, N. and M. Mungal (1992). “2-Dimensional and 3-Dimensional Effects in the Supersonic Mixing Layer”. In: *AIAA Journal* 30.4, pp. 973–981.
- Dimotakis, P. E. and G. L. Brown (1976). “The mixing layer at high Reynolds number: large-structure dynamics and entrainment”. In: *Journal of Fluid Mechanics* 78.3, pp. 535–560.
- Dullien, F. A. L. (1979). *Porous Media*. Academic Press, NY, NY.
- Egorov, I., E. Vasilevskii, A. Novikov, and I. Ezhov (2015). “Tangential Blowing to a Supersonic Flow on a Blunted Nose”. In: *53rd AIAA Aerospace Sciences Meeting*. AIAA-2015-0212. AIAA.

- Estorf, M., T. Wolf, and R. Radespiel (2003). *Experimental and Numerical Investigations on the operation of the Hypersonic Ludwieg tube Braunschweig*. Tech. rep. Technical University at Braunschweig.
- Fedorov, A. V. (2011). "Transition and stability of high-speed boundary layers". In: *Annual review of fluid mechanics* 43, pp. 79–95.
- Fedorov, A. V., N. D. Malmuth, A. Rasheed, and H. G. Hornung (2001). "Stabilization of hypersonic boundary layers by porous coatings". In: *AIAA Journal* 39.4, pp. 605–610.
- Fedorov, A. V., V. G. Soudakov, and I. A. Leyva (2014). "Stability analysis of high-speed boundary-layer flow with gas injection". In: *AIAA 7th Theoretical Fluid Mechanics Conference*. AIAA-2014-1271. AIAA.
- Fedorov, A. V. and A. Tumin (2011). "High-speed boundary-layer instability: old terminology and a new framework". In: *AIAA Journal* 49.8, pp. 1647–1657.
- Forchheimer, P. (1901). "Wasserbewegung durch boden". In: *Z. Ver. Deutsch. Ing* 45.1782.
- Frederking, T. H. K., W. A. Hepler, S. W. K. Yuan, and W. F. Feng (1986). "Determination of the Darcy Permeability of Porous Media Including Sintered Metal Plugs". In: *Advances in Cryogenic Engineering*, pp. 505–515.
- Fujii, K. and H. G. Hornung (2001). *A procedure to estimate the absorption rate of sound propagating through high temperature gas*. Tech. rep. FM 2001.004. Pasadena, CA (USA): California Institute of Technology.
- Fulghum, M. R. (2014). "Turbulence measurements in high-speed wind tunnels using focusing laser differential interferometry". PhD thesis. The Pennsylvania State University.
- Gehre, R. M., V. Wheatley, and R. R. Boyce (2015). "Combustion regimes in inlet-fueled, low compression scramjets". In: *20th AIAA International Space Planes and Hypersonic Systems and Technologies Conference*. AIAA 2015-3507. AIAA.
- Glass, I. I. and H. Kawada (1962). *Prandtl-Meyer flow of dissociated and ionized gases*. Tech. rep. 85. University of Toronto.
- Haley, R. and P. R. Smy (1988). "An inexpensive light source for high-speed schlieren photography". In: *Journal of Physics E: Scientific Instruments*.
- Jewell, J. S., I. A. Leyva, N. J. Parziale, and J. E. Shepherd (2012). "Effect of gas injection on transition in hypervelocity boundary layers". In: *28th International Symposium on Shock Waves*. Springer Berlin Heidelberg, pp. 735–740.
- Kee, Robert J., Michael E. Coltrin, and Peter Glarborg (2003). *Chemically Reacting Flow: Theory and Practice*. 1st ed. Wiley-Interscience.
- Kovansznay, L. S. G. (1950). "The Hot Wire Anemometer in supersonic flow". In: *Journal of the Aeronautical Sciences* 17.9, pp. 565–572.

- Kraposhin, M., A. Bovtrikova, and S. Strijhak (2015). “Adaptation of Kurganov-Tadmor Numerical Scheme for applying in combination with the PISO method in numerical simulation of flows in a wide range of Mach numbers”. In: *Procedia Computer Science* 66, pp. 43–52.
- Ladberman, A. J. and A. Demetriades (1976). “Detection of Boundary-Layer-transition with a laser-beam”. In: *AIAA Journal* 14.1, pp. 102–104.
- Laurence, S. J., A. Wagner, and K. Hanneman (2014). “Schlieren-based techniques for investigating instability development and transition in a hypersonic boundary layer”. In: *Experiments in Fluids* 55.8, 1782. doi: [10.1007/s00348-014-1782-9](https://doi.org/10.1007/s00348-014-1782-9).
- Laurence, S. J., A. Wagner, K. Hanneman, V. Wartemann, H. Ludeke, H. Tanno, and K. Ito (2012). “Time-Resolved visualization of instability waves in a hypersonic boundary layer”. In: *AIAA Journal* 50.6, pp. 243–246.
- Leyva, I. A., J. S. Jewell, S. J. Laurence, H. G. Hornung, and J. E. Shepherd (2009). “On the impact of injection schemes on transition in hypersonic boundary layers”. In: *16th AIAA International Space Planes and Hypersonic Systems and Technologies Conference*. 2009-7204. AIAA.
- Li, Fei, Meelan Choudhari, Chau-Lyan Chang, and Jeffery White (2013). “Effects of injection on the instability of boundary layers over hypersonic configurations”. In: *Physics of Fluids* 25.
- Macdonald, I. F., M. S. El-Sayed, K. Mow, and F. A. L. Dullien (1979). “Flow through porous media - the Ergun equation revisited”. In: *Industrial and Engineering Chemistry Fundamentals* 18.3, pp. 199–208.
- Mack, L. M. (1965). “Computations of the Stability of the Laminar Compressible Boundary Layer”. In: *Methods in Computational Physics*. Ed. by B. Alder, S. Fernback, and M. Rotenberg. Vol. 4. New York: Academic Press, pp. 247–299.
- (1984). *Boundary-layer linear stability theory*. Tech. rep. AD-P004 046. Pasadena, CA (USA): Jet Propulsion Laboratory and California Institute of Technology.
- Mahesh, K. (2013). “The Interaction of Jets with Crossflow”. In: *Annual Review of Fluid Mechanics* 45, pp. 379–407.
- Marvin, J. G. and C. M. Akin (1970). “Combined Effects of Mass Addition and Nose Bluntness on Boundary-Layer Transition”. In: *AIAA Journal* 8.5, pp. 857–863.
- Menke, W. and J. Menke (2012). *Environmental Data Analysis with MATLAB*. Elsevier.
- Merzkirch, W. (1987). *Flow Visualization*. Academic Press.
- Michalke, A. (1965). “On spatially growing disturbances in an inviscid shear layer”. In: *Journal of Fluid Mechanics* 23, pp. 521–544.
- Milonni, P. W. and J. H. Eberly (1988). *Lasers*. Wiley.

- Mouton, C. A. (2007). "Transition between Regular Reflection and Mach Reflection in the Dual-Solution Domain". PhD thesis. California Institute of Technology.
- Neufeld, P. D., A. R. Janzen, and R. A. Aziz (1972). "Empirical Equations to Calculate 16 of the transport collision integrals $\Omega(I,s)^*$ for the Lennard-Jones (12-6) Potential". In: *The Journal of Chemical Physics* 57.3, pp. 1100–1102.
- Ogawa, H., B. Capra, and P. Lorrain (2015). "Numerical investigation of upstream fuel injection through porous media for scramjet engines via surrogate-assisted evolutionary algorithms". In: *53rd AIAA Aerospace Sciences Meeting*. AIAA 2015-0884. AIAA.
- Ogorodnikov, D. A., V. T. Grin, and H. N. Zakharov (1972). "Controlling the Boundary Layer in Hypersonic Air Intakes". In: *1st International Symposium on Air-Breathing Engines*. FTD-HT-23-1349-72.
- O'Hagan, D. (2008). "Understanding organofluorine chemistry. An introduction to the C-F bond". In: *Chemical Society Reviews* 37, pp. 308–319.
- Papamoschou, D. (1987). "Experimental Investigation of Heterogeneous Compressible Shear Layers". PhD thesis. California Institute of Technology.
- (1989). "Structure of the compressible turbulent shear layer". In: *27th AIAA Aerospace Sciences Meeting*. 89-0126.
- Papamoschou, D. and A. Roshko (1988a). "Observations of supersonic free shear layers". In: *Sadhana* 12, pp. 1–14.
- (1988b). "The compressible turbulent shear layer: an experimental study". In: *Journal of Fluid Mechanics* 197.1, pp. 453–477.
- Pappas, C. C. and A. Okuno (1960). "Measurements of Skin Friction of the Compressible Turbulent Boundary Layer on a Cone with Foreign Gas Injection". In: *Journal of the Aero/Space Sciences* 27, pp. 321–333.
- (1964). *Heat-Transfer Measurement for Binary Gas Laminar Boundary Layers with High Rates of Injection*. Tech. rep. NASA TN-D-2473. NASA.
- Parziale, N. J. (2013). "Slender-body hypervelocity boundary-layer instability". PhD thesis. Pasadena, CA (USA): California Institute of Technology.
- Parziale, N. J., J. S. Damazo, B. E. Schmidt, P. S. Wang, H. G. Hornung, and J. E. Shepherd (2015). "Pulsed Laser Diode for use as a Light Source for Short-Exposure, High-Frame-Rate Flow Visualization". In: *AIAA SciTech 2015*. AIAA-2015-0530. AIAA.
- Parziale, N. J., J. E. Shepherd, and H. G. Hornung (2013a). "Differential Interferometric Measurement of Instability at Two Points in a Hypervelocity Boundary Layer". In: *AIAA 51st Aerospace Sciences Meeting*. 2013-0521. AIAA.
- (2013b). "Differential Interferometric Measurement of Instability in a Hypervelocity Boundary Layer". In: *AIAA Journal* 51.3.

- Parziale, N. J., J. E. Shepherd, and H. G. Hornung (2014). "Free-stream density perturbations in a reflected-shock tunnel". In: *Experiments in Fluids* 55.1665.
- (2015). "Observations of hypervelocity boundary-layer instability". In: *Journal of Fluid Mechanics*.
- Poling, Bruce E., John M. Prausnitz, and John P. O'Connell (2001). *The Properties of Gases and Liquids*. 5th ed. McGraw-Hill.
- Praxair Inc. (2015). *Octafluorocyclobutane Safety Data Sheet P-4671*.
- Sahoo, N., V. Kulkarni, S. Saravanan, G. Jagadeesh, and K. P. J. Reddy (2005). "Film cooling effectiveness on a large angle blunt cone flying at hypersonic speed". In: *Physics of Fluids* 17.036102.
- Sanderson, S. R. (2005). "Simple, adjustable beam splitting element for differential interferometers based on photoelastic birefringence of a prismatic bar". In: *Review of Scientific Instruments* 76.
- Sandham, N. and W. Reynolds (1991). "3-Dimensional Simulations of Large Eddies in the Compressible Mixing Layer". In: *Journal of Fluid Mechanics* 224, pp. 133–158.
- Schmidt, B. E., N. P. Bitter, H. G. Hornung, and J. E. Shepherd (2014). "Experimental Investigation of Gas Injection into the Boundary Layer on a Slender Body in Supersonic Flow". In: *Aviation 2014: Stability and Transition*. AIAA-2014-2496. AIAA.
- (2015). "Injection into Supersonic Boundary Layers". In: *AIAA Journal*. doi: 10.2514/1.J054123.
- Schmidt, B. E. and J. E. Shepherd (2015a). "Analysis of focused laser differential interferometry". In: *Applied Optics* 54.28, pp. 8459–8472.
- (2015b). "Oscillations in cylinder wakes at Mach 4". In: *Journal of Fluid Mechanics* 785.
- Schneider, S. P. (2010). "Hypersonic Boundary-Layer Transition with Ablation and Blowing". In: *Journal of Spacecraft and Rockets* 47.2.
- Settles, G. S. (2001). *Schlieren and Shadowgraph Techniques*. First. Springer Berlin Heidelberg.
- Shepherd, J. E. and D. R. Begeal (1988). *Transient compressible flow in porous materials*. Tech. rep. SAND-83-1788. Albuquerque, NM (USA): Sandia National Labs.
- Smeets, G. (1972). "Laser interferometer for high sensitivity measurements on transient phase objects". In: *IEEE Transactions on Aerospace and Electronic Systems* AES-8.2.
- (1974). "Observational techniques related to differential interferometry". In: *11th International Conference on High Speed Photography*, pp. 283–288.

- Smeets, G. (1977). "Flow Diagnostics by Laser Interferometry". In: *IEEE Transactions on Aerospace and Electronic Systems* AES-13.2, pp. 82–90.
- Steel, W. H. (1967). *Interferometry*. Cambridge University Press.
- Stetson, K. F. (1987). *On predicting hypersonic boundary layer transition*. Technical Memorandum AFWAL-TM-87-160-FIMG. Air Force Wright Aeronautical Laboratories.
- Taylor, G. I. and J. W. MacColl (1933). "The air pressure on a cone moving at high speeds. I." In: *Proceedings of the Royal Society of London A: Mathematical, Physical, and Engineering Sciences* 139.838, pp. 278–297.
- Wagnild, R. M., G. V. Candler, I. A. Leyva, J. S. Jewell, and H. G. Hornung (2009). "Carbon dioxide injection for hypervelocity boundary layer stability". In: *48th Aerospace Sciences Meeting*. AIAA 2009-1287. AIAA. Orlando, FL.
- Ward, C. A. C., R. R. Greenwood, A. D. Abney, and S. P. Schneider (2013). "Boundary-Layer Transition Experiments in a Hypersonic Quiet Wind Tunnel". In: *43rd AIAA Fluid Dynamics Conference*.
- Weller, H. G., G. Tabor, H. Jasak, and C. Fureby (1998). "A tensorial approach to computational continuum mechanics using object-oriented techniques". In: *Computers in Physics* 12.6, pp. 620–631.
- White, Frank M. (1991). *Viscous Fluid Flow*. Second. McGraw-Hill.
- White, M. D. (2010). "High-order parabolic beam approximation for aero-optics". In: *Journal of Computational Physics* 229, pp. 5465–5485.
- Wilke, C. R. and C. Y. Lee (1955). "Estimation of diffusion coefficients for gases and vapors". In: *Industrial and Engineering Chemistry* 47.6, pp. 1253–1257.
- Zhuang, M., P. E. Dimotakis, and T. Kubota (1990). "The effect of walls on a spatially growing supersonic shear layer". In: *Physics of Fluids*.

A p p e n d i x A

MASS DIFFUSION IN OPENFOAM

The validity of the unity Schmidt number assumption made by the OpenFOAM solver can be assessed by estimating the diffusivity for each species into nitrogen (the free stream gas) and computing the Schmidt number as a function of temperature. This is done by evaluating the Chapman-Enskog relation for diffusivity with the method outlined in Section 11-3 of Poling et al. (2001). The diffusion coefficient for species *A* into species *B*, D_{AB} , is given by Equation A.1 (Equation 11-3.2 in Poling et al. (2001)) assuming an ideal gas and setting the correction term in the Chapman-Enskog relation to one:

$$D_{AB} = \frac{0.00266T^{\frac{3}{2}}}{pW_{AB}^{\frac{1}{2}}\sigma_{AB}^2\Omega_D} . \quad (\text{A.1})$$

Written this way, D_{AB} is the diffusion coefficient in cm^2/s , T is the temperature in Kelvin, p is the pressure in bar, σ_{AB} is the characteristic length of the selected intermolecular force law in Angstroms, and Ω_D is the dimensionless collision integral for diffusion, which is a function of temperature and the characteristic energy ϵ of the chosen intermolecular force law. W_{AB} is a function of the molecular weights of gases A and B:

$$W_{AB} = \frac{2}{\frac{1}{W_A} + \frac{1}{W_B}} . \quad (\text{A.2})$$

The 12-6 Lennard-Jones potential is a popular choice for the intermolecular force law, and values of σ and ϵ are tabulated for many common gases, including nitrogen and helium. The interaction values σ_{AB} and ϵ_{AB} are commonly computed from the values of σ and ϵ for the individual species by taking the geometric mean of the ϵ 's and the arithmetic mean of the σ 's:

$$\epsilon_{AB} = (\epsilon_A \epsilon_B)^{\frac{1}{2}} , \quad (\text{A.3})$$

$$\sigma_{AB} = \frac{\sigma_A + \sigma_B}{2} . \quad (\text{A.4})$$

Ω_D is tabulated as a function of the reduced temperature $\frac{kT}{\epsilon}$ where k is Boltzmann's constant for the 12-6 Lennard-Jones potential, and the accurate analytical approxi-

mation of Neufeld et al. (1972) is used to compute it here; the relation is listed as Equation 11-3.6 in Poling et al. (2001).

Values for σ and ϵ are not tabulated for RC318, so they are estimated using the method of Wilke and Lee (1955). The relations are

$$\sigma = 1.18V_b^{\frac{1}{3}} \quad , \quad (\text{A.5})$$

$$\frac{\epsilon}{k} = 1.15T_b \quad , \quad (\text{A.6})$$

where V_b is the liquid molar volume at the normal boiling point (at 1 atm pressure) in cm^3/mol and T_b is the normal boiling point in Kelvin. The values for σ and $\frac{\epsilon}{k}$ are given in Table A.1 for the three gases.

Gas	$\sigma [\text{\AA}]$	$\frac{\epsilon}{k} [\text{K}]$
Helium	2.55	10.22
Nitrogen	3.80	71.4
RC318	5.86	307

Table A.1: Parameters from the Lennard-Jones potential model for the three gases for computing diffusion coefficients.

Instead of computing the diffusion coefficients by themselves, the density-weighted diffusion coefficients can be computed by substituting for the pressure in Equation A.1 with the ideal gas law. This eliminates the pressure dependence and allows the Schmidt number to be easily computed as a function of temperature since the viscosity is only a function of temperature when Sutherland's formula is used:

$$\rho D_{AB} = \frac{0.0266T^{\frac{1}{2}}}{R_A W_{AB}^{\frac{1}{2}} \sigma_{AB}^2 \Omega_D} \quad . \quad (\text{A.7})$$

R_A is the specific gas constant for gas A. The coefficient in Equation A.7 is adjusted such that if σ_{AB} is given in Angstroms and W_{AB} in g/mol, all other quantities are in m-k-s units.

The computed Schmidt number is plotted for each species diffusing into nitrogen as a function of temperature in Figure A.1. The temperature range is restricted to those relevant for experiments in the Caltech Ludwig Tube. The Schmidt number is approximately constant for each species with respect to temperature and is of order one for helium and nitrogen, so the unity Schmidt number assumption made by the

solver is reasonable in cases with helium and nitrogen injection. It is somewhat smaller than unity for RC318 diffusing into nitrogen, however, so the unity Schmidt number approximation made by the solver may produce some errors in cases with RC318 injection.

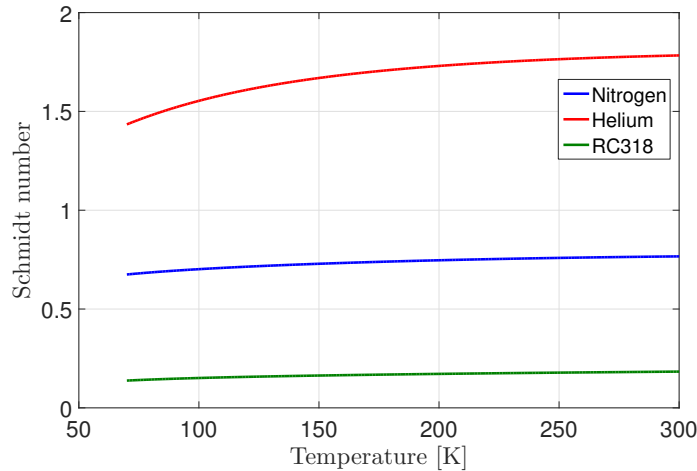


Figure A.1: Schmidt number as a function of temperature for each injected gas diffusing into nitrogen.

A second test was applied to assess the accuracy of the OpenFOAM solver in solving diffusion problems. We consider a one-dimensional box at constant temperature and pressure that is filled on the right half with nitrogen and on the other half with a test gas, either nitrogen, helium, or RC318, for $t < 0$. At $t = 0$, the gases are allowed to mix. Equation 2.19 reduces to a simple diffusion equation when written in terms of the mole fraction instead of mass fraction:

$$\frac{\partial X_1}{\partial t} = D \frac{\partial^2 X_1}{\partial x^2} . \quad (\text{A.8})$$

The value for D is the value predicted from Equation A.7 for the test gas into nitrogen. D is independent of composition in a binary mixture, so it is a constant in this test case where pressure and temperature are held constant. The solution to Equation A.8 is found from separation of variables. A Neumann boundary condition at the ends of the box is used to ensure zero flux of species through the walls.

The problem is also solved using the OpenFOAM solver on a spatial grid of 2000 points. Velocity is set to zero at the ends of the box and temperature, pressure, and species concentrations are specified to have zero gradient at the ends. The interface is sharp at $t = 0$.

Figure A.2a shows the evolution of the species concentration profiles on the left side of the box (initially filled with the test gas) for both the analytic solution (dashed

lines) and the solution from OpenFOAM (solid lines) for the case with nitrogen as the test gas. The mass fraction is computed from the analytical solution, which is initially in terms of the mole fraction, by using the definition of mole and mass fractions:

$$Y_i = \frac{X_i W_i}{\sum X_i W_i} . \quad (\text{A.9})$$

In all the figures that follow the dashed lines represent the analytical solution and the solid lines represent the solution from OpenFOAM. Figure A.2b shows the associated percent error in the OpenFOAM solution.

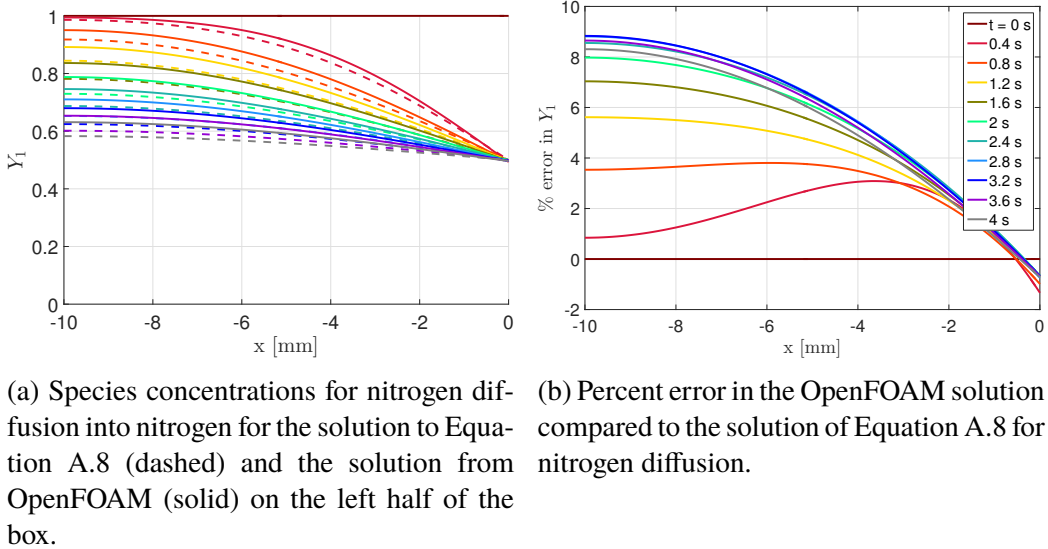
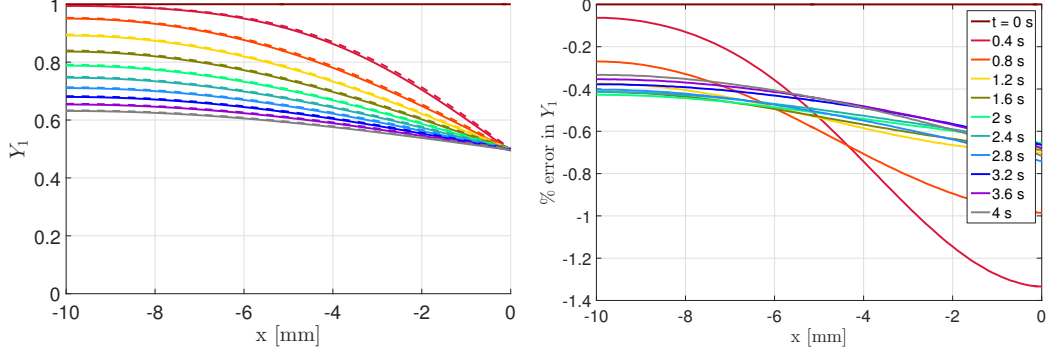


Figure A.2: Comparison of results of the diffusion box test case for nitrogen.

The error is at most about 10% even for late times. It is straightforward to assess what portion of this error is due to the OpenFOAM solver's assumption of a unity Schmidt number by substituting that value for D into Equation A.8. The results for that case are shown in Figure A.3.

The error in this case is dramatically reduced and is almost zero at the box boundary. This is the expected result because no errors are incurred by using the mass fractions to compute the diffusive flux in Equation 2.19 instead of the mole fractions if the molecular weights of the species are equal.

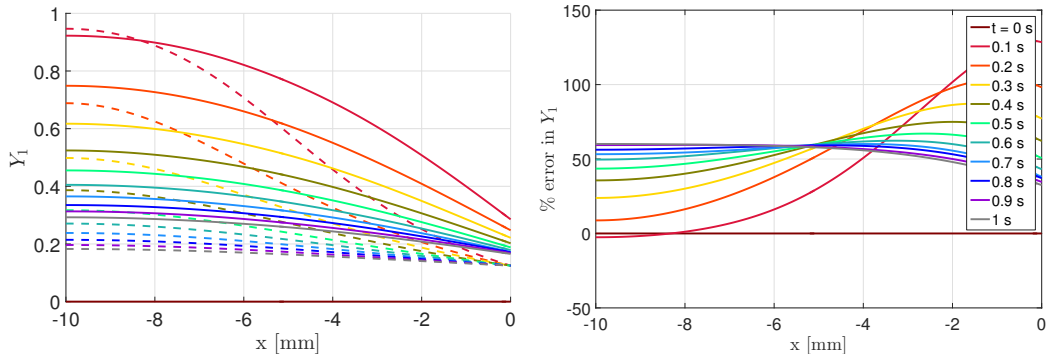
Figures A.4 and A.5 show the results from identical test cases with helium and RC318 as the test gas, respectively. The diffusivity D used by OpenFOAM varies as a function of composition with μ and ρ , which are both weighted by the mass concentrations of the species present. This changes the behavior of the solution as diffusion progresses.



(a) Species concentrations for nitrogen diffusion into nitrogen for the solution to Equation A.8 assuming $Sc = 1$ (dashed) and the solution from OpenFOAM (solid) on the left half of the box.

(b) Percent error in the OpenFOAM solution compared to the solution of Equation A.8 with $Sc = 1$ for nitrogen diffusion.

Figure A.3: Comparison of results of the diffusion box test case for nitrogen assuming $Sc = 1$ in Equation A.8.

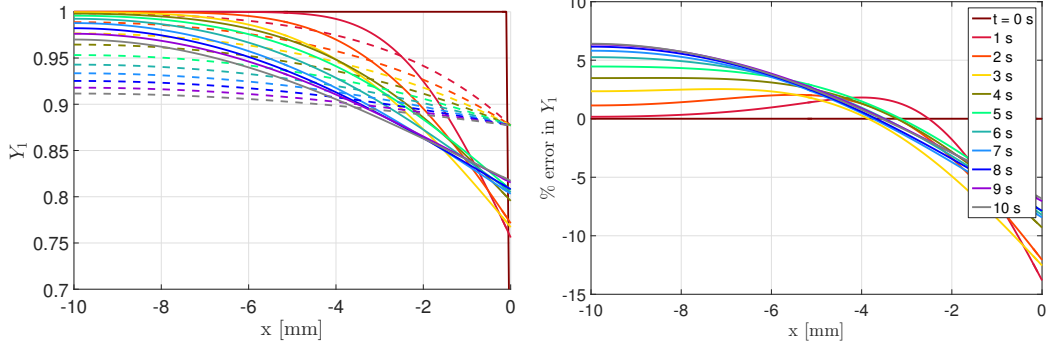


(a) Species concentrations for helium diffusion into nitrogen for the solution to Equation A.8 (dashed) and the solution from OpenFOAM (solid) on the left half of the box.

(b) Percent error in the OpenFOAM solution compared to the solution of Equation A.8 for helium diffusion.

Figure A.4: Comparison of results of the diffusion box test case for helium.

Several observations can be made from these results. First, the error in the OpenFOAM simulation is appreciable especially at late times, on the order of 50% in helium diffusion cases. The error in cases with diffusion of gases with different molecular weights is a combined effect of both the unity Schmidt number assumption and the use of mass fraction instead of mole fraction to compute diffusive fluxes without employing a correction velocity. The trend in the error can be predicted from Figure A.1 for short times where the concentration of nitrogen is low. OpenFOAM over-predicts diffusion in helium-nitrogen diffusion cases and under-



(a) Species concentrations for RC318 diffusion into nitrogen for the solution to Equation A.8 (dashed) and the solution from OpenFOAM (solid) on the left half of the box.
(b) Percent error in the OpenFOAM solution compared to the solution of Equation A.8 for RC318 diffusion.

Figure A.5: Comparison of results of the diffusion box test case for RC318.

predicts diffusion in RC318-nitrogen cases. As the diffusion coefficient changes with increasing nitrogen concentration as diffusion progresses, diffusion becomes under-predicted in helium-nitrogen cases and the under-prediction becomes worse in RC318-nitrogen cases.

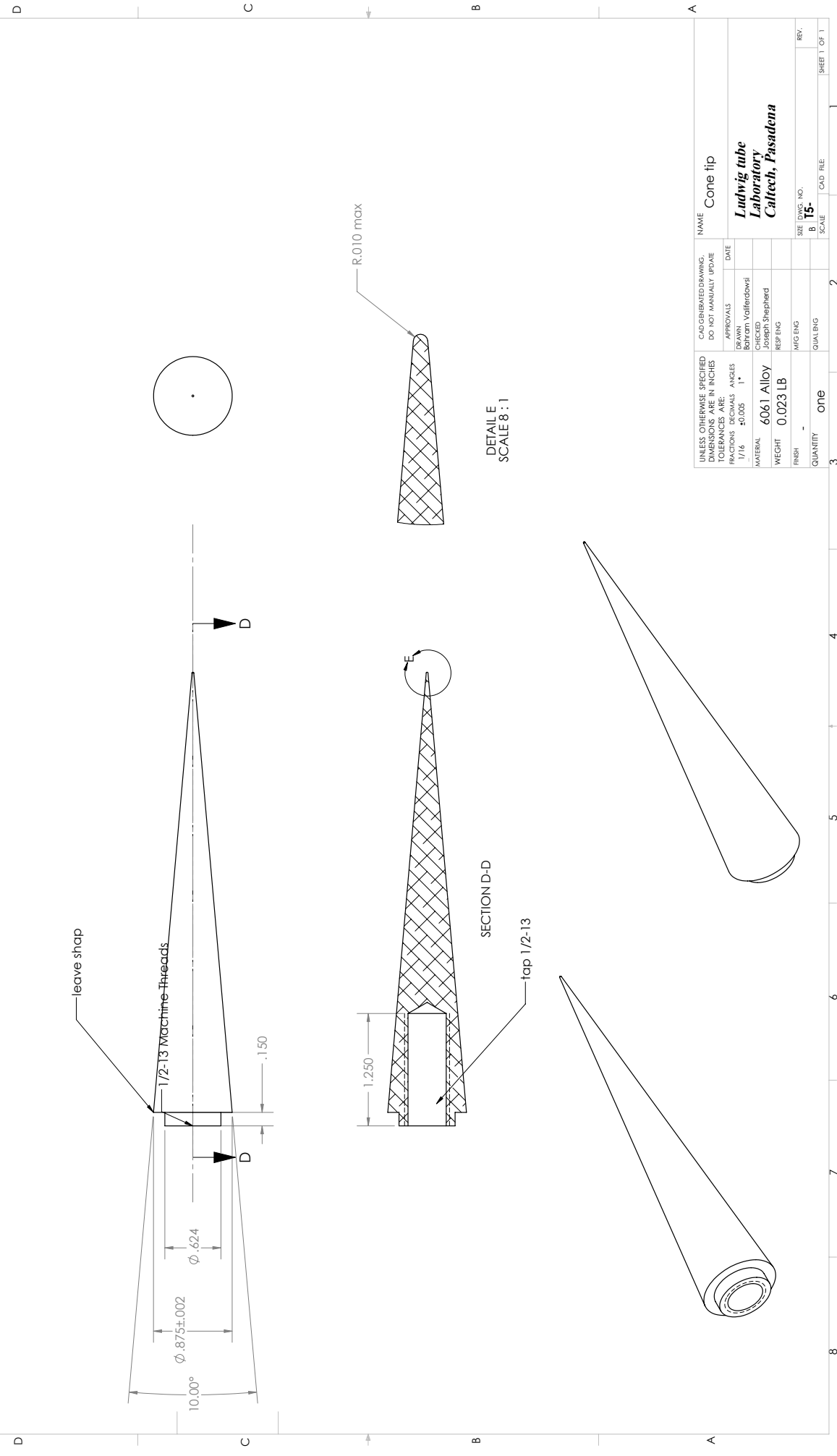
The conclusion of this analysis is that the OpenFOAM solver's handling of diffusion produces systematic errors which introduce some uncertainty into the computations performed for the current study. The uncertainty in simulations of supersonic flow with injection is unknown, but it is anticipated that the errors may be significant in cases with helium and/or RC318 injection.

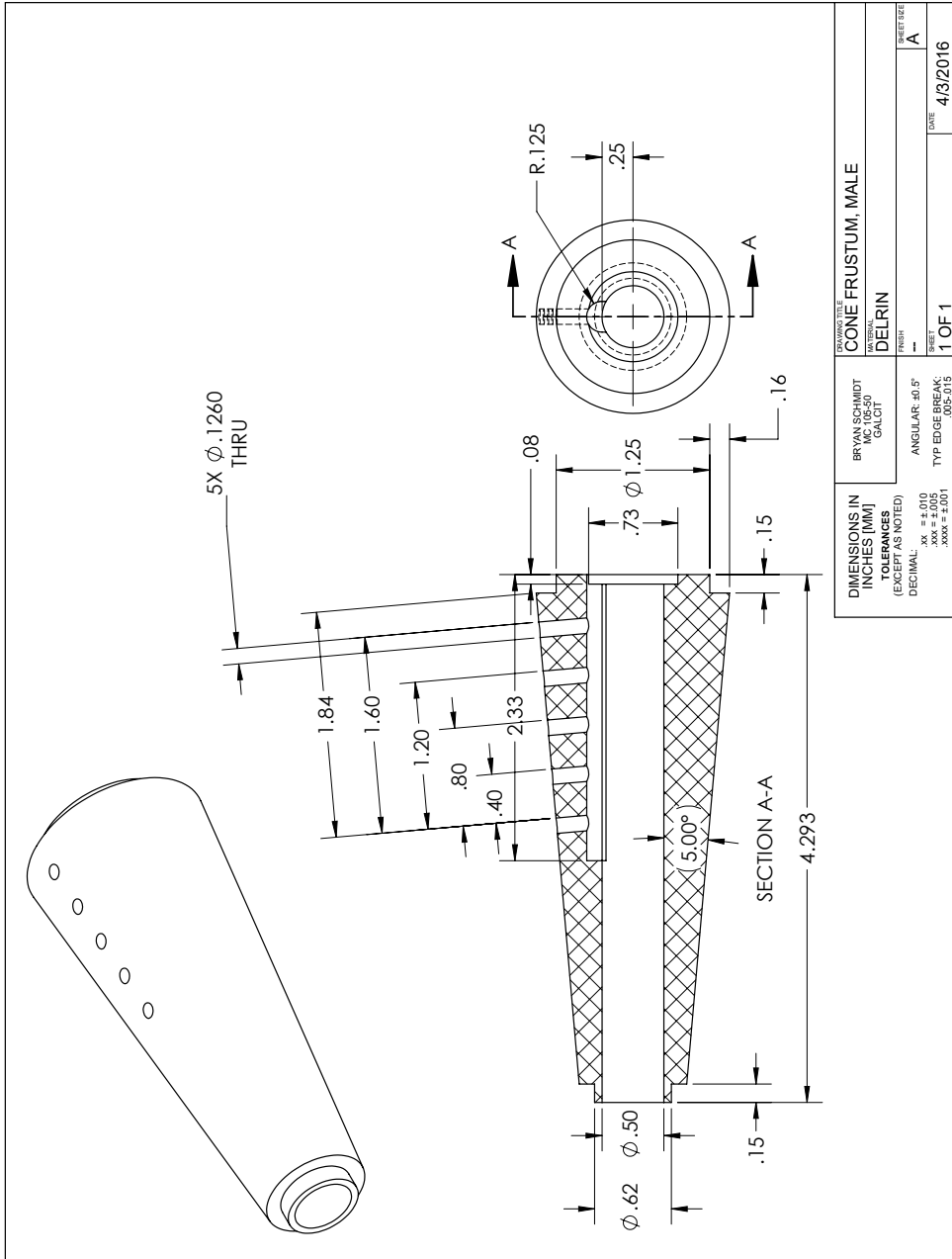
Appendix B

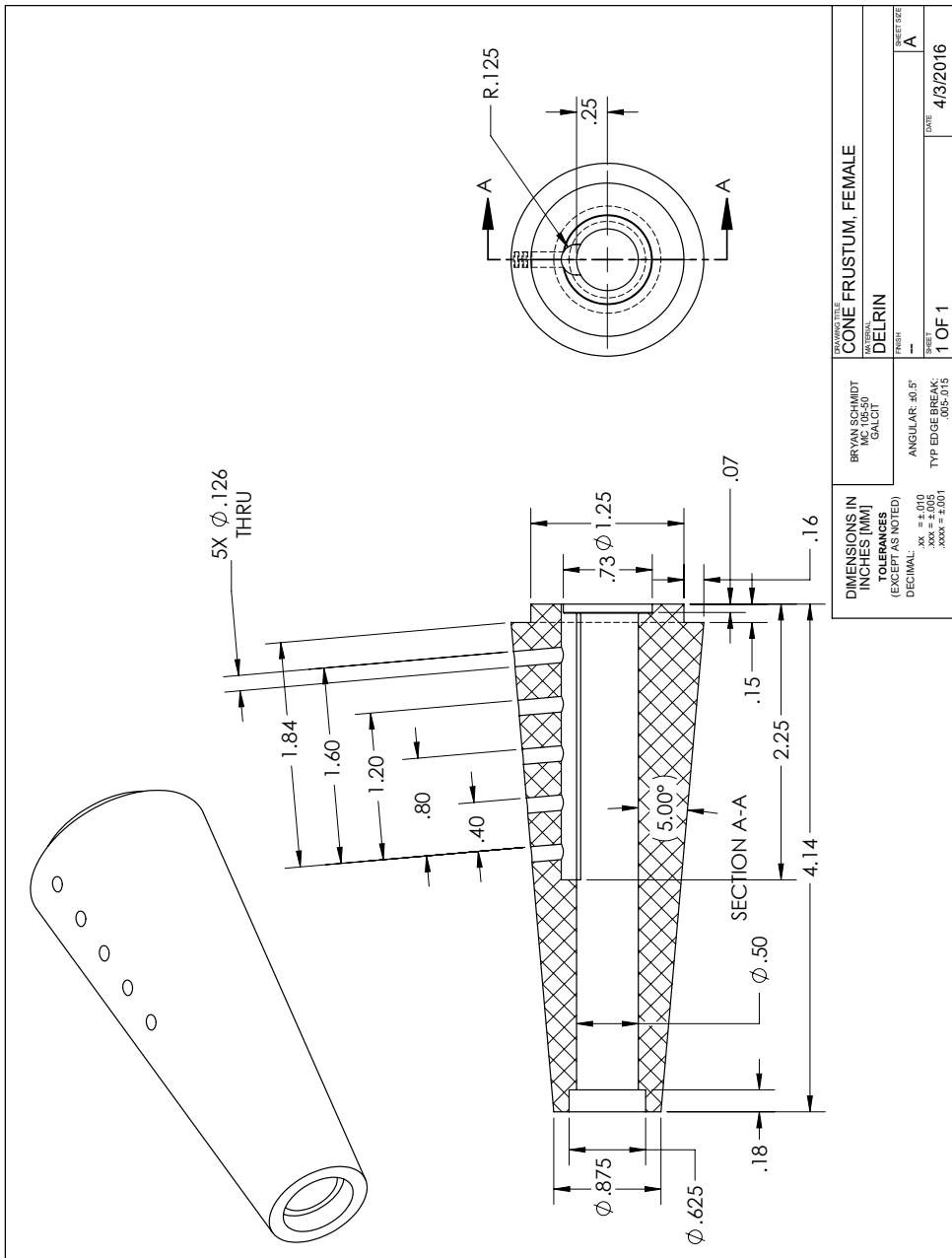
MACHINE DRAWINGS

Test article drawings

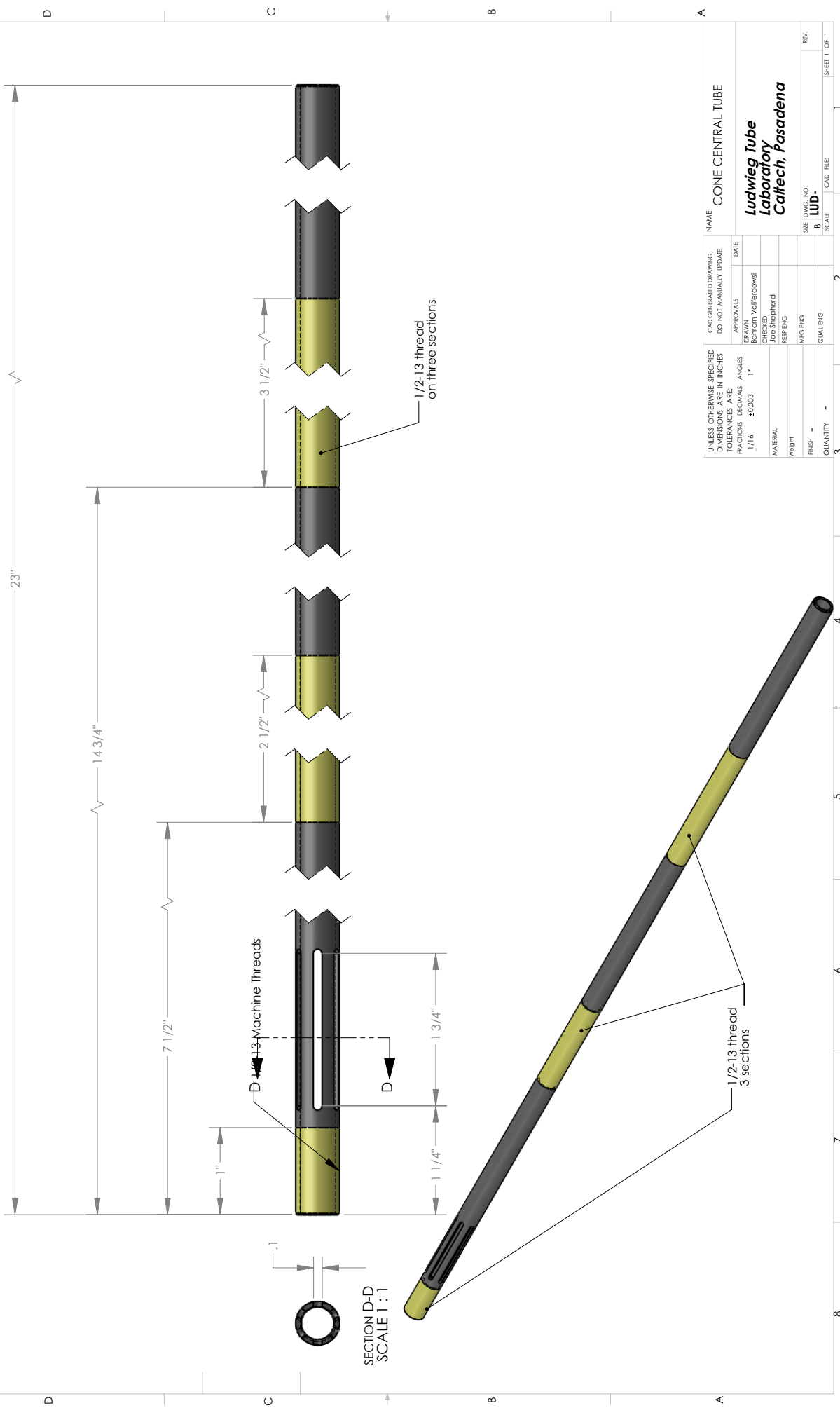
8 7
 THE INFORMATION CONTAINED IN THIS DRAWING IS THE SOLE PROPERTY OF
 <<CALIFORNIA INSTITUTE OF TECHNOLOGY>> AND REPRODUCTION IN PART OR WHOLE, WITHOUT
 THE WRITTEN PERMISSION OF <<BRANIFF AIRLINES COMPANY>>, IS PROHIBITED.

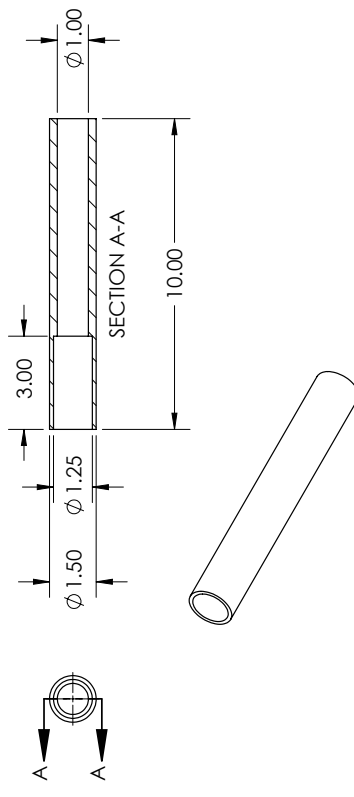




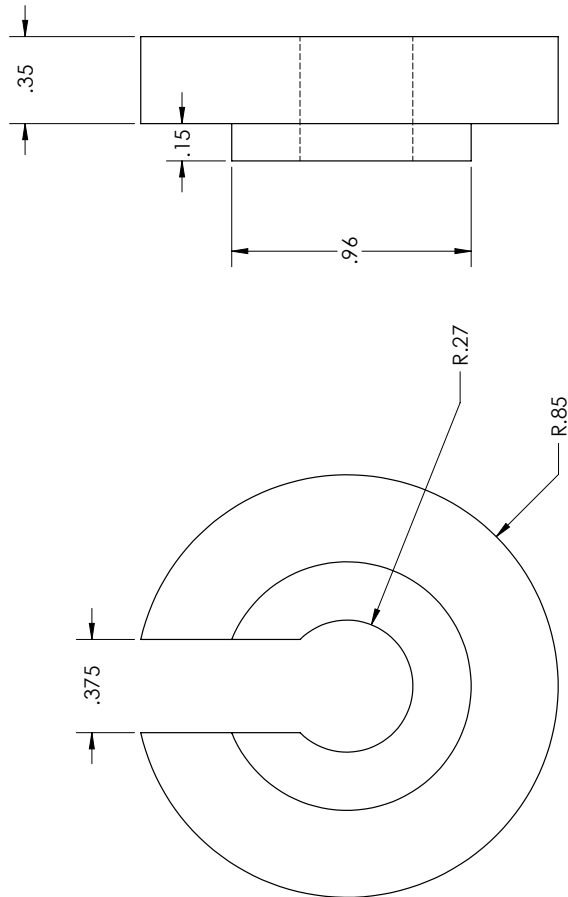


8
7
THE INFORMATION CONTAINED IN THIS DRAWING IS THE SOLE PROPERTY OF
<<CALIFORNIA INSTITUTE OF TECHNOLOGY>> AND REPRODUCTION IN PART OR WHOLE, WITHOUT
THE WRITTEN PERMISSION OF <<BRANSON VALVE CO., INC.>>, IS PROHIBITED.



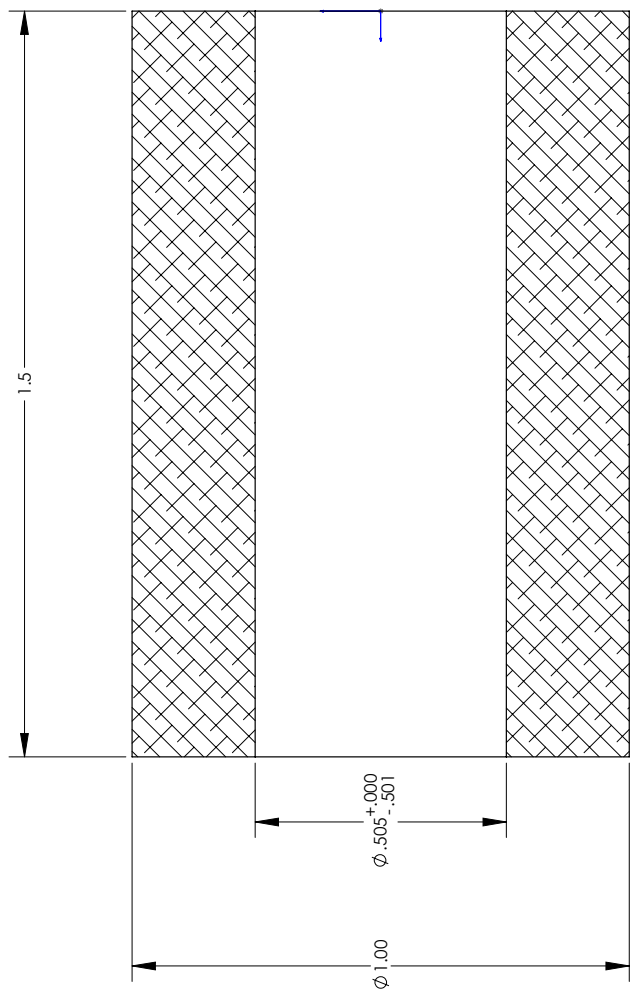


DIMENSIONS IN INCHES [MM]		DRAWING TITLE CONE MOUNTING SLEEVE	
BRYAN SCHMIDT MC10550 GALCIT		MATERIAL: ALUMINUM	SCALE: 1:1
TOLERANCES (EXCEPT AS NOTED)		FINISH:	
DECIMAL: $\pm .010$		ANGULAR: $\pm 40.5^\circ$	
$xxx = \pm .005$		TY6 EDGE BREAK:	
$xxxx = \pm .001$.005-.015	
SHEET 1 OF 1		SHEET 1 OF 1	A
DATE: 4/3/2016		DATE: 4/3/2016	

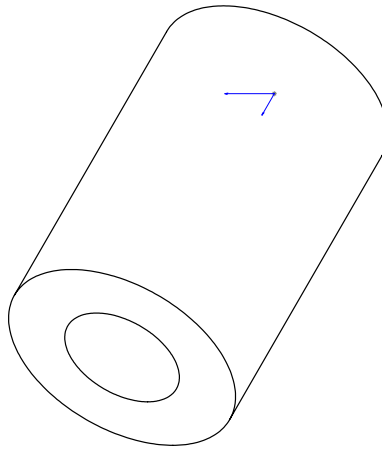


DIMENSIONS IN INCHES [MM]		DRAWING TITLE	
TOLERANCES (EXCEPT AS NOTED)		CONE BACKPLATE	
DECIMAL	ANGULAR: $\pm 40.5^\circ$	UNIVERSAL	3D PRINT PLASTIC
.35	$\pm .010$	FRSH	SHEET SIZE A
.15	$\pm .005$	—	DATE 4/3/2016
.96	$\pm .001$	1 OF 1	.005-.015

8
7
THE INFORMATION CONTAINED IN THIS DRAWING IS THE SOLE PROPERTY OF
<<CALIFORNIA INSTITUTE OF TECHNOLOGY>> AND REPRODUCTION IN PART OR WHOLE, WITHOUT
THE WRITTEN PERMISSION OF <<BRANSON VALVE CO., INC.>>, IS PROHIBITED.



C
C

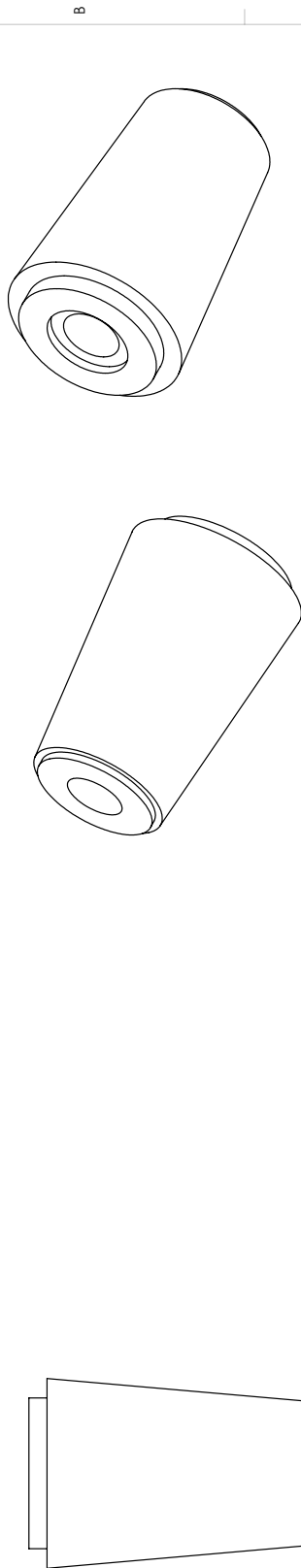
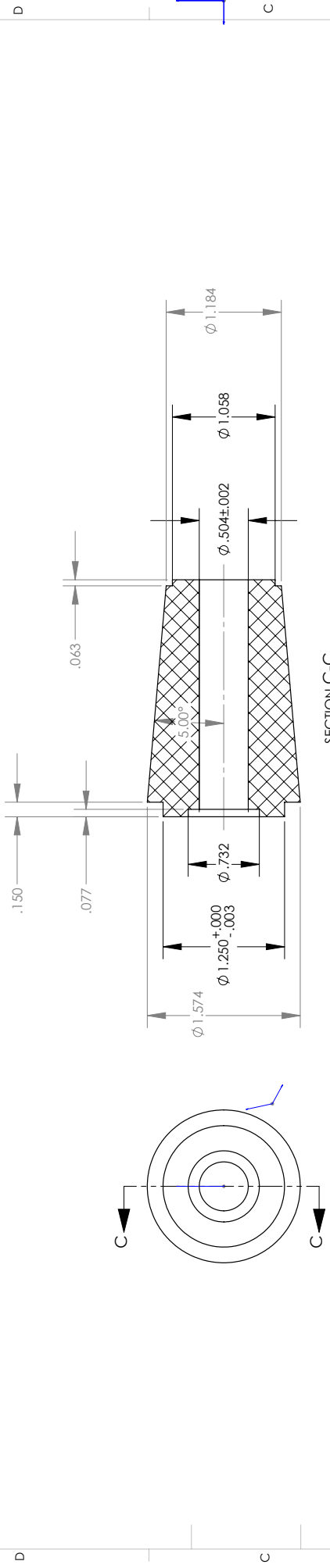


UNLESS OTHERWISE SPECIFIED DIMENSIONS ARE IN INCHES TOLERANCES ARE: FRACTIONS DECIMALS ANGLES		NAME CONIE SPACER
1/16	±0.010	APPROVALS
DRAWN Boyle van Vollenbroek		DR AWN
CHECKED Chris Shepherd		CHCKD
REVIEWED LDS/Shepherd		REV ENG
MFG ENG		MFG ENG
SIZE / DRAWING NO. B	QUANTITY ONE	QUALITY
SCALE	3	C.D. FILE: 2
REV. 1		SHEET 1 OF 1

Ludwig Tube
Laboratory
Caltech, Pasadena

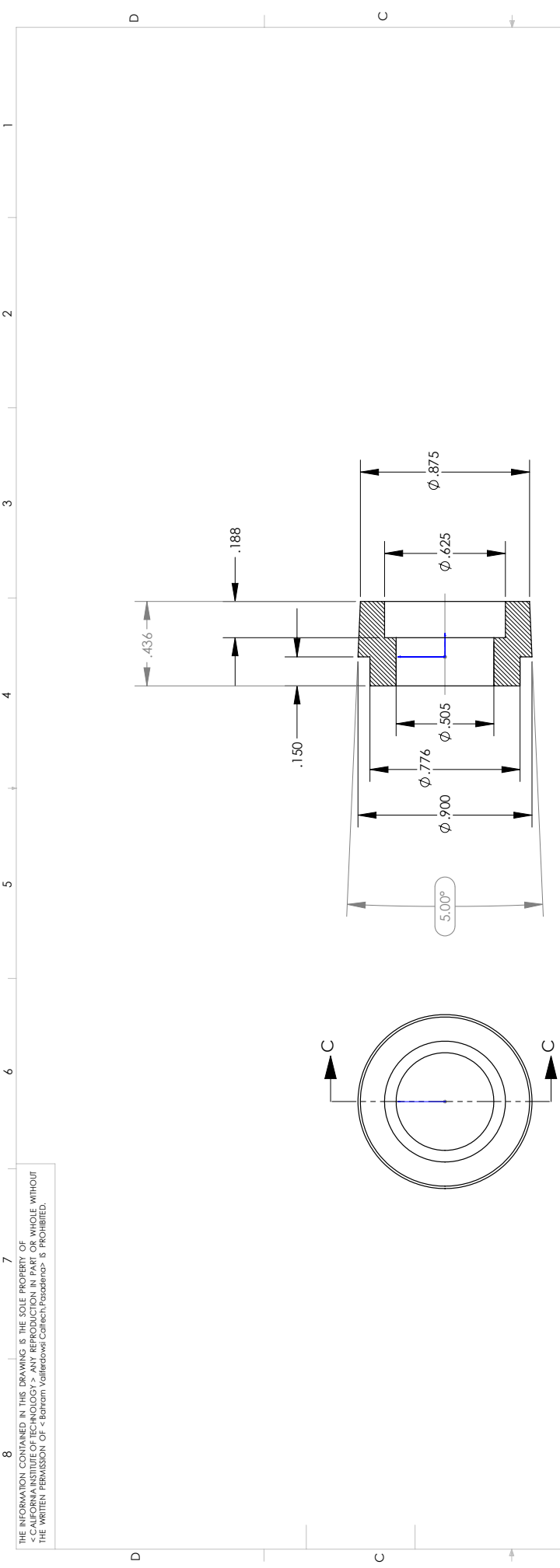
8
7
6
5
4
3
2
1
A

THE INFORMATION CONTAINED IN THIS DRAWING IS THE SOLE PROPERTY OF
<C> INFORIA INSTITUTE OF TECHNOLOGY </C> AND REPRODUCTION IN PART OR WHOLE, WITHOUT
THE WRITTEN PERMISSION OF Baran Vafeagoo
is Prohibited.

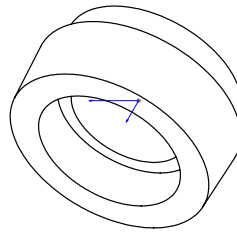


Material: Delrin 2700 NC010, Low Viscosity Acetal Copolymer (SS)	
NAME: CONE FRUSTUM FOR CONICAL INJECTOR	
CAO GENERATED DRAWING. DO NOT MANUALLY UPDATE.	
UNLESS OTHERWISE SPECIFIED, DIMENSIONS ARE IN INCHES. TOLERANCES ARE: FRACTIONS, DECIMALS, ANGLES	
APPROVALS	DATE
DRAWN Baran Vafeagoo	
CHECKED Loyd Shepherd	
REVISED REV ENG	
WEIGHT	
FINISH -	
MFG ENG	
QUALITY -	
SIZE DRAWING NO. B	SCALE
3	2
REV. 1 OF 1	

8 7
 THE INFORMATION CONTAINED IN THIS DRAWING IS THE SOLE PROPERTY OF
 <C> INFORMA INSTITUTE OF TECHNOLOGY & INDUSTRY. REPRODUCTION IN PART OR WHOLE, WITHOUT
 THE WRITTEN PERMISSION OF Baran VafeagooCzechTechS, IS PROHIBITED.

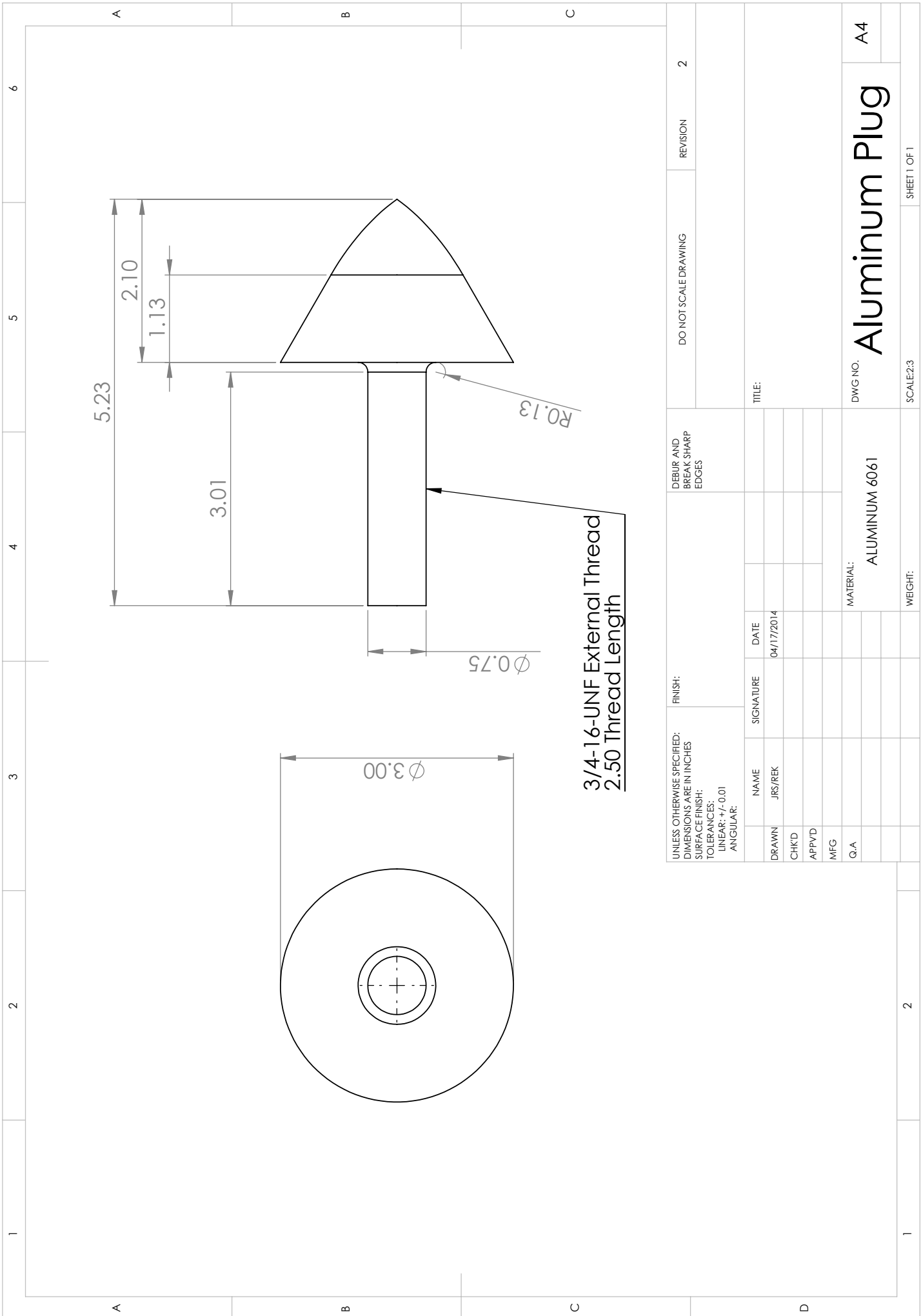


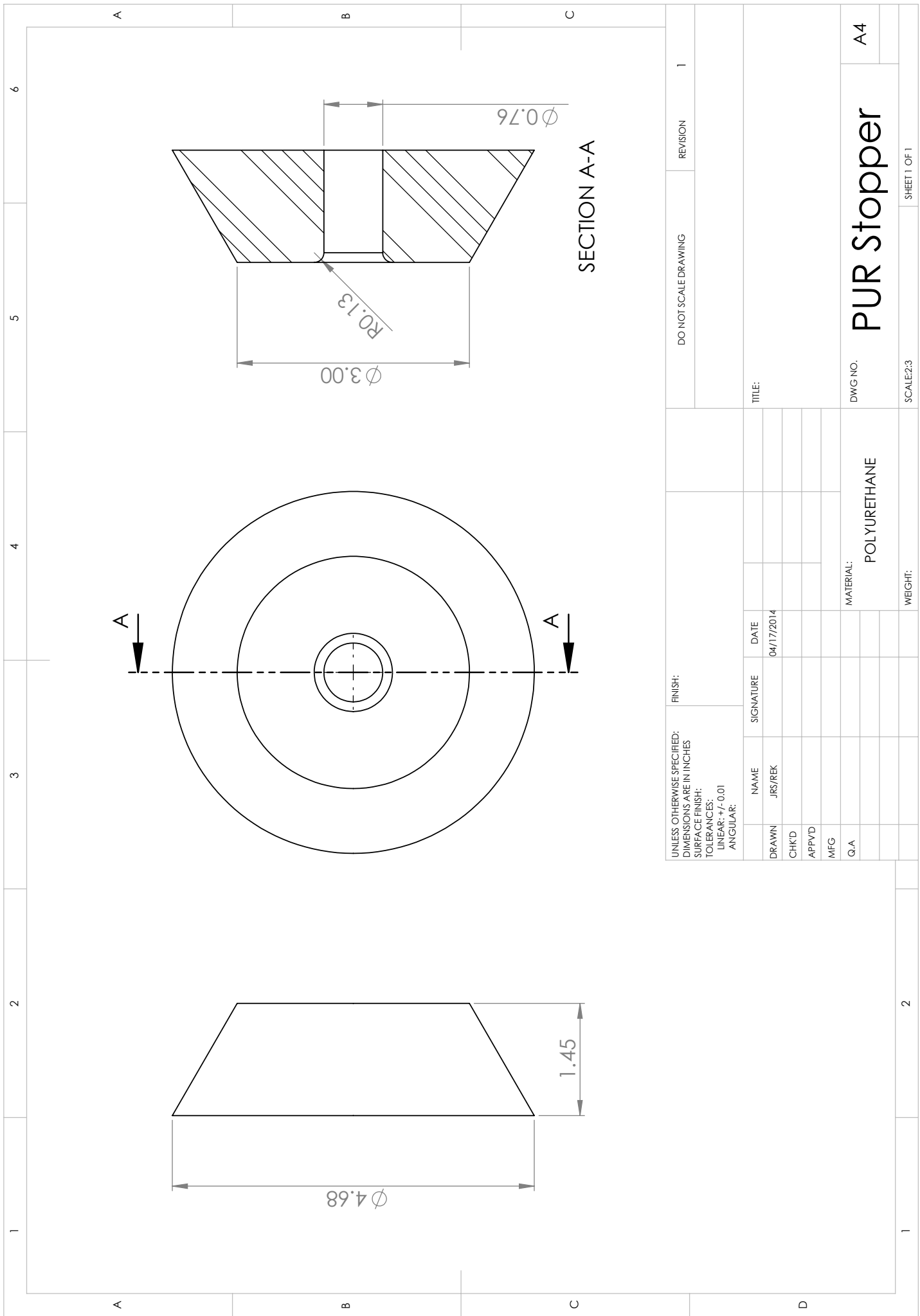
SECTION C-C

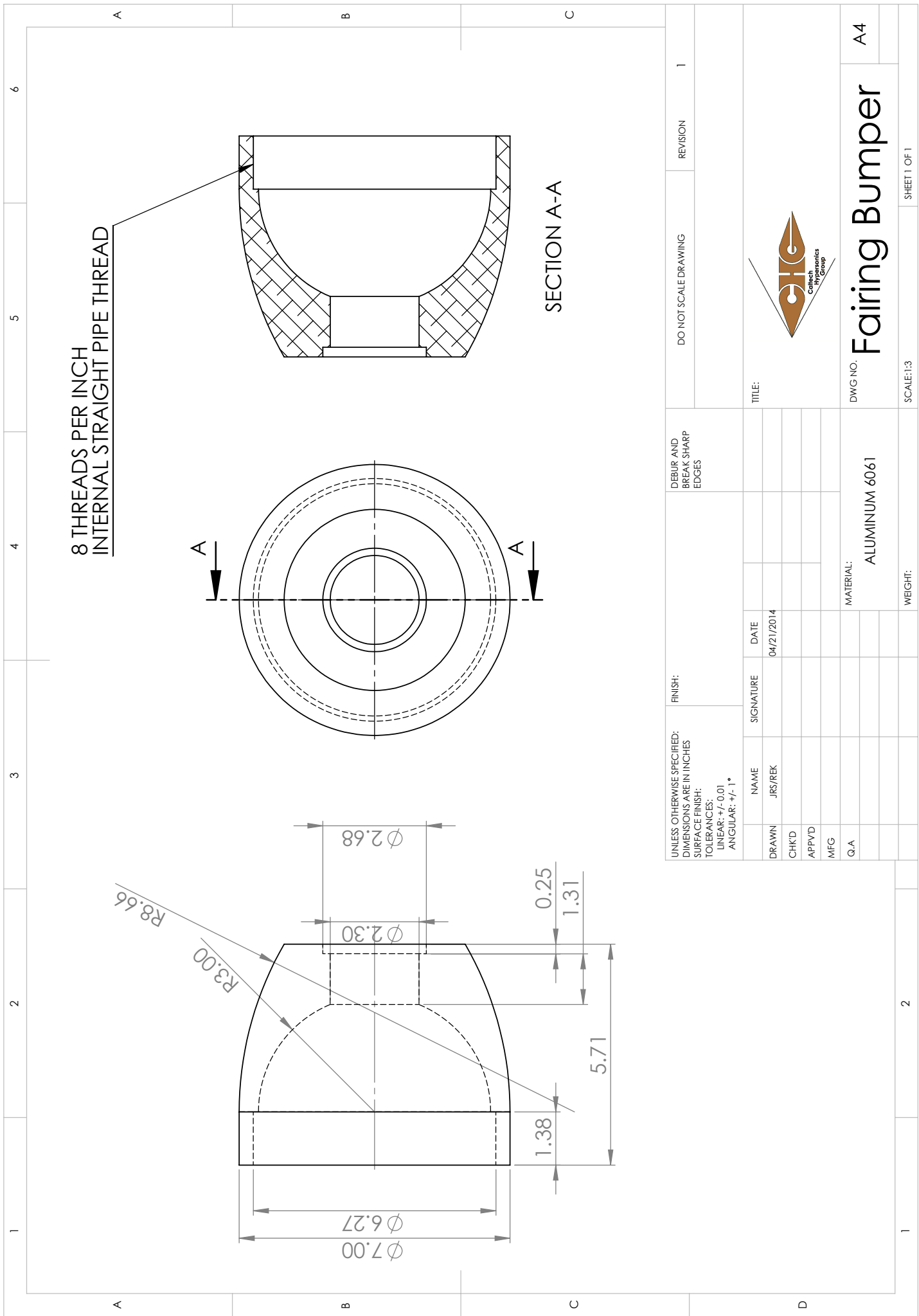


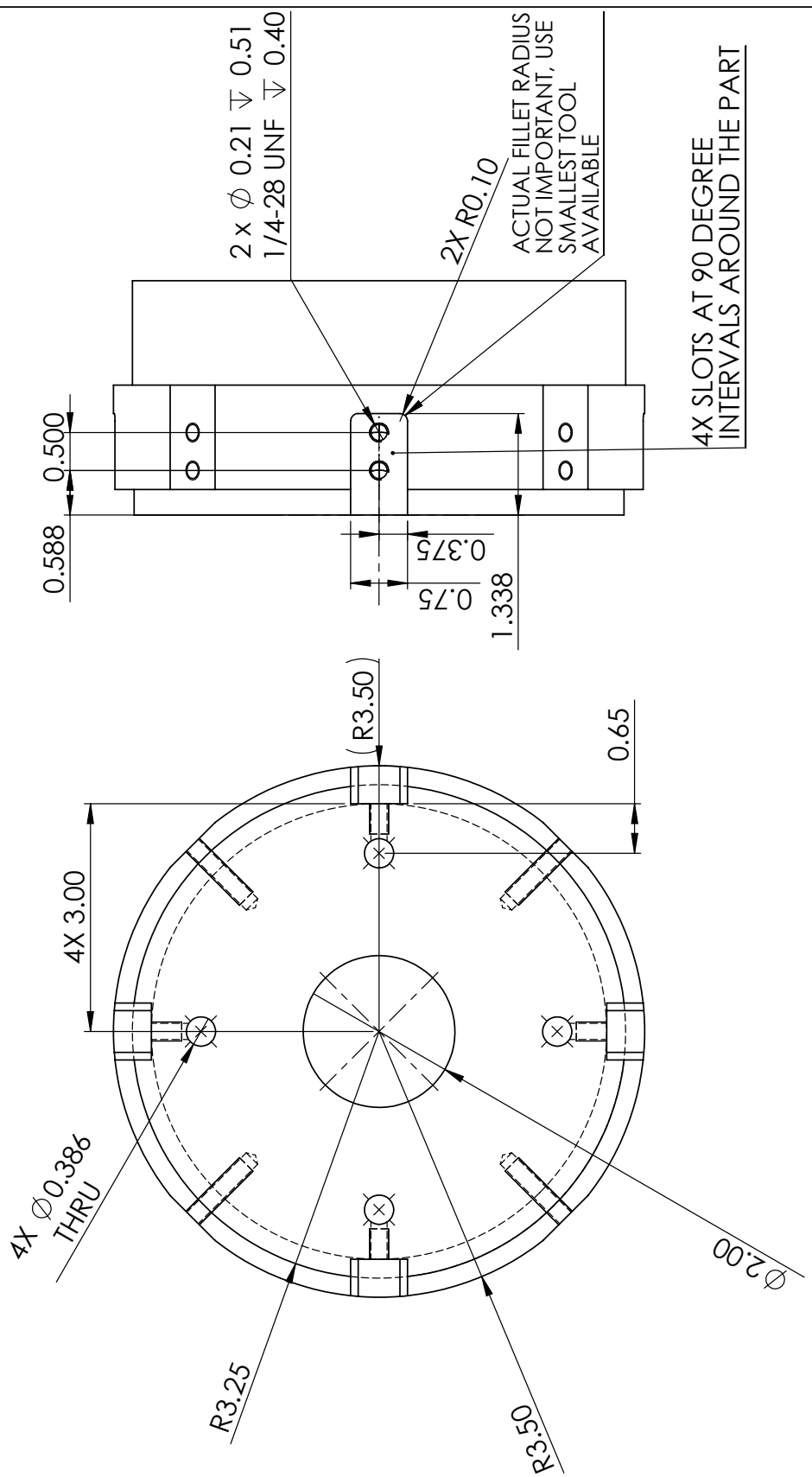
UNLESS OTHERWISE SPECIFIED DIMENSIONS ARE IN INCHES TOLERANCES ARE: FRACTIONS DECIMALS ANGLES		NAME: CONE ADAPTER FOR CONICAL INJECTOR	
1/16 ±0.003		DR AWN	DATE
		Brian Van Vellerdewi	
		Chris Red	
		Los Shepherd	
		REV ENG	
MATERIAL: Delrin		SIZE: DRAWING NO:	REV.
WEIGHT: 0.05 LB		B	SHEET 1 OF 1
FINISH: -		QUALITY: -	
QUANTITY: 3	C.D. F.R.E: 2	SCALE: 2	

Pneumatic valve drawings



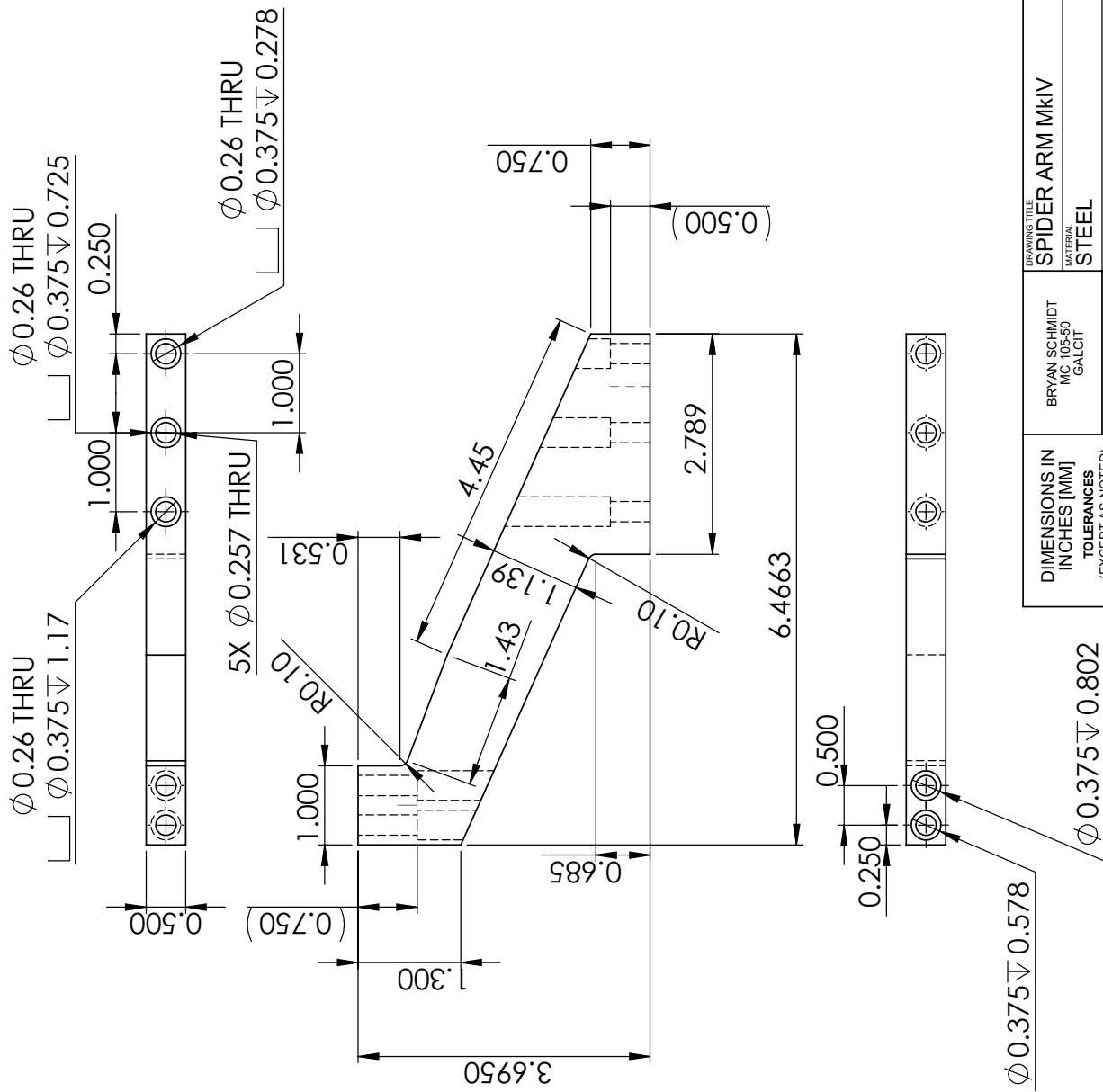




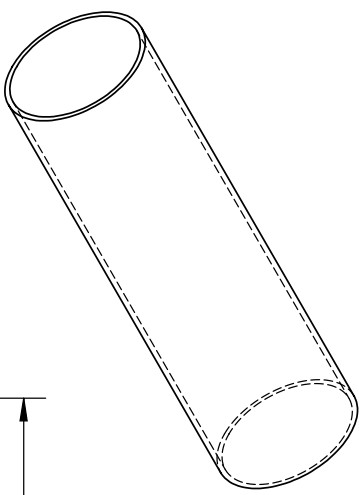
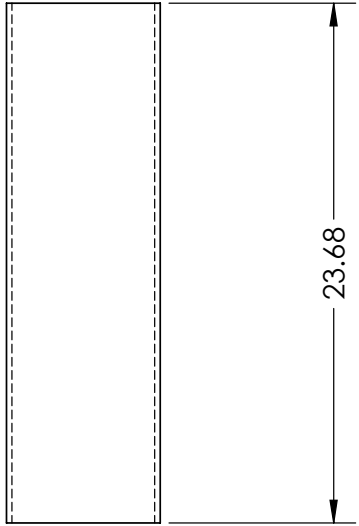
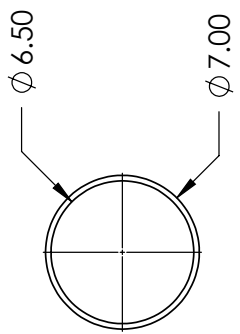


DIMENSIONS IN INCHES [MM]	BRYAN SCHMIDT MC 105-50 GALCIT	DRAWING TITLE FRONT END CAP MKIII
TOLERANCES (EXCEPT AS NOTED)	ALLUMINUM	MATERIAL
DECIMAL: .XX = ± 0.010 .XXX = ± 0.005 .XXXX = $\pm .001$	ANGULAR: $\pm 0.5^\circ$	FINISH
	TYP EDGE BREAK: .005-.015	SHEET SIZE A
		DATE 4/3/2016
	1 OF 1	

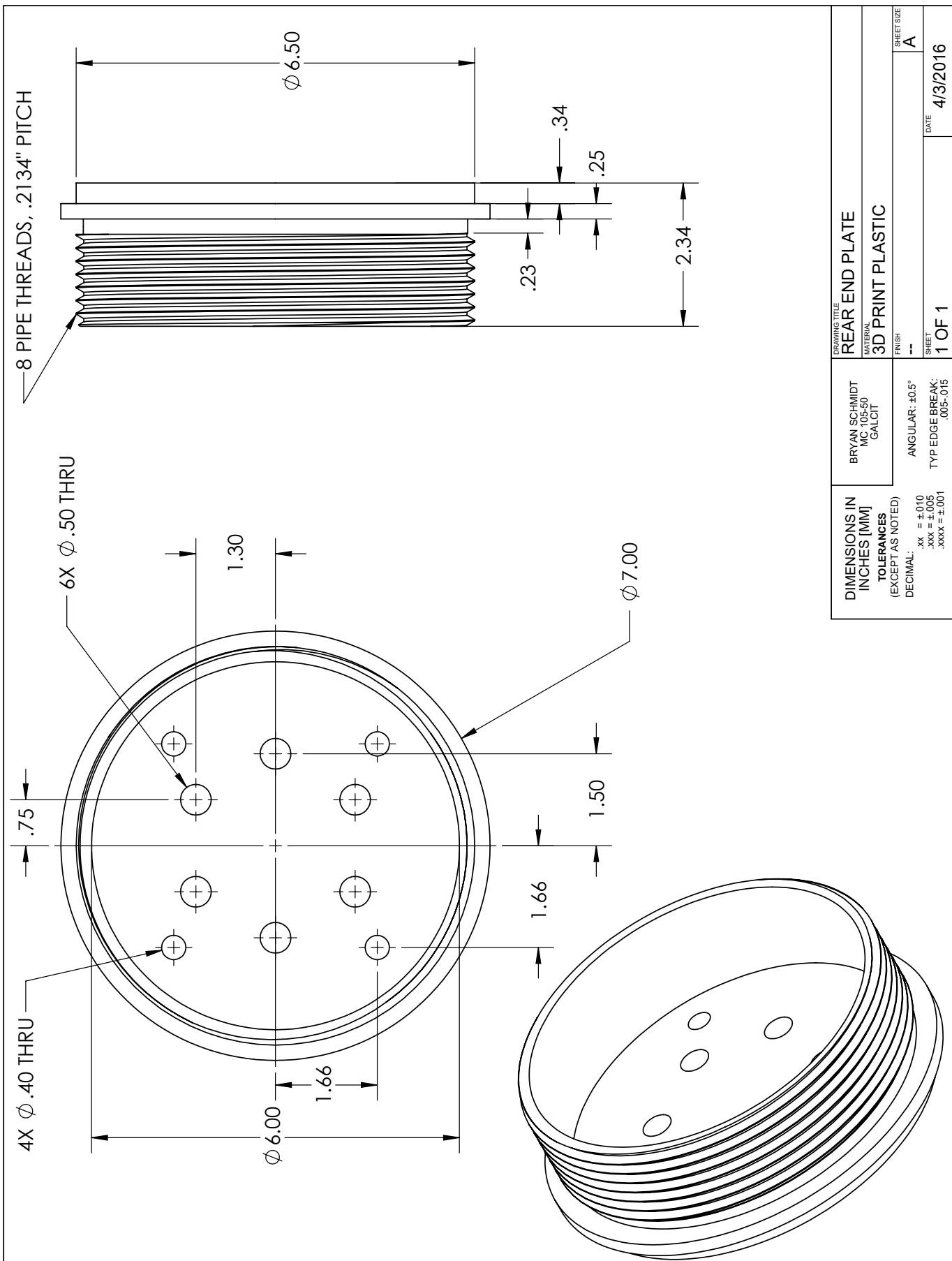
4 REQUIRED

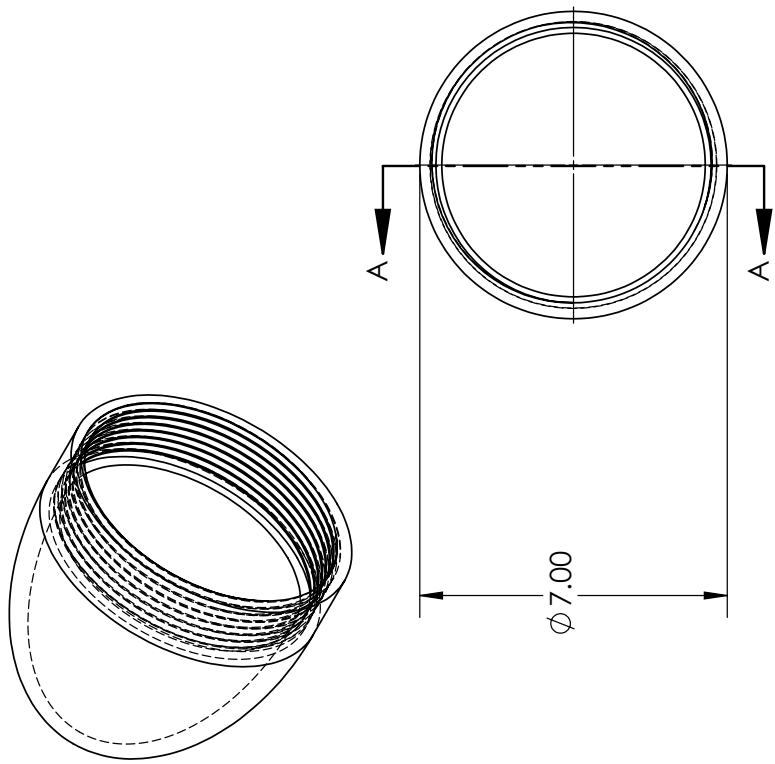


DIMENSIONS IN INCHES [MM]	BRYAN SCHMIDT MC 105-50 GALCIT	DRAWING TITLE SPIDER ARM MkIV
TOLERANCES (EXCEPT AS NOTED)		MATERIAL STEEL
DECIMAL: .XX = ± .010 .XXX = ± .005 .XXXX = ± .001	ANGULAR: ± 0.5°	FINISH
	TYP EDGE BREAK: .005-.015	SHEET SIZE A
		DATE 4/3/2016

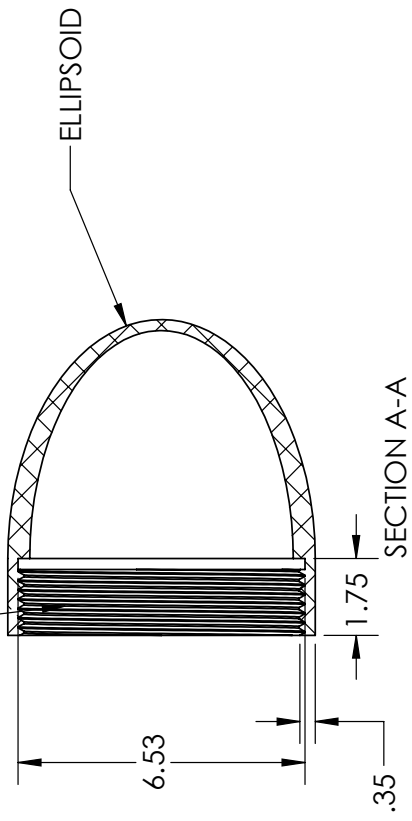


DIMENSIONS IN INCHES [MM]	BRYAN SCHMIDT MC 105-50 GALCIT	DRAWING TITLE PISTON SHROUD
TOLERANCES (EXCEPT AS NOTED)	MATERIAL ACRYLIC	MATERIAL SIZE A
DECIMAL: .XX = ± 0.010 .XXX = ± 0.005 .XXXX = $\pm .001$	ANGULAR: $\pm 0.5^\circ$	FINISH
	TYP EDGE BREAK: .005-.015	SHEET DATE 1 OF 1 4/3/2016



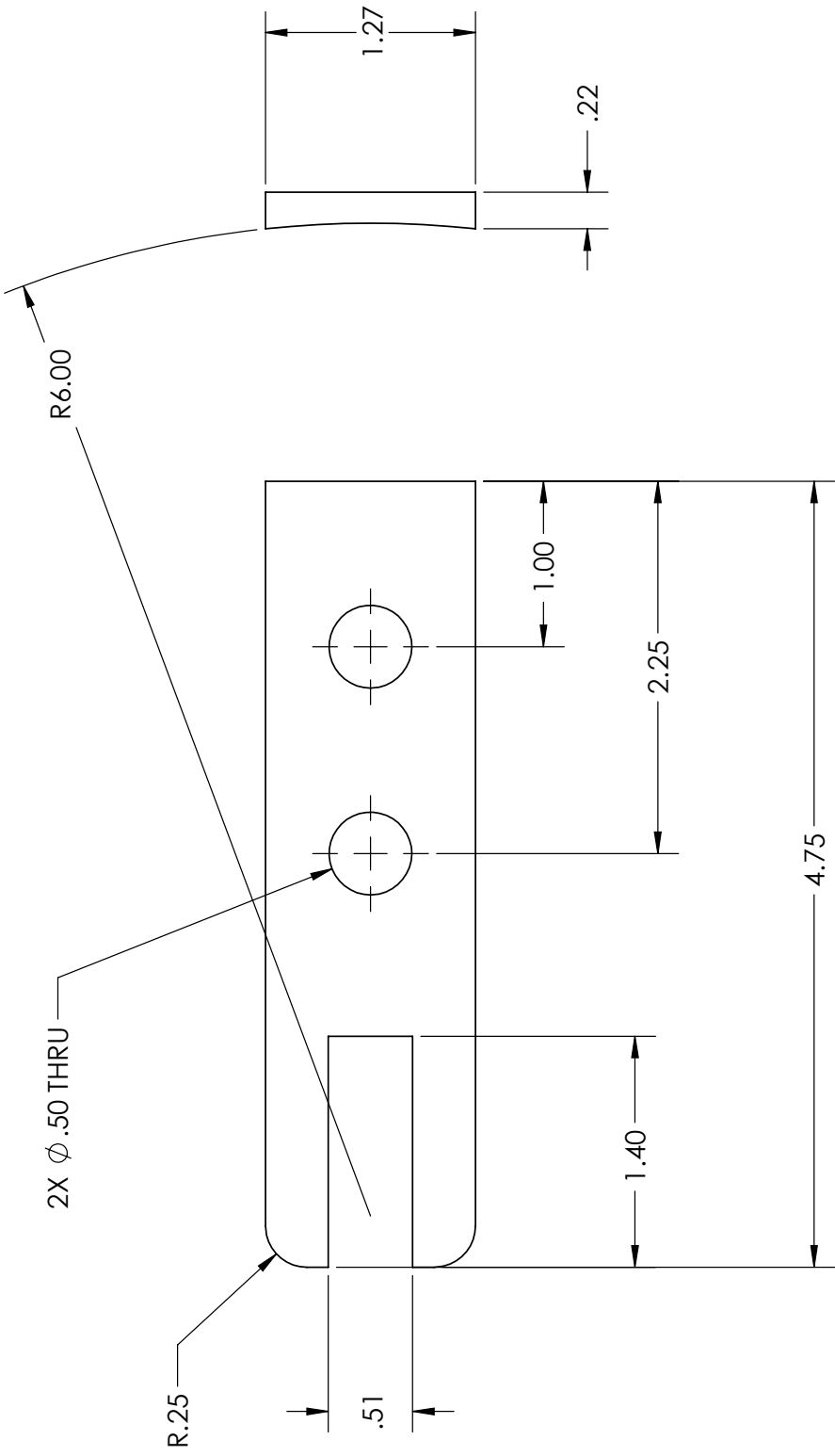


8 PIPE THREADS WITH 0.2134" PITCH
TO MATE WITH REAR END PLATE



DIMENSIONS IN INCHES [MM] TOLERANCES (EXCEPT AS NOTED)	BRYAN SCHMIDT MC 105-50 GALCIT	DRAWING TITLE REAR FAIRING	SHEET SIZE A
		MATERIAL 3D PRINT PLASTIC	
DECIMAL: .XX = ± 0.010 .XXX = ± 0.005 .XXXX = ± .001	ANGULAR: ± 0.5°	FINISH --	
	TYP EDGE BREAK: .005-.015	SHEET 1 OF 1	DATE 4/3/2016

4 REQUIRED



DIMENSIONS IN INCHES [MM]	BRYAN SCHMIDT MC 105-50 GALCIT	DRAWING TITLE FLANGE SLOT COVER
TOLERANCES (EXCEPT AS NOTED)		MATERIAL 3D PRINT PLASTIC
DECIMAL: .XX = ±.010 .XXX = ±.005 .XXXX = ±.001	ANGULAR: ±0.5°	FINISH
		--
		SHEET 1 OF 1
		DATE 4/3/2016

Appendix C

ANALYSIS OF FOCUSED LASER DIFFERENTIAL INTERFEROMETRY

This appendix contains a reproduction of Schmidt and Shepherd (2015a). The full citation is Schmidt, B. E. and J. E. Shepherd (2015). "Analysis of focused laser differential interferometry". In: *Applied Optics* 54.28, pp. 8459-8472.

C.1 Introduction

Focused laser differential interferometry is a promising technique for measuring density disturbances in supersonic and hypersonic flows, particularly in measuring boundary-layer instabilities. Focused laser differential interferometry is a subset of laser differential interferometry, a field with many examples in the literature, e.g. Azzazy et al. (1987), Laderman and Demetriades (1976), and Smeets (1974) and others. Texts that describe the general principles of interferometry and describe several types of interferometers are abundant, e.g. Steel (1967). The focused laser differential interferometer (FLDI) was first described by Smeets (1972) where it was used to measure density fluctuations in wind tunnel flows and turbulent jets in a desktop-type experiment. The technique was limited in its usefulness at that time because of limitations on photodetectors and data acquisition systems as well as the availability of suitable lasers. Parziale revitalized the technique in 2013 Parziale et al. (2013a,b, 2015) to measure instabilities in a hypervelocity boundary layer on a slender body in the T5 hypervelocity tunnel at Caltech and to make measurements of the free stream environment in T5 (Parziale et al., 2014). This paper will develop some general results for the FLDI but will concentrate on the application of measuring second-mode (Mack) waves in hypersonic boundary layers (Mack, 1984).

The FLDI is a very attractive instrument for making such measurements for several reasons. It has high frequency response of greater than 10 MHz, spatial resolution on the order of hundreds of microns in the streamwise direction, and a high signal-to-noise ratio. Additionally, because of the focusing ability of the FLDI, it rejects much of the unwanted signal away from the flow feature of interest near the instrument's best focus. A key advantage then is that for many flows the FLDI is largely immune to large-amplitude density disturbances created by the shear layers of a wind tunnel

with a free jet inside the test section. Preliminary qualitative evidence of this property of the FLDI has been observed in experiments involving translating a small turbulent jet, e.g. Section 3.2.3 of Parziale (2013). The effect was examined in detail by Fulghum in Section 3.10.2 of Fulghum (2014) and is also studied in this paper.

As more researchers use the technique, it is critical to better understand how the FLDI signal is produced and how to properly analyze experimental results to extract meaningful quantitative information about the fluctuating density field in the flow. Fulghum presents a very thorough description of the FLDI technique from an aero-optical point of view and derives system transfer functions for the instrument for a few simple flow geometries (Fulghum, 2014). This paper presents a computational method for simulating the response of the FLDI to arbitrary density fields in order to determine the sensitivity of the instrument to more complicated flows with a special emphasis on measurements in hypersonic boundary layers.

C.2 FLDI Theory

The essential operating principles of the FLDI are presented here; for a more complete explanation the reader is referred to Section 3.6 of the Ph.D. thesis by Fulghum (Fulghum, 2014). The FLDI is a non-imaging shearing interferometer. A sketch of the instrument layout is shown in Figure C.1. The linearly-polarized laser beam is expanded and sheared by a prism by a small angle σ which is placed at the focal point of a converging lens. This fixes the shear distance between the beams to Δx . The two beams have mutually-orthogonal polarization. Wollaston prisms are the most common choice of prism in the literature, but Fulghum demonstrates great success with Sanderson prisms (Sanderson, 2005), where the divergence angle can be adjusted and the aperture can be larger so as not to truncate the expanded beam. Sanderson prisms are also generally less expensive than Wollaston prisms with small divergence angles. The choice of prism does not change the fundamental characteristics of the interferometer (Biss et al., 2008) or impact the analysis presented here. An illustration of the operation of a prism is shown in Figure C.2.

After the prism, the focusing lens brings the beams to a sharp focus. The system is symmetric about the focus so that the beams can be recombined by means of a second polarizer and the interference signal is measured by a change in intensity on a photodetector. Inhomogeneities are spatially filtered by the beams, with a much stronger filtering effect where the beam diameter is large, which makes the

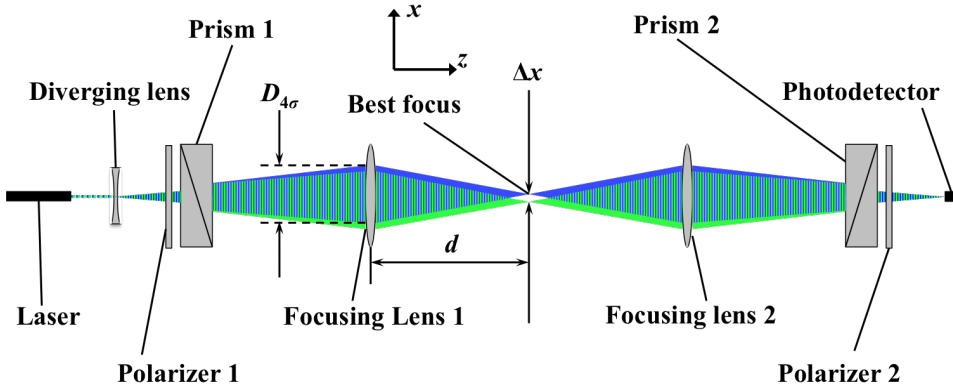


Figure C.1: Schematic of an FLDI setup. The two beams are shown as blue and green. Regions where the beams overlap are shown as striped. The coordinate system shown will be the one used throughout this paper.

instrument most sensitive near the point of best focus and least sensitive close to the focusing lenses on either side of the focus, which in a free-jet wind tunnel would be close to the turbulent shear layers at the edges of the test flow. This spatial filtering effect allows the FLDI to "see through" the strong turbulence at the edges of a wind tunnel flow and measure density fluctuations of much lower intensity in the region of interest in the core of the tunnel.

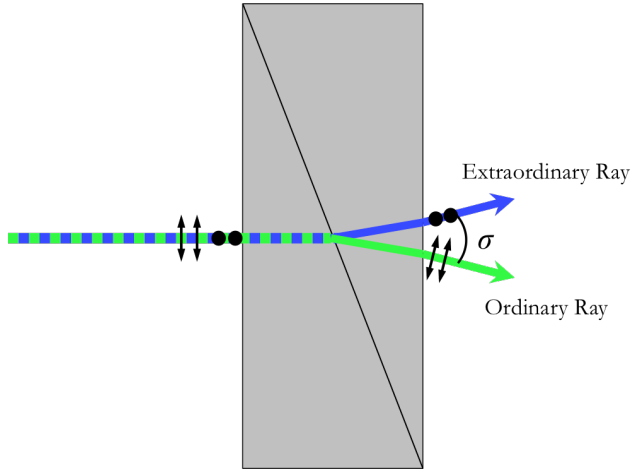


Figure C.2: Illustration of a prism (here, a Wollaston prism). The incident beam of arbitrary polarization is split into two beams by an angle σ , and the two beams at the exit have mutually orthogonal polarization. The ordinary ray is linearly polarized in the direction of beam separation and the extraordinary ray is polarized 90 degrees from the direction of separation.

As an interferometer, the FLDI is sensitive to phase differences between the two beams of the instrument. Equations describing the interference of two superimposed

waves are derived in Section 7.2 of Born and Wolf (1999). The equations in this section follow directly by considering a set of rays that are integrated over a detector. A phase difference is created by a change in the index of refraction of a transparent medium along the paths of two rays according to Equation C.1.

$$\Delta\phi = \frac{2\pi}{\lambda} \left(\int_{s_1}^{D(\xi,\eta)} n(\underline{x}_1) ds_1 - \int_{s_2}^{D(\xi,\eta)} n(\underline{x}_2) ds_2 \right) \quad (\text{C.1})$$

Here n is the index of refraction field through which the rays pass, the vector \underline{x}_i represents the ray path parametrized by s_i , i.e. $\underline{x}_i = (x(s_i), y(s_i), z(s_i))$, $D(\xi, \eta)$ is the point on the detector where beams 1 and 2 terminate, and λ is the wavelength of the laser used. ξ and η are the coordinates on the detector face. Note that both rays terminate at the same point on the detector. Corresponding rays are separated in the test region by Δx in the x -direction, $\underline{x}_1 = \underline{x}_2 + \Delta x \hat{x}$. If the rays are interfered in an infinite fringe configuration, as they are in the FLDI, the intensity of the interfered ray at point (ξ, η) on the photodetector is given by Equation C.2

$$I(\xi, \eta) = I_1(\xi, \eta) + I_2(\xi, \eta) + 2\sqrt{I_1(\xi, \eta)I_2(\xi, \eta)} \cos(\Delta\phi(\xi, \eta)) \quad (\text{C.2})$$

If we assume that the two rays have the same initial intensity, $I_1 = I_2 = \frac{I_0}{2}$, then Equation C.2 simplifies to

$$\frac{I(\xi, \eta)}{I_0(\xi, \eta)} = 1 + \cos(\Delta\phi(\xi, \eta)) \quad (\text{C.3})$$

where $I_0(\xi, \eta)$ is the normalized intensity profile of the beam. In practice we adjust the instrument to the middle of an interference fringe such that there is a constant phase shift of $-\pi/2$ between the two beams so that Equation C.3 can be linearized for $\Delta\phi \ll 1$.

$$\frac{I(\xi, \eta)}{I_0(\xi, \eta)} = 1 + \sin(\Delta\phi(\xi, \eta)) \approx 1 + \Delta\phi(\xi, \eta) \quad (\text{C.4})$$

The signal output by the detector $\Delta\Phi$ is proportional to the integral of Equation C.4 over the detector face D which gives the total weighted average phase change $\Delta\Phi$:

$$\Delta\Phi = \iint_D (I(\xi, \eta) - I_0(\xi, \eta)) d\xi d\eta = \iint_D I_0(\xi, \eta) \Delta\phi(\xi, \eta) d\xi d\eta \quad (\text{C.5})$$

Or, substituting Equation C.1

$$\begin{aligned}\Delta\Phi &= \iint_D (I(\xi, \eta) - I_0(\xi, \eta)) d\xi d\eta \\ &= \frac{2\pi}{\lambda} \iint_D I_0(\xi, \eta) \left(\int_{s_1}^{D(\xi, \eta)} n(\underline{x}_1) ds_1 - \int_{s_2}^{D(\xi, \eta)} n(\underline{x}_2) ds_2 \right) d\xi d\eta\end{aligned}\quad (\text{C.6})$$

Finally, the index of refraction n in a gas is related to the density of the gas by the Gladstone-Dale relation:

$$n = K\rho + 1 \quad (\text{C.7})$$

This allows the output of the FLDI to be related to the density field of the gas being probed.

The photodetector converts the total intensity to a voltage. Large phase changes ($\Delta\Phi > \pi/2$) causes phase ambiguity to occur, as the interference wraps over several periods of light waves. Therefore it is best to keep the phase change small enough such that the sine function can be linearized. For the FLDI, it is most useful to interpret the output not as a phase change $\Delta\Phi$ between the two closely-spaced beams, but rather as a finite-difference approximation to the first derivative of the phase change, $\Delta\Phi/\Delta x$. For small values of Δx , this approximates the first derivative of phase change in the direction of beam separation. Smaller values of Δx result in more accurate approximations of the derivative and therefore increased frequency response, but smaller beam separations result in lower signal magnitudes overall, which becomes an issue in practice as the electronic noise floor is approached.

The first prism (Prism 1 in Figure C.1) not only splits the light beams, but the two beams exit the prism polarized orthogonally to one another. Therefore in order to compute the response of the instrument at the photodetector after the beams have been recombined, it is necessary to consider the state of polarization of the light along the beam paths and perform an analysis like the one in Section 3.6.1 of Fulghum (2014). However, if the light is polarized at 45 degrees relative to the separation angle of the prism before entering the first prism, the equations governing the polarization state simplify considerably, as each beam leaving the prism will have equal amplitude and the beams can be recombined and mixed on the detector

side without explicitly using Jones vectors to combine the electric fields as long as the polarization is not rotated by the optical system. This is the configuration used by Parziale (Parziale, 2013).

C.3 Computational Method

As analytically determining the response of the FLDI instrument for a given density field is extremely difficult for all but the simplest flow geometries, a computational model of the FLDI is developed to numerically evaluate Equation C.6 for a given arbitrary density field that can vary in space and time and simulate the FLDI output. The software described in this section is referred to as the FLDI software throughout this paper. The software replicates the FLDI configuration used at Caltech (Parziale et al., 2013a) but can be modified to suit the dimensions of any FLDI setup. Dimensions are given in Table C.1. The general procedure followed by the software is to first compute the region traversed by the FLDI beams and then to discretize the domain as described in this section. Finally, the integral in Equation C.6 is evaluated numerically along the beam paths.

Divergence angle of prisms (σ)	2 arc minutes
$1/e^2$ beam diameter at focusing lens ($D_{4\sigma}$)	48 mm
Focal length of focusing lenses (f)	300 mm
Distance from focusing lens to focus (d)	515 mm
Laser wavelength (λ)	532 nm

Table C.1: Optical parameters for simulated FLDI.

The beams are assumed to have equal Gaussian intensity distributions $I_0(\xi, \eta)$ and the beams are assumed to propagate according to Gaussian beam propagation. Assuming Gaussian propagation means that the angle of paraxial rays and higher-order terms can be neglected from the full electromagnetic wave propagation equations. This is a good approximation as long as all the rays form a sufficiently small angle with the primary beam axis such that the small-angle approximation can be invoked. The validity of this assumption is examined later in this section. For a more detailed discussion of the approximations involved in assuming Gaussian beam propagation, see Chapter 4 of Born and Wolf (1999).

The beam separation Δx is calculated by simple trigonometry to be

$$\Delta x = 2f \tan \frac{\sigma}{2} = 174.5 \mu\text{m} \quad (\text{C.8})$$

This calculation is confirmed to be accurate by photographing the beams of the physical FLDI setup at Caltech near the best focus with a CCD camera and neutral density filters to prevent saturation.

Equations C.9-C.11 can be found in Section 14.5 of Milonni and Eberly (1988). The beam waist radius at best focus w_0 is computed for Gaussian beams using Equation C.9, which is found by substitution for the divergence angle of a Gaussian beam.

$$w_0 \approx \frac{\lambda}{\pi \theta_d} \approx \frac{2\lambda d}{\pi D_{4\sigma}} \quad (\text{C.9})$$

For a diffraction-limited beam, this corresponds to a spot size of about 7 μm . The $1/e^2$ radius of the beam as a function of z , the coordinate along the beam path, is given by Equation C.10 where $z = 0$ at the beam waist.

$$w(z) = \sqrt{w_0^2 \left(1 + \left[\frac{\lambda z}{\pi w_0^2} \right]^2 \right)} \quad (\text{C.10})$$

Figure C.3 shows computed beam widths near the best focus of the FLDI. For simplicity when calculating the beam profile, polar-cylindrical coordinates are used with \hat{r} and $\hat{\theta}$ orthogonal to \hat{z} and $r^2 = x^2 + y^2$. The normalized beam intensity cross-section at a point in z is then:

$$I_0(r) = \frac{2}{w^2(z)\pi} \exp\left(\frac{-2r^2}{w^2(z)}\right) \quad (\text{C.11})$$

The computational domain encompassing the beams between the focusing lenses is discretized into a uniform grid of 10300 points along the beam paths, corresponding to a dimensional step size of 100 μm which is found to be sufficient that the computation is not affected by the step size. Convergence is shown below in Section

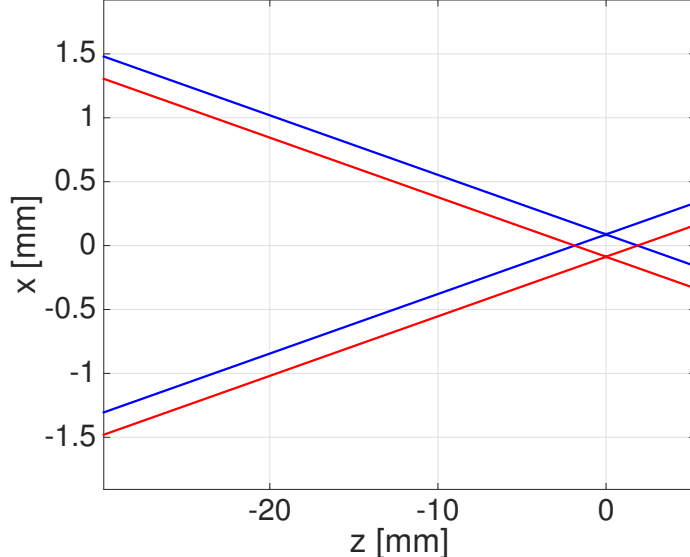


Figure C.3: Computed beam widths (out to $1/e^2$) within 30 mm of the best focus. One beam is outlined in red and the other in blue. The width of the beams at the waist is too small to see on this scale.

C.4. The beam cross-section is divided into a polar grid with r non-dimensionalized by $w(z)$, the local $1/e^2$ beam radius. Therefore each point (r_0, θ_0) on the polar grid at a point z_1 is on the same ray as the point (r_0, θ_0) at any other location in z . In this way the software can be considered to be performing geometric ray-tracing, except the eikonal equation is not used to evaluate ray deflections due to the density field. Density perturbations are approximated as small enough (in magnitude and in extent along the ray path) that they only cause a change to the phase of each individual ray but do not cause the rays to refract significantly. The beam profiles and rays are calculated assuming a zero-disturbance field first, and then the total change in phase of the beams are calculated using an input density field. Alternatively the method can be thought of as computing a pixel-wise phase change for each beam on the face of the detector where each grid point at a cross-section in z is a pixel. Such a method is shown to produce accurate results compared to the parabolic beam method developed by White and the Rayleigh-Sommerfeld equation as long as the beam is not analyzed close to an aperture (M. D. White, 2010). Because the polar grid is normalized by the local beam radius, integration occurs along each individual ray path instead of along the z -axis.

The polar cross-section grid extends to $r/w = \bar{r} = 2$, which contains 99.99% of the beam energy. We can now consider if assuming Gaussian beam propagation is accurate. The maximum angle formed by a beam in the domain will be the angle

formed by a beam at the outer edge of the grid. Using Equations C.9 and C.10 and Table C.1, the maximum ray angle is calculated to be 5.32° or 92.9 mrad. The small-angle approximation for this angle gives an error of 0.14%, hence assuming Gaussian beam propagation is clearly justified. The grid has 300 equally-spaced points in the $\hat{\theta}$ -direction, and grid points are chosen in the \hat{r} -direction such that each cell has an aspect ratio as close to 1 as possible. Points are computed starting at $\bar{r} = 2$ inward to a specified limiting radius \bar{r}_0 , which is chosen to be 0.001, resulting in 363 points in \hat{r} . Each point is computed using the previous point according to

$$\bar{r}_k = \bar{r}_{k-1} \left(\frac{2 - \delta\theta}{2 + \delta\theta} \right) \quad (\text{C.12})$$

where $\delta\theta$ is the step size in the $\hat{\theta}$ -direction. The grid also contains one point in the center at $\bar{r} = 0$, bringing the total number of points at each cross-sectional grid to 108901. The grid is shown in Figure C.4. The resolution was determined by limiting the error of numerically integrating a Gaussian using the trapezoidal rule on the grid to less than 1%.

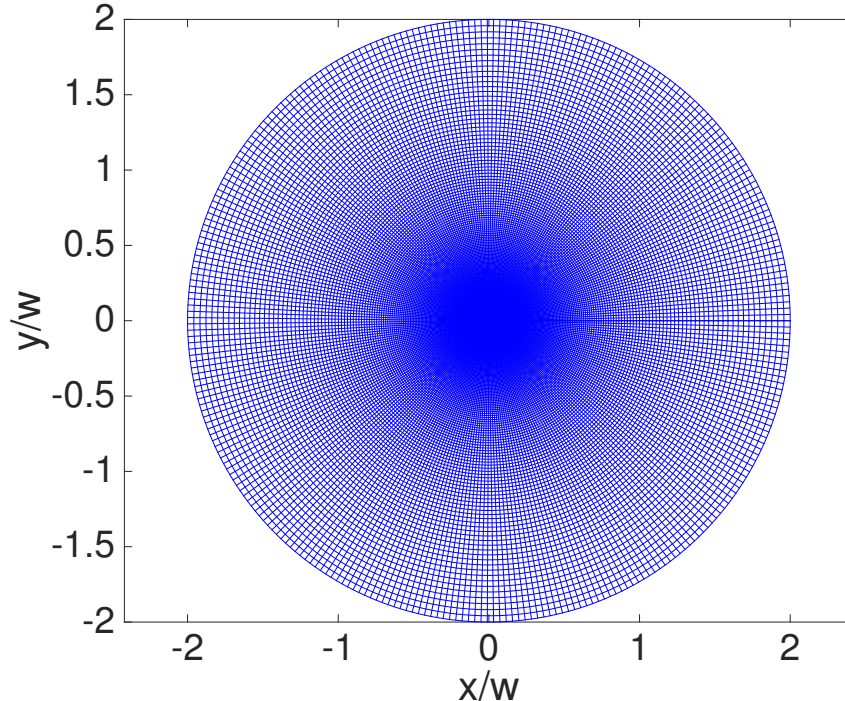


Figure C.4: Polar grid cross-section non-dimensionalized by the local beam waist size

The simulated FLDI response to an input density field $\rho(x, y, z)$ is computed by numerically evaluating Equation C.6. The integral in z is calculated using Simpson's Rule and the 2-D integral over the face of the beam is calculated using trapezoidal integration.

C.4 Software Verification

System Transfer Functions

It is possible to analytically derive an overall system transfer function H as a function of wavenumber for simple density disturbance fields. This is performed in detail in Fulghum (2014), the essence of which is summarized in this paper. Here H is defined as the ratio of the output of the instrument to the actual first derivative of the phase field as shown in Equation C.13.

$$H \equiv \frac{\left(\frac{\Delta\Phi}{\Delta x}\right)_{\text{meas.}}}{\frac{d\Phi}{dx}} \quad (\text{C.13})$$

H for the FLDI is the convolution of two filters, one resulting from the finite beam separation approximating a derivative, and the other resulting from the Gaussian intensity distribution of the beams. In wavenumber (k) domain, these filters are simply multiplied together to give the overall $H(k)$ for the system. Here k is the wavenumber of the density disturbance field, not the wavenumber of the laser. In general, $H(k)$ will be different for every density field geometry in (x, y, z) -space. One simple field geometry that can be analyzed analytically is a sinusoidal disturbance in x that is uniform in y and infinitesimally-thin in z at $z = 0$, i.e. $n' = A \sin(kx)\delta(z)$ where A is some arbitrary disturbance amplitude and δ is the Dirac delta function. The transfer function from the Gaussian intensity distribution of the beam $H_w(k)$ can be derived from Equations C.6, C.11, and C.13. We consider a detector over all space with the detector coordinates ξ and η aligned with Cartesian

coordinates x and y and take the limit as the beam separation Δx approaches zero.

$$\begin{aligned}
 H_w(k) &= \frac{1}{\frac{d}{dx} [\sin(kx)]_{x=0}} \lim_{\Delta x \rightarrow 0} \left[\frac{1}{\Delta x} \iint_{-\infty}^{\infty} I_0(x, y) \right. \\
 &\quad \left(\int_{s_1}^{D(x,y)} \sin(kx)\delta(z) ds_1 - \int_{s_2}^{D(x,y)} \sin(kx)\delta(z) ds_2 \right) dx dy \Big] \\
 &= \frac{1}{\frac{d}{dx} [\sin(kx)]_{x=0}} \iint_{-\infty}^{\infty} I_0(x, y) \frac{d}{dx} [\sin(kx)] dx dy \tag{C.14} \\
 &= \frac{1}{k} \iint_{-\infty}^{\infty} \frac{2}{w^2 \pi} \exp\left(\frac{-2(x^2 + y^2)}{w^2}\right) k \cos(kx) dx dy \\
 &= \exp\left(-\frac{w^2 k^2}{8}\right)
 \end{aligned}$$

At $z = 0$ this is simply

$$H_{w,0}(k) = \exp\left(-\frac{w_0^2 k^2}{8}\right) \tag{C.15}$$

Equation C.14 reveals how the FLDI rejects unwanted signal away from the best focus. The FLDI rapidly attenuates disturbances with wavelengths sufficiently smaller than the local beam diameter where the product of w and k is large. w is approximately linear in z away from the best focus so a disturbance with a given wavenumber is attenuated with Gaussian decay as it moves away from the focus.

The FLDI software can compute the response for a single beam probing $k \cos(kx)$ at a beam cross-section at $z = 0$ over relevant wavenumbers for disturbances in supersonic and hypersonic flows, and this is compared with the analytical result of Equation C.15 in Figure C.5. The computed response curve is nearly identical to the analytical result. The response curve is flat with a value of 1 for low wavenumbers (long wavelength) with a sharp exponential rolloff beginning at about $k = 100/mm$, which is a disturbance wavelength of $63 \mu m$, much smaller than most relevant waves in supersonic flows. From Equation C.14 it is apparent that the rolloff point occurs at lower wavenumbers for larger beam diameter, i.e. further from best focus. This is what makes the FLDI immune to density disturbances away from the focus, such as the turbulent shear layers at the edges of a free-jet supersonic wind tunnel.

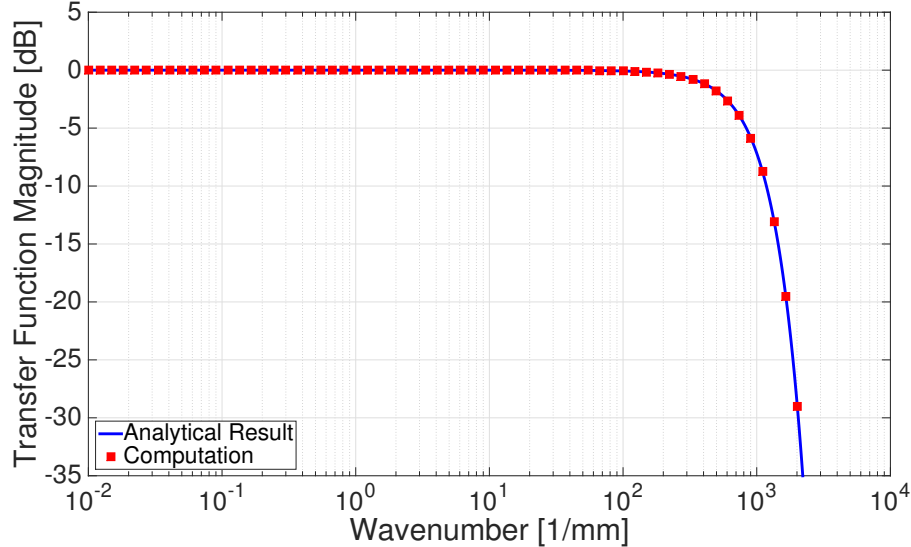


Figure C.5: Transfer function $H_w(k)$ for a single beam for 1-D sinusoidal disturbances in x in an infinitesimally-thin plane at $z = 0$

Note however that since the FLDI is actually measuring a finite difference approximation to the first derivative of density along the direction of beam separation, the magnitude of the raw signal will be smallest where that derivative is smallest, i.e. at low wavenumbers. Therefore the effect of the electronic noise floor will become significant for low-wavenumber disturbances. The issue of the noise floor will be discussed later in this section.

$H_w(k)$ can also be computed analytically for a disturbance field that is uniform in z but has a finite width $2L$, i.e. $n' = A \sin(kx)(U(z + L) - U(z - L))$ where U is the Heavyside step function. This is a more physically meaningful transfer function than Equation C.15. $H_w(k)$ is simply the integral of Equation C.14 from $-L$ to L in z divided by $2L$.

$$\begin{aligned}
 H_w(k) &= \frac{1}{2L} \int_{-L}^L \exp\left(-\frac{w_0^2 k^2}{8} \left(1 + \left[\frac{\lambda z}{\pi w_0^2}\right]^2\right)\right) dz \\
 &= \frac{\pi w_0 \sqrt{2\pi}}{k L \lambda} \exp\left(-\frac{w_0^2 k^2}{8}\right) \operatorname{erf}\left(\frac{k L \lambda}{2\sqrt{2\pi} w_0}\right)
 \end{aligned} \tag{C.16}$$

Equation C.16 is plotted for various values of L , the density disturbance half-width in z , in Figure C.6. As L increases, rolloff begins at lower values of k because the instrument is integrating over portions of the beam where the diameter is larger,

thus filtering high wavenumber disturbances according to Equation C.14. The error function in Equation C.16 introduces a k^{-1} rolloff that extends until the Gaussian decay cuts in at a wavenumber of about $10^3/\text{mm}$.

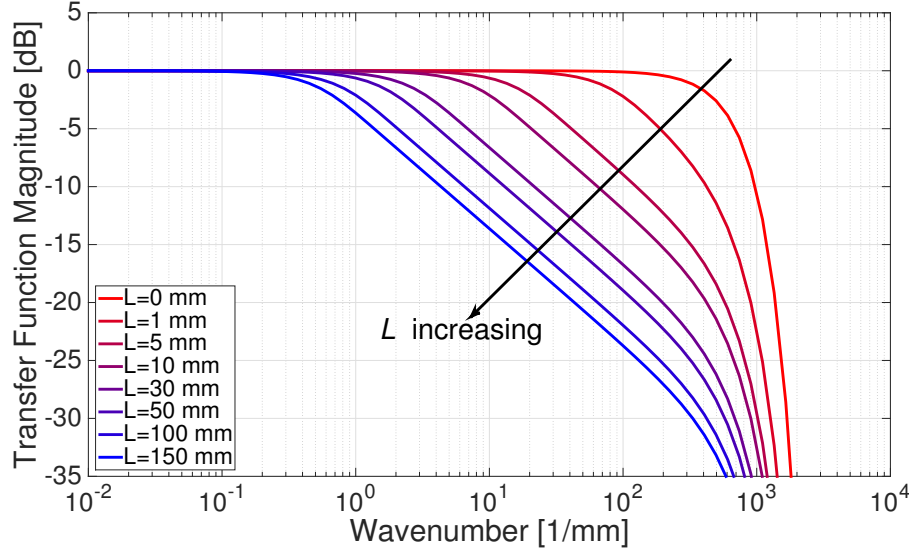


Figure C.6: Transfer function of Equation C.16 plotted for various values of L . As L increases, or, as more signal away from best focus is considered, the error function in Equation C.16 contributes a k^{-1} rolloff beginning at lower values of k . This leads to attenuation of high-wavenumber disturbances away from best focus.

Figures C.7 and C.8 compare the output of the FLDI software with the analytical result from Equation C.16 for two values of L , 10 mm and 30 mm. Excellent

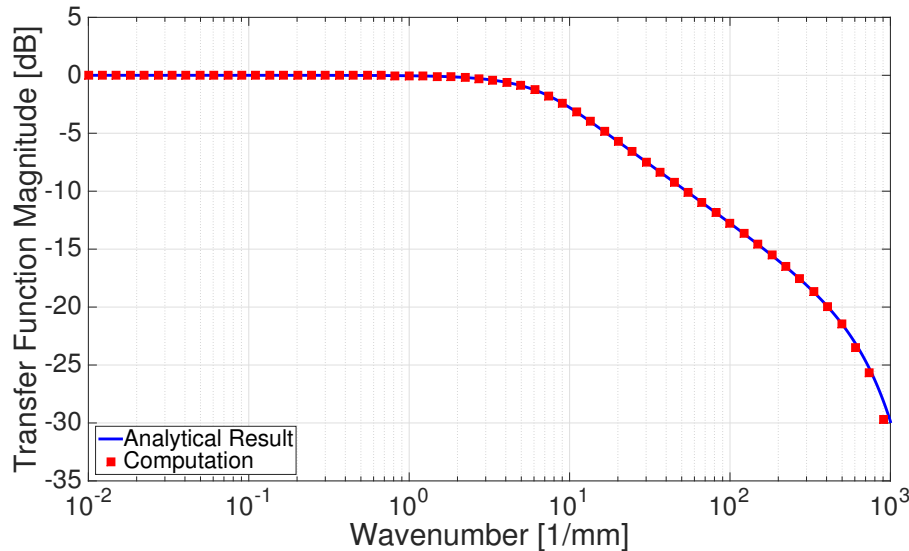


Figure C.7: Transfer function $H_w(k)$ for a single beam for uniform 2-D sinusoidal disturbances in x between $z = \pm 10$ mm centered at $z = 0$.

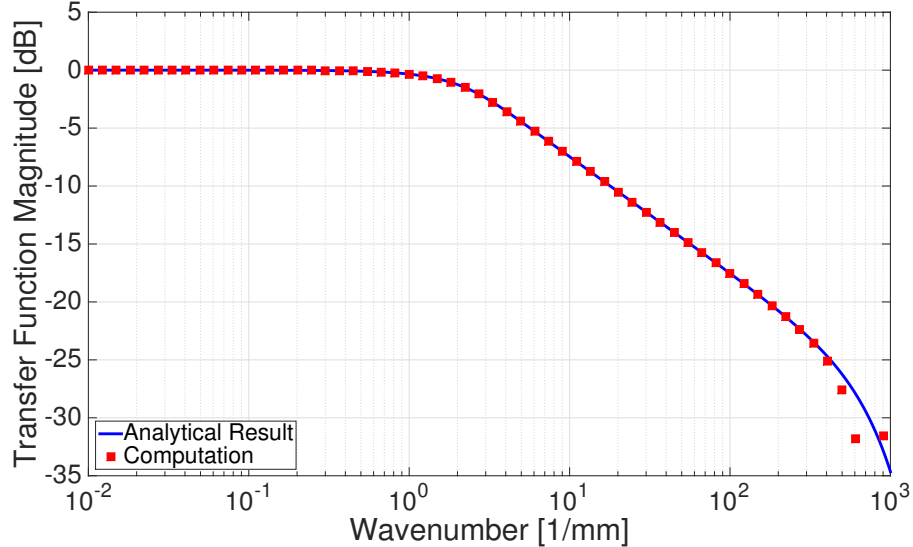


Figure C.8: Transfer function $H_w(k)$ for a single beam for uniform 2-D sinusoidal disturbances in x between $z = \pm 30$ mm centered at $z = 0$.

agreement is again observed between the analytical and computed transfer functions except at high wavenumbers where numerical errors manifest away from best focus where the beam is larger and the cross-sectional grid is therefore coarser with respect to the high-wavenumber disturbances.

In addition to the filtering effect due to the changing beam size there is a second filter due to the beams being separated by a finite distance. $H_s(k)$, the transfer function based on beam separation, is calculated by computing the response of the FLDI by approximating the FLDI as two point-detectors separated by Δx , again compared to the ideal case of the true derivative of the disturbance:

$$H_s(k) = \frac{2 \sin\left(\frac{k\Delta x}{2}\right)}{\Delta x \frac{d}{dx} [\sin(kx)]_{x=0}} = \frac{2 \sin\left(\frac{k\Delta x}{2}\right)}{k\Delta x} \quad (\text{C.17})$$

This is a sinc function, which has zeros for $k = \frac{2n\pi}{\Delta x}$ for integers n . This will only be true for strictly two-dimensional disturbances, which is not physical. Fulghum (2014) has shown by Monte-Carlo simulation that for randomly-oriented disturbances the transfer function is not oscillatory and does not contain zeros. The precise form of the transfer function can in theory be determined by similar means using the FLDI software presented here, but the process is very time-consuming and it has been observed that the effect from $H_w(k)$ is much more significant.

$H_w(k)$ and $H_s(k)$ are combined for strictly two-dimensional disturbances here for verification purposes because an overall transfer function can be derived analytically. Because the transfer functions are written in wavenumber space, the overall transfer function $H(k)$ is simply the product of $H_w(k)$ and $H_s(k)$. For instance, for density disturbances in the infinitesimal plane at best focus, the overall transfer function is

$$H(k) = \frac{2}{k\Delta x} \sin\left(\frac{k\Delta x}{2}\right) \exp\left(-\frac{w_0^2 k^2}{8}\right) \quad (\text{C.18})$$

Three overall transfer functions for $L = 0 \text{ mm}$ (infinitesimal plane at best focus), $L = 10 \text{ mm}$, and $L = 30 \text{ mm}$, respectively, are shown in Figures C.9-C.11. Excellent agreement is observed between the FLDI software (points in Figures C.9-C.11) and the analytical functions (lines in Figures C.9-C.11), affirming the accuracy of the computational method. The apparent oscillations in the transfer functions result from the sinc filter because of the strictly two-dimensional nature of the disturbance field simulated. It is also worth noting here that there is no filtering effect resulting from the overlap of the beams away from best focus as can be seen in Figure C.3. In other words, the FLDI does not reject signals by "common-mode" rejection because the beams overlap away from the best focus, but because the beam diameter is large compared to the wavelengths of the disturbances being measured. The fact that the beams overlap in space is irrelevant to signal rejection.

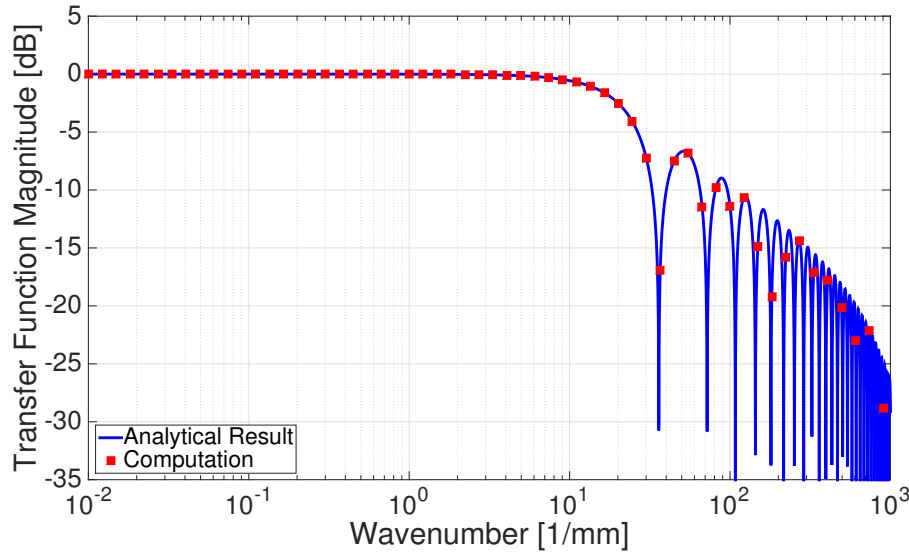


Figure C.9: Transfer function $H(k)$ for the two-beam FLDI for 1-D sinusoidal disturbances in x in an infinitesimally-thin plane at $z = 0$.

A convergence study was performed by computing the total sum-of-squares error for the transfer function shown in Figure C.11 as a function of the resolution in z ,

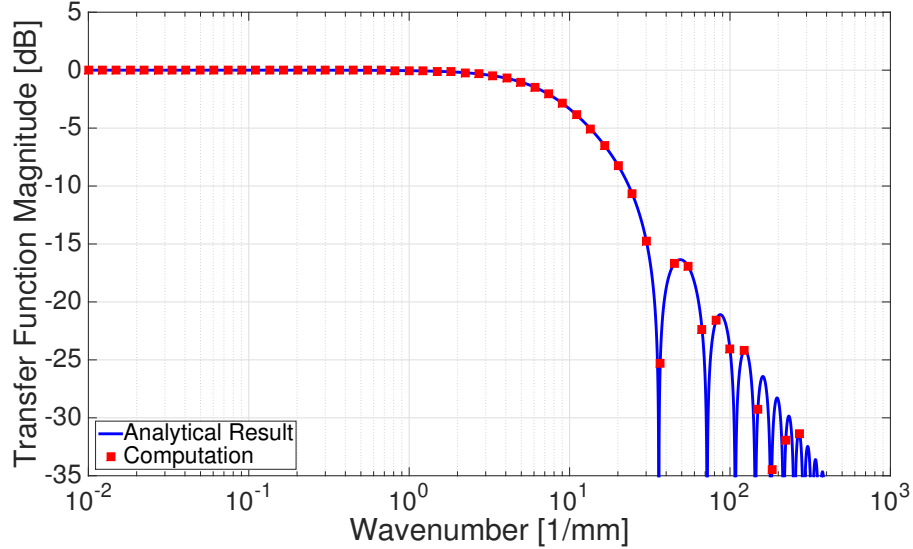


Figure C.10: Transfer function $H(k)$ for the two-beam FLDI for uniform 2-D sinusoidal disturbances in x between $z = \pm 10$ mm centered at $z = 0$.

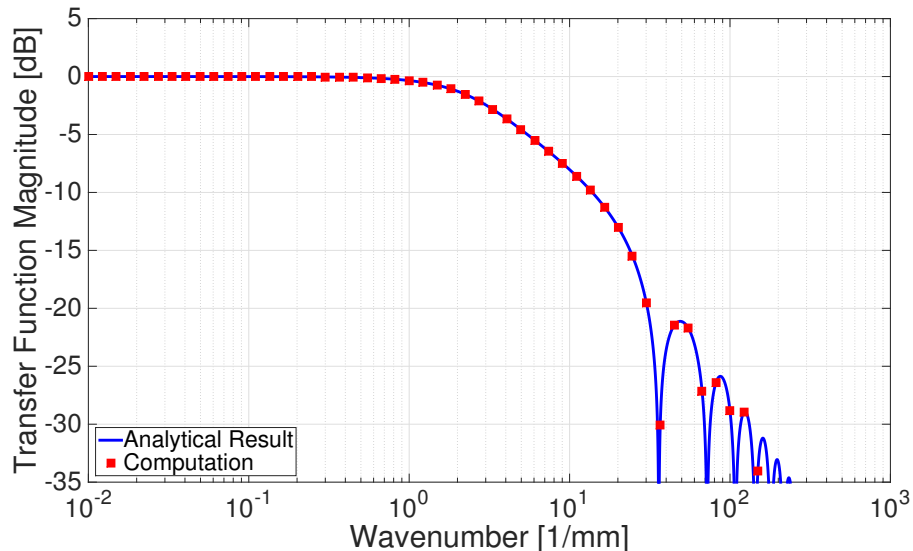


Figure C.11: Transfer function $H(k)$ for the two-beam FLDI for uniform 2-D sinusoidal disturbances in x between $z = \pm 30$ mm centered at $z = 0$.

the direction of mean beam propagation. This is shown in Figure C.12 with the red square indicating the chosen resolution. Absolute error is chosen over relative error because the small absolute errors at small values of the transfer function at high wavenumbers are not important to the output of the software, but these dominate the relative error. The grid is converged with approximately 4000 points in z , corresponding to a step size of 257.5 μm . The chosen step size of 100 μm is therefore sufficiently small.

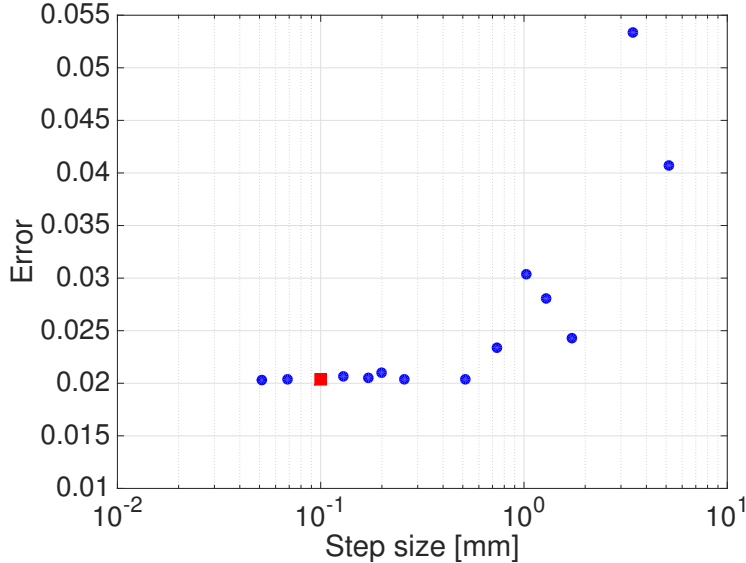


Figure C.12: Convergence study for the transfer function shown in Figure C.11. The red square indicates the chosen resolution.

The issue of the electronic noise floor can best be seen here. Figure C.13 shows the absolute response of the instrument for a disturbance propagating between ± 10 mm on either side of the focus in terms of intensity due to a difference in phase change, which is converted to voltage by the photodetector. The density field is the same as used to compute the transfer function of Figure C.10. Although the FLDI can accurately measure the derivative of a density field at wavenumbers below the rolloff, the magnitude of the output signal decreases on either side of the rolloff point. Evaluating the magnitude of density disturbances from an FLDI signal necessarily involves integration to counteract the differentiation performed by the instrument and this resolves the issue of the output signal being lower for low wavenumbers, but one must be aware of this issue in order to avoid the electronic noise floor of the physical FLDI system.

Comparison with Experiment

An experiment with a controlled density gradient was devised to compare the FLDI software against experimental data. A gravitationally-stabilized argon jet with a high-aspect ratio, rectangular cross-section is probed with the beams of the FLDI experimentally, and a model of the resulting density field is input into the FLDI software so that the results can be compared. The experimental apparatus is shown in Figure C.14. The primary component is a rectangular cavity of length 165 mm, width 10 mm, and depth 152 mm. Argon is fed through the hole at the bottom of

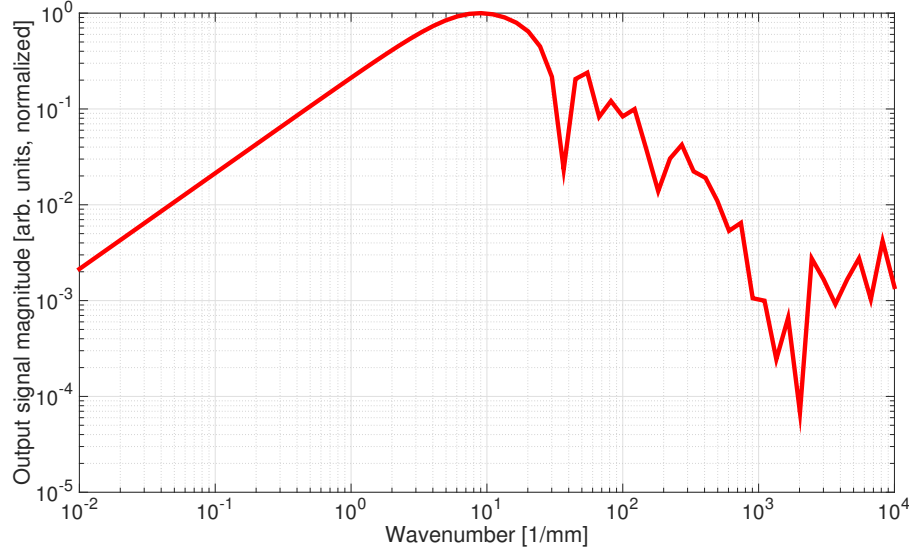


Figure C.13: Normalized FLDI output signal for sinusoidal disturbances within ± 10 mm of the focus in z , corresponding to the transfer function plotted in Figure C.10.

the chamber at a specified pressure using a needle valve. The chamber is filled with 20-40 mesh size (approximately 400-800 μm diameter) corn cob abrasive media to ensure the flow at the exit of the chamber is laminar and uniform across the exit plane. The top of the chamber is covered with a woven-wire steel cloth with 230-by-230 μm openings to contain the abrasive media.

The jet was imaged using schlieren visualization and is found to achieve the stable configuration shown in Figure C.15. The argon is moving vertically upward at the chamber exit with an average velocity of 0.22 m/s, computed from the measured flow rate delivered by a King Instruments rotameter, but stops and reverses direction due to gravity. The maximum height achieved at $y = 0$ is determined by the flow rate and is typically about 15 mm. A 2D planar computation was performed using OpenFOAM with the rhoReactingFoam solver (Weller et al., 1998). Figure C.16 shows the steady-state result of the computation, with velocity vectors on the left and streamlines on the right with both superimposed on a contour plot of argon mass fraction. Numerical schlieren from the computation exhibits qualitative agreement with the schlieren image in Figure C.15.

The flow is observed to be uniform along the length of the chamber in z , stable in time, and laminar. The chamber is placed in the test section of the Caltech Ludwieg Tube and made parallel to the z -axis of the FLDI beams by using a level suspended between two parallel circular cavities.

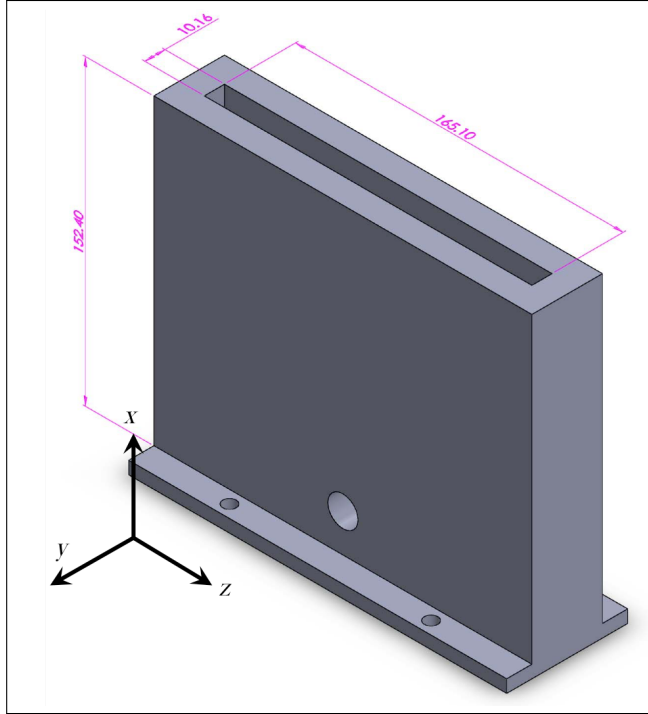
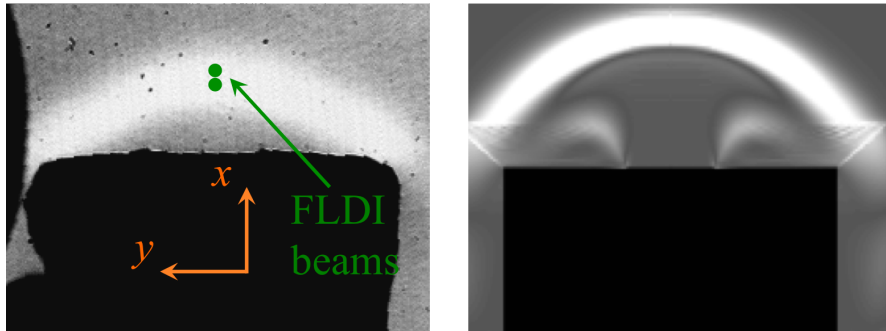


Figure C.14: A solid model of the chamber for the argon jet with dimensions given in mm. The coordinate system shown corresponds to the orientation of the coordinate system of the FLDI beams.



- (a) Schlieren image of the argon jet in the $x-y$ plane. The top of the jet is about 15 mm from the chamber exit and is observed to be uniform across the jet cross-section, temporally stable, and laminar.
- (b) Pseudo-schlieren image of the argon jet showing the vertical gradient in density for comparison with the experiment.

Figure C.15

The FLDI beams are separated in the x -direction and located at the interface of the argon and air, such that they measure the density change across the interface as shown in Figure C.15a. The resulting phase change is less than $\pi/2$ so the small-angle

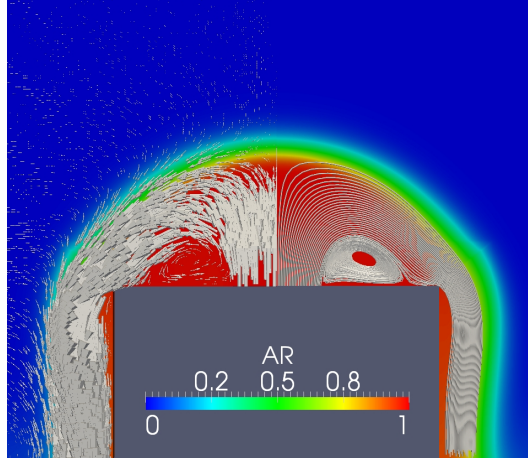


Figure C.16: Steady-state result of OpenFOAM computation of the flow out of the argon jet. Velocity vectors are shown on the left and streamlines on the right. Both are superimposed on a contour plot of argon mass fraction. L_{jet} is the length out of the page (in z) that the cross-section shown here extends.

approximation can be invoked as in Section C.2. Portions of the jet can be covered with tape such that only sections of the jet are active. Fluctuations in the ambient air are negligible compared to the density difference across the interface. The optical index field can therefore be approximated for computational purposes as varying in x and being uniform in y and z over the portion(s) where the chamber exit is not covered, and uniform everywhere else, i.e. $n' = n_{\text{jet}}(x)(U(z_0 + L/2) - U(z_0 - L/2))$. This allows for comparison between the FLDI software and experiment for a number of different configurations. At each condition the flow rate of the argon is adjusted to produce the maximum FLDI signal, meaning that the beams are centered on the maximum of the density gradient. Test cases performed are presented in Table C.2 by total length of the jet in z (L_{jet}) and the center of the jet in z (z_0).

The variation in index of refraction in the x -direction across the argon-air interface is shown in Figure C.17. Cubic spline interpolation is used in the FLDI software when evaluating the index of refraction on the computational grid. The index of refraction for a mixture of gases is calculated from Equation C.19, which is derived from Equation B29 in Glass and Kawada (1962) by substituting the definition of mass fraction (Y):

$$n' = Y_{\text{Ar}} (\rho_{\text{Ar}} + \rho_{\text{air}}) (K_{\text{Ar}} - K_{\text{air}}) + K_{\text{air}} (\rho_{\text{Ar}} + \rho_{\text{air}} - \rho_{\text{air}}|_{x \rightarrow \infty}) \quad (\text{C.19})$$

The computational and experimental FLDI phase change outputs for each case in Table C.2 are plotted versus one another in Figure C.18. Uncertainty in the

Configuration	L_{jet}	z_0
A	165	0
B	130	0
C	110	0
D	90	0
E	70	0
F	50	0
G	30	0
H	20	0
I	10	0
J	82.5	41.25
K	20	10
L	20	20
M	20	30
N	32.5	66.25

Table C.2: Argon jet configurations tested (dimensions in mm).

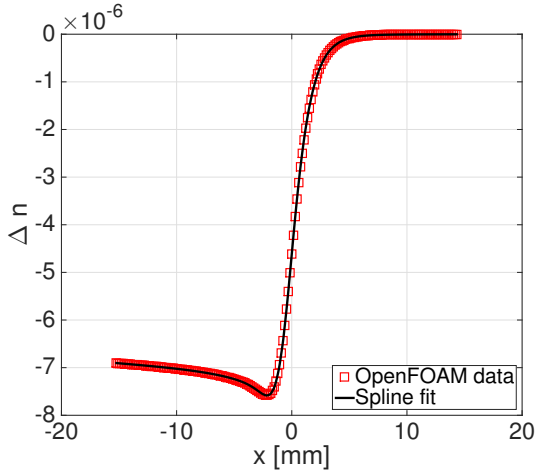


Figure C.17: Index of refraction field from the OpenFOAM computation with spline interpolation.

experiment is difficult to quantify, but errors are believed to be largely due to three-dimensional effects at the ends of the jet. The error bars in Figure C.18 are a bound on the error from calculating the response with an additional 5 mm of jet length on either side of the jet for each configuration. Three-dimensional effects have a larger influence on shorter jet lengths, which explains the scatter in the data at the low-response end of the figure. A linear regression analysis was carried out to test the correlation of experimental data and numerical results. The regression line has a slope of 0.99 and an intercept of 0.00, compared to the ideal values of 1 and

0 for slope and intercept, respectively, and all but one of the individual points lie on the regression line within the computed uncertainty. The FLDI software can therefore be considered verified versus analytical calculations and validated against experimental data with a high degree of confidence.

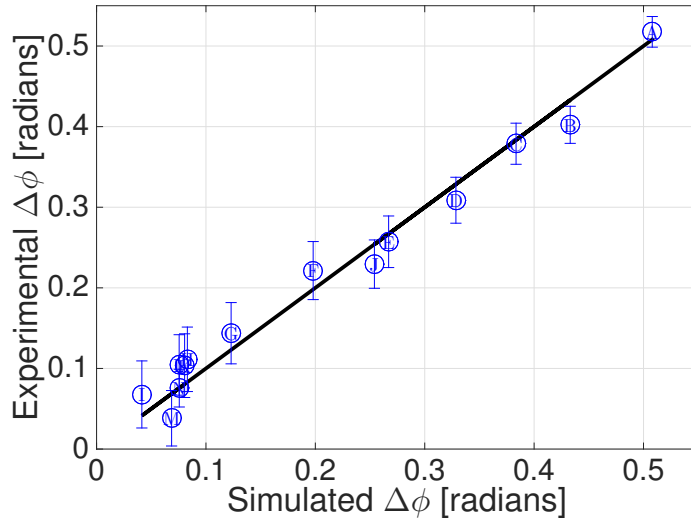


Figure C.18: Experimental vs. numerical data for the argon jet experiments detailed in Table C.2. The letters marking each data point correspond to the configurations in Table C.2. The line is the ideal line $y = x$.

C.5 Simulated Measurements

Description

One of the more promising applications of the FLDI is measuring instability waves in hypervelocity boundary layers where other more conventional techniques such as surface-mounted pressure transducers or hot-wire anemometry are not suitable. The FLDI is capable of making such measurements because of its high temporal resolution and ability to reject signals away from best focus. This was done by Parziale at Caltech in his PhD thesis (Parziale, 2013). These instability waves are Mack-mode waves and propagate two-dimensionally in the mean flow direction. Because the waves are two-dimensional, one can assume that waves only propagate along the x -axis of the FLDI. As such, the FLDI is quite capable of measuring their frequency, but because of the path-integrated nature of FLDI measurements it is impossible to determine their amplitude from the FLDI output alone. This point is possibly made clearest by Smeets himself (Smeets, 1977): "From the signals received [from a 2D shear layer], primarily qualitative information could be achieved, e.g., on the frequency spectra of the turbulent fluctuations near the focal point. The deduction of quantitative data on the level of local density fluctuations

is only possible by means of assumptions and approximations. The accuracy of the results is, therefore, only moderate."

From Equation C.6 we see that the change in phase between the two FLDI beams, which is converted to a voltage by the photodetector, is an integrated function of the density fluctuations along the beam paths.

$$\frac{\Delta\Phi(t)}{\Delta x} = \frac{2\pi K}{\lambda \Delta x} \iint_D I_0(\xi, \eta) \left(\int_{s_1}^{D(\xi, \eta)} \rho'(\underline{x}_1, t) ds_1 - \int_{s_2}^{D(\xi, \eta)} \rho'(\underline{x}_2, t) ds_2 \right) d\xi d\eta \quad (\text{C.20})$$

where ρ' represents the local density fluctuations. We seek the amplitude of ρ' , the density fluctuation. If Δx is sufficiently small and recalling that $\underline{x}_1 = \underline{x}_2 + \Delta x \hat{x}$, we can write this equation in terms of derivatives in x instead of finite differences and approximate the two beam paths in Equation C.20 as being common.

$$s_1 \approx s_2 \approx s \quad (\text{C.21})$$

$$\rho(\underline{x}_1) \approx \rho(\underline{x}_2) + \frac{\partial \rho}{\partial x} \Delta x \quad (\text{C.22})$$

$$\frac{d\Phi(t)}{dx} \approx \frac{2\pi K}{\lambda} \iint_D I_0(\xi, \eta) \int_s \frac{\partial \rho'(\underline{x}, t)}{\partial x} ds d\xi d\eta \quad (\text{C.23})$$

Since the output of the FLDI is a function of time, not space, it is much more useful to take derivatives with respect to time. This conversion can be done using Taylor's hypothesis $x = c_r t$ for a constant phase speed c_r . We then have

$$\frac{d\Phi(t)}{dt} \approx \frac{2\pi K}{\lambda} \iint_D I_0(\xi, \eta) \int_s \frac{\partial \rho'(\underline{x}, t)}{\partial t} ds d\xi d\eta \quad (\text{C.24})$$

We can then apply the mean value theorem for integrals to the right-hand side to obtain

$$\frac{d\Phi}{dt} = \frac{2\pi K}{\lambda} Z \overline{\frac{\partial \rho'}{\partial t}} \quad (\text{C.25})$$

Here $\overline{\frac{\partial \rho'}{\partial t}}$ represents the averaged value of the time-derivative of ρ' over the spatial integral. Z is an unknown parameter with units of length that makes $\overline{\rho'}$ equal to the

actual ρ' fluctuation in the boundary layer. It is approximately equal to the length of the region where the FLDI is probing the boundary layer, but it cannot be determined *a priori* from experimental data alone. However, Z is primarily a function of the flow geometry, and can be calculated with knowledge from the FLDI software for a given geometry and used with experimental data for the same flow. It is sensitive to the spatial filtering of the FLDI as indicated in Equation C.16, so care must be taken to ensure that the wavelengths being measured are not significantly attenuated.

We can then integrate the FLDI output in time to obtain the density fluctuations as a function of time

$$\frac{c_r}{\Delta x} \int_0^t \Delta\Phi(\tau) d\tau = \frac{2\pi K}{\lambda} Z \bar{\rho}'(t) \quad (\text{C.26})$$

or, solving for $\bar{\rho}'$

$$\bar{\rho}'(t) = \frac{c_r \lambda}{2\pi \Delta x Z K} \int_0^t \Delta\Phi(\tau) d\tau \quad (\text{C.27})$$

The integral can be evaluated using standard numerical integration methods, e.g. Simpson's rule. Alternatively, since instability waves are often analyzed in frequency space, we can write the Fourier transform in time of Equation C.27

$$\mathcal{F}[\bar{\rho}'] = \frac{c_r \lambda}{2\pi \Delta x Z K} \frac{1}{i\omega} \mathcal{F}[\Delta\Phi] \quad (\text{C.28})$$

The FLDI software can be used to make simulated measurements of a Mack mode wave packet in a boundary layer, and the result of that simulation can be used to calculate a value for Z that can be used in experiments to determine the magnitude of the fluctuations. The wavepacket is calculated for T5 shot number 2789. The boundary layer edge conditions are as follows:

M_e	4.55
T_e	2105 K
U_e	4191 m/s
p_e	47.1 kPa
Re/m	$4.76 \times 10^6 /m$
ρ_e	0.0777 kg/m ³

Table C.3: Boundary layer edge conditions for T5 shot 2789.

The FLDI measurement location is 710 mm from the tip of a 5-degree half-angle cone model as shown in Figure C.19. Wave packet characteristics are calculated using the method described in Bitter and Shepherd (2015) and Mack (1965).

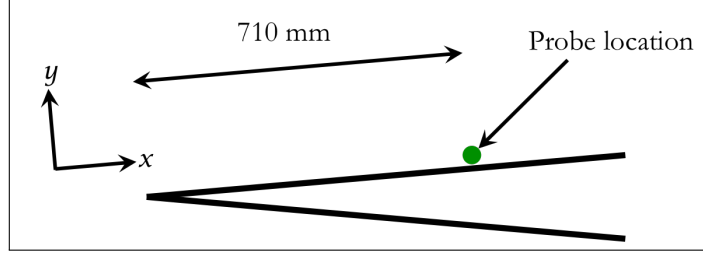


Figure C.19: Cone model used in T5 studies

The density field in a hypersonic boundary layer contains a propagating disturbance that can be approximated as

$$\rho(x, y, t) = \bar{\rho}(x, y) + \rho'(x, y, t) \quad (\text{C.29})$$

a mean spatial density field $\bar{\rho}(x, y)$ and a fluctuating component ρ' representing a wave packet containing high-frequency waves representative of Mack (second mode) instabilities.

$$\rho' = \rho_{\text{SF}} E(x, t) \rho'^* \quad (\text{C.30})$$

Here ρ_{SF} is a dimensional scale factor that determines the amplitude of the density fluctuation. It is chosen such that the maximum density fluctuation is 0.1% of the free stream value. $E(x, t)$ is an envelope describing the extent of the wave packet in x , and ρ'^* is a non-dimensional fluctuation of the form

$$\rho'^* = \text{Re}[g(y) \exp(i(\alpha x - \omega t))] \quad (\text{C.31})$$

where g is a complex eigenfunction in y , α is a complex wavenumber containing information on both the spatial wavenumber ($\alpha_r = k$) and the spatial growth rate (α_i), and ω is the temporal frequency of the wave. Written in terms of real and imaginary parts, ρ'^* is

$$\rho'^* = \exp(-\alpha_i x) (g_r(y) \cos(\alpha_r x - \omega t) - g_i(y) \sin(\alpha_r x - \omega t)) \quad (\text{C.32})$$

The eigenfunctions and eigenvalues were computed by Bitter (Bitter and Shepherd, 2015) using parallel flow linear stability theory for a boundary layer on a cone with flow conditions given in Table C.3. The real and imaginary eigenfunctions are plotted versus height above the cone surface in Figure C.20 along with the mean density profile through the boundary layer.

From Figure C.20c and examination of the cone geometry it is determined that the FLDI beams are inside the boundary layer within about 10 mm on either side of

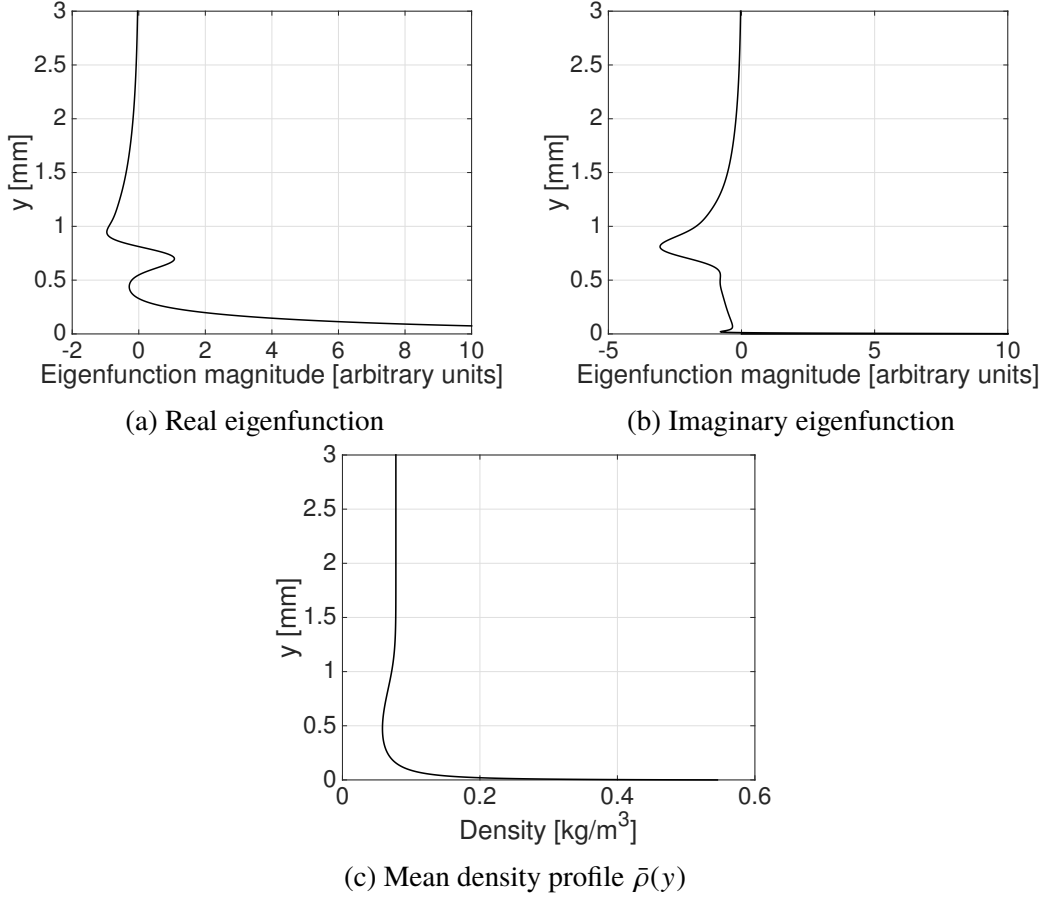


Figure C.20

the best focus. The envelope is chosen to be a Gaussian that it contains about 15 wavelengths inside the region where its value is greater than 1%. Functionally, this has the form

$$E(x, t) = \exp\left(\frac{-A(x - c_r t - x_0)^2}{l^2}\right) \quad (\text{C.33})$$

for envelope length l and spatial starting location x_0 .

Equation C.30 has the final form

$$\begin{aligned} \rho' = \rho_{\text{SF}} \exp\left(\frac{-A(x - c_r t - X_0)^2}{l^2} - \alpha_i x\right) & (g_r(y) \cos(\alpha_r x - \omega t) \\ & - g_i(y) \sin(\alpha_r x - \omega t)) \quad (\text{C.34}) \end{aligned}$$

The parameters in Equation C.34 have the values given in Table C.4. It is important to recognize that we should not expect significant spatial filtering for $\alpha_r = 2.116/\text{mm}$ based on Figure C.10. Note that Figure C.10 does not represent the transfer function for this cone boundary layer flow but is the transfer function for two-dimensional

disturbances propagating in x and uniform in z from $-10 < z < 10$ mm and so the exact magnitude of the transfer function at a given wavenumber is not directly applicable here. Still, Figure C.10 does predict whether or not a particular wavenumber will be appreciably attenuated.

ρ_{SF}	$2.276 \times 10^{-20} \text{ kg/m}^3$
A	$-\ln 0.01 = 4.6$
l	$14\pi/\alpha_r = 20.8 \text{ mm}$
x_0	$710 \text{ mm} - l = 689.2 \text{ mm}$
c_r	3633 m/s
α_i	$-0.0488/\text{mm}$
$\alpha_r = k$	$2.116/\text{mm}$
$\omega = 2\pi f = c_r \alpha_r$	$7.697 \times 10^6 \text{ rad/s}$

Table C.4: Boundary layer wave packet parameters.

The FLDI beams are positioned in the simulation at the local maximum of the density eigenfunction at $y = 0.81$ mm. The density fluctuations are converted to refractive index fluctuations by the Gladstone-Dale relation (Equation C.7) with $K = 0.227 \times 10^{-3} \text{ m}^3/\text{kg}$. The wavepacket is assumed to be axisymmetric with respect to the cone axis. The local density is transformed from the FLDI coordinate system (subscript f) to a coordinate system relative to the cone surface normal (subscript c) so that Equation C.34 can be evaluated by a series of trigonometric operations for cone half-angle θ_c . Note that at $z_f = 0$, $(x_f, y_f) = (x_c, y_c)$ as expected.

$$y_c = \cos \theta_c \left(\sqrt{\left[(x_f - y_f \tan \theta_c) \tan \theta_c + \frac{y_f}{\cos \theta_c} \right]^2 + z_f^2} - \tan \theta_c (x_f - y_f \tan \theta_c) \right) \quad (\text{C.35})$$

$$x_c = x_f + \tan \theta_c (y_c - y_f) \quad (\text{C.36})$$

The index of refraction change, relative to the index of refraction outside the boundary layer, at a point (x_c, y_c, t) is

$$\Delta n = K(\bar{\rho}(y_c) + \rho'(x_c, y_c, t) - \rho_e) \quad (\text{C.37})$$

Functions $\bar{\rho}$, g_r , and g_i are tabulated on a uniform stencil in y_c with step size $0.74 \mu\text{m}$, and values are interpolated from the tabulated functions for each simulated ray in the FLDI software. The wave packet is propagated in time and the sample rate of the simulated FLDI is 20 MHz, sufficient to fully temporally resolve the wave packet.

Results

The output of the simulation is shown in Figure C.21 along with the input density disturbance at the probe location in x , which is halfway between the two FLDI beams, and $z = 0$, i.e. best focus. Note that the output is in phase change, as it would be if output from a photodetector in a physical FLDI setup, and that the output is proportional to the time derivative of the input wave packet as indicated by Equation C.27.

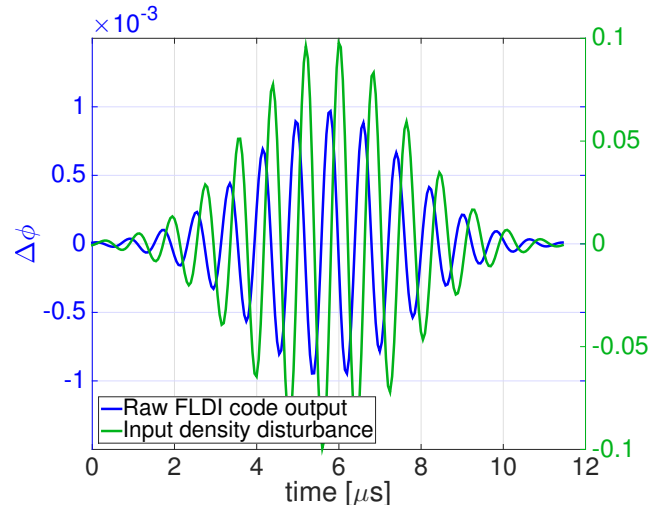


Figure C.21: Output of the FLDI simulation compared to the input boundary layer wave packet density disturbance. The y-axis on the left corresponds to the FLDI output and the y-axis on the right corresponds to the input density at the location of the beams at $z = 0$.

Equation C.27 is applied to the simulated FLDI output and Z is determined by means of iteration until the peak magnitude of the measured power spectral density of the simulated output is equal to that of the input. For the flow geometry studied here, Z is calculated to be 12.6 mm. Figure C.22 shows the both the measured and input density fluctuations with respect to time. Note that the only difference between the two is that the measured fluctuations are slightly ahead of the input with respect to time. This is simply a consequence of the conical geometry of the flow: the wave packet will first be observed by the FLDI beams away from the focus. Equations C.35 and C.36 make the issue clear. For $z \neq 0$, $y_c > y_f$ so $x_c > x_f$.

Figure C.23 shows the power spectral density of the input and output density fluctuations. The two curves match each other almost exactly with the appropriate value of Z except that the simulated measurement has higher noise away from the peak in frequency. Presumably even more noise would be present in an experiment, so this

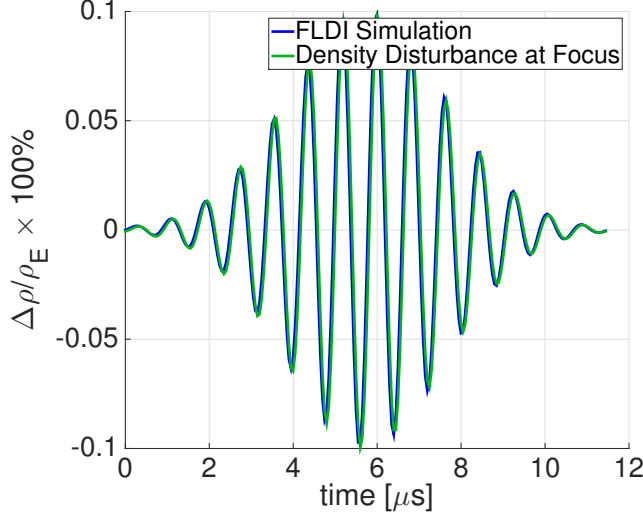


Figure C.22: Output of the FLDI simulation, scaled with Equation C.27, compared to the input boundary layer wave packet for the optimum value of $Z = 12.6$ mm.

slight increase in noise is inconsequential.

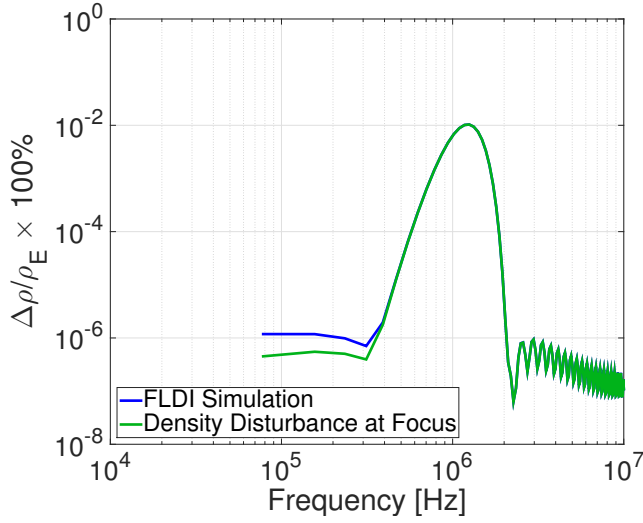


Figure C.23: PSD of the FLDI simulation, scaled with Equation C.27 and optimum Z value, compared to the PSD of the input boundary layer wave packet.

The parameters in Table C.4, namely α_r and c_r , are changed to determine the universality of the value of Z for wave packets of different spatial wavenumber and frequency. The values for α_r and c_r are given in Table C.5 along with the computed frequency and the error in the peak amplitude of the simulated measurement relative to the peak magnitude of the input wave packet.

The error in the peak amplitude of the wave packet is appreciable only in cases 3 and 4. The reason for the large error can be deduced by examining the values of α_r

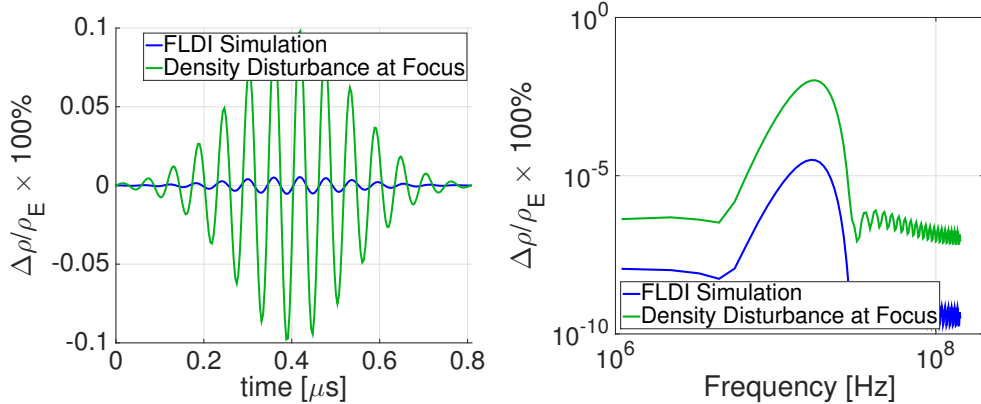
Case No.	α_r [1/mm]	c_r [m/s]	f [Hz]	% Error
1	2.116	3633	1.22×10^6	0.0
2	0.4	3633	2.31×10^5	4.0
3	7	3633	4.05×10^6	-26
4	30	3633	1.73×10^7	-94
5	2.116	2500	8.42×10^5	0.0
6	2.116	5000	1.68×10^6	0.0

Table C.5: Wave packet properties tested with fixed value of Z .

in these cases and consulting Figure C.10. Recall again that the transfer functions plotted in Figures C.9-C.11 are not transfer functions for the conical boundary layer under examination in this section, but nonetheless they lend some insight to when the instrument will begin to roll off in wavenumber space. Notice that at $\alpha_r = 7/\text{mm}$, the transfer function has dropped to about -2 dB, which corresponds to about a 35% reduction in signal magnitude, close to the observed error in Table C.5. Similarly, for $\alpha_r = 30/\text{mm}$, the transfer function is approximately equal to -17 dB, corresponding to a 98% reduction in magnitude which is again quite close to the error in Table C.5 for case 4. Physically, this means that the wavelength of the Mack-mode waves is sufficiently small that it is comparable in size to the beam width in the region where the FLDI is probing the boundary layer and therefore the waves are being heavily spatially filtered by the beams.

It is interesting to examine further the output from the FLDI software for case 4 where $\alpha_r = 30/\text{mm}$. The density change as a function of time and the power spectral density of the disturbance are shown in Figure C.24. As Table C.5 indicates, the measured signal magnitude is significantly reduced compared to the input disturbance using the same value of Z calculated for case 1 where there is very little spatial filtering by the instrument. Interestingly, though, the FLDI is able to measure the frequency of the signal correctly. This is a somewhat surprising result because if one were to approximate the FLDI as two point measurements separated by the beam separation Δx , one would predict spatial aliasing if the wavenumber of the disturbance is greater than $\frac{\pi}{\Delta x}$, which would be 18 mm here. This spatial aliasing would become temporal aliasing when Taylor's hypothesis is applied. Figure C.24b clearly does not display this behavior, however, so the finite beam diameter seems to prevent spatial aliasing based on wavenumber. An FLDI will only suffer from aliasing if the sampling frequency is not sufficiently high compared to the frequency of the disturbance being measured. The only effect of high wavenumbers is the attenuation of the

signal due to spatial filtering, which will lead to a limitation from the electronic noise floor of the system.



(a) Output of the FLDI simulation for case 4 in Table C.5 scaled with the same value of Z found in case 1 compared to the actual density disturbance at the focus.

(b) Power spectral density of the FLDI simulation for case 4 compared to the PSD of the input boundary layer wave packet at the focus

Figure C.24

Based on this analysis we conclude that the value of Z in Equation C.27 is only a function of the geometry of the density field being probed and the attenuation of the signal due to spatial filtering based on wavenumber. If the attenuation is sufficiently small for all wavenumbers of interest in the experiment then only a single value of Z needs to be calculated to accurately compute the density change quantitatively. Even if the wavenumbers of interest are high enough to be filtered by the FLDI, new values of Z can be calculated for given wavenumbers without much difficulty. The measurement will still be a point measurement at the focus of the FLDI and the phase speed of the disturbance must be known *a priori*, but for the specific application of measuring Mack-mode waves on a slender-body boundary layer these restrictions are not problematic. The phase speed can either be calculated from stability theory as is done here or it can be measured as in Laurence, Wagner, and Hanneman (2014). One also needs some knowledge regarding the shape of the density eigenfunctions.

To summarize, the routine to accurately compute the density change of Mack-mode waves in a hypervelocity boundary layer from FLDI data is as follows:

1. Compute wave properties and eigenfunctions from linear stability analysis, e.g. in Bitter and Shepherd (2015)
2. Input this data into FLDI software such as the one in the current study

3. Compute a value for Z in Equation C.27 by matching the results of step 2 to the specified density change of the input wavepacket
4. Apply Equation C.27 to the experimental FLDI data using the value of Z from step 3, taking care to ensure that the wavenumber of the Mack mode wave is not appreciably spatially filtered by the FLDI

The simple procedure used in Parziale (2013) for computing the density disturbance magnitude for T5 shot 2789 can give an estimate accurate within an order of magnitude if the "integration length" is estimated based on the length through which the FLDI beams are inside the cone boundary layer. However, such a procedure makes significant approximations that limit its accuracy to within about a factor of 2. The routine outlined above, on the other hand, requires knowledge of the form of the disturbances and is limited in accuracy by experimental uncertainty and any uncertainties associated with the computations performed in step 1. One could alternatively simply make an estimate of Z based on the boundary layer geometry and skip directly to step 4 above. Estimating Z would likely give results that are more accurate than the procedure in Parziale (2013) because Equation C.27 takes into account the fact that the FLDI is differentiating the density disturbance in space while the simplified procedure does not, but the results would be less accurate than those obtained by following the full routine outlined above.

There is a caveat to these results. The free stream disturbances outside the boundary layer have been neglected in this analysis, but in an experiment the FLDI beams integrate through these disturbances and they will contribute to the output signal. Therefore care must be taken to ensure that the free stream disturbances do not occupy the same frequency space as the disturbance of interest at the focus, or that the wavenumber of the free stream disturbance at the frequency of the disturbance of interest is sufficiently high that it is heavily spatially filtered by the FLDI away from the focus. It is important to recognize that the characteristic velocity of the free stream disturbances can be different from the characteristic velocity of the disturbance of interest, as it is for hypervelocity boundary layers. Based on measurements taken in T5, it appears that the frequency range over which there is significant FLDI signal in the free stream is significantly below the 1.2 MHz of a typical Mack-mode wave packet, so signal contamination from the free stream is not expected to be problematic when using the FLDI to measure Mack-mode waves on a cone boundary layer. The effect of free stream disturbances on the output signal

ought to be evaluated for each facility on a case-by-case basis for future experiments before attempting to quantify boundary layer instability measurements to ensure the measurements are accurate. This is particularly true for low-enthalpy facilities where the frequency content of the free stream disturbances and that of Mack-mode waves are not as far apart as they are in high-enthalpy flow.

Another word of caution is warranted regarding measuring Mack-mode waves in hypervelocity boundary layers with an FLDI. From Figure C.20, it is clear that the magnitude of density fluctuations varies significantly with height in the boundary layer, and as such the output of the FLDI is quite sensitive to the location above the cone surface where the disturbance is measured. Indeed, if the measurement location is moved only $400 \mu\text{m}$ from the specified measurement location of $y = 0.81 \text{ mm}$ to $y = 1.2 \text{ mm}$, the error in the measurement using the value of Z calculated for case 1 in Table C.5 is greater than 50%. Therefore great care must be taken to accurately measure the height of the beam centers from the model surface in an experiment.

C.6 Conclusions

Focused laser differential interferometry is a promising technique for measuring localized, high-frequency density disturbances in supersonic and hypersonic flows. In particular, the FLDI is an attractive instrument for measuring Mack-mode instability waves in hypersonic boundary layers. A computational tool has been developed here that has been verified against analytical predictions of the FLDI response as well as experimental measurements with a physical FLDI setup. Using the FLDI software, it is possible to calculate the output of an FLDI to an arbitrary density field. Such a prediction can only be made analytically for very simple density fields. These computations allow FLDI experiments to give quantitative measurements of the density fluctuation amplitude if certain details about the flow in question are known by applying correction factors to the computational output such that the FLDI output matches the input density disturbance of interest. This procedure is shown to work well for hypersonic boundary layer disturbances where the disturbance is localized near the best focus of the FLDI, is two-dimensional in nature, and the phase speed of the instabilities can be accurately predicted from theory.

Some general statements can be made concerning using the FLDI to make measurements in compressible flows. The FLDI does reject signals away from its best focus, but this signal rejection is not related to common-mode rejection associated with the beams sharing common paths. The rejection is in fact attenuation due to spatial

filtering because of the increasing beam diameters away from the focus. As such, disturbances with small enough wavenumbers (long enough wavelengths) will not be attenuated away from the FLDI focus and will therefore contribute to the FLDI signal over a significant extent of the beam paths. As a result the FLDI can accurately measure the frequency content of density disturbances in a flow, but it does not in general yield information as to where along the beam path the disturbances are located or their amplitude at any given point along the beam path. In order to extract quantitative density information, details regarding the geometry of the density disturbance field, the preferred direction of the disturbances (if any), and the characteristic velocity of the disturbances must be known. If these are known, then the FLDI output can be simulated using a procedure such as the one presented here, or, if the flowfield is simple enough, by analytical methods, and then experimental measurements can be adjusted as necessary such that the density fluctuation magnitude is correct. The authors are not aware of any other method to extract suitably accurate quantitative density fluctuation magnitudes from FLDI data.

Appendix D

EXPERIMENTAL CONDITIONS

Flow conditions

Shot No.	Injected Gas	p_{fill} [kPa]	\dot{m}_{inj} [g/s]	$F \times 10^3$	$J \times 10^4$	p_{∞} [kPa]	$Re_{L,\infty}$ [$10^6/\text{m}$]
425	N/A	204	N/A	N/A	N/A	1.21	9.16
441	N/A	202	N/A	N/A	N/A	1.20	9.06
444	Nitrogen	403	0.097	0.45	0.0066	2.40	17.98
445	Nitrogen	202	0.097	0.91	0.026	1.20	9.01
446	Nitrogen	394	0.40	1.94	0.12	2.34	17.81
447	Nitrogen	204	0.42	3.89	0.48	1.21	9.14
448	Nitrogen	399	0.61	2.87	0.26	2.37	17.99
449	Nitrogen	203	0.65	6.01	1.17	1.20	9.05
450	Nitrogen	403	0.68	3.20	0.33	2.39	17.97
451	Nitrogen	203	0.71	6.65	1.41	1.21	9.09
452	Nitrogen	403	0.90	4.22	0.57	2.40	18.17
453	Nitrogen	203	0.88	8.24	2.16	1.21	9.09
454	Nitrogen	401	1.075	5.09	0.82	2.38	17.89
455	Nitrogen	200	1.14	10.79	3.70	1.19	8.95
456	Nitrogen	402	1.28	6.03	1.16	2.39	18.11
457	Nitrogen	201	1.32	12.39	4.88	1.20	9.04
458	Nitrogen	401	1.49	7.02	1.57	2.38	18.03
459	Nitrogen	203	1.56	14.58	6.76	1.20	9.05
460	Nitrogen	399	1.66	7.89	1.98	2.37	17.95
461	Nitrogen	201	1.70	16.04	8.19	1.19	8.97
462	Nitrogen	402	1.83	8.60	2.35	2.39	18.09
463	Nitrogen	201	1.97	18.54	10.93	1.19	9.03
464	Nitrogen	403	0.091	0.43	0.0058	2.39	18.02
465	Nitrogen	202	0.081	0.76	0.018	1.20	9.03
466	Nitrogen	400	0.33	1.57	0.079	2.38	18.09
467	Nitrogen	201	0.36	3.35	0.36	1.20	9.03
468	Nitrogen	404	0.57	2.69	0.23	2.40	18.15
469	Nitrogen	202	0.59	5.51	0.96	1.20	9.03
470	Nitrogen	403	0.69	3.26	0.34	2.39	18.17
471	Nitrogen	202	0.71	6.67	1.42	1.20	9.06
472	Nitrogen	401	0.90	4.26	0.58	2.38	18.02

Shot No.	Injected Gas	p_{fill} [kPa]	\dot{m}_{inj} [g/s]	$F \times 10^3$	$J \times 10^4$	p_{∞} [kPa]	$Re_{L,\infty}$ [$10^6/\text{m}$]
473	Nitrogen	201	0.92	8.67	2.39	1.19	8.99
474	Nitrogen	402	1.17	5.49	0.96	2.39	18.26
475	Nitrogen	199	1.22	11.58	4.27	1.18	9.00
476	Nitrogen	402	1.37	6.45	1.32	2.39	18.11
477	Nitrogen	201	1.40	13.12	5.47	1.20	9.10
478	Nitrogen	402	1.50	7.04	1.58	2.39	18.28
479	Nitrogen	201	1.59	14.93	7.09	1.19	9.08
480	Nitrogen	401	1.71	8.07	2.07	2.38	18.10
481	Nitrogen	204	1.76	16.32	8.48	1.21	9.20
482	Nitrogen	403	2.05	9.60	2.93	2.40	18.29
483	Nitrogen	205	2.12	19.56	12.17	1.22	9.25
524	Helium	401	0.059	0.28	0.017	2.38	18.20
525	Helium	202	0.063	0.59	0.077	1.20	9.11
526	Helium	403	0.16	0.76	0.13	2.39	18.07
527	Helium	202	0.17	1.56	0.54	1.20	9.02
528	Helium	404	0.20	0.96	0.21	2.40	18.02
529	Helium	203	0.21	2.00	0.89	1.20	9.09
530	Helium	404	0.23	1.07	0.25	2.40	18.28
531	Helium	202	0.23	2.20	1.08	1.20	9.07
532	Helium	404	0.28	1.34	0.40	2.40	18.05
533	Helium	201	0.30	2.79	1.74	1.19	9.01
534	Helium	404	0.34	1.62	0.59	2.40	18.05
535	Helium	202	0.35	3.28	2.40	1.20	9.05
536	Helium	404	0.40	1.87	0.78	2.40	18.23
537	Helium	202	0.40	3.74	3.12	1.20	9.13
538	Helium	403	0.45	2.09	0.97	2.40	18.16
539	Helium	202	0.45	4.23	3.98	1.20	9.07
540	Helium	406	0.48	2.23	1.11	2.41	18.27
541	Helium	202	0.49	4.59	4.69	1.20	9.10
542	Helium	403	0.55	2.60	1.50	2.40	18.19
543	Helium	202	0.56	5.28	6.21	1.20	9.08
544	Helium	413	0.060	0.27	0.017	2.45	18.55
545	Helium	202	0.062	0.58	0.77	1.20	9.12
546	Helium	403	0.15	0.72	0.12	2.40	18.26
547	Helium	202	0.16	1.48	0.49	1.20	9.06
548	Helium	404	0.19	0.91	0.18	2.40	18.13
549	Helium	202	0.20	1.88	0.79	1.20	9.04
550	Helium	401	0.21	1.00	0.22	2.38	18.16
551	Helium	202	0.22	2.06	0.95	1.20	9.12
552	Helium	401	0.27	1.29	0.37	2.38	18.18

Shot No.	Injected Gas	p_{fill} [kPa]	\dot{m}_{inj} [g/s]	$F \times 10^3$	$J \times 10^4$	p_{∞} [kPa]	$Re_{L,\infty}$ [$10^6/\text{m}$]
553	Helium	204	0.28	2.60	1.51	1.21	9.21
554	Helium	402	0.34	1.61	0.58	2.39	18.25
555	Helium	204	0.35	3.26	2.37	1.21	9.22
556	Helium	403	0.39	1.84	0.75	2.40	18.14
557	Helium	203	0.39	3.62	2.92	1.21	9.10
558	Helium	402	0.43	2.04	0.93	2.39	18.26
559	Helium	204	0.45	4.17	3.88	1.21	9.20
560	Helium	404	0.47	2.22	1.10	2.49	18.15
561	Helium	203	0.48	4.48	4.48	1.20	9.09
562	Helium	404	0.55	2.56	1.46	2.40	18.32
563	Helium	203	0.54	5.02	5.60	1.20	9.12
580	RC318	405	0.84	3.96	0.070	2.40	18.05
581	RC318	202	0.81	7.61	0.26	1.20	9.09
582	RC318	404	1.30	6.08	0.16	2.40	18.23
583	RC318	203	1.38	12.90	0.74	1.21	9.12
584	RC318	405	1.61	7.53	0.25	2.41	18.13
585	RC318	203	1.52	14.13	0.89	1.21	9.12
586	RC318	404	1.52	7.14	0.23	2.40	18.23
587	RC318	203	1.73	16.09	1.15	1.21	9.14
588	RC318	404	1.94	9.12	0.37	2.40	18.08
589	RC318	203	2.15	20.05	1.79	1.21	9.12
590	RC318	404	2.42	11.30	0.57	2.40	18.36
591	RC318	205	2.67	24.66	2.70	1.22	9.26
592	RC318	405	2.62	12.26	0.67	2.40	18.19
593	RC318	204	2.82	26.20	3.05	1.21	9.15
594	RC318	404	3.04	14.25	0.90	2.40	18.26
595	RC318	204	3.07	28.53	3.62	1.21	9.16
596	RC318	405	3.11	14.51	0.94	2.40	18.29
597	RC318	203	3.28	30.55	4.15	1.21	9.16
598	RC318	404	3.43	16.07	1.15	2.40	18.20
599	RC318	203	3.65	33.98	5.13	1.21	9.14
600	RC318	404	0.16	0.73	0.0024	2.40	18.24
601	RC318	202	0.61	5.74	0.15	1.20	9.12
602	RC318	404	1.08	5.05	0.11	2.40	18.07
603	RC318	205	1.10	10.19	0.46	1.22	9.15
604	RC318	403	1.37	6.41	0.18	2.40	18.20
605	RC318	205	1.44	13.27	0.78	1.22	9.25
606	RC318	404	1.61	7.57	0.25	2.40	18.09
607	RC318	205	1.66	15.38	1.05	1.22	9.15
608	RC318	405	1.97	9.20	0.38	2.41	18.33

Shot No.	Injected Gas	p_{fill} [kPa]	\dot{m}_{inj} [g/s]	$F \times 10^3$	$J \times 10^4$	p_{∞} [kPa]	$Re_{L,\infty}$ [$10^6/\text{m}$]
609	RC318	203	2.01	18.78	1.57	1.21	9.16
610	RC318	412	2.49	11.44	0.58	2.45	18.49
611	RC318	202	2.28	21.48	2.05	1.20	9.02
612	RC318	403	2.63	12.33	0.68	2.39	18.26
613	RC318	202	2.83	26.41	3.10	1.20	9.15
614	RC318	404	3.22	15.11	1.01	2.40	18.14
615	RC318	205	3.15	29.11	3.77	1.22	9.20
616	RC318	404	3.08	14.41	0.92	2.40	18.24
617	RC318	206	3.37	30.97	4.26	1.22	9.26
618	RC318	406	3.65	17.08	1.30	2.41	18.12
619	RC318	205	3.61	33.39	4.96	1.22	9.15
637	N/A	206	N/A	N/A	N/A	1.22	9.26
639	N/A	205	N/A	N/A	N/A	1.22	9.29

Diagnostic conditions

Shot No.	Experiment Type	Framing Rate [fps]	Pulse Width [ns]	Resolution [pixels]
425	Cone with trip	N/A, PCB only	N/A	N/A
441	Cone	N/A, PCB only	N/A	N/A
444	Injection, full field	30,262	40	912 x 240
445	Injection, full field	30,262	40	912 x 240
446	Injection, full field	30,262	40	912 x 240
447	Injection, full field	30,262	40	912 x 240
448	Injection, full field	30,262	40	912 x 240
449	Injection, full field	30,262	40	912 x 240
450	Injection, full field	30,262	40	912 x 240
451	Injection, full field	30,262	40	912 x 240
452	Injection, full field	30,262	40	912 x 240
453	Injection, full field	30,262	40	912 x 240
454	Injection, full field	30,262	40	912 x 240
455	Injection, full field	30,262	40	912 x 240
456	Injection, full field	30,262	40	912 x 240
457	Injection, full field	30,262	40	912 x 240
458	Injection, full field	30,262	40	912 x 240
459	Injection, full field	30,262	40	912 x 240
460	Injection, full field	30,262	40	912 x 240
461	Injection, full field	30,262	40	912 x 240
462	Injection, full field	30,262	40	912 x 240
463	Injection, full field	30,262	40	912 x 240
464	Injection, high speed	289,361	25	224 x 64
465	Injection, high speed	289,361	25	224 x 64
466	Injection, high speed	289,361	25	224 x 64
467	Injection, high speed	289,361	25	224 x 64
468	Injection, high speed	289,361	25	224 x 64
469	Injection, high speed	289,361	25	224 x 64
470	Injection, high speed	289,361	25	224 x 64
471	Injection, high speed	289,361	25	224 x 64
472	Injection, high speed	289,361	25	224 x 64
473	Injection, high speed	289,361	25	224 x 64
474	Injection, high speed	289,361	25	224 x 64
475	Injection, high speed	289,361	25	224 x 64
476	Injection, high speed	289,361	25	224 x 64
477	Injection, high speed	289,361	25	224 x 64
478	Injection, high speed	289,361	25	224 x 64
479	Injection, high speed	289,361	25	224 x 64

Shot No.	Experiment Type	Framing Rate [fps]	Pulse Width [ns]	Resolution [pixels]
480	Injection, high speed	289,361	25	224 x 64
481	Injection, high speed	289,361	25	224 x 64
482	Injection, high speed	289,361	25	224 x 64
483	Injection, high speed	289,361	25	224 x 64
524	Injection, full field	30,262	40	912 x 240
525	Injection, full field	30,262	40	912 x 240
526	Injection, full field	30,262	40	912 x 240
527	Injection, full field	30,262	40	912 x 240
528	Injection, full field	30,262	40	912 x 240
529	Injection, full field	30,262	40	912 x 240
530	Injection, full field	30,262	40	912 x 240
531	Injection, full field	30,262	40	912 x 240
532	Injection, full field	30,262	40	912 x 240
533	Injection, full field	30,262	40	912 x 240
534	Injection, full field	30,262	40	912 x 240
535	Injection, full field	30,262	40	912 x 240
536	Injection, full field	30,262	40	912 x 240
537	Injection, full field	30,262	40	912 x 240
538	Injection, full field	30,262	40	912 x 240
539	Injection, full field	30,262	40	912 x 240
540	Injection, full field	30,262	40	912 x 240
541	Injection, full field	30,262	40	912 x 240
542	Injection, full field	30,262	40	912 x 240
543	Injection, full field	30,262	40	912 x 240
544	Injection, high speed	289,361	25	224 x 64
545	Injection, high speed	289,361	25	224 x 64
546	Injection, high speed	289,361	25	224 x 64
547	Injection, high speed	289,361	25	224 x 64
548	Injection, high speed	289,361	25	224 x 64
549	Injection, high speed	289,361	25	224 x 64
550	Injection, high speed	289,361	25	224 x 64
551	Injection, high speed	289,361	25	224 x 64
552	Injection, high speed	289,361	25	224 x 64
553	Injection, high speed	289,361	25	224 x 64
554	Injection, high speed	289,361	25	224 x 64
555	Injection, high speed	289,361	25	224 x 64
556	Injection, high speed	289,361	25	224 x 64
557	Injection, high speed	289,361	25	224 x 64
558	Injection, high speed	289,361	25	224 x 64
559	Injection, high speed	289,361	25	224 x 64

Shot No.	Experiment Type	Framing Rate [fps]	Pulse Width [ns]	Resolution [pixels]
560	Injection, high speed	289,361	25	224 x 64
561	Injection, high speed	289,361	25	224 x 64
562	Injection, high speed	289,361	25	224 x 64
563	Injection, high speed	289,361	25	224 x 64
580	Injection, full field	30,262	40	912 x 240
581	Injection, full field	30,262	40	912 x 240
582	Injection, full field	30,262	40	912 x 240
583	Injection, full field	30,262	40	912 x 240
584	Injection, full field	30,262	40	912 x 240
585	Injection, full field	30,262	40	912 x 240
586	Injection, full field	30,262	40	912 x 240
587	Injection, full field	30,262	40	912 x 240
588	Injection, full field	30,262	40	912 x 240
589	Injection, full field	30,262	40	912 x 240
590	Injection, full field	30,262	40	912 x 240
591	Injection, full field	30,262	40	912 x 240
592	Injection, full field	30,262	40	912 x 240
593	Injection, full field	30,262	40	912 x 240
594	Injection, full field	30,262	40	912 x 240
595	Injection, full field	30,262	40	912 x 240
596	Injection, full field	30,262	40	912 x 240
597	Injection, full field	30,262	40	912 x 240
598	Injection, full field	30,262	40	912 x 240
599	Injection, full field	30,262	40	912 x 240
600	Injection, high speed	289,361	25	224 x 64
601	Injection, high speed	289,361	25	224 x 64
602	Injection, high speed	289,361	25	224 x 64
603	Injection, high speed	289,361	25	224 x 64
604	Injection, high speed	289,361	25	224 x 64
605	Injection, high speed	289,361	25	224 x 64
606	Injection, high speed	289,361	25	224 x 64
607	Injection, high speed	289,361	25	224 x 64
608	Injection, high speed	289,361	25	224 x 64
609	Injection, high speed	289,361	25	224 x 64
610	Injection, high speed	289,361	25	224 x 64
611	Injection, high speed	289,361	25	224 x 64
612	Injection, high speed	289,361	25	224 x 64
613	Injection, high speed	289,361	25	224 x 64
614	Injection, high speed	289,361	25	224 x 64
615	Injection, high speed	289,361	25	224 x 64

Shot No.	Experiment Type	Framing Rate [fps]	Pulse Width [ns]	Resolution [pixels]
616	Injection, high speed	289,361	25	224 x 64
617	Injection, high speed	289,361	25	224 x 64
618	Injection, high speed	289,361	25	224 x 64
619	Injection, high speed	289,361	25	224 x 64
637	Cone, full field	30,262	40	912 x 240
639	Cone, high speed	345,177	25	384 x 40